

Université du Québec
Institut National de la Recherche Scientifique
Centre Énergie, Matériaux et Télécommunications

**STM and DFT Study of 2D Self-Assembled
Molecular Nanostructures on Surfaces**

Par
Riccardo Gatti

Mémoire présentée pour l'obtention du grade de Maître (M.Sc.)
en sciences de l'énergie et des matériaux

Jury d'évaluation

Président du jury et examineur interne	Prof. Luca Razzari INRS-ÉMT
Examineur externe	Prof. Jérôme Claverie Département de Chimie UQAM
Examineur interne	Prof. Luca Razzari INRS-ÉMT
Directeur de recherche	Prof. Federico Rosei INRS-ÉMT

ACKNOWLEDGEMENTS

I thank Prof. F. Rosei for having given me the opportunity of doing my Master's degree in his group at INRS, in an international and stimulating environment. For me coming to Montreal was important also for personal reasons, so I thank him twice. I thank Stefany for being next to me in these two beautiful years, and my family for having always supported me. I want to thank many people working at INRS starting from the research associates J. Lipton-Duffin and J. MacLeod, who were always available for technical and non-technical discussions. I owe them most of the things I learned in these two years at INRS. I thank my co-workers L. Cardenas, L.E. Dinca, M. El-Garah and C. Fu for helpful discussions. I thank C. Chabanier and C. Harnagea for their help any time it was asked. I thank G. Chen, L. Cardenas, H. Black and M.A. Mezour for help in the lengthy preparation of the gold samples. I thank L.E. Dinca for the fun afternoons at INRS attacking each other's office. I thank the Italians "Il Burlone", F. De Marchi, "Il Conte", L. Corbellini, Yoann "Dzeeur" and many other people at INRS for the fun lunches and table tennis matches at INRS. I thank D. Bongiovanni "Dominkio" for the several babyfoot matches he made me lose "TEN-ZEROS" and all the other players, Belete, Tan Long, Simon and others.

STATEMENT OF ORIGINALITY

The work presented herein is original in all his aspects and was not reported before elsewhere. All experimental procedures, including sample preparation and deposition were developed by the Author, save for the STM work, which was performed in collaboration with J.M. MacLeod, and the XPS experiments, which were performed in collaboration with C. Chabanier and J.A. Lipton-Duffin. The gold sample preparation was done in collaboration with L. Cardenas. The theoretical calculations were performed in collaboration with J.A. Lipton-Duffin and J.M. MacLeod. The molecular precursors were synthesized by our collaborators from McGill University and Université de Laval.

RÉSUMÉ

Nous avons étudié l'auto-assemblage de molécules organiques sur des surfaces à l'interface liquide-solide avec le microscope à effet tunnel. C'est une technique qui permet la visualisation des atomes et molécules avec une résolution sub-nanométrique. En s'appuyant sur cette technique de caractérisation, ainsi que des calculs théoriques, nous avons eu un aperçu de la nature des liaisons faibles contribuant à la stabilisation latérale des systèmes étudiés. Nous avons également étudié la polymérisation de surface, qui est importante pour des applications pratiques puisse qu'elle permet une meilleure stabilité et de meilleurs propriétés électroniques.

L'auto-assemblage est une technique puissante pour la fabrication de couches minces organiques et pour le nano-design des surfaces dans l'approche bottom-up (de bas en haut). Ce travail caractérise les aspects de base de l'auto-assemblage à l'échelle nanométrique. Bien que l'auto-assemblage soit utilisé aujourd'hui dans les dispositifs utilisant des petites molécules, beaucoup reste encore à faire pour comprendre ce phénomène fascinant, particulièrement pour le contrôler méthodiquement.

En 1947 le premier transistor fut inventé par Bardeen, Brattain et Shockley au sein des laboratoires Bell. Quelques années plus tard, le premier transistor en silicium est fabriqué par Texas Instrument. Peu de temps après chez Texas Instrument toujours, Kilby et Noyce ont fabriqué le premier circuit intégré. Enfin le premier transistor à effet de champ à grille isolée a vu le jour en 1960 aux Laboratoires Bell, ouvrant ainsi la voie à l'électronique moderne. Dans les derniers cinquante ans, les dimensions des composants électroniques sont réduites, suivant ainsi la loi empirique de Moore ¹, qui dit que le nombre de transistors dans les circuits intégrés est doublé tous les 18 mois. (Figure R 1a). Jusqu'à aujourd'hui, l'industrie électronique suit la loi de Moore avec le cout de fabrication de transistor qui diminue exponentiellement, et pour conséquence le cout des machines lithographies augmente (Figure R 1b). Cependant, il faut noter que durant ces derniers vingt ans, la photolithographie, qui est la technique la plus utilisée dans l'industrie, a atteint ses limites fondamentales ².

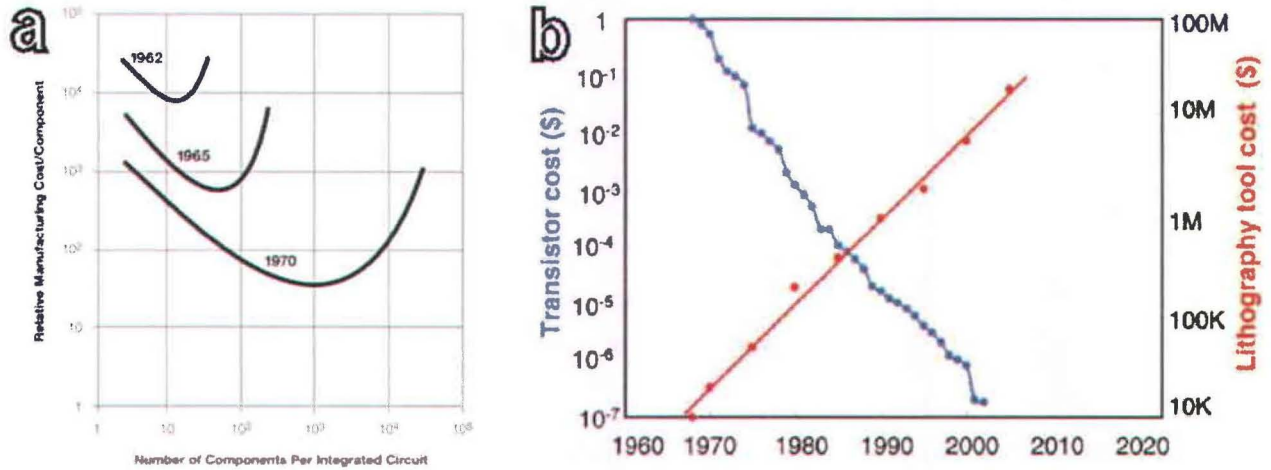


Figure R 1: a) Prédiction du nombre des éléments dans les circuits intégrés. b) Le cout des transistors et des machines lithographiques vs. année. Reproduits de a) réf. ¹ et b) réf. ³.

Ces limites ont motivé la communauté scientifique à chercher des solutions qui permettront la fabrication des éléments électroniques de plus en plus petits et donc des ordinateurs plus performants. Néanmoins, la taille réduite des composants électroniques induit quelques problèmes. Nous pouvons citer, comme exemple, la prédominance de la résistance parasite et la limite du transistor à effet de champ à grille isolée plan (Figure R 2). En plus des techniques lithographiques alternatives conventionnelles, des méthodes non conventionnelles qui ne utilisent pas de rayons de lumière ont été proposées, dans une approche top-down et bottom-up.

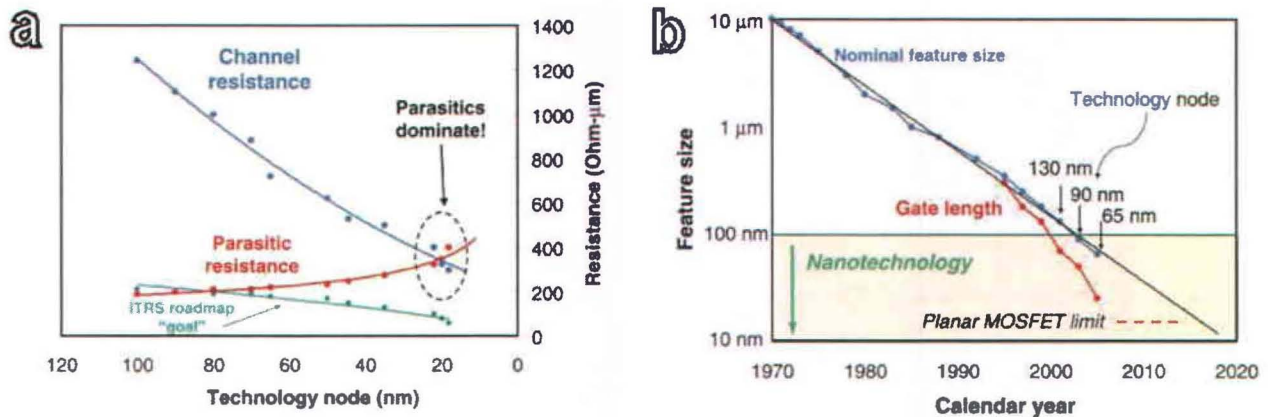


Figure R 2 a) Résistance parasite et du canal conducteur vs. niveau de la technologie. b) Longueur de la grille du transistor vs. année. Reproduits de réf. ³.

L'auto-assemblage est une technique pour le nano design de surfaces qui s'intègre dans une approche bottom-up ⁴. Au niveau moléculaire, un nombre infini de structures possibles peut être obtenu en changeant correctement les groupes fonctionnels des composantes de base, ce qui mène à des motifs moléculaires spécifiques. De plus, l'auto-assemblage moléculaire est primordial pour la fabrication de couches minces organiques, ces dernières sont intéressantes pour des applications telles que les dispositifs organiques qui émettent de la lumière, les semi-conducteurs organiques et dans le domaine du photovoltaïque.

L'Auto-assemblage, ou encore la formation automatique des systèmes ordonnés, est considéré par des experts du domaine comme étant l'un des plus importants concepts du 21^{ème} siècle ⁵. Une des raisons fondamentale est que l'auto-assemblage existe dans toutes les échelles, on les trouve de la galaxie et des objets macroscopiques jusqu'aux molécules et aux atomes (Figure R 3). L'auto-assemblage moléculaire est intéressant pour ses aspects fondamentaux, puisqu'il est la base de la vie, ainsi que pour des aspects pratiques présentés auparavant. Les réseaux moléculaires auto-assemblés sont des systèmes thermodynamiquement stables où les molécules sont liées avec des liaisons non covalentes (systèmes supramoléculaires ⁶). Ces systèmes se forment spontanément sur des surfaces si les molécules sont plus stables dans l'état ordonné au sein d'un réseau organique à deux dimensions que dans l'état désordonné.

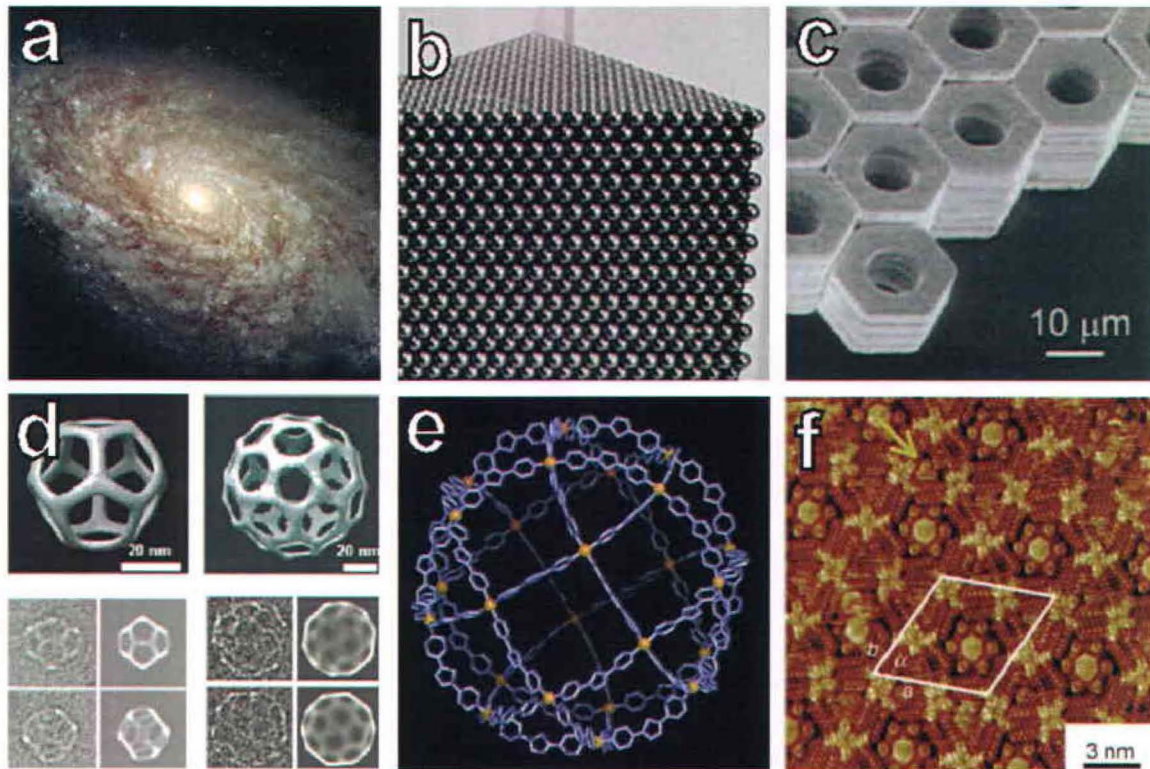


Figure R 3: a) La galaxie NGC 4414; b) balles d'acier auto-assemblés; c) objets micrométriques assemblés par forces capillaires; d) polyèdre de DNA auto-assemblé; e) cage moléculaire à trois dimensions; f) nanostructure moléculaire à deux dimensions avec quatre composants auto-assemblée. Reproduits de a) réf. ⁷, b) réf. ⁸, c) réf. ⁹, d) réf. ¹⁰, e) réf. ¹¹ et f) réf. ¹².

En plus d'être utilisé comme méthode pour le nano design, l'auto-assemblage est utile pour la fabrication de surfaces fonctionnelles avec des propriétés spécifiques, comme la chiralité et l'hydrophobicité. Par exemple, des mailles moléculaires poreuses peuvent être utilisées pour la détection des molécules, tandis que les molécules semi-conducteurs peuvent être utilisés pour la fabrication des transistors organiques.

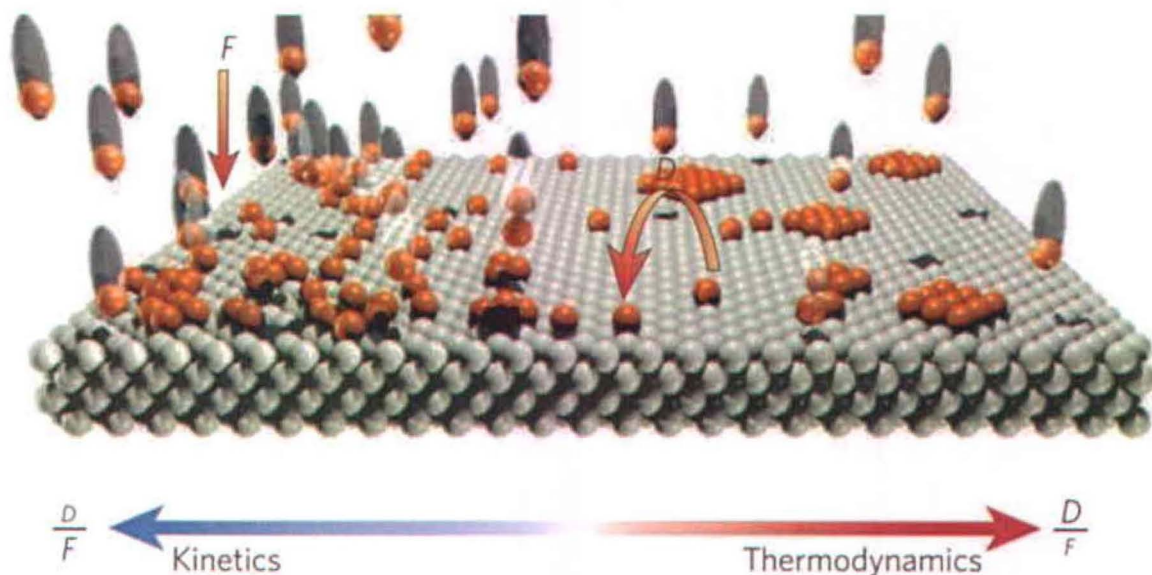


Figure R 4: Visualisation atomistique des processus de croissance de couches moléculaires sur surfaces. Reproduit de réf. ¹³.

Les réseaux moléculaires auto-assemblés peuvent être stabilisés par plusieurs forces non-covalents, telles que la force de Van der Waals, le π - π stacking, la liaison hydrogène ou par la coordination métallique (Figure R 5). L'équilibre délicat entre les interactions intermoléculaires et les interactions molécule-substrat mène à la stabilisation des structures auto-assemblées ¹³. Dans ce travail les systèmes étudiés sont stabilisés latéralement par des interactions de Van der Waals entre les chaînes alkyles, des liaisons hydrogène entre les groupes carboxyliques et par un autre type de force intermoléculaire faible: le lien halogène.

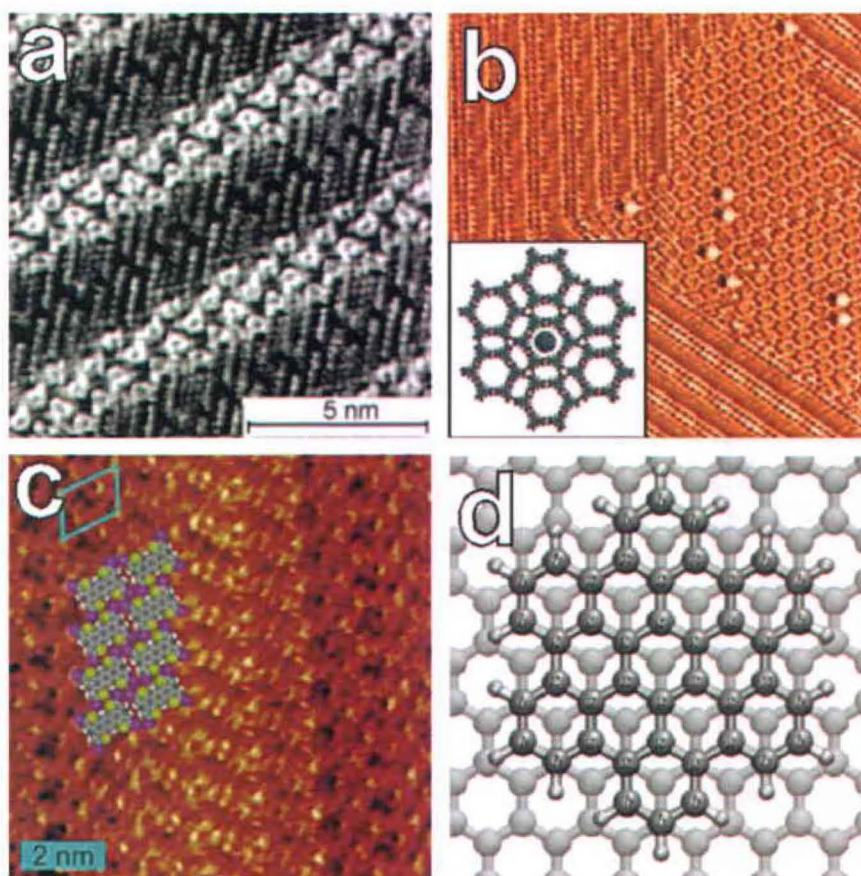


Figure R 5: Mailles organiques auto-assemblées peuvent être stabilisées par interactions comme a) van der Waals, b) lien hydrogène, c) lien halogène et d) π - π stacking. Reproduits de a) réf. ¹⁴, b) réf. ¹⁵, c) réf. ¹⁶ et d) réf. ¹⁷.

Les structures à deux dimensions stabilisées par des liens halogènes sont intéressantes parce que les halogènes ont une double polarisation très particulière (Figure R 6). L'extrémité du lien carbone-halogène est chargée positivement (σ -hole), alors que sur l'halogène il y a un cercle d'accumulation de charge négative ¹⁸. Le potentiel électrostatique moléculaire du σ -hole devient plus positif quand on descend dans le septième groupe de la table périodique des éléments.

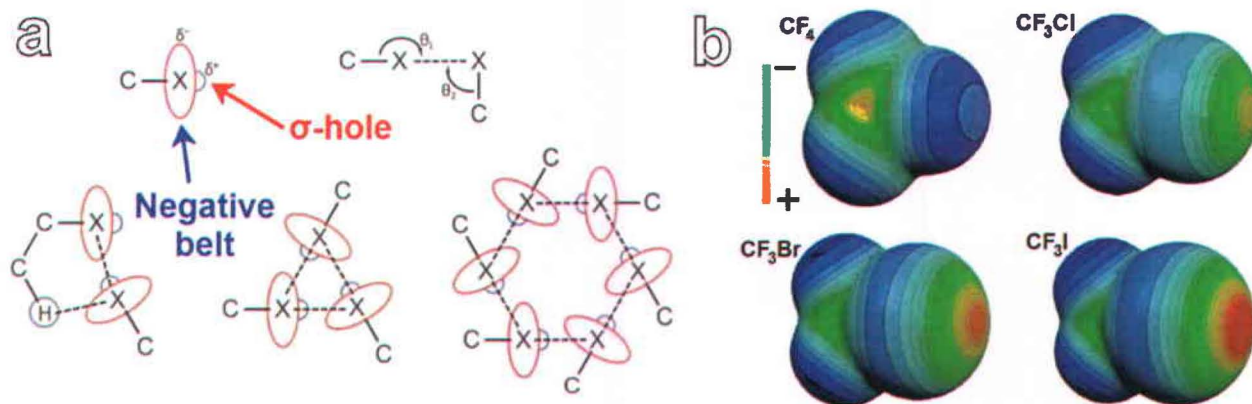


Figure R 6: Plan de la polarisation au lien carbone-halogène; b) Potentiel à la σ -hole en fonction de la dimension de l'halogène. Reproduit de a) réf. ¹⁹, et b) réf. ¹⁸.

En plus de l'intérêt de l'auto-assemblage pour une approche fondamentale, le fait d'utiliser cette méthode pour fabriquer des dispositifs doit être accompagné d'une amélioration de la stabilité de ces structures liées faiblement. Durant la dernière quinzaine d'années, les chercheurs ont étudié la polymérisation de surface afin de résoudre ce problème, celle-ci augmenterait la stabilité chimique et thermodynamique des structures auto-assemblées (Figure R 7). En outre, la polymérisation de surface permet de meilleures propriétés électroniques, grâce aux orbitales conjuguées. Les réactions de polymérisation de surface peuvent être activées par différentes méthodes : avec un catalyseur, en fournissant de l'énergie thermique, avec des rayons de lumière ou encore avec la pointe d'un microscope à effet tunnel. Dans ce travail, la polymérisation de surface a été étudiée en utilisant une radiation ultra-violettes ainsi que l'énergie thermique en présence d'un catalyseur (réaction d'Ullmann).

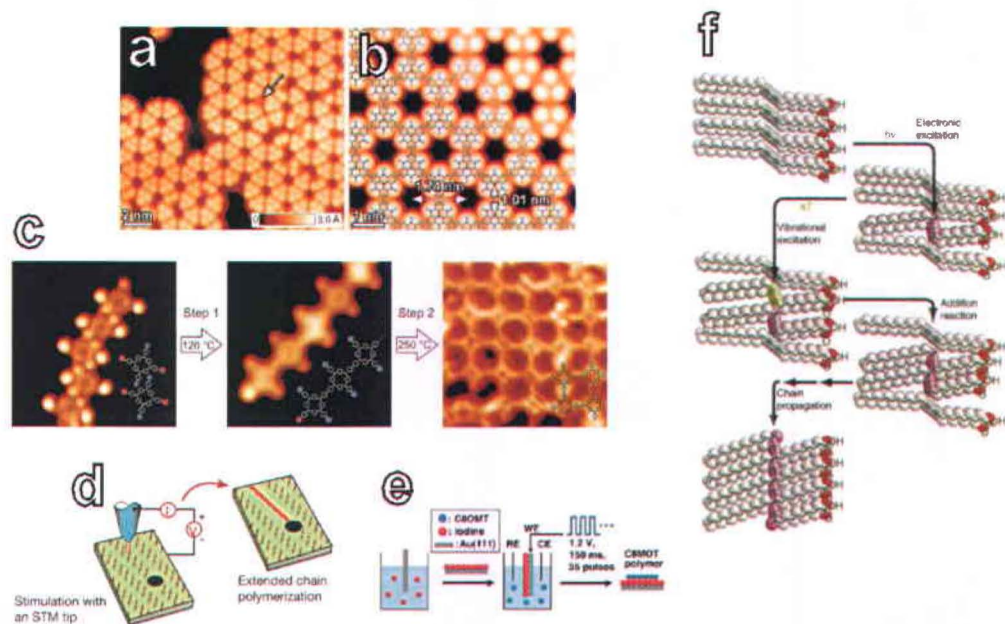


Figure R 7: Image de microscopie à effet tunnel a) expérimentale et b) simulée de mailles covalentes à deux dimensions; c) les pas pour obtenir une maille covalente à deux dimensions avec la réaction d'Ullmann; d) polymérisation à une dimension activé par la pointe du microscope à effet tunnel; e) la polymérisation électrochimique; f) le mécanisme de la polymérisation à une dimension de diacétylènes. Reproduits de a),b) réf. ²⁰, c) réf. ²¹, d) réf. ²², e) réf. ²³ et f) réf. ²⁴.

Comme nous l'avons déjà décrit auparavant, dans ce projet les systèmes sont caractérisés par microscopie à effet tunnel. Cette technique est utilisée typiquement pour la caractérisation et la manipulation de systèmes à deux dimensions à l'échelle nanométrique. Inventée par Binnig et Rohrer en 1981 aux Laboratoires Bell, le microscope à effet tunnel permet la visualisation des atomes et molécules (Figure R 8a). Il est composé d'une pointe aiguisée et électriquement conductrice, celle-ci est montée sur des transducteurs piézoélectriques qui permettent le déplacement dans les trois directions (Figure R 8b). Quand la pointe est assez proche d'une surface conductrice, par exemple à une distance entre 1 et 10 Å, les électrons peuvent alors passer de la surface vers la pointe et vice versa.

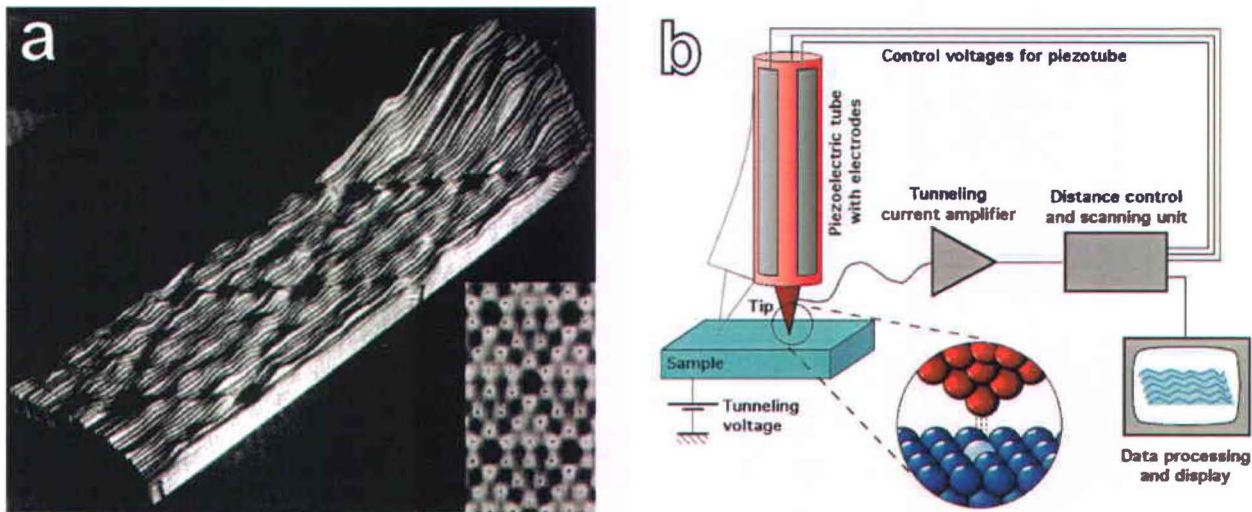


Figure R 8: a) La première image de microscopie à effet tunnel jamais obtenue (1983), montrant le relief des deux cellules de la surface Si(111) reconstruit; b) visualisation schématique du microscope à effet tunnel. Reproduits de a) réf. ²⁵ et b) réf. ⁷.

Les images obtenues par microscopie à effet tunnel fournissent typiquement des informations concernant la densité des états proches du niveau de Fermi. En plus, la microscopie à effet tunnel permet d'étudier soit les états électroniques occupés, soit les états vides en changeant simplement la polarité de la tension appliquée à la pointe (Figure R 9). Il faut noter que lorsque l'on image des couches moléculaires, les états occupés et vides sont référés aux orbitales moléculaires occupées et vides, même si cette approximation ne prend pas en compte que la microscopie à effet tunnel relate les états électroniques des molécules et du substrat sur lequel elles sont déposées.

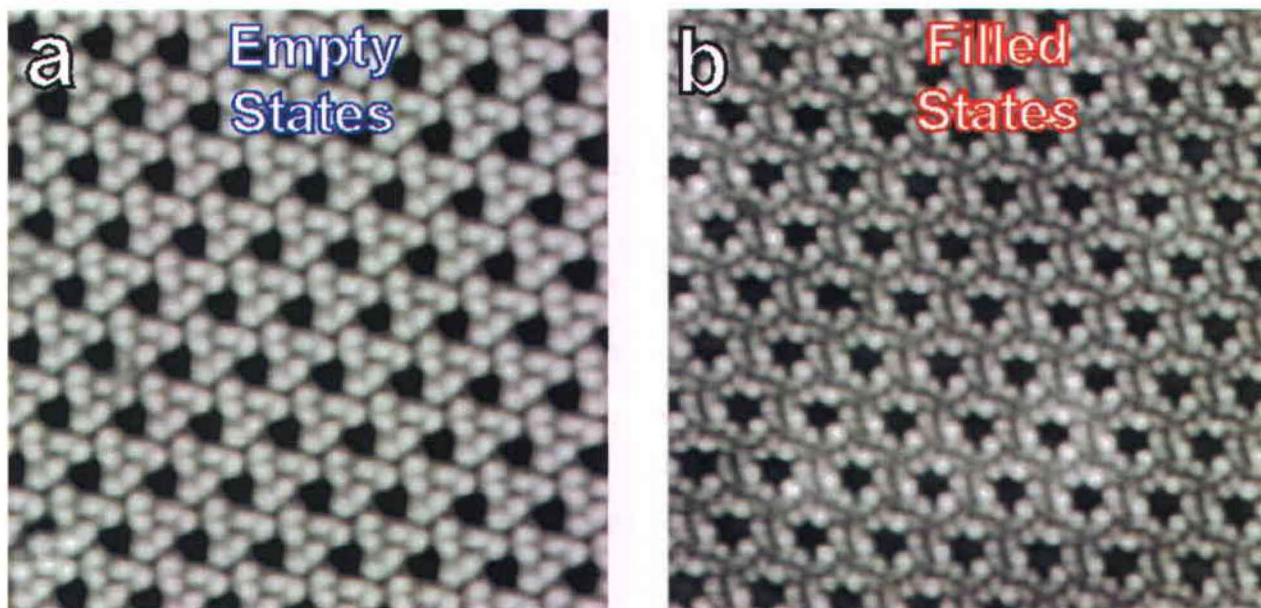


Figure R 9: Image du microscope à effet tunnel montrant les états électronique a) vides et b) pleins des molécules 1,3,5-triphenyl-benzene adsorbées sur une surface B-Si(111) à 77 K. Reproduits de réf. ²⁶.

En la microscopie à effet tunnel, au lieu de la microscopie à force atomique par exemple, la topographie de la surface dépend de sa structure électronique. En fait, une image de microscopie à effet tunnel est une carte de la convolution de la densité des états électroniques de la pointe et de la surface proche du niveau de Fermi. Figure R 10a est une belle preuve de ça, étant une image de les états propres d'un corral quantique fait de 48 atomes de fer sur une surface Cu(111). Le contraste ondulé à l'intérieur du corral n'est pas dû à la topographie de la surface, plutôt à la modulation de la densité des états des atomes de fer.

En plus à sa résolution exceptionnelle, le microscope à effet tunnel est très puissant parce qu'il permet la manipulation de la matière à l'échelle atomique, par des interactions entre la pointe et la surface que peuvent être modifiées en changeant le voltage appliqué entre le deux (Figure R 10).

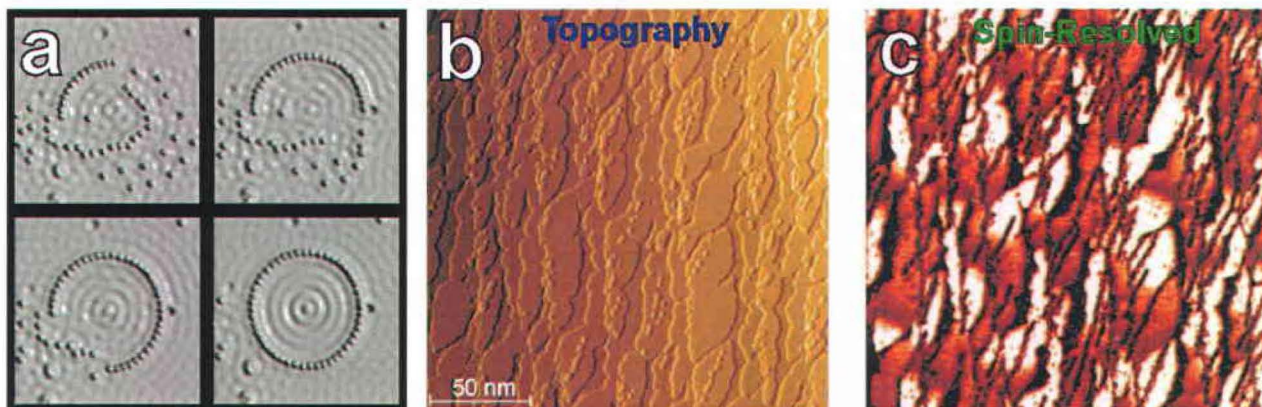


Figure R 10: a) Les pas pour la fabrication d'un anneau de 48 atomes de fer sur une surface Cu(111); b) topographie et c) image avec les états de spin résolus d'une couche de fer nanocrystalline. Reprécus de réf. ²⁷ et b),c) réf. ²⁸.

En parallèle de la microscopie à effet tunnel, les systèmes de ce projet ont été caractérisés avec des calculs théoriques. Un des plus importants exploits du dernier siècle est la mécanique quantique (peut-être avec la théorie de la relativité d'Einstein), une branche de la physique entièrement nouvelle qui décrit les lois de la nature depuis l'échelle moléculaire aux particules subatomiques. La théorie de la fonctionnelle de la densité est une technique vraiment puissante développée dans les années 1960, qui permet de résoudre les équations fondamentales des atomes et molécules, à savoir l'équation de Schrödinger ²⁹.

L'avantage de cette théorie comparée avec les autres méthodes théoriques utilisées en chimie quantique est qu'elle permet d'obtenir la structure électronique d'un matériel en simplifiant un problème à N électrons en principe plus compliqué. Dans les décennies passées, cette théorie est non plus seulement utilisée par quelques experts scientifiques, mais est devenue également un outil puissant dans plusieurs domaines, comme la physique, la chimie, les sciences de matériaux et la géologie. Une étude récente a montré que les trois articles les plus cités dans la famille des journaux Physical Review sont tous des articles concernant la théorie de la fonctionnelle de la densité. De la même façon, quatre des cinq articles les plus cités par les chimistes en 2003 ³⁰, ainsi que l'article le plus cité par les physiciens depuis 1994, sont aussi des articles de la théorie de la fonctionnelle de la densité. Cette théorie a contribué de manière très importante à la progression scientifique, de la synthèse de l'ammonie par catalyse hétérogène à l'étude de la fragilité des métaux par impuretés en passant par l'élaboration des modèles pour la formation des planètes.

Dans ce projet nous avons étudié l'auto-assemblage à deux dimensions en surface en utilisant des molécules halogénées et des molécules qui contiennent un groupe diacétylène, c'est-à-dire avec deux liaisons triple carbone-carbone alternées par des liaisons simples. Le travail sur les molécules halogénées a été fait en collaboration avec le groupe du Prof. D.F. Perepichka's du Département de Chimie de l'Université McGill, alors que le travail avec les molécules diacétylènes a été réalisé en collaboration avec le groupe du Prof. J.-F. Morin du Département de Chimie de l'Université Laval. Les collaborateurs ont contribué à ce projet avec la synthèse des molécules.

Les mailles organiques auto-assemblées ont été étudiées à l'interface entre une solution et les substrats graphite et Au(111). Grâce à leur basse réactivité, ces substrats sont idéals pour les expériences dans l'air. Les résultats avec le graphite nous permettent d'étudier les interactions intermoléculaires, puisque l'interaction molécule-substrat est faible, alors que les résultats avec les surfaces d'or nous donnent des informations sur les interactions entre les molécules et le substrat. En plus, les expériences avec Au(111) nous permettent d'étudier la polymérisation de surface, rendue possible grâce aux propriétés de l'or en tant que catalyseur.

L'étude systématique des molécules halogénées TIPT et TBPT montre que sur le graphite les deux mailles organiques sont similaires (Figure R 11 et Figure R 12). Ces structures sont différentes des structures reportées dans la littérature pour les molécules similaires TIPB et TBPB sur graphite³¹⁻³². Les calculs théoriques montrent que les structures à deux dimensions de TIPT et TBPT sont stabilisées latéralement par liaisons hydrogène faibles du type $X\cdots H$, où X est l'halogène et H l'atome d'hydrogène. En plus, le centre triazine de la TIPT et TBPT rend ces molécules plus raides que TBPB et TIPB. Ceci est important du point de vue entropique, parce qu'une molécule raide a moins d'états entropiques initiales accessibles, ainsi l'auto-assemblage de TIPT et TBPT est plus favorable que celui de TIPB et TBPB. Il est intéressant de noter qu'en variant le solvant, la TBPT forme une maille à deux dimensions qui n'est pas observée dans le cas de la TIPT, soulignant la pertinence de l'énergie de ces systèmes stabilisés par liaisons non covalentes faibles.

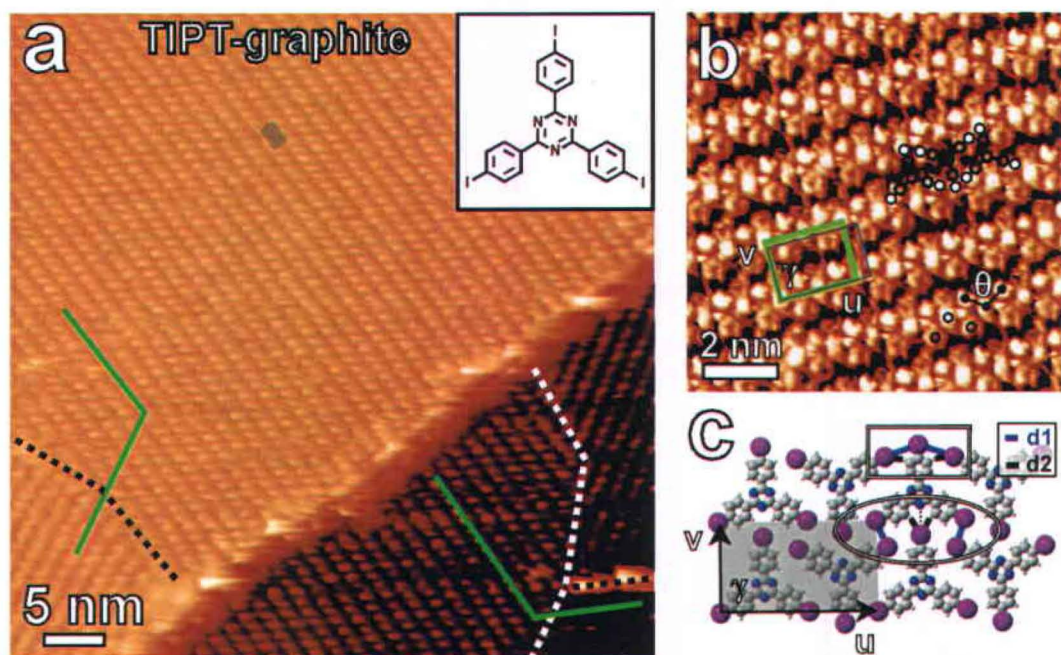


Figure R 11: a),b) Images de microscopie à effet tunnel et c) modélisé des molécules TIPT sur graphite – a) ($56.8 \times 56.8 \text{ nm}^2$, $V_s = -0.85 \text{ V}$ $I_t = 165 \text{ pA}$) et b) ($9.8 \times 9.8 \text{ nm}^2$, $V_s = -1.0 \text{ V}$ $I_t = 150 \text{ pA}$). Les paramètres de la cellule unitaire sont $u = 2.04 \pm 0.09 \text{ nm}$, $v = 1.54 \pm 0.09 \text{ nm}$ and $\gamma = 90 \pm 5^\circ$.

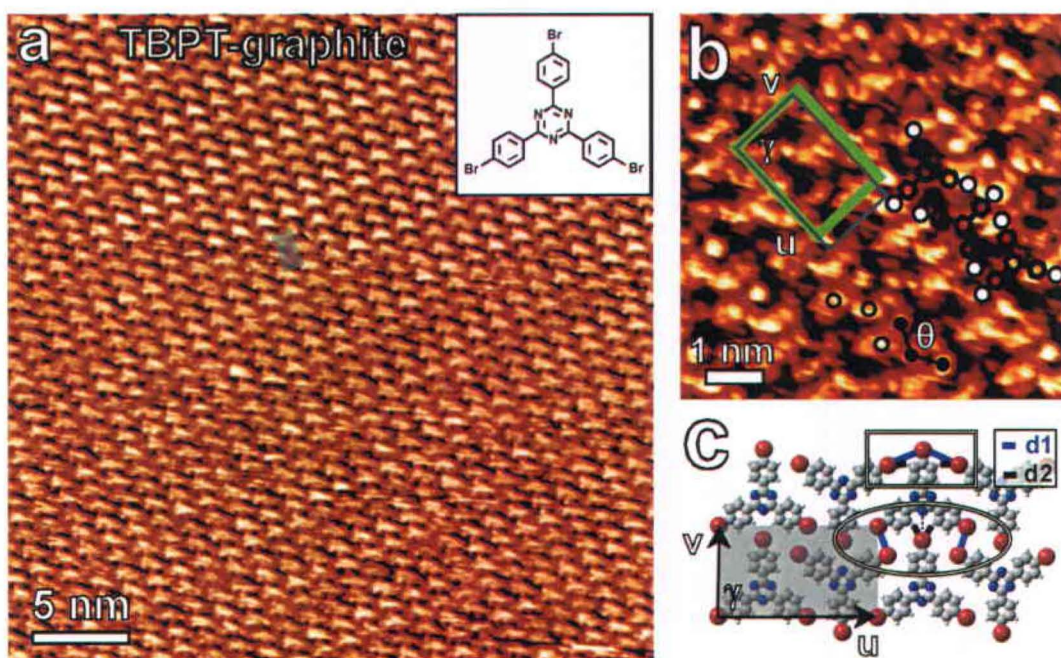


Figure R 12: a),b) Images de microscopie à effet tunnel et c) modélisé des molécules TBPT sur graphite – a) ($36.4 \times 36.4 \text{ nm}^2$, $V_s = -1.20 \text{ V}$ $I_t = 120 \text{ pA}$) et b) ($6.6 \times 6.6 \text{ nm}^2$, $V_s = -1.60 \text{ V}$ $I_t = 117 \text{ pA}$). Les paramètres de la cellule unitaire sont $u = 2.05 \pm 0.09 \text{ nm}$, $v = 1.47 \pm 0.08 \text{ nm}$ and $\gamma = 89 \pm 5^\circ$.

La TIPT et la TBPT se comportent différemment sur Au(111). Alors que la TIPT s'auto-assemble avec domaines similaires à l'homologue TIPB (Figure R 13a,b), comme reporté dans la littérature, le motif obtenu avec la TBPT a montré des caractéristiques intéressants dû à l'effet du substrat. Les molécules TBPT s'assemblent en deux phases différentes sur les deux zones fcc et hcp du substrat d'or reconstruit (Figure R 13c). Cette dernière est la première molécule reportée qui est sensible à ces deux régions du substrat à l'interface avec une solution. Puisque ce comportement n'a pas été reporté pour la molécule homologue TBPB, nous croyons que c'est dû à la présence du centre triazine. Ce centre, en faisant les molécules TBPT plus raides, mène à des interactions entre les molécules et le substrat qui sont plus fortes. La présence des deux phases est aussi favorisée par la similarité entre le deux polymorphes.

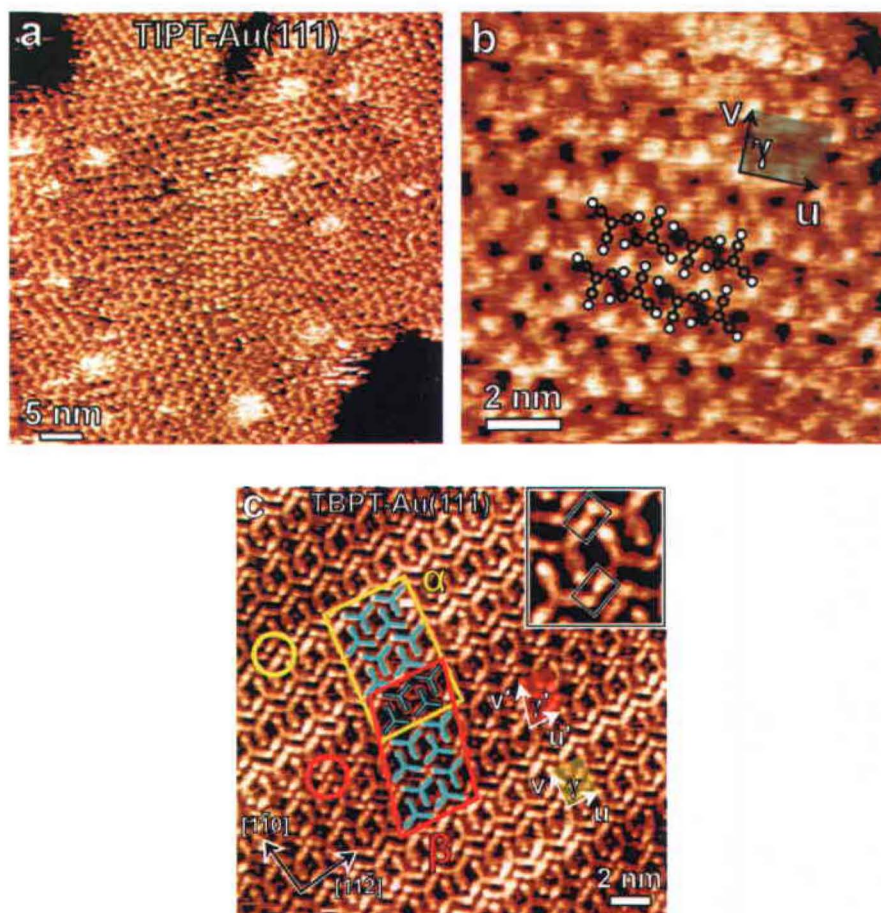


Figure R 13: Images de microscopie à effet tunnel des molécules a),b) TIPT et c) TBPT sur Au(111) – a) ($50.0 \times 50.0 \text{ nm}^2$, $V_s = -0.62 \text{ V}$ $I_t = 177 \text{ pA}$), b) ($11.7 \times 11.7 \text{ nm}^2$, $V_s = -0.79 \text{ V}$ $I_t = 231 \text{ pA}$) et c) ($20.7 \times 20.7 \text{ nm}^2$, $V_s = +0.10 \text{ V}$ $I_t = 200 \text{ pA}$).

L'étude sur les diacétylènes montre que l'organisation des molécules Maude-2-041 sur le graphite est défavorable pour la polymérisation (Figure R 14a). En particulier, les carbones 1,4 sont très loin en conséquence de l'entrave imposée par les anneaux phényles. Étant donné que la maille à deux dimensions des molécules Maude-2-041 sur le graphite est défavorable pour la polymérisation, on a étudié d'autres molécules contenant des atomes d'azote, SR-10-152 et SR-10-134. L'objectif était d'obtenir une configuration d'adsorption des anneaux phényles verticale par les paires d'électrons des azotes, ce qui présente une interaction plus forte que l'adsorption planaire, celle-ci serait favorable pour obtenir la polymérisation. Nos résultats indiquent que probablement cette interaction plus forte entre les molécules et la surface est en fait présente, vu qu'il y a des régions du substrat avec sub-monolayer couverture (Figure R 14b). De toute façon, les mailles organiques ordonnées à deux dimensions n'ont pas été obtenues, donc finalement nous n'avons pas réussi à obtenir des polymères de surface.

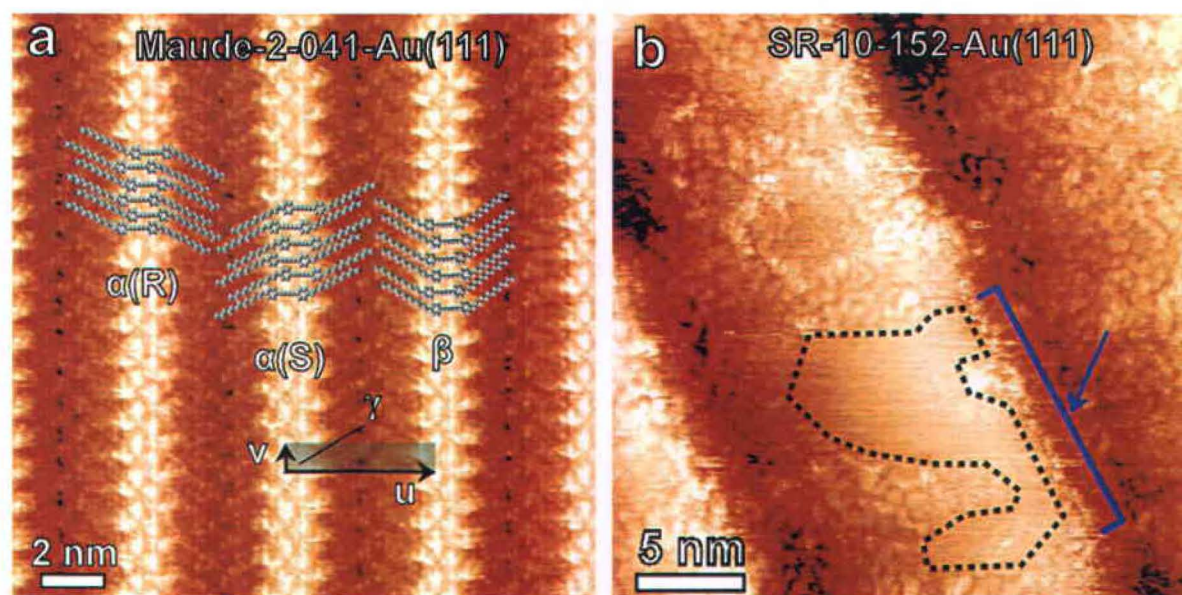


Figure R 14: Images de microscopie à effet tunnel des molécules a) Maude-2-041 sur graphite et b) SR-10-152 sur Au(111) – a) ($18.6 \times 18.6 \text{ nm}^2$, $V_s = -0.85 \text{ V}$, $I_t = 150 \text{ pA}$), b) ($27.4 \times 27.4 \text{ nm}^2$, $V_s = -0.43 \text{ V}$, $I_t = 168 \text{ pA}$).

Les études futures avec les molécules halogénées pourraient être basées sur la compréhension des mécanismes à sub-monolayer sur Au(111). Ce projet serait très intéressant pour une meilleure compréhension de l'équilibre entre les interactions

moléculaires et les interactions entre les molécules et le substrat. Les calculs théoriques qui prennent en compte aussi la présence du substrat peuvent être vraiment utiles dans cette perspective. En ce qui concerne la polymérisation à l'interface entre la surface et une solution, il y a encore de travail à faire pour la TBPT et la TIPT. En particulier, il serait très important de comprendre le mécanisme d'adsorption moléculaire quand les solutions sont déposées sur un substrat à haute température.

Il y a aussi de travail à faire pour les diacétylènes. Obtenir la configuration d'adsorption avec les anneaux phényles verticales sur Au(111) est plus difficile que les expériences sur le graphite. Réaliser des expériences sous vide pourrait être une solution, grâce à un environnement plus contrôlé. Une étude en fonction de la température pourrait résoudre des problèmes quant aux barrières d'activation qui peuvent inhiber la formation des mailles organiques ordonnées de plusieurs dizaines de nanomètres.

ABSTRACT

The self-assembly of organic molecules was investigated on surfaces at the liquid-solid interface with scanning tunneling microscopy (STM), a technique that allows real-space imaging of single molecules with sub-nm resolution. Combining the experimental data with density functional theory (DFT) calculations provides insight in the nature of the weak intermolecular bonds involved in the lateral stabilization of the investigated systems. Surface polymerization of the assembled structures was also attempted, an important step towards practical applications thanks to the higher stability and better electronic properties of the polymerized structures.

Self-assembly is a powerful technique for the fabrication of organic thin layers and the bottom-up nanopatterning of surfaces. This work describes fundamental aspects of self-assembly at the sub-molecular scale. Despite being important in small-molecule devices, much still has to be learned about this fascinating phenomenon, especially in terms of rationally controlling the assembly. This work contributes to the basic understanding of molecular self-assembly.

TABLE OF CONTENTS

ACKNOWLEDGEMENTS	i
STATEMENT OF ORIGINALITY	ii
RÉSUMÉ	iii
ABSTRACT	xix
TABLE OF CONTENTS	xx
LIST OF TABLES	xxiii
LIST OF FIGURES	xxv
LIST OF EQUATIONS	xli
LIST OF ACRONYMS	xlii
Chapter 1. INTRODUCTION	1
Chapter 2. SELF-ASSEMBLY	3
Chapter 3. SURFACE POLYMERIZATION	10
Chapter 4. SCANNING TUNNELING MICROSCOPY	13
4.1 THE NANOSCOPE III.....	19
Chapter 5. THEORETICAL METHODS:	
DENSITY FUNCTIONAL THEORY	22
5.1 THE EXCHANGE-CORRELATION FUNCTIONALS USED:	
B3LYP, M06-L AND M06-2X	28
5.1.1 THE B3LYP FUNCTIONAL	35
5.1.2 THE M06-L FUNCTIONAL	37
5.1.3 THE M06-2X FUNCTIONAL.....	39

5.2 THE BASIS SET	40
5.2.1 ALL-ELECTRONS POPLER BASIS SETS: 6-31G AND 3-21G.....	44
5.2.2 EFFECTIVE CORE POTENTIAL BASIS SETS: LanL2DZ.....	45
Chapter 6. THE INVESTIGATED MOLECULES.....	46
6.1 HALOGENATED PRECURSORS	47
6.2 DIACETYLENE PRECURSORS.....	48
Chapter 7. SUBSTRATES	49
7.1 HOPG.....	50
7.2 Au(111).....	52
Chapter 8. RESULTS AND DISCUSSION.....	59
8.1 THE CHOICE OF THE FUNCTIONAL.....	59
8.2 THE CHOICE OF THE BASIS SET	63
8.3 HALOGENATED MOLECULES.....	66
8.3.1 TIPT ON HOPG.....	66
8.3.2 TBPT ON HOPG	78
8.3.3 TBPT-co-HEPTANOIC ON HOPG	83
8.3.4 TBPT ON Au(111).....	94
8.3.5 TIPT ON Au(111)	118
8.4 DIACETYLENE MOLECULES	121
8.4.1 MAUDE-2-041 ON HOPG	122
8.4.2 SR-10-152 ON HOPG	131
8.4.3 SR-10-134 ON HOPG	137
Chapter 9. CONCLUSIONS AND PERSPECTIVES	139
LIST OF PUBLICATIONS	141

LIST OF ATTENDED CONFERENCES	142
CURRICULUM VITAE	143
REFERENCES	145

LIST OF TABLES

Table 8.1: Summary of the tested functionals.....	60
Table 8.2: Performance of the tested functionals for the TBPT ² polymorph of Table 8.5, using the 6-31G** basis set. See Figure 8.1 for labels. The central processing unit (CPU) times were normalized to the number of iterations of the optimization.	61
Table 8.3: Effect of polarized functions on the 6-31G basis set. Calculations for the 2D SAMN of TBPT molecules of Figure 8.1, using the M06-2X functional. Note that this functional is the most computationally expensive of Table 8.2. See Figure 8.1 for labels. The CPU times were normalized to the number of iterations of the optimization.....	64
Table 8.4: Experimental and computed unit cell parameters and computed interatomic distances (see Figure 8.5c and Figure 8.15c for labels) of the TIPT and TBPT molecular network at the solution-HOPG interface (M06-L/LanL2DZ and 6-31G** levels of theory). Bold distances refer to intermolecular bonds shorter than the sum of the vdW radii of the atoms involved ($2r^I = 3.96 \text{ \AA}$, $r^I + r^H = 3.18 \text{ \AA}$, $r^I + r^N = 3.53 \text{ \AA}$, $2r^{Br} = 3.70 \text{ \AA}$, $r^{Br} + r^H = 3.05 \text{ \AA}$, $r^{Br} + r^N = 3.40 \text{ \AA}$). ¹⁷⁷	67
Table 8.5: DFT-optimized geometries of TIPT and TBPT SAMNs on HOPG (M06-L/LanL2DZ level of theory). Polymorphs labeled “1” and “1*” are two different geometries obtained from starting geometries with the unit cell 1 of Figure 8.11. Polymorphs labeled “2” refer to the unit cell 2 of Figure 8.11.	74
Table 8.6: Computed interatomic distances (see Figure 8.20d for labels) of the TBPT molecular network at the heptanoic acid-HOPG interface (M06-L/6-31G** level of theory). Bold distances refer to intermolecular bonds shorter than the sum of the vdW radii of the atoms involved ($r^{Br} + r^H = 3.05 \text{ \AA}$, $r^{Br} + r^O = 3.37 \text{ \AA}$, $r^O + r^H = 2.72 \text{ \AA}$). ¹⁷⁷	91
Table 8.7: Width of the hcp regions (A), the fcc regions (B) and their ratio (B/A) for pristine gold as reported in the literature and for the experiments reported in this work before and after deposition (see Figure 8.29).	99
Table 8.8: Experimental and computed unit cell parameters and energy (see Figure 8.33 for labels).	103

Table 8.9: Experimental and computed unit cell parameters and computed interatomic distances (see Figure 8.31b for labels) of the α and β phase in the TBPT molecular network at the phenyloctane-Au(111) interface – M06-L/6-31G** level of theory.¹⁷⁷ 104

LIST OF FIGURES

Figure 1.1: a) Prediction on the number of components per IC in the original Moore's paper; b) transistor cost and lithographic tool cost vs. year. Reproduced from ref. ¹ and ref. ³	1
Figure 1.2: a) Estimated total planar complementary metal-oxide semiconductor (CMOS) parasitic and channel resistance vs. technology node. Note that parasitic resistance becomes larger than the intrinsic channel resistance for channel lengths smaller than 20 nm. b) Logic technology node and transistor gate length vs. calendar year. Reproduced from ref. ³	2
Figure 2.1: a) The spiral galaxy NGC 4414, reproduced from ref. ⁷ ; b) self-assembled steel ball bearings, reproduced from ref. ⁸ ; c) micrometer plates assembled by capillary forces, reproduced from ref. ⁹ ; self-assembled DNA polyhedra, reproduced from ref. ¹⁰ ; e) 3D molecular cage, reproduced from ref. ¹¹ ; f) four-component 2D molecular self-assembled nanostructure, reproduced from ref. ¹²	3
Figure 2.2: Atomic-scale view of growth processes at surfaces, reproduced from ref. ¹³	5
Figure 2.3: SAMNs can be stabilized by interactions such as a) vdW, b) hydrogen-bonding, c) halogen bonding and d) π - π stacking. Reproduced from a) ref. ¹⁴ , b) ref. ¹⁵ , c) ref. ¹⁶ and d) ref. ¹⁷	8
Figure 2.4: a) Scheme of the polarization at the C-X bond and possible geometries of halogen bonded structures, reproduced from ref. ¹⁹ . b) Potential at the σ -hole as a function of the halogen substituent size, reproduced from ref. ¹⁸	9
Figure 3.1: a) Experimental and b) simulated STM image of a 2D porous nitrogen-containing carbon covalent network, reproduced from ref. ²⁰ ; c) steps to achieve a 2D covalent network via Ullmann coupling, <i>i.e.</i> aryl-aryl coupling after thermally activated dehalogenation, reproduced from ref. ²¹ ; d) STM tip pulse activated one-dimensional (1D) polymerization of diacetylene monomers, reproduced from ref. ²² ; e) scheme of electrochemical polymerization, reproduced from ref. ²³ ; f) mechanism of the UV-activated 1D polymerization of diacetylenes, reproduced from ref. ²⁴	10
Figure 3.2: a) STM image of polymerized 1D chains, identified by the bright line (tens of nm long), and b) model of the polymerized system, reproduced from ref. ²⁴ ; c) diacetylene polymerization reaction and d) topochemical parameters, reproduced from ref. ⁸³	11

Figure 3.3: Ullmann polymerization of conjugated thiophene monomers, reproduced from ref. ⁸⁶ 12

Figure 4.1: First high-impact STM image ever recorded (1983), showing the relief of two cells of the 7x7 reconstructed Si(111) surface; the inset is a top-view of the relief. b) Schematic view of an STM. Reproduced from a) ref. ²⁵ and b) ref. ⁷ 13

Figure 4.2: Energy landscape of the 1D system with a particle tunneling through a barrier of width s , when a voltage V is applied between tip and sample. Reproduced from ref. ⁹¹ 14

Figure 4.3: STM images of the a) empty and b) filled states of 1,3,5-triphenyl-benzene (THB) assembled on a boron-passivated Si(111) surface, in UHV at 77 K. Reproduced from ref. ²⁶.
..... 16

Figure 4.4: a) Steps for the fabrication of a 48-atom Fe ring on a Cu(111) surface. The bottom right image clearly shows the strong modulation of the LDOS inside the ring. b) STM topograph and c) spectroscopic spin-polarized STM (SP-STM) image of a nanocrystalline Fe film, showing the correlation between magnetic and grain structure at sub-nm scale spatial resolution. Reproduced from a) ref. ²⁷ and b),c) ref. ²⁸ 17

Figure 4.5: a)-c) Photographs of the STM Nanoscope III; d),e) optical micrographs of a mechanically cut Pt/Ir tip; the inset in e) is a scanning electron microscopy (SEM) image of the tip apex (courtesy of C. Harnagea). f) SEM image of a polycrystalline tungsten tip etched in KOH (courtesy of Prof. P. Grutter from the Department of Physics at McGill University). ... 19

Figure 4.6: a) STM image of trimesic acid (TMA) molecules assembled at the heptanoic acid-highly oriented pyrolytic graphite (HOPG) interface ($15.0 \times 15.0 \text{ nm}^2$, $V_s^{\text{HOPG}} = -0.02 \text{ V}$ and $V_s^{\text{SAMN}} = -1.08 \text{ V}$, $I_t = 324 \text{ pA}$). During image acquisition the tip changes its physical properties, perhaps due to a TMA or solvent molecule attached to it. b),c) STM images of a single benzene molecule adsorbed on Au(111) taken at negative and positive sample bias, respectively, which hence depict the filled and empty state densities of the surface, respectively. d) STM image of benzene molecules adsorbed above a monoatomic step of the substrate. b)-d) reproduced from ref. ⁹⁸. 20

Figure 4.7: The tunneling transmittivity decreases exponentially with the tunneling distance, in vacuum about a factor of 10 for every Å. Therefore, assuming a tungsten tip, the current through the thicker arrow is approximately 40 times larger. Reproduced from ref. ⁸⁹. 21

Figure 5.1: Illustration of J. Perdew's classification of DFT functionals, starting from the Hartree world of unrealistically weak or missing bonding to the five steps to the heaven of

chemical accuracy. The physical ingredients included in the functionals from each rung are summarized on the right. Reproduced from ref. ¹⁰¹33

Figure 5.2: Binding energy curves for the C₆H₆···CH₄ complex with the 6-311+G(2df,2p) basis as functions of the distance between the carbon atom in CH₄ and the C₆H₆ plane. Reproduced from ref. ¹¹⁸37

Figure 5.3: Comparison of the quality of the least-squares fit of a 1s Slater function ($\zeta = 1.0 \text{ \AA}^{-2}$) obtained at the STO-1G, STO-2G and STO-3G levels. Reproduced from ref. ¹³⁹41

Figure 5.4: The addition of s-type and p-type basis functions is used to allow for polarization of the real electron density of the s-type orbital along the direction imposed by the polarization p-type orbital. Reproduced from ref. ¹⁴²42

Figure 6.1: Molecular structure of a) TIPT and c) TBPT optimized in gas-phase DFT. The structure of b) TIPB and d) TBPB is reported for comparison. Highest occupied molecular orbital (HOMO) and lowest unoccupied molecular orbital (LUMO) of e) TIPT and f) TBPT were computed at the 0.015 electrons Bohr⁻³ isodensity surface. Green and red isosurfaces are, respectively, positive and negative phases of the orbitals. Calculations performed at the B3LYP/LanL2DZ level of theory.....47

Figure 6.2: Molecular structure, HOMO and LUMO of a) Maude-2-041, b) SR-10-134 and c) SR-10-152 optimized and computed, respectively, in gas-phase DFT at the B3LYP/6-31G** level of theory. Molecular orbitals computed at the 0.02 electrons Bohr⁻³ isodensity surface; green and red isosurfaces are, respectively, positive and negative phases of the orbitals.48

Figure 7.1: a) Carbon phase diagram from *ab initio* molecular dynamics. Allotropes of carbon include b) graphite, c) diamond, d) C₆₀, e) graphene and f) carbon nanotubes. Reproduced from a) ref. ¹⁵⁶ and b)-f) ref. ⁷50

Figure 7.2: a) Top view and b) perspective view of a graphite crystal. c) Calculated charge density of graphite at the Fermi level ρ_{Fermi} at a height of 200 pm over the surface plane, ranging from 0.3 to 1.6 electrons per nm³. The maxima are at the β atom positions. Reproduced from ref. ¹⁵⁷51

Figure 7.3: a) Model of the herringbone reconstruction. Atoms of the topmost layer are drawn as empty circles (black circles refer to the *fcc* and *hcp* regions whereas the red atoms refer to the faulted solitons). Atoms of the second layer are indicated by full orange circles. The unit cell of the reconstruction is indicated by the blue rectangle. b)-d) Top- and side-views of the model for the transition from *fcc* to *hcp* structure. Yellow, black and white circles represent

gold atoms of the 1st, 2nd and 3rd layer, respectively. Note that in a) the two layers were not superimposed according to the actual *fcc* stacking structure of the unreconstructed Au(111) surface, but in a way that shows the relative displacement with respect to the *fcc* structure. This displays more clearly the effect of the compression.....53

Figure 7.4: a),b) STM images of the (22 x $\sqrt{3}$) herringbone reconstruction of the Au(111) surface. c) Magnification of an elbow, imaged with atomic resolution in d). In d) the blue circles mark the apparent centers of the underlying Au atoms, while the light blue color corresponds to the coordinatively unsaturated atoms, which exhibit increased reactivity. e) Model of the herringbone reconstruction. Reproduced from a) ref. ¹⁶⁷, b) ref. ⁹¹, c) ref. ¹⁶⁸, d) ref. ¹⁵⁹ and e) ref. ¹⁶⁵54

Figure 7.5: a)-c) Growth stages of Ni islands on Au(111); a) clean reconstructed Au(111) surface, b) nucleation of Ni islands at elbows at Ni coverage (θ) 0.01 monolayer (ML); c) completed nucleation and polygonal shape of Ni islands at $\theta = 0.014$ ML. a) and c) have same scale bar. d) STM image at 77 K of the reconstructed Au(111) surface with 0.01 ML of CH₃SH molecules, imaged as bright protrusions. The image shows preferential adsorption of CH₃SH on the elbow sites. a)-c) Reproduced from ref. ¹⁷⁰, d) from ref. ¹⁵⁹55

Figure 7.6: Integrated *d*-band centers with respect to the Fermi level for all atoms in the *siX*-layer Au 22 x $\sqrt{3}$ unit cell. Reproduced from ref. ¹⁶³56

Figure 7.7: Steps involved in the deposition of thin Au(111) films on mica.57

Figure 7.8: Scheme of the evaporation setup used for the growth of thin Au(111) films. The evaporation rate measured with the quartz balance overestimates the actual deposition rate at the mica substrate (quadratic dependence with the distance). The evaporation was performed using a shutter, which allowed for precise control over the deposition duration. ...58

Figure 8.1: Interatomic distances in the assembly TBPT² of Table 8.5.....61

Figure 8.2: Plot of the CPU time in function of the HF percentage of exact exchange of the used functionals. The fitted curve is a power law of the HF percentage, with exponent equal to 2.51 (data from Table 8.2).62

Figure 8.3: Plot of the CPU time in function of the primitive gaussians (PG) of the basis set, *i.e.* in function of the polarized functions added to the 6-31G basis set (data from Table 8.3). The CPU time increases with a power law in function of the number of primitive gaussians. .63

Figure 8.4: Single-point (SP) DFT-computed energies of complexes of two chlorobenzene, bromobenzene and iodobenzene molecules in function of the halogen-to-halogen distance

($d^{X\cdots X}$), using the M06-L functional and the a) 3-21G* and b) LanL2DZ basis sets. The complexes are bonded in the geometry shown in the inset in b). The graphs show that the 3-21G* basis set underestimates the binding energy of iodobenzenes complexes, whereas the LanL2DZ basis sets accurately predicts the trend $BE^{\text{iodobenzene}} > BE^{\text{bromobenzene}} > BE^{\text{chlorobenzene}}$. The graphs also show that halogen bonding stabilizes the molecular complexes even for distances larger than the sum of the vdW of the involved halogens (vertical dotted lines).65

Figure 8.5: a) Large-scale STM image of TIPT (inset) molecules assembled at the TCB-HOPG interface ($56.8 \times 56.8 \text{ nm}^2$, $V_s = -1.75 \text{ V}$, $I_t = 200 \text{ pA}$). Dotted black and white lines indicate grain boundaries between neighboring domains; the gray box indicates the molecular unit cell. b) High-resolution STM image of the molecular overlayer ($9.8 \times 9.8 \text{ nm}^2$, $V_s = -1.0 \text{ V}$, $I_t = 150 \text{ pA}$). TIPT molecules are shown schematically; full and empty circles indicate the iodine atoms of trimeric halogen-bonded motifs pointing down and up, respectively, which define the trimeric angle θ . The experimentally determined unit cell, with parameters $u = 2.04 \pm 0.09 \text{ nm}$, $v = 1.54 \pm 0.09 \text{ nm}$ and $\gamma = 90 \pm 5^\circ$, and the DFT-optimized cell (Table 8.4) are drawn in green and grey, respectively. c) DFT-calculated structure of SAMN (M06-L/LanL2DZ level); d1 and d2 are the iodine-to-iodine and iodine-to-hydrogen bonds, respectively. The rectangle and the circle highlight the intra-row and the inter-row interactions, respectively. The dotted line indicates the possible attractive interaction between iodine and nitrogen.66

Figure 8.6: STM images of TIPB molecules on a) c) HOPG and d) on Au(111). In e) is reported a STM image of THB molecules assembled on a Si(111)-B surface in UHV at 100 K. The reported SAMNs were obtained in a) phenyloctane, b) 1-octanol and c),d) nonanoic acid (9A). Reproduced from a),b) ref. ³², c),d) from ref. ¹⁵³ and e) from ref. ⁵⁶68

Figure 8.7: a) STM) image showing TIPT molecules assembled at the TCB-HOPG interface (lower part) and the underlying graphite lattice with atomic resolution (upper part) ($10.2 \times 10.2 \text{ nm}^2$, $I_t = 141 \text{ pA}$, $V_s^{\text{HOPG}} = -0.02 \text{ V}$ and $V_s^{\text{SAMN}} = -0.64 \text{ V}$) and b) corresponding 2D FFT. The spots of the HOPG lattice are highlighted by black circles, whereas the blue dotted and solid lines lie along one of the $\langle 10\bar{1}0 \rangle$ armchair high-symmetry directions of graphite and along the u vector of the unit cell, respectively. The SAMN is rotated CW by an angle $\beta = 94 \pm 5^\circ$ with respect to the HOPG substrate. The unit cell vectors are $u = 2.04 \pm 0.09 \text{ nm}$, $v = 1.54 \pm 0.09 \text{ nm}$ and the angle between them is $\gamma = 90 \pm 5^\circ$69

Figure 8.8: a) STM image showing TIPT molecules assembled at the TCB-HOPG interface (upper part) and the underlying graphite lattice with atomic resolution (lower part) ($11.1 \times 11.1 \text{ nm}^2$, $I_t = 133 \text{ pA}$, $V_s^{\text{HOPG}} = -0.02 \text{ V}$ and $V_s^{\text{SAMN}} = -1.61 \text{ V}$) and b) corresponding 2D-FFT. The spots originating from the HOPG lattice are highlighted by black circles, whereas the red dotted and solid lines lie along one of the $\langle 10\text{--}10 \rangle$ armchair high-symmetry directions of graphite and along the u vector of the unit cell, respectively. The SAMN is rotated CCW by an angle $\beta = 94 \pm 5^\circ$ with respect to the HOPG substrate. The unit cell vectors are $u = 2.04 \pm 0.09 \text{ nm}$, $v = 1.54 \pm 0.09 \text{ nm}$ and the angle between them is $\gamma = 90 \pm 5^\circ$70

Figure 8.9: a) Only the β atoms (black full dots) of the graphite lattice are imaged in STM (see also Figure 7.2). b) The 2D FFT of the a STM image containing the HOPG lattice such as the one in a) provides information of the high-symmetry directions of the substrate. Red and blue lines indicate the armchair and zig-directions of the HOPG surface.71

Figure 8.10: Molecular ESP map (M06-L/LanL2DZ) of a),b) TIPT and c),d) TBPT molecules in the a),c) isolated state (3D view) and b),d) in the assembly (top-view), expressed in a.u. at the 0.004 electrons Bohr⁻³ isodensity surface (blue and red areas of single molecules and of the SAMNs correspond to a potential of $\pm 2 \times 10^{-2}$ a.u., respectively). The dotted and solid black squares show the ESP map of the halogen atoms of TIPT and TBPT molecules in the isolated state, seen along (σ -hole) and orthogonal (negatively charged ring) to the C–X bond direction; blue and red areas of the σ -hole correspond to a potential of $\pm 6 \times 10^{-2}$ a.u., respectively; blue and red areas of the ring correspond to a potential of $\pm 1 \times 10^{-2}$ a.u., respectively.72

Figure 8.11: High-resolution STM image of the TIPT molecular overlayer at the TCB-HOPG interface ($9.8 \times 9.8 \text{ nm}^2$, $V_s = -1.0 \text{ V}$, $I_t = 150 \text{ pA}$). The apparent unit cell, with parameters $u = 1.02 \pm 0.09 \text{ nm}$, $v = 1.54 \pm 0.09 \text{ nm}$ and $\gamma = 90 \pm 5^\circ$, is indicated in grey; the physically possible unit cells are indicated in color.73

Figure 8.12: STM image of TIPT molecules assembled at the phenyloctane-HOPG interface ($25.0 \times 25.0 \text{ nm}^2$, $V_s = -1.15 \text{ V}$, $I_t = 66 \text{ pA}$).75

Figure 8.13: DFT computed energies for conformations of TBPT and TBPB with increasing dihedral rotation angle (δ) of the side groups (see TBPT molecule in the inset). For each molecule, energies are plotted relative to the least stable geometry. The diagram shows that TBPT is most stable when it is planar ($\delta = 0^\circ$), whereas for TBPB this occurs when $\delta \approx 40^\circ$. Calculations performed at the B3LYP/6-31G** level of theory.76

Figure 8.14: Both for TBPT (X = Br) and TIPT (X = I), intramolecular attractive interactions ($d^{N\cdots H} = 2.46 \text{ \AA}$ vs. $r^N + r^H = 2.75 \text{ \AA}$) take place between the nitrogen atoms of the triazine core and the hydrogen atoms at the ortho-positions of the halo-phenyl side groups (where the atomic positions are defined with respect to the bond with the central core). The C–H bonds at the ortho-positions are bent by 1° towards the electrophilic triazine core. These interactions render TXPT molecules more planar and stiffer precursors than TXPB molecules (namely molecules with the benzene core instead of the triazine core). Calculations performed at the B3LYP/6-31G** level.....77

Figure 8.15: a) Large-scale and b) high-resolution STM image of TBPT molecules (inset) assembled at the phenyloctane-HOPG interface - a) $36.4 \times 36.4 \text{ nm}^2$, $V_s = -1.20 \text{ V}$, $I_t = 120 \text{ pA}$, b) $6.6 \times 6.6 \text{ nm}^2$, $V_s = -1.60 \text{ V}$, $I_t = 117 \text{ pA}$. TBPT molecules are schematically indicated in b); full and empty circles indicate the bromine atoms of trimeric halogen-bonded motifs pointing down and up, respectively, which define the trimeric angle θ . The experimentally determined unit cell, with parameters $u = 2.05 \pm 0.09 \text{ nm}$, $v = 1.47 \pm 0.09 \text{ nm}$ and $\gamma = 89 \pm 5^\circ$, and the DFT-optimized cell (Table 8.4) are drawn in green and grey, respectively. b) SAMN computed with gas-phase DFT calculations at the M06-L/LanL2DZ level; d1 and d2 are the bromine-to-Bromine and bromine-to-hydrogen bonds, respectively. The rectangle and the circle highlight the intra-row and the inter-row interactions, respectively. The dotted line indicates the potential attractive interaction between bromine and nitrogen.78

Figure 8.16: a) STM image showing TBPT molecules assembled at the phenyloctane-HOPG interface (upper part) and the underlying graphite lattice with atomic resolution (lower part) ($10.4 \times 10.4 \text{ nm}^2$, $I_t = 102 \text{ pA}$, $V_s^{\text{HOPG}} = -0.02 \text{ V}$ and $V_s^{\text{SAMN}} = -1.21 \text{ V}$) and b) corresponding 2D-FFT. The spots of the HOPG lattice are highlighted by black circles, whereas the blue dotted and solid lines lie along one of the $\langle 10\bar{1}0 \rangle$ armchair high-symmetry directions of graphite and along the u vector of the unit cell, respectively. The SAMN is rotated CW by an angle $\beta = 93 \pm 5^\circ$ with respect to the HOPG substrate. The unit cell vectors are $u = 2.05 \pm 0.09 \text{ nm}$, $v = 1.47 \pm 0.09 \text{ nm}$ and the angle between them is $\gamma = 89 \pm 5^\circ$79

Figure 8.17: a) STM image showing TBPT molecules assembled at the phenyloctane-HOPG interface (lower part) and the underlying graphite lattice with atomic resolution (upper part) ($10.6 \times 10.6 \text{ nm}^2$, $I_t = 139 \text{ pA}$, $V_s^{\text{HOPG}} = -0.02 \text{ V}$ and $V_s^{\text{SAMN}} = -1.21 \text{ V}$) and b) corresponding 2D-FFT. The spots of the HOPG lattice are highlighted by black circles, whereas the blue

dotted and solid lines lie along one of the $\langle 10\text{--}10 \rangle$ armchair high-symmetry directions of graphite and along the u vector of the unit cell, respectively. The SAMN is rotated CCW by an angle $\beta = 93 \pm 5^\circ$ with respect to the HOPG substrate. The unit cell vectors are $u = 2.05 \pm 0.09$ nm, $v = 1.47 \pm 0.09$ nm and the angle between them is $\gamma = 89 \pm 5^\circ$80

Figure 8.18: SAMN of TBPB molecules (inset) at the UHV-HOPG interface. Reproduced from ref. ³¹.80

Figure 8.19: Model of the unit cells of the CW and CCW domains of the TIPT (darker green and red lines) and TBPT (lighter green and red lines) networks on HOPG. The dotted blue line indicates the armchair direction of the HOPG substrate to which the rotation of the u -vectors is referred to (see figures with FFTs). The semitransparent black regions represent the experimental uncertainty on the unit cell parameters, whereas the colored semitransparent regions represent the uncertainty on the rotation of the adlayer with respect to the substrate, measured on 2D FFTs. From the experimental data it is not possible to unambiguously infer the adlayer unit cell commensurate with the substrate.82

Figure 8.20. a) Large-scale and b) high-resolution STM image of TBPT molecules assembled at the heptanoic acid-HOPG interface – a) 38.5×38.5 nm², $V_s = -1.40$ V $I_t = 50$ pA, b) 11.2×11.2 nm², $V_s = -1.40$ V $I_t = 50$ pA. In a), the unit cell is indicated by the grey box. In b), the dotted and solid circles indicate a bright protrusion and a pore within the assembly (1.7 nm diameter, measured from X to X), respectively. The two-headed arrow indicates two bromine atoms, 1.3 ± 0.1 nm apart, of a TBPT molecule, whereas the single-headed arrow indicates the unusual internal contrast of TBPT molecules. Grey triangles superimposed to TBPT molecules highlight the chirality within the 2D lattice. c) DFT-computed bi-component SAMN at the M06-L/6-31G** level of theory (in the top-left part of the image the HOPG substrate is shown underneath the molecular network. d) Zoom of the computed network highlighting the stabilizing lateral interactions of the system. The experimentally determined unit cell is: $u = v = 2.7 \pm 0.1$ nm, $\gamma = 60 \pm 5^\circ$ 84

Figure 8.21: a) STM image and b) model of terthienobenzenetricarboxylic acid (TTBTA) molecules (inset) assembled at the heptanoic acid-HOPG interface. c) STM image and d) model of 2,5,8-tribromobenzo[1,2-*b*:3,4-*b'*:5,6-*b''*]trithiophene (inset) assembled at the TCB-HOPG interface. e) STM image of TBPB molecules assembled at the UHV-Ag(111) interface taken at 80 K. Hexameric synthons (grey hexagons) are linked between each other with a

single TBPB molecule (blue circles). a),b) reproduced from ref. ¹⁹⁴, c),d) from ref. ¹⁹ and e) from ref. ¹⁴⁹.86

Figure 8.22: a) STM image showing TBPT molecules assembled at the heptanoic acid-HOPG interface (upper part) and the underlying graphite lattice with atomic resolution (lower part) ($9.8 \times 9.8 \text{ nm}^2$, $I_t = 57 \text{ pA}$, $V_s^{\text{HOPG}} = -0.02 \text{ V}$ and $V_s^{\text{SAMN}} = -1.89 \text{ V}$) and b) corresponding 2D-FFT. The spots of the HOPG lattice are highlighted by black circles, whereas the pink dotted line lies along one of the $\langle 10\text{-}10 \rangle$ armchair high-symmetry directions of graphite, which bisects the unit cell. The SAMN is rotated by an angle $\beta = 30 \pm 5^\circ$ with respect to the HOPG armchair directions, hence it is aligned along the zig-zag directions. The unit cell vectors are $u = v = 2.7 \pm 0.1 \text{ nm}$ and the angle between them is $\gamma = 60 \pm 5^\circ$88

Figure 8.23: Plot of the forces gradient and total energy varying during the DFT optimization (M06-L/6-31G** level of theory) of the bi-component system TBPT + heptanoic acid. After the 15th iteration the optimized geometries oscillate around configurations of local minima. For the computational results of this system discussed in the MS we refer to the 12th iteration (black arrow), configuration with the lowest forces gradient (0.0047 a.u./Bohr vs. the Gaussian09 default threshold of 0.003 a.u./Bohr).90

Figure 8.24: a),b) Schematic model of the two enantiomers of TPTZ. c) STM image of TPTZ molecules assembled at the UHV-Au(111) interface and magnified image of a molecule marked by the dashed triangle in c). e) Simulated STM image of a R-TPTZ molecule on Au(111) with a sample bias of 1.5 V at a constant height of 3 Å. Reproduced from ref. ²⁰⁴.91

Figure 8.25: Simulated STM images (blue squares) indicate different apparent in-plane rotations by varying the molecular side groups out-of-plane rotation (reported on top of each square). Reproduced from ref. ¹⁵².92

Figure 8.26: a) STM image of TBPT molecules assembled at the phenyloctane-Au(111) interface, showing the SAMN modulated by the underlying reconstructed surface ($100 \times 100 \text{ nm}^2$, $V_s = -0.40 \text{ V}$ $I_t = 200 \text{ pA}$); b) wavelet filtering of image a) enhancing the $22 \times \sqrt{3}$ reconstruction of the gold substrate underlying the adlayer. The features typical of the reconstructed Au(111) surface, *i.e* the *fcc*- and *hcp*-stacked regions as well as the soliton walls bridging them, are indicated by the arrows.95

Figure 8.27: STM image of TBPT molecules assembled at the phenyloctane-Au(111) interface ($7.6 \times 7.6 \text{ nm}^2$, $V_s = +0.15 \text{ V}$ $I_t = 400 \text{ pA}$); dotted white circles highlight the bright

protrusions possibly due to the bromine atoms cleaved from TBPT molecules and adsorbed on the Au(111) surface, whereas the arrows indicate the phenyl ring and the halogen atom of a sub-molecularly resolved TBPT molecule.....96

Figure 8.28: XPS spectrum of one monolayer of TBPT molecules assembled on Au(111). ...97

Figure 8.29: a) STM image of the clean reconstructed Au(111) surface prior deposition of TBPT molecules ($47.3 \times 47.3 \text{ nm}^2$, $V_s = -0.64 \text{ V}$ $I_t = 70 \text{ pA}$). The inset is a FFT filtering of the STM image, with the *fcc* regions labeled B and the *hcp* regions labeled A. b) FFT filtering of the STM image in Figure 8.26a, enhancing the periodicity of the upper rotational domain of the herringbone reconstruction. The herringbone periodicity before and after molecular deposition is, respectively, $8.3 \pm 0.3 \text{ nm}$ and $9.7 \pm 0.3 \text{ nm}$. Hence, molecular adsorption causes a partial lifting of the surface reconstruction, which enlarges by 17%.....98

Figure 8.30: STM images of a) clean Au(111) and b) high-coverage PPh₃ on Au(111) after annealing at 220 K. The *fcc*, *hcp*, and soliton regions of the surface are indicated, as are the surface lattice vectors. b) The large-scale image shows that PPh₃ forms molecular domains confined by the soliton walls of the herringbone reconstruction. Scale bars = 10 nm. Reproduced from ref. ²¹⁷100

Figure 8.31: a) STM image of TBPT molecules assembled at the phenyloctane-Au(111) interface ($20.7 \times 20.7 \text{ nm}^2$, $V_s = +0.10 \text{ V}$, $I_t = 200 \text{ pA}$), showing the SAMN modulated by the reconstructed underlying substrate whose crystallographic directions are indicated by the black arrows. The α phase ($u = 1.7 \pm 0.2 \text{ nm}$, $v = 2.2 \pm 0.2 \text{ nm}$, $\gamma = 82 \pm 8^\circ$) is highlighted by the yellow rectangle while the β phase ($u' = 1.7 \pm 0.2 \text{ nm}$, $v' = 2.3 \pm 0.2 \text{ nm}$, $\gamma' = 72 \pm 8^\circ$) by the red rectangle. The two phases share one common molecular row (phase boundary), highlighted by the cyan molecules with black contour. The inset is a zoom of a high resolution STM image ($3.5 \times 3.5 \text{ nm}^2$, $V_s = +0.10 \text{ V}$ $I_t = 200 \text{ pA}$), with the black and white rectangles highlighting the closest contacts between the substituent end groups. The circles indicate the different bonding motifs in the two phases. b) DFT model of SAMN (M06-L/6-31G**); the two polymorphs were computed separately, constraining two intermolecular angles to account for the experimentally observed effect of the substrate (yellow and red circles superimposed to TBPT molecules). Rectangles and circles highlight intermolecular interactions within each row and between neighboring rows, respectively.101

Figure 8.32: a) STM image of TBPT molecules assembled at the phenyloctane-Au(111) interface, showing the SAMN modulated by the underlying reconstructed surface (50×50

nm^2 , $V_s = -0.10 \text{ V}$ $I_t = 200 \text{ pA}$); b) wavelet filtering of image a) enhancing the reconstruction of the gold substrate underlying the adlayer. The blue line in a) and b) indicates the $[1-10]$ direction of the substrate. The v vector in the α and β phases is rotated CW by $12 \pm 6^\circ$ and $26 \pm 6^\circ$, respectively, with respect to the $[1-10]$ crystallographic direction of the substrate..102
 Figure 8.33: Zoomed regions of STM images containing a) the α and b) β TBPT polymorphs on Au(111). DFT optimized geometries c),d) without and e),f) with constraints.....103
 Figure 8.34: STM images of a)-c) three different phases of TBPB molecules (inset) at the liquid-Au(111) interface and d) at the UHV-Au(111) interface. The molecular layers are not sensitive to the *fcc* and *hcp* regions of the substrate. Reproduced from a)-c) ref. ¹⁵¹ and d) ref. ¹⁵⁰105
 Figure 8.35. STM image of TBPT molecules assembled at the phenyloctane-Au(111) interface ($50 \times 50 \text{ nm}^2$, $V_s = +0.10 \text{ V}$ $I_t = 200 \text{ pA}$), showing the SAMN modulated by the reconstructed underlying substrate with TBPT molecules superimposed (cyan tripods) to highlight the α (yellow lines) and β phase (red lines) occurring in the assembly process. The labels on the right indicate different stacking structures of the underlying gold substrate as a consequence of the 4.34% compression of the topmost atomic layer along $[1-10]$.¹⁶³ The numbers on the left of the yellow lines indicate how many molecular rows are present in sets of aligned TBPT rows in the α phase. Each set of molecular rows (yellow lines) share one molecular row with the two neighboring phases, hence neglecting the shared phase boundaries the actual number of molecular rows would be the one reported minus two.....106
 Figure 8.36. a) STM image of TBPT molecules assembled at the phenyloctane-Au(111) interface ($50 \times 50 \text{ nm}^2$, $V_s = +0.10 \text{ V}$ $I_t = 200 \text{ pA}$), showing the SAMN modulated by the reconstructed underlying substrate whose crystallographic directions are indicated by the black and white arrows. Cyan TBPT molecules have been superimposed on the micrograph to highlight the α (yellow rectangle) and β phase (red rectangle) occurring in the assembly process. The angle between $[11-2]$ and that aligned along the rows of TBPT molecules (*i.e.* the u vector in the α phase and the u' vector in the β phase) measured in the non-corrected image is approximately 10° . b) α (yellow) and β (red) domains of image a) with respect to the reconstructed Au(111) surface, whose faulted soliton walls are indicated by solid black and white lines. In this diagram, half of each shared molecular rows has been assigned to the α phase and the other half to the β phase. White regions indicate defective areas of the SAMN

(the regions circled in black are due to defects of the underlying gold substrate rather than to the transition between two different phases).....107

Figure 8.37: Theoretical calculations have shown that the most stable adsorption configuration of TPTZ (inset) on a fcc Au(111) surface is with the triazine core and molecular side groups on hollow sites.²⁰⁴ Such configurations are achieved for specific rotations of the molecular side groups with respect to the substrate. White and black circles indicate different hollow sites (we do not specify here the type of hollow site). Note that when the core is adsorbed on an fcc hollow site the aryl side groups are adsorbed on a hcp site (and *vice versa*). Labels Y and Z indicate the molecular configurations observed for TBPT on Au(111) – see Figure 8.38.....109

Figure 8.38. a),b) Experimentally determined unit cell vectors (solid black lines) with the experimental uncertainty (semitransparent regions). The unit cell vectors that account for an adlayer commensurate with the substrate (solid, dashed and dotted red and yellow lines) are within the experimental uncertainty (yellow vectors are for the α phase and red vectors for the β phase). The two types of hollow sites of the top layer are represented by white and black circles (fcc vs. hcp sites depend on how the three top layers of the gold crystal are stacked with respect to each other). In the fcc and hcp regions of the substrate the type of hollow sites is inverted. c) Model in scale of the TBPT network on gold featuring the two phases on the different regions of the substrate (whose crystallographic directions are indicated by the black arrows). In reference to the text, the two molecules Y and Z per unit cell are also indicated. In the model, the lattice constant of the substrate in the unfaulted wider fcc (darker green atoms) and narrower hcp regions (brighter green atoms) is equal to that in the bulk (2.88 Å). In the soliton walls (light blue atoms), six gold atoms were “squeezed” and shifted along [11–2] to account for the $22\times\sqrt{3}$ herringbone reconstruction. TBPT molecules are drawn in scale with the substrate, with intramolecular distances obtained from gas-phase DFT optimization (Figure 6.1). The aryl rings are drawn as hexagons with dimensionless atoms, whereas the bromine atoms are drawn with size equal to 80% of their actual vdW radius.110

Figure 8.39: a) STM image of the Au(111) surface at 4 K. The herringbone reconstruction and surface-state standing waves are clearly visible. b) STM image of benzene molecules at 77 K along a monoatomic step edge on Cu(111) perturb the electronic structure of the adjacent surface thereby setting up adsorption sites for subsequent rows of molecules. The arrow A indicates the empty surface electronic states above the step edge. c) External potential map

of the reconstructed Au(111) surface derived from the density map acquired with STM. d) Electronic potential perpendicular to the Au(111) reconstruction white line in c). Reproduced from a) ref. ²²² , b) ref. ²²⁴ and c),d) ref. ²²³	113
Figure 8.40: STM images of a),b) DBAQs and c) TPTZ at the UHV-Au(111) interface. In both systems the adlayer is not sensitive to the differently reconstructed regions of the Au(111) substrate. Reproduced from a),b) ref. ²³⁰ and c) ref. ²⁰⁴	114
Figure 8.41: STM images of a),b) FePc, c) azobenzene, d) subphthalocyanine (SubPc) and e),f) benzene on Au(111). Reproduced from a),b) ref. ²³⁵ , c) ref. ²³³ , d) ref. ²³⁶ and e),f) ref. ⁹⁸	115
Figure 8.42: STM images of the bi-component system melamine and PTCDI on a) $\sqrt{3} \times \sqrt{3}$ R30° Ag/Si(111) and b) $22 \times \sqrt{3}$ Au(111). In b) the sub-ML adlayer is sensitive to the <i>fcc</i> and <i>hcp</i> regions of the substrate. Reproduced from a) ref. ²³⁷ and b) ref. ²⁰⁵	116
Figure 8.43: STM image of a dimer of TBPT molecules at the air-Au(111) interface (25×25 nm ² , $V_s = -0.4$ V $I_t = 194$ pA). The inset shows a zoom of the dimer with the model superimposed.	117
Figure 8.44: STM images of a) TBPB dimers (inset) and b) COFs of various shapes obtained from TIPB monomers. Reproduced from a) ref. ¹⁵¹ and b) ref. ¹⁵³	117
Figure 8.45: a),b) STM images of TIPT molecules (schematically superimposed) assembled at the TCB-Au(111) interface a) (50.0×50.0 nm ² , $V_s = -0.62$ V, $I_t = 177$ pA), b) (11.7×11.7 nm ² , $V_s = -0.79$ V, $I_t = 231$ pA). The experimentally determined unit cell parameters are $u = 2.2 \pm 0.2$ nm, $v = 1.6 \pm 0.2$ nm and $\gamma = 90 \pm 8^\circ$	118
Figure 8.46: STM image of TIPT molecules assembled at the TCB-Au(111) interface, showing STM tip instability – central part vs. upper and lower parts (72.9×72.9 nm ² , $V_s = +0.10$ V $I_t = 200$ pA).	119
Figure 8.47: a) Molecularly resolved STM image of TIPT molecules adsorbed on Au(111) with b) model of the structures superimposed (molecules drawn as black tripods, 37.2×8.1 nm ² , $V_s = +0.05$ V $I_t = 400$ pA). c) Reports the model of b) without the background STM image; the domain A is similar to TIPT-HOPG and the domain B similar to the structure of TBPT on Au(111).	120
Figure 8.48: Edge-on adsorption geometry of nitrogen-containing molecules on Au(111). Reproduced from ref. ²³⁸	121

Figure 8.49: Large-scale STM images of Maude-2-041 molecules (inset) assembled at the heptanoic acid-HOPG interface ($200.0 \times 161.3 \text{ nm}^2$, $V_s = -1.40 \text{ V}$, $I_t = 670 \text{ pA}$; $50.0 \times 50.0 \text{ nm}^2$, $V_s = -0.95 \text{ V}$, $I_t = 200 \text{ pA}$). The adlayer comprises three symmetrically equivalent domains, rotated by 120° between each other.122

Figure 8.50: High-resolution STM image of Maude-2-041 molecules assembled at the heptanoic acid-HOPG interface ($18.6 \times 18.6 \text{ nm}^2$, $V_s = -0.85 \text{ V}$, $I_t = 150 \text{ pA}$), with the packing model for the different phases superimposed. The unit cell is also reported ($u = 4.85 \pm 0.08 \text{ nm}$, $v = 1.06 \pm 0.08 \text{ nm}$ and $\gamma = 90 \pm 2^\circ$). Note that the molecules in the $\alpha(R)$ and $\alpha(S)$ phase constitute a pair of enantiomers, since one is the mirror image of the other.123

Figure 8.51: STM image of Maude-2-041 molecules assembled at the heptanoic acid-HOPG interface after 50 minutes of UV-light irradiation ($25 \times 25 \text{ nm}^2$, $V_s = 0.51 \text{ V}$, $I_t = 260 \text{ pA}$). The lack of a bright line along the dotted blue line suggests that the polymerization has not occurred.....124

Figure 8.52: Plot of the angle φ between the stacking axis and the rigid backbone vs. the stacking distance d . The dashed lines refer to constant values of the distance R between the 1,4-carbon atoms. Empty and full circles represent inactive and active structures, respectively. Therefore, only structures with $R < 4 \text{ \AA}$ can essentially lead to topochemical polymerization. Reproduced from ref. ⁸³.126

Figure 8.53: High-resolution STM image of Maude-2-041 molecules assembled at the heptanoic acid-HOPG interface (upper part) and the underlying HOPG substrate (lower part) ($8.4 \times 8.4 \text{ nm}^2$, $V_s^{\text{HOPG}} = -0.02 \text{ V}$ and $V_s^{\text{SAMN}} = -0.85 \text{ V}$, $I_t = 150 \text{ pA}$). The packing model has been superimposed to highlight the experimental topochemical parameters.....127

Figure 8.54: a) High-resolution STM image of Maude-2-041 molecules assembled at the heptanoic acid-HOPG interface (upper part) and the underlying HOPG substrate (lower part) ($8.4 \times 8.4 \text{ nm}^2$, $V_s^{\text{HOPG}} = -0.02 \text{ V}$ and $V_s^{\text{SAMN}} = -0.85 \text{ V}$, $I_t = 150 \text{ pA}$). The packing model and the graphite top-layer lattice have been superimposed. The side alkyl chains and the diacetylene core are aligned along the *zig-zag* and *armchair* directions of the HOPG substrate, respectively. b) 2D FFT of the image in a).128

Figure 8.55: Different molecular arrangements in SAMNs of diacetylene monomers on HOPG. a) Without alkyl chains the molecules self-assemble with an angle favorable for topochemical

polymerization, but b),c) if an alkyl chain is added to the rigid backbone very high angles are achieved, regardless the number of unsaturated repeat units. Reproduced from ref. ²³⁹130

Figure 8.56: a),c) STM images of SR-10-152 molecules (inset) assembled at the heptanoic acid- and TCB-HOPG interface, respectively. The underlying graphite lattice is also resolved with atomic resolution ($7.7 \times 7.7 \text{ nm}^2$, $I_t = 89 \text{ pA}$, $V_s^{\text{HOPG}} = -0.02 \text{ V}$ and $V_s^{\text{SAMN}} = -0.92 \text{ V}$; $12.1 \times 12.1 \text{ nm}^2$, $I_t = 151 \text{ pA}$, $V_s^{\text{HOPG}} = -0.02 \text{ V}$ and $V_s^{\text{SAMN}} = -0.90 \text{ V}$). Note that the different imaging of the adlayer in the upper and lower part of c) is not due to a change in the polarity of the bias voltage, rather to a change in the tip state as a consequence of the scanning of the HOPG lattice during image acquisition. b),d) 2D-FFTs of a) and c), respectively. The spots of the HOPG lattice are highlighted by red circles. The green dotted and solid lines lie along one of the $\langle 1010 \rangle$ armchair high-symmetry directions of graphite and along the v vector of the unit cell, respectively. The SAMN is rotated clockwise by an angle $\beta = 2 \pm 1^\circ$ with respect to the HOPG substrate when heptanoic acid is used as solvent, while in TCB this angle is $\beta' = 23 \pm 1^\circ$. The unit cell vectors are $u = 1.57 \pm 0.02 \text{ nm}$, $v = 1.18 \pm 0.03 \text{ nm}$ and the angle between them is $\gamma = 89 \pm 2^\circ$132

Figure 8.57: STM images of SR-10-152 molecules assembled at the TCB-Au(111) interface. The dotted path in a) highlights an uncovered region of the substrate. The blue arrow indicates the step-edge of a Au(111) terrace with adsorbed molecules. c) Is a zoom of the square in b); the blue arrows indicate the boundaries (solitons) between *fcc*- and *hcp*-stacked (green arrows) regions of the Au(111) substrate. The red circle indicates a U-turn defect typical of reconstructed Au(111) surfaces. a) $27.4 \times 27.4 \text{ nm}^2$, $V_s = -0.43 \text{ V}$, $I_t = 168 \text{ pA}$; b) $66.4 \times 66.4 \text{ nm}^2$, $V_s = -1.30 \text{ V}$, $I_t = 123 \text{ pA}$; c) $22.7 \times 22.7 \text{ nm}^2$, $V_s = -1.43 \text{ V}$, $I_t = 32 \text{ pA}$134

Figure 8.58: a) Dimethyl sulfide molecules adsorb with their nucleophilic sulphur atom above step edges of a Cu(111) surface. b) Carbon disulfide molecules, on the other hand, adsorb with their electrophilic carbon atom below step edges of a Au(111) surface. Reproduced from refs. ²⁴³ and ²²⁶135

Figure 8.59: a) Scheme of the ideal edge-on adsorption geometry of SR-10-152 molecules on Au(111), favorable for polymerization at the diacetylene moieties. b) Energy competition between the two configurations of SR-10-152 (left most stable), computed in DFT at the B3LYP/6-31G**136

Figure 8.60: Large-scale and high-resolution STM images of SR-10-134 molecules (inset) assembled at the a),b) TCB-, c),d) heptanoic acid- and e),f) phenyloctane-HOPG interface. Black solid lines in large-scale images and dotted blue lines in high-resolution images indicate the molecular stacking axis. Six equivalent domains are observed within the adlayer, rotated by multiples of 30° between each other - see image c). a) $100 \times 100 \text{ nm}^2$, $V_s = -0.89 \text{ V}$, $I_t = 100 \text{ pA}$; b) $12.7 \times 12.7 \text{ nm}^2$, $V_s = -0.55 \text{ V}$, $I_t = 80 \text{ pA}$; c) $42.7 \times 42.7 \text{ nm}^2$, $V_s = -1.17 \text{ V}$, $I_t = 47 \text{ pA}$; d) $12.0 \times 12.0 \text{ nm}^2$, $V_s = -1.06 \text{ V}$, $I_t = 78 \text{ pA}$; e) $68.8 \times 68.8 \text{ nm}^2$, $V_s = -1.00 \text{ V}$, $I_t = 39 \text{ pA}$; f) $19.5 \times 19.5 \text{ nm}^2$, $V_s = -1.16 \text{ V}$, $I_t = 34 \text{ pA}$ 137

Figure 8.61: STM image of SR-10-134 molecules assembled at the TCB-HOPG interface, obtained at both positive and negative bias polarity ($17.8 \times 17.8 \text{ nm}^2$, $V_s = \pm 1.0 \text{ V}$, $I_t = 372 \text{ pA}$). The unit cell vectors are $u = 2.00 \pm 0.10 \text{ nm}$, $v = 1.20 \pm 0.05 \text{ nm}$ and the angle between them is $\gamma = 90 \pm 2^\circ$ 138

LIST OF EQUATIONS

2.1.....	5
2.2.....	6
2.3.....	6
2.4.....	6
2.5.....	7
2.6.....	7
4.1.....	14
4.2.....	15
4.3.....	15
4.4.....	15
4.5.....	17
5.1.....	23
5.2.....	24
5.3.....	25
5.4.....	26
5.5.....	26
5.6.....	26
5.7.....	27
5.8.....	31
5.9.....	32
5.10.....	35
5.11.....	39
5.12.....	40
5.13.....	40
5.14.....	40
7.1.....	57
8.1.....	72
8.2.....	87

LIST OF ACRONYMS

- 1,2,4-trichlorobenzene (TCB), 46
1,3,5-tri(4-bromophenyl)benzene (TBPB), 47
1,3,5-tri(4-iodophenyl)benzene (TIPB), 47
1,3,5-triphenyl-benzene (THB), 16
2,4,6-tris(2-pyridyl)-1,3,5-triazine (TPTZ), 92
2,4,6-tris(4-bromophenyl)-1,3,5-triazine (TBPT), 47
2,4,6-tris(4-iodophenyl)-1,3,5-triazine (TIPT), 47
3,4,9,10-perylenetetracarboxylic diimide (PTCDI), 116
Atomic Force Microscopy (AFM), 17
Basis-Set Superposition Effect (BSSE), 59
Binding Energy (BE), 7
Bipolar Junction Transistor (BJT), 1
Boundary Conditions (BCs), 15
Carbon Nanotubes (CNTs), 50
Central Processing Unit (CPU), 61
Clockwise (CW), 69
Complementary Metal-Oxide Semiconductor (CMOS), 2
Contracted-GTOs (CGTOs), 40
Counter-Clockwise (CCW), 69
Counterpoise (CP), 59
Covalent Organic Framework (COF), 117
Density Functional Theory (DFT), xix
Density of States (DOS), 15
dibromianthraquinones (DBAQs), 115
Double-Zeta (DZ), 41
Effective Core Potential (ECP), 45
Exchange-Correlation (XC), 25
exempli gratia (*e.g.*), 2
Fast Fourier Transform (FFT), 69
Field Ion Microscopy (FIM), 13
Gaussian-Type Orbitals (GTOs), 40
Generalized Gradient Approximation (GGA), 31
Hartree-Fock (HF), 29
Highest Occupied Molecular Orbital (HOMO), 47
Highly Oriented Pyrolytic Graphite (HOPG), 20
Hohenberg-Kohn (HK), 25
id est (*i.e.*), 3
Integrated Circuit (IC), 1
iron(II) phthalocyanine (FePc), 116
Kohn-Sham (KS), 22
Local Density Approximation (LDA), 30
Local Density of States (LDOS), 17
Local-Spin-Density Approximation (LSDA), 31
Lowest Unoccupied Molecular Orbital (LUMO), 47
Metal-Oxide-Semiconductor Field-Effect Transistor (MOSFET), 1
Molecular Beam Epitaxy (MBE), 56
Molecular Electrostatic Potential (ESP), 9
Monolayer (ML), 55
One-Dimensional (1D), 10
Perdew-Burke-Ernzerhof Functional (PBE), 32
Perdew-Wang Functional (PW91), 32
Periodic Boundary Conditions (PBCs), 59
Polycyclic Aromatic Hydrocarbons (PAHs), 71
Primitive Gaussians (PG), 63
Quadruple-Zeta (QZ), 42
Random-Phase Approximation (RPA), 33
Room Temperature (RT), 12
Scanning Electron Microscopy (SEM), 19
Scanning Tunneling Microscopy (STM), xix
Self-Assembled Molecular Networks (SAMNs), 3
Slater-Type Orbitals (STOs), 40
Spectroscopic Spin-Polarized STM (SP-STM), 17
subphthalocyanine (SubPc), 116
Tao-Perdew-Staroverov-Scuseria Functional (TPSS), 32
Temperature Programmed Desorption (TPD), 50
terthienobenzenetricarboxylic acid (TTBTA), 87

Three-Dimensional (3D), 3
Transmission Electron Microscopy (TEM),
13
Trimesic Acid (TMA), 20
triphenylphosphine (PPh₃), 100
Triple-Zeta (TZ), 42
Two-Dimensional (2D), 3
Ultra-High Vacuum (UHV), 7
Ultra-Violet (UV), 10

Ultra-Violet Photolithography (UV-PL), 1
Uniform Electron Gas (UEG), 30
van der Waals (vdW), 7
Vosko-Wilk-Nusair Correlation Functional
III (VWN3), 35
Wave Function Theory (WFT), 29
X-Ray Photoelectron Spectroscopy (XPS),
97

Chapter 1. INTRODUCTION

In 1947 the first transistor, a germanium bipolar junction transistor (BJT), was invented by Bardeen, Brattain and Shockley at Bell Laboratories (Physics Nobel Prize in 1956)³³. A few years later the first silicon transistor was reported by Texas Instruments³⁴, which soon after also reported the first integrated circuit (IC) fabricated by Kilby (Physics Nobel Prize in 2000) and Noyce³⁵. Eventually, the first metal-oxide-semiconductor field-effect transistor (MOSFET) was invented in 1960 again at Bell Labs³⁶, hence paving the way to modern electronics. In the last fifty years we have witnessed an ever decreasing size in electronic components in agreement with the empirical Moore's law, which states that the number of transistors in ICs doubles every 18 months¹ (Figure 1.1a). So far the IC industry has kept up with Moore's law, with the cost per transistor decreasing exponentially with time (with consequent exponential increase of the lithographic tools cost)³ - Figure 1.1b. However, in the past two decades ultra-violet photolithography (UV-PL), the main patterning technique used in the IC industry, has reached its fundamental limits².

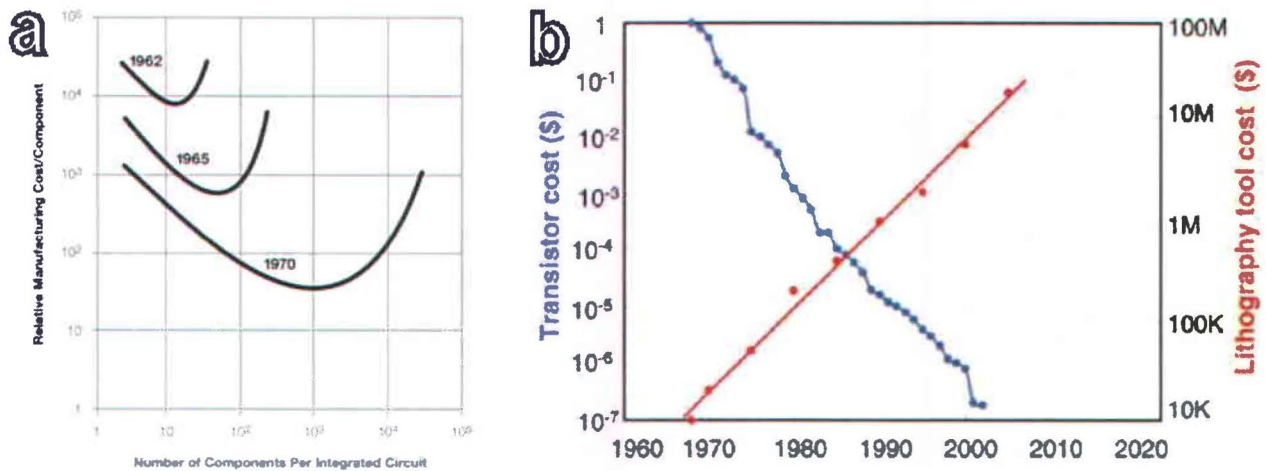


Figure 1.1: a) Prediction on the number of components per IC in the original Moore's paper; b) transistor cost and lithographic tool cost vs. year. Reproduced from ref. ¹ and ref. ³.

This motivated the scientific community to search for a solution to this problem, which would allow for the fabrication of ever smaller electronic components and hence faster computers. In

scaling down transistors fundamental issues arise, e.g. the predominance of parasitic resistance and the limit itself of the planar MOSFET ³ (Figure 1.2), hence research in this respect is still ongoing. In addition to alternative conventional lithographic techniques, unconventional methods involving patterning without the use of light have been proposed, both in the form of top-down and bottom-up approaches ³⁷.

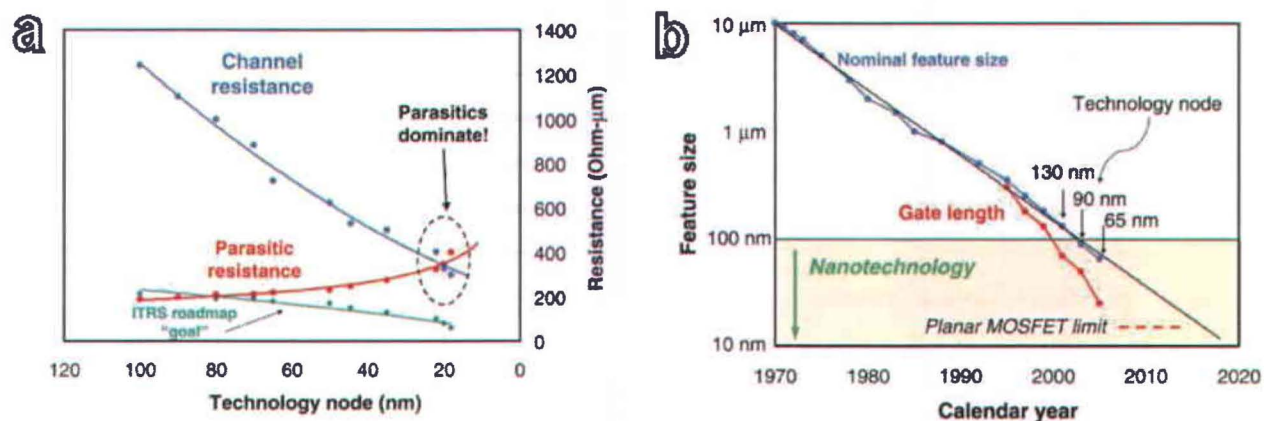


Figure 1.2: a) Estimated total planar complementary metal-oxide semiconductor (CMOS) parasitic and channel resistance vs. technology node. Note that parasitic resistance becomes larger than the intrinsic channel resistance for channel lengths smaller than 20 nm. b) Logic technology node and transistor gate length vs. calendar year. Reproduced from ref. ³.

Self-assembly is a powerful pathway for the bottom-up patterning of surfaces ^{4, 13}. At the molecular level, a virtually infinite number of possible structures can be obtained by properly tuning the molecular functionalities of the building blocks, which in turn lead to specific molecular packings and hence characteristic patterns ³⁸. Furthermore, molecular self-assembly is relevant to the fabrication of organic thin films, which have attracted interest in the last two decades in applications such as organic light-emitting devices ³⁹, organic semiconductors ⁴⁰ and in photovoltaics ⁴¹.

Chapter 2. SELF-ASSEMBLY

Self-assembly, the formation of ordered systems without human intervention, has been regarded from experts of the field as one of the most important concepts of the 21st century ⁵. This is in part due to the fact that self-assembly occurs at all scales, from galaxies and macroscopic objects down to the molecular and atomic level (Figure 2.1) ⁴². Molecular self-assembly is interesting for both fundamental and technological aspects: from a fundamental perspective, molecular self-assembly is important because it is at the basis of life ⁴³ (e.g. protein folding), whereas from a technological point of view it is an interesting bottom-up method for surface patterning and for the fabrication of three-dimensional (3D) molecular structures ⁴. In this work we will discuss only two-dimensional (2D), monolayer self-assembled molecular networks (SAMNs). SAMNs are thermodynamically stable, non-covalently bonded systems (*i.e.* supramolecular systems ⁶) that spontaneously form on surfaces if the precursors, when packed into a 2D molecular lattice, are more stable than in the isolated, disassembled state.

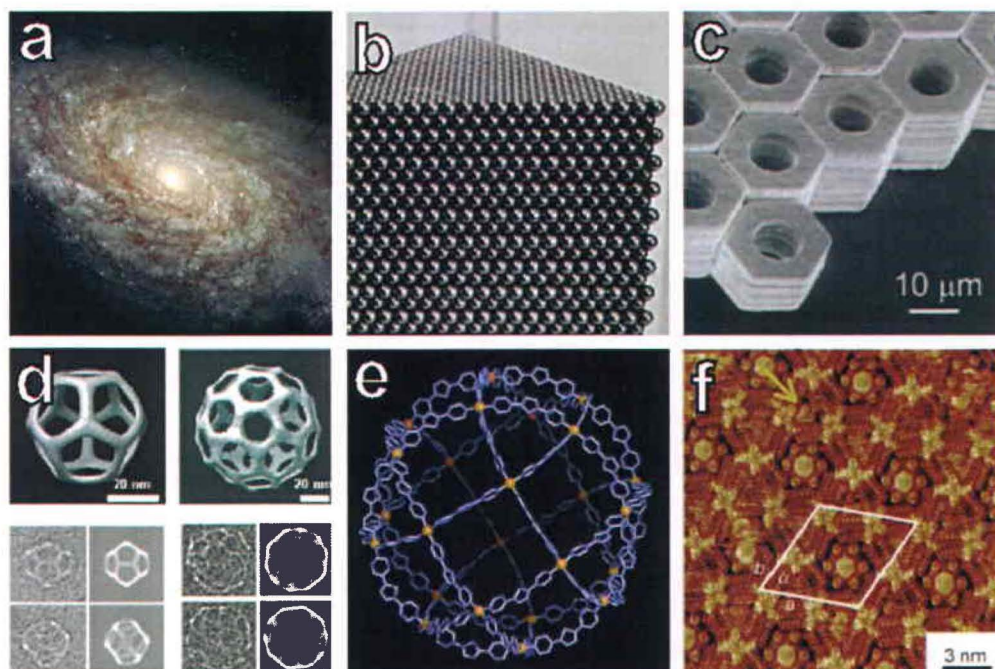


Figure 2.1: a) The spiral galaxy NGC 4414, reproduced from ref. ⁷; b) self-assembled steel ball bearings, reproduced from ref. ⁸; c) micrometer plates assembled by capillary forces, reproduced from ref. ⁹; self-assembled DNA polyhedra, reproduced from ref. ¹⁰; e) 3D molecular cage, reproduced from ref. ¹¹; f) four-component 2D molecular self-assembled nanostructure, reproduced from ref. ¹².

In addition to its use as a bottom-up patterning method, self-assembly is a powerful route also for the fabrication of functional surfaces whose properties (e.g. chirality^{16, 44}, hydrophobicity⁴⁵⁻⁴⁶, and so on) can again be controlled through a judicious combination of the substrate and the molecular building blocks⁴⁷⁻⁴⁸. For instance, porous networks can be useful for sensing the adsorption of guest molecules⁴⁹⁻⁵⁰, organic semiconducting precursors can be used for the fabrication of organic transistors¹⁹ and chiral systems are able to recognize specific molecular species⁵¹⁻⁵².

Self-assembly is a process based on atomistic events dictated by the competition between kinetics and thermodynamics¹³. After the molecules are deposited on the surface, either from vacuum, ambient or from a solution, they must diffuse in order to find the most stable configuration. For this to occur, the system must be at a finite temperature, so that single molecules have enough mobility to overcome diffusion barriers on the surface⁵. Indeed, molecular mobility is a necessary parameter for the formation of SAMNs. For instance, at low temperature, molecules adsorbed on reactive surfaces such as transition metals typically tend to “stick” to their adsorption site, preventing the formation of ordered long-range structures. In such cases, increasing the system’s thermal energy promotes molecular mobility, and thereby facilitates the formation of ordered structures. In spite of this, SAMNs are also observed when the single precursors form strong covalent bonds with the surface (chemisorption), e.g. alkanethiolate species on gold surfaces. In these cases the mobility is typically provided by the mobile surface adatoms to which the molecules are bonded⁵³.

The growth of self-assembled nanostructures is dictated by a multitude of atomistic processes. If F is the molecular deposition rate and D the diffusivity of molecules on the surface, *i.e.* the mean square distance a molecule travels per unit time, then the ratio D/F indicates the average distance an adsorbate has to travel to meet another adsorbed species. When the deposition rate is much higher than the diffusivity, the growth is governed by kinetics. A typical example is the low-temperature growth of metal nanostructures. On the other hand, when the diffusivity is much higher than the deposition rate, the growth phenomena occur close to equilibrium (e.g. molecular systems)¹³ – Figure 2.2.

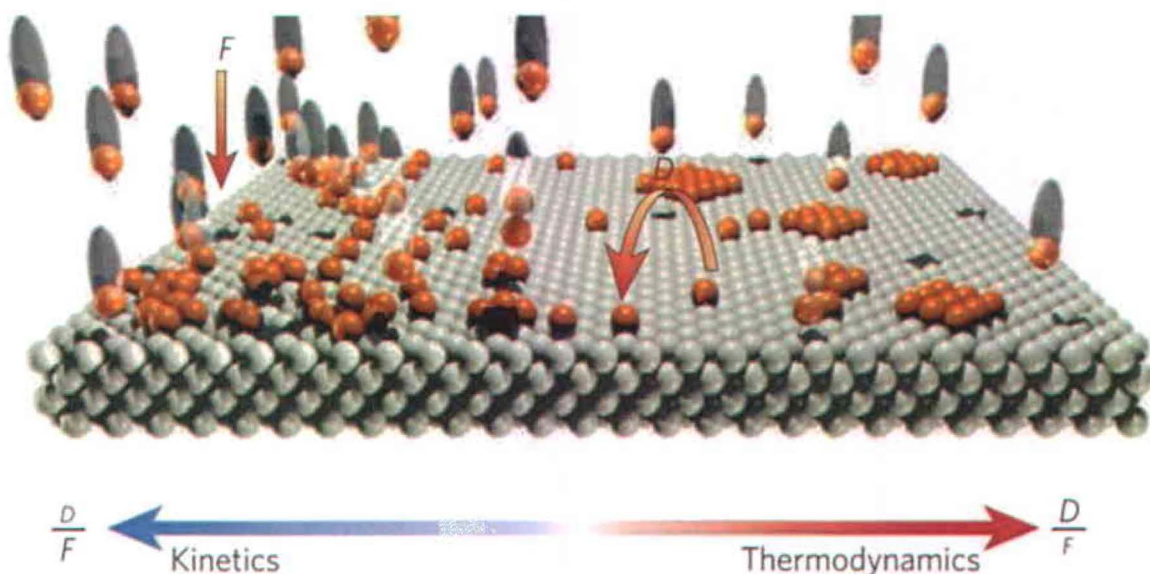


Figure 2.2: Atomic-scale view of growth processes at surfaces, reproduced from ref. ¹³.

As with any chemical-physical process, the variation of Gibbs free energy (ΔG) associated with molecular self-assembly is given by

$$\Delta G = \Delta H - T\Delta S, \quad 2.1$$

where ΔH is the variation of enthalpy, T the temperature and ΔS the variation of entropy. From Eq. 2.1 one can see that self-assembly is intrinsically unfavorable from an entropic point of view, given that the system evolves from a disordered state to an ordered state, hence losing rotational and translational degrees of freedom. For this reason, SAMNs typically exhibit tightly packed structures that maximize the number of stabilizing interactions between neighboring molecules, maximizing the enthalpic term of Eq. 2.1. Similarly, low initial absolute entropy states are favorable because these minimize the inevitable entropic cost of association ⁵.

In a statistical mechanical description of molecular self-assembly, knowledge of the partition function of the system in the initial and final states allows quantitative predictions, which are mandatory for a deterministic understanding of self-assembly ⁵. In statistical mechanics, as

well as any other kind of statistics, the predictability of an event increases with maximizing information. In the approximation of time-independence, in which all the variables of state are constant (*thermal equilibrium*), and in the approximation of independence between events, each event can be described in terms of its statistical weight (*frequency*), and the predictability (or probability) P_B of the event χ_B , when normalized over all possible events (i), increases with its frequency $f(\chi_B)$ ⁵ as

$$P_B = \frac{f(\chi_B)}{\sum_i f(\chi_i)}. \quad 2.2$$

According to the approach used by Boltzmann to explain the atomistic theory of gases, any event can be regarded as a collection of microscopic states of the system (*microstates*) with energy E_j . In this way, the frequency of the event can be approximated by

$$f(\chi_B) = \sum_{j \in B} e^{-\beta E_j} \quad 2.3$$

with β being the Boltzmann's factor equal to $1/kT$ (where k is the Boltzmann's constant). From Eq. 2.3 it is clear that the probability of event B, proportional to its frequency through Eq. 2.2, depends exponentially on the energy of its microstates – indicating that low-energy microstates are more likely to occur (higher statistical weight). By substituting Eq. 2.3 into Eq. 2.2 one obtains

$$P_B = \frac{f(\chi_B)}{\sum_i f(\chi_i)} = \frac{\sum_{j \in B} e^{-\beta E_j}}{\sum_i e^{-\beta E_i}} = \frac{Z_B}{Z}, \quad 2.4$$

where the normalization factor in the denominator is called the *partition function* (Z), representing all the possible microstates of the system. Knowledge of the system's partition function permits calculation of thermodynamic quantities such as the Helmholtz free energy (F) and entropy (S).

$$F = -kT \ln Z|_{T_0, V_0}, \quad 2.5$$

$$S \equiv -\frac{\partial F}{\partial T} = \frac{\partial(kT \ln Z)}{\partial T}|_{T_0, V_0}. \quad 2.6$$

On the basis of this description, thermodynamic control of self-assembly at thermal equilibrium can be accomplished by maximizing the partition function of the final (assembled) state and minimizing that of the initial (disassembled) state. This is done by minimizing the total number of degrees of freedom as well as the accessible states of the initial system (*low initial absolute entropy*) and minimizing the energy of the final system (*low final enthalpy, i.e. high enthalpic stabilization*) – Eq.2.5. Typically, low initial-entropy states can be achieved with building blocks of low molecular weight, or by designing them to be symmetric and stiff. During this project self-assembly was investigated at the liquid-solid interface, where the solvent also plays as a variable. Ideally, good solvation of solute molecules is required for assembly of single building blocks and not of aggregates of these. At the same time, competition between solvation and adsorption on the surface is the key for achieving self-assembly (together with other factors)⁵. Also note that at the liquid-solid interface, on-surface diffusion may be less relevant than it is in ultra-high vacuum (UHV) systems. Indeed, by tuning the solution concentration, diffusion on and off of the surface can predominate over on-surface diffusion.

In 2D self-assembly the substrate not only serves as physical support, but also plays a pivotal role driving pattern formation. Furthermore, studying molecular self-assembly at surfaces is favourable because the substrate minimizes the accessible states in the initial system, therefore decreasing the inevitable and unfavorable entropy loss upon assembly.

Large final state partition functions can only be achieved by “playing” with the enthalpy, given that ordered SAMNs are low entropy systems – Eq. 2.1. For this reason, molecular precursors are chemically designed to maximize the binding energy (BE) per molecule, both in terms of number of lateral interactions (*coordination number*) and of molecular recognition. SAMNs can be typically stabilized by a number of non-covalent forces such as van der Waals (vdW)^{14, 54-55}, π - π stacking⁵⁶⁻⁵⁷, hydrogen bonding^{15, 58} or metal coordination⁵⁹⁻⁶⁰. The subtle

interplay between molecule-molecule and molecule-substrate interactions ultimately leads to the stabilization of the assembled structures. In this project we investigated systems laterally stabilized by vdW interactions between tightly packed alkyl chains, hydrogen bonding between carboxylic groups and by one other type of weak intermolecular force, namely halogen bonding⁶¹ (note that in addition to these forces, non-covalent molecule-substrate interactions also stabilize the systems, typically in the form of π - π interactions).

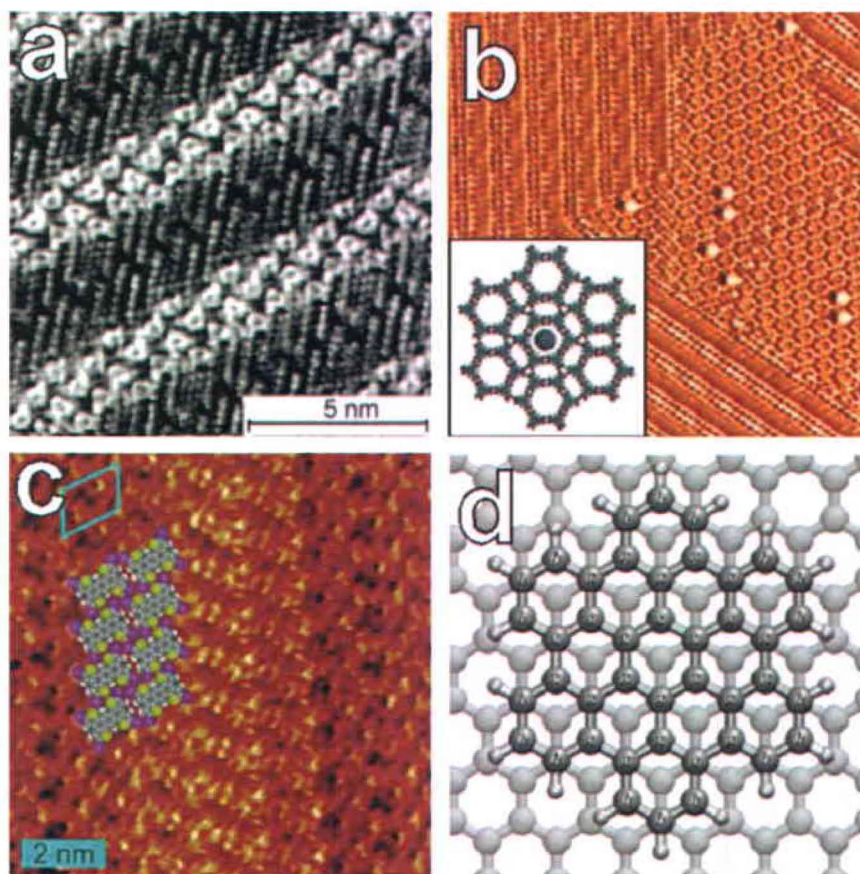


Figure 2.3: SAMNs can be stabilized by interactions such as a) vdW, b) hydrogen-bonding, c) halogen bonding and d) π - π stacking. Reproduced from a) ref.¹⁴, b) ref.¹⁵, c) ref.¹⁶ and d) ref.¹⁷.

Halogen-bonded 2D structures^{16, 19, 62-65} are interesting due to the peculiar double polarisation of the carbon-halogen (C-X) bond, which permits the formation of geometrically stable structures with the halogen termination participating in more than one interaction (Figure 2.4a)^{19, 66-67}. The tip of the C-X bond exhibits a positively charged cap (or σ -hole), while a negative ring-like charge distribution is established around the C-X bond⁶⁸. The

molecular electrostatic potential (ESP) at the σ -hole becomes more positive with decreasing position in the seventh group of the periodic table ¹⁸, meaning that the strength of the interaction can be adjusted by varying the halogen substituent (Figure 2.4b).

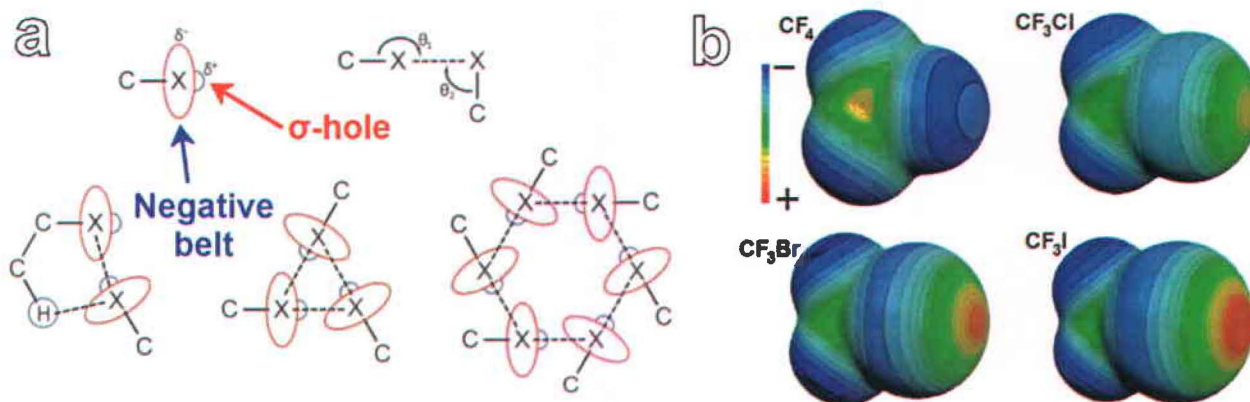


Figure 2.4: a) Scheme of the polarization at the C-X bond and possible geometries of halogen bonded structures, reproduced from ref. ¹⁹. b) Potential at the σ -hole as a function of the halogen substituent size, reproduced from ref. ¹⁸.

Chapter 3. SURFACE POLYMERIZATION

Besides the interest in self-assembly from a fundamental scientific perspective, to exploit this bottom-up strategy for the large-scale fabrication of actual devices requires the improvement of the stability of weakly bonded supramolecular structures⁶⁹. In the past fifteen years⁷⁰ researchers have investigated surface polymerization to address this problem, which would increase the chemical and thermal stability of molecular structures necessary for applications in typical adverse ambient conditions^{21, 71-75}. In addition, surface polymerization is also important for electrical properties in terms of high charge carrier mobility, thanks to conjugated π -orbitals rather than weak non-covalent bonds.⁷⁶⁻⁷⁷ Ideally, a tunable graphene-like 2D structure is desirable because of its excellent mechanical and electrical properties⁷⁸⁻⁸¹ – Figure 3.1a,b. Surface polymerization reactions can be achieved in several ways: catalytically, thermally, electrochemically, by excitation by radiation or with a STM tip pulse (Figure 3.1c-f). In the systems presented in this work surface polymerization was attempted using ultra-violet (UV) radiation and thermal energy in presence of a catalytic surface (*via* Ullmann aryl-aryl coupling⁸²).

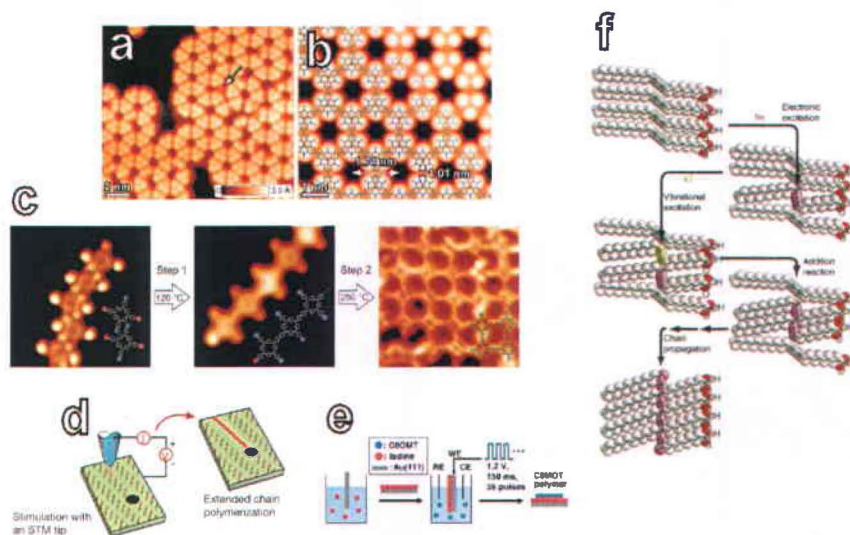


Figure 3.1: a) Experimental and b) simulated STM image of a 2D porous nitrogen-containing carbon covalent network, reproduced from ref.²⁰; c) steps to achieve a 2D covalent network *via* Ullmann coupling, *i.e.* aryl-aryl coupling after thermally activated dehalogenation, reproduced from ref.²¹; d) STM tip pulse activated one-dimensional (1D) polymerization of diacetylene monomers, reproduced from ref.²²; e) scheme of electrochemical polymerization, reproduced from ref.²³; f) mechanism of the UV-activated 1D polymerization of diacetylenes, reproduced from ref.²⁴.

UV polymerization was the first method used (1997) for the fabrication of surface polymers (1D polymerized chains – Figure 3.2a). In this kind of chain-reaction, precursors featuring a diacetylene moiety are used – *i.e.* with two triple carbon–carbon bonds alternated by single bonds (Figure 3.2c). When diacetylenes are properly arranged, 1,4-carbon addition of adjacent units leads to the formation of 1D conjugated polymers through a chain-reaction (see Figure 3.2d for labeling). By exciting the system either thermally, radiative or with a STM tip pulse, one of the triple bonds can be broken. If enough vibrational energy is provided, the excitation can propagate through neighbouring diacetylene moieties for several tens of nm, thus leading to 1D polymers *via* addition reactions. Using STM, the formation of 1D polymeric chains is easily verified by the presence of bright lines, which are a consequence of the fact that upon polymerization the 1D chain is lifted off the surface (Figure 3.2b). This reaction is called *topochemical polymerization*, given that specific geometrical parameters must be satisfied for the polymerization to occur. In fact, the chain-reaction is achieved only if three conditions are simultaneously fulfilled (Figure 3.2d): 1) the monomers must be arranged in such a way that the angle (ϕ) between the stacking axis and the diacetylene moiety is roughly 45° ; 2) the stacking distance (R_V) between the monomers in the array must be approximately 5 \AA ; 3) the distance between the 1,4-carbon atoms (R) must be less than 4 \AA ⁸³.

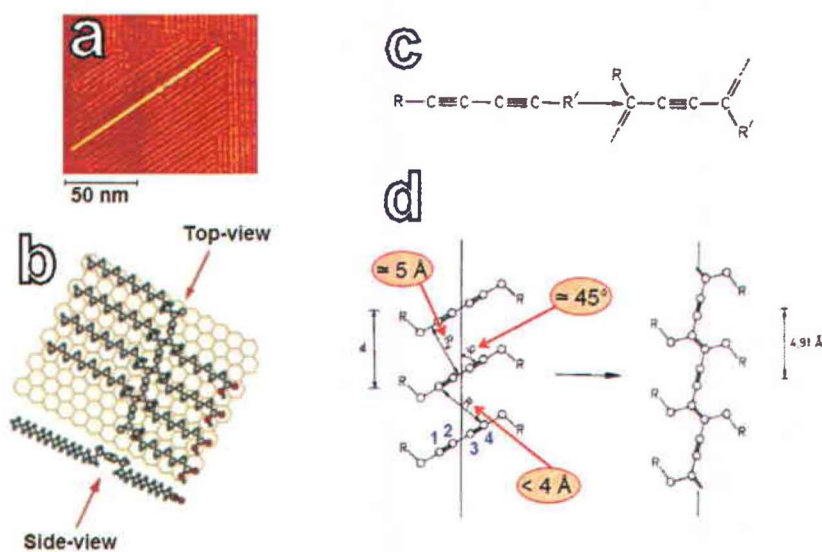


Figure 3.2: a) STM image of polymerized 1D chains, identified by the bright line (tens of nm long), and b) model of the polymerized system, reproduced from ref. ²⁴; c) diacetylene polymerization reaction and d) topochemical parameters, reproduced from ref. ⁸³.

The other type of polymerization attempted for the systems investigated in this project is Ullmann aryl-aryl coupling (1904)⁸², named after German chemist Fritz Ullmann (1875 - 1939), a strategy widely used in our research group to create surface polymers⁸⁴⁻⁸⁶. Originally, the Ullmann reaction involved polymers obtained from aryl halides (*i.e.* substituents made of an aromatic ring functionalized with a halogen atom) with a copper catalyst, however nowadays the term is generally extended to refer to any type of aryl halide with any type of metal catalyst (*e.g.* nickel, platinum, silver, *etc.*). The first step of the Ullmann coupling is the cleavage of the C–X bond, which is typically thermally activated although on very reactive surfaces it can also occur at temperatures as low as ambient room temperature (RT) – Figure 3.3. The C–X bond strength decreases with increasing size of halogen atom, namely it is strongest for fluorine and weaker for iodine¹⁸. This can be useful depending on the experiment to be performed – see for example Figure 3.1c where as a first step only the iodine atoms were cleaved (to form a 1D polymer) and in a second step the bromine atoms were also detached by increasing the temperature (to convert rows of 1D polymers to a 2D polymer)²¹.

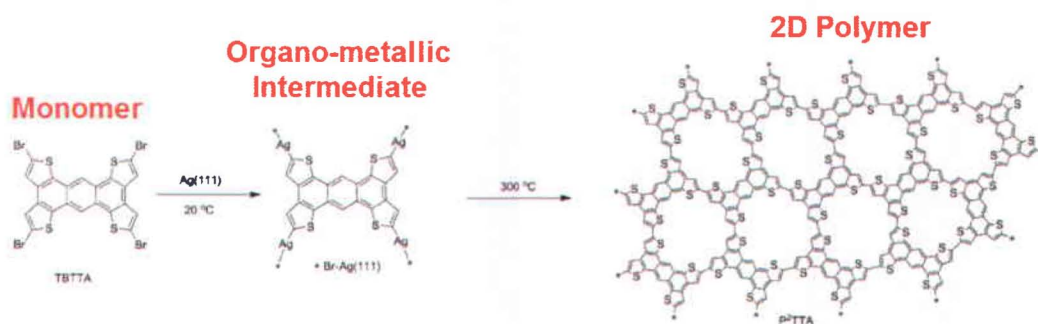


Figure 3.3: Ullmann polymerization of conjugated thiophene monomers, reproduced from ref.⁸⁶.

After the halogen atoms are detached, the formed radicals either bind to surface metal atoms forming intermediate organo-metallic species or bind with other radicals, hence forming polymeric structures (Figure 3.3). The formation of intermediate steps depends on the energy barrier between the organo-metallic and polymeric species. Despite the fact that the Ullmann reaction was first reported more than 100 years ago, the formation of such intermediate organo-metallic entities has not been studied widely and research in this respect is ongoing^{59-60, 87-88}.

Chapter 4. SCANNING TUNNELING MICROSCOPY

Scanning tunneling microscopy is a technique used for the nanoscale characterization and manipulation of 2D systems, based on the quantum mechanical phenomenon known as *tunneling*⁸⁹. Invented by Binnig and Rohrer (1986 Physics Nobel Prize) at IBM Labs in 1981⁹⁰, together with transmission electron microscopy (TEM) and field ion microscopy (FIM) it allows real-space visualization of single atoms (Figure 4.1a). An STM consists of a sharp, electrically conductive tip (chemically etched or mechanically cut) mounted on piezoelectric transducers that control its position in three dimensions (Figure 4.1b). When the tip is approached close to an electrically conductive surface (tip-to-surface distance $\approx 1\text{--}10 \text{ \AA}$), electrons can tunnel through the vacuum gap between the two. In the classical regime this gap prevents any form of electrical connection, however at small scale nature does not obey the classical laws of physics.

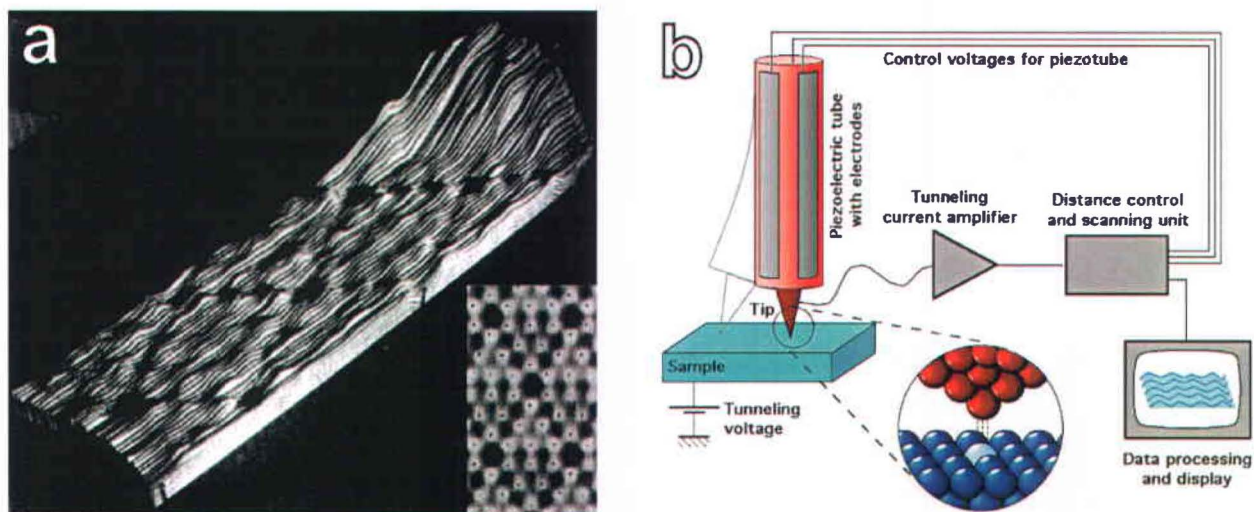


Figure 4.1: First high-impact STM image ever recorded (1983), showing the relief of two cells of the 7x7 reconstructed Si(111) surface; the inset is a top-view of the relief. b) Schematic view of an STM. Reproduced from a) ref.²⁵ and b) ref.⁷.

Following the quantum mechanical description of nature, there is a finite probability that a particle can penetrate a potential barrier even if its energy is lower than the barrier. An analogy with the classical case would be that a ball with kinetic energy smaller than the

potential energy necessary to overcome a mountain could actually tunnel through the mountain, hence “overcoming” it. This counterintuitive principle is permitted in quantum mechanics, but is only typically observable at small length scales. A quantum mechanical system, e.g. an electron moving through a potential, is described by its wave function $\psi(z)$ (or *eigenstate*), which satisfies the Schrödinger equation:

$$H\psi(z) = -\frac{\hbar^2}{2m} \frac{d^2}{dz^2} \psi(z) + U(z)\psi(z) = E\psi(z), \quad 4.1$$

where the electron possesses energy E in a potential $U(z)$ and H is the Hamiltonian operator describing the system – note that Eq.4.1 is the simplest form of the Schrödinger equation, *i.e.* the 1D, time-independent and non-relativistic case. The Schrödinger equation for the problem of an electron tunneling from the tip to the sample, *i.e.* for the energy landscape of Figure 4.2, can be solved treating separately the classically allowed case ($E > U$) and the classically forbidden case ($E < U$).

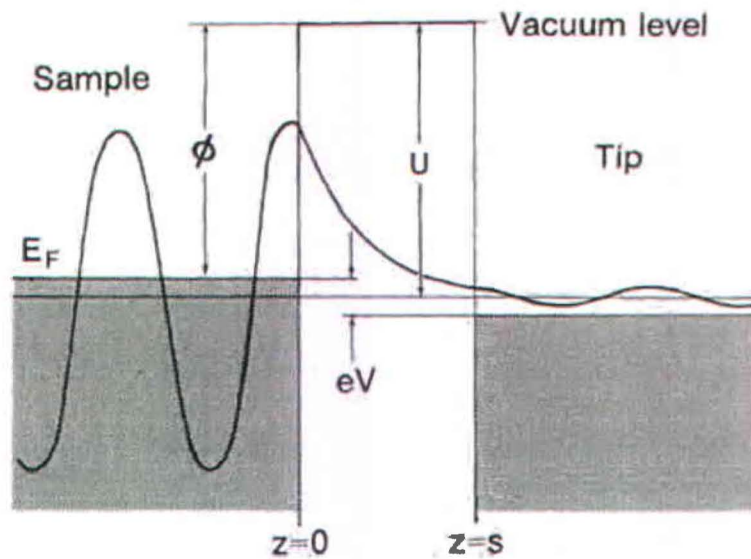


Figure 4.2: Energy landscape of the 1D system with a particle tunneling through a barrier of width s , when a voltage V is applied between tip and sample. Reproduced from ref. ⁹¹.

This is done by properly using boundary conditions (BCs) that make the total wave function continuous between the different regions. In the classically allowed region the electron behaves as a travelling plane wave, and within the barrier its wave function decays exponentially with the gap width:

$$\psi(z) = \psi(0)e^{\pm ik_1 z} , \quad E > U \quad 4.2$$

$$\psi(z) = \psi(0)e^{-k_2 z} , \quad E < U \quad 4.3$$

where $\psi(0)$ is a normalization constant, which ensures probabilities ≤ 1 , and the wave vectors k_1 and k_2 are equal to $\sqrt{2m(E - U)}/\hbar$ and $\sqrt{2m(U - E)}/\hbar$, respectively. Note that Eq.4.2 is equal to the solution obtained for a wave in the classical framework.

By applying a bias (V) between the tip and the sample, electrons in the energy range between the Fermi level (E_F) and $E_F - eV$ can tunnel through the vacuum barrier. In the approximation that eV is much smaller than the tip and sample work functions (ϕ , assumed to be the same for both), all the states between E_F and $E_F - eV$ have same energy $-\phi$, taking the vacuum level as reference (*i.e.* $E_{vac} = 0$). The total tunneling current, therefore, is given by the sum of the probabilities of all the n electrons in the states between E_F and $E_F - eV$ to tunnel from the sample to the tip (or *vice versa*):

$$I \sim \sum_{E_n = E_F - eV}^{E_F} |\psi_n(0)|^2 e^{-2kS} , \quad 4.4$$

where S is the barrier width and k the wavevector, equal to $\sqrt{2m\phi}/\hbar$. In STM experiments the bias voltage is typically smaller than the metals workfunctions, *e.g.* with absolute value < 2 V. This is important because at large bias voltages the exponential dependence of the tunneling current with the gap width (given by Eq.4.4), which translates into lateral resolution (see below), is lost (this is known as the *Fowler-Nordheim regime*). For this reason, STM images typically provide information only of the density of states (DOS) near the Fermi level (*i.e.* of

the least bound electronic states, which are the ones of greatest interest given that these are the states involved in interactions with other systems, e.g. chemical bonding). Furthermore, STM allows the investigation of either the filled or empty electronic states near the Fermi level, simply by changing the polarity of the applied bias voltage. If the voltage is such that electrons tunnel from the tip to the sample, the STM image represents the empty states of the sample (Figure 4.3a). On the other hand, if electrons tunnel from the sample to the tip, the STM image represents the filled states of the sample (Figure 4.3b). Note that in case of molecular adsorbates on surfaces, the filled and empty states are often referred to as occupied or unoccupied molecular orbitals, however this is not rigorously correct given that in a STM image the electronic structure of the adsorbates (*i.e.* the adsorbed molecules) cannot be treated separately from that of the surface (see below) – in addition to the presence of the STM tip.

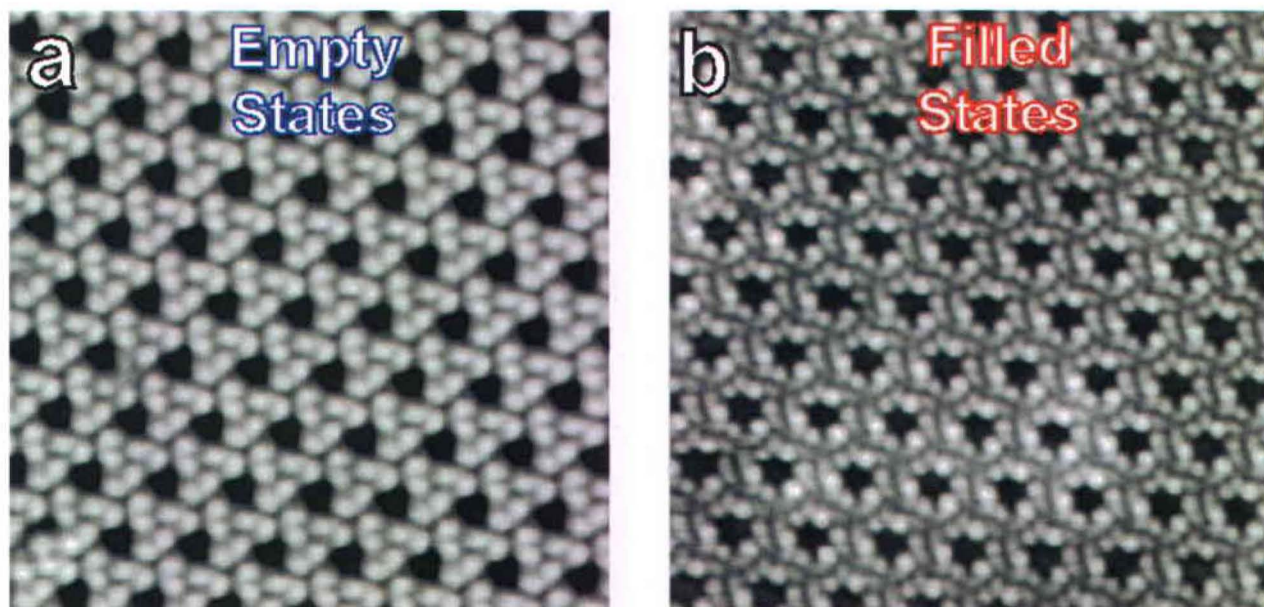


Figure 4.3: STM images of the a) empty and b) filled states of 1,3,5-triphenyl-benzene (THB) assembled on a boron-passivated Si(111) surface, in UHV at 77 K. Reproduced from ref. ²⁶.

In the approximation of a spherical tip with radius R much larger than the tip-to-sample distance, the lateral current distribution is

$$I(\Delta x) = I_0 e^{-2k \frac{\Delta x^2}{2R}} . \quad 4.5$$

Eq.4.5 shows that at a given ratio I/I_0 , the smaller the tip radius (ideally only one atom) the smaller the lateral resolution.

In STM, as opposed to atomic force microscopy (AFM) for instance, the topography of surfaces or adsorbates is always discerned on the basis of their electronic structure. Indeed, a STM image is nothing but a map of the convolution of the local density of states (LDOS) of the tip and the LDOS at the Fermi level of the sample, where the contrast is given by a combination of topography and overlap of the substrate and adsorbate DOS. In STM experiments, substrate and adsorbates are always referred to as the sample as a whole, given that their electronic properties cannot be treated separately.

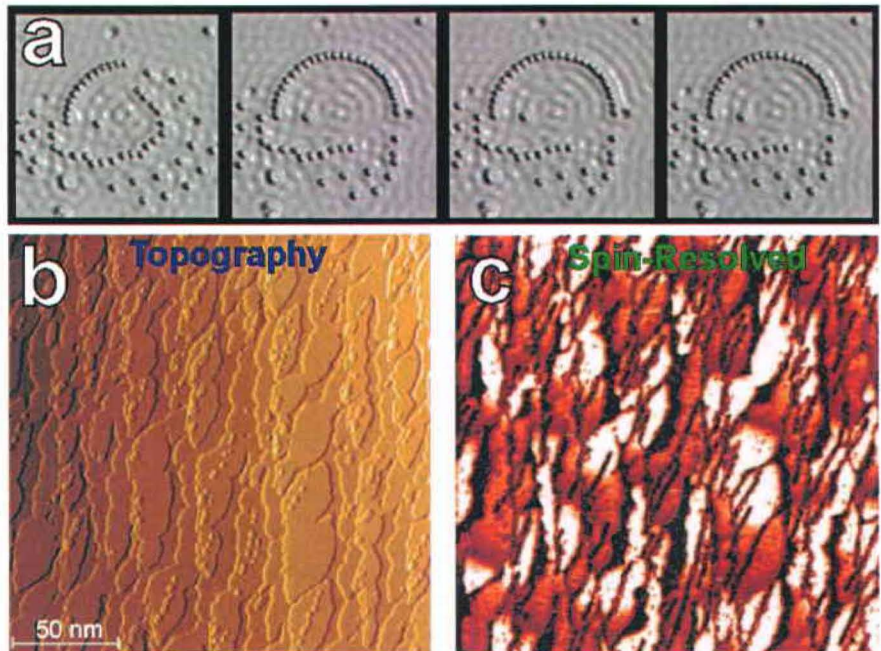


Figure 4.4: a) Steps for the fabrication of a 48-atom Fe ring on a Cu(111) surface. The bottom right image clearly shows the strong modulation of the LDOS inside the ring. b) STM topograph and c) spectroscopic spin-polarized STM (SP-STM) image of a nanocrystalline Fe film, showing the correlation between magnetic and grain structure at sub-nm scale spatial resolution. Reproduced from a) ref. ²⁷ and b),c) ref. ²⁸.

Figure 4.4a is a nice demonstration of this, being a real-space image of the energy eigenstates of a quantum corral made of 48 iron (Fe) atoms on a Cu(111) surface ²⁷. The wavy contrast inside the Fe ring is not due to the topography of the surface, rather it arises from the strong modulation of the LDOS by the Fe atoms on the surface. In other words, this effect is due to the scattering between the surface electronic wave functions of the iron atoms as a consequence of the confinement of surface state electrons ²⁷.

In addition to its astonishing resolution, STM is an extremely powerful tool also because it allows manipulation of matter at the atomic scale, *via* tip-sample interactions that can be tuned changing the bias voltage ^{27, 92-93} (Figure 4.4a). Furthermore, an STM can also be used to perform electronic or vibrational spectroscopy of single molecules ⁹⁴⁻⁹⁶ as well as to do spin-resolved spectroscopy ²⁸ (Figure 4.4b,c). We will not discuss these aspects in further detail since during this project STM was only used as an imaging technique.

4.1 THE NANOSCOPE III

The STM experiments reported in this work were performed with a Digital Instruments Nanoscope III (Figure 4.5a-c) using metallic tips mechanically cut from 80/20 Pt/Ir wire (Nanoscience Instruments Inc.), which were immersed in a drop of solution applied onto the substrate. All STM images were acquired in the constant-current mode at room temperature (where a feedback loop maintains the tunneling current constant by varying the tip-to-sample distance accordingly) and processed with the free WSxM software.⁹⁷ Pt/Ir mechanically cut tips (Figure 4.5d,e) are typically used for experiments in ambient conditions, as opposed to chemically etched tips (e.g. made of tungsten) that are used for experiments in UHV (Figure 4.5f).

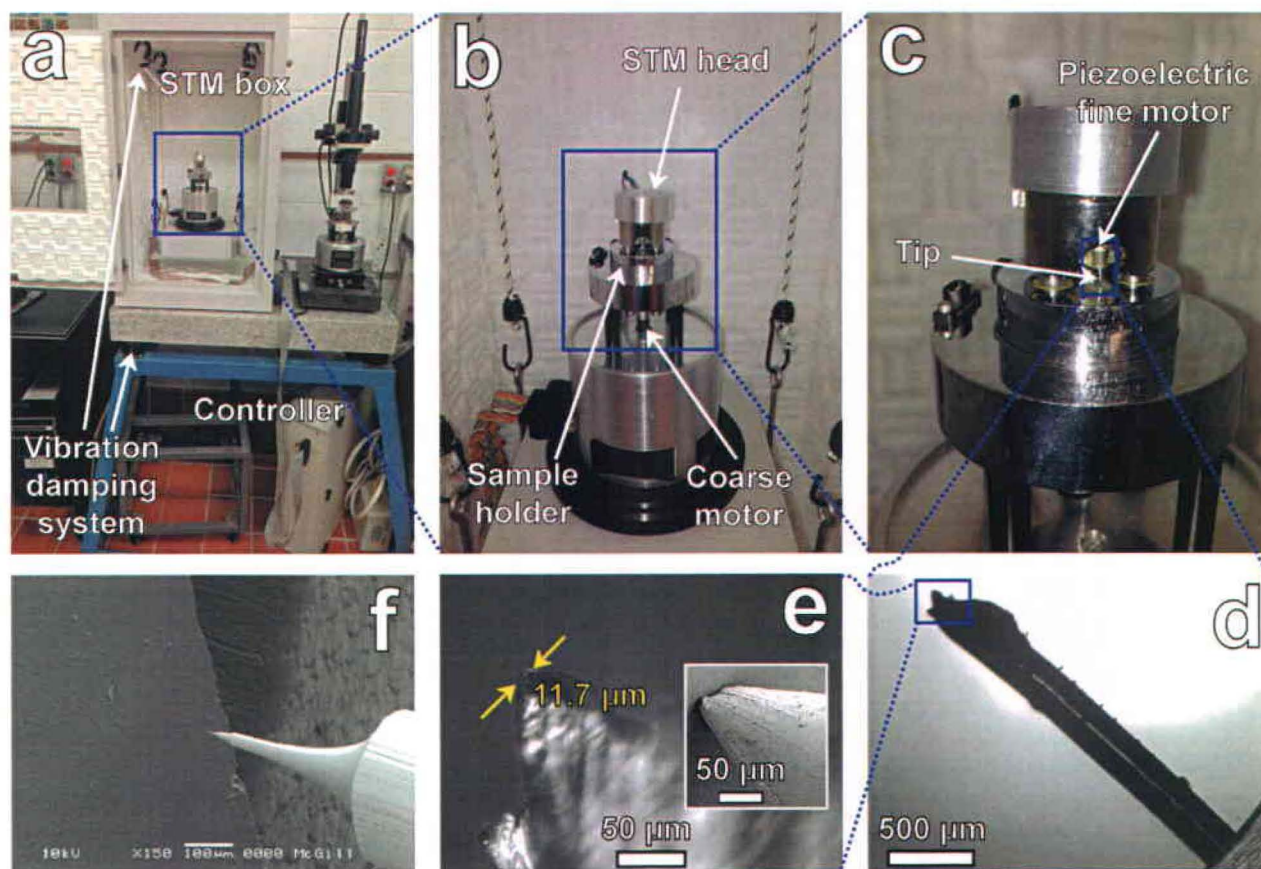


Figure 4.5: a)-c) Photographs of the STM Nanoscope III; d),e) optical micrographs of a mechanically cut Pt/Ir tip; the inset in e) is a scanning electron microscopy (SEM) image of the tip apex (courtesy of C. Harnagea). f) SEM image of a polycrystalline tungsten tip etched in KOH (courtesy of Prof. P. Grutter from the Department of Physics at McGill University).

A STM tip must be as narrow and sharp as possible, ideally with one single atom at its very end. This is important for achieving high resolution and avoiding artifacts. Moreover, scanning molecular adsorbates with STM has the further challenge that molecules can be “picked up” by the tip during image acquisition, hence changing the physical state of the tip. This is illustrated in Figure 4.6a where during image acquisition the tip changed its state, as proved by the different contrast arising from the molecular assembly in the green and red regions. Figure 4.6b,c shows a high-resolution STM image of the benzene molecule in the square of Figure 4.6d, taken with a benzene molecule attached to the tip. In this case the corrugation of the substrate gold atoms is enhanced and the benzene molecules appear as depressions.

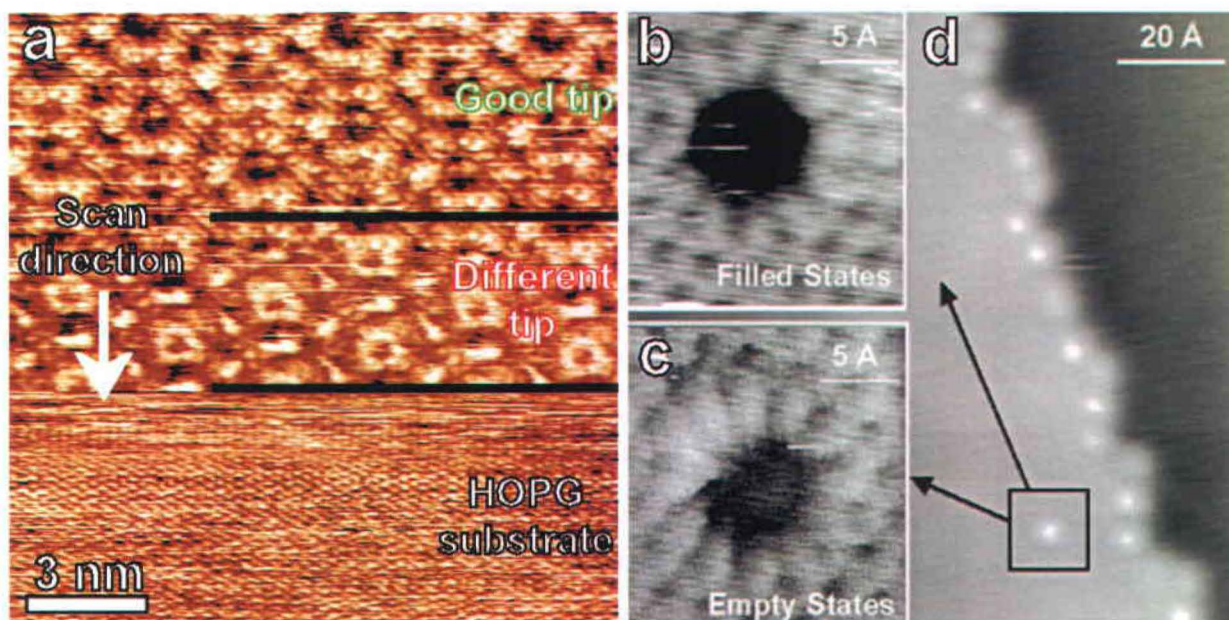


Figure 4.6: a) STM image of trimesic acid (TMA) molecules assembled at the heptanoic acid-highly oriented pyrolytic graphite (HOPG) interface ($15.0 \times 15.0 \text{ nm}^2$, $V_s^{\text{HOPG}} = -0.02 \text{ V}$ and $V_s^{\text{SAMN}} = -1.08 \text{ V}$, $I_t = 324 \text{ pA}$). During image acquisition the tip changes its physical properties, perhaps due to a TMA or solvent molecule attached to it. b),c) STM images of a single benzene molecule adsorbed on Au(111) taken at negative and positive sample bias, respectively, which hence depict the filled and empty state densities of the surface, respectively. d) STM image of benzene molecules adsorbed above a monoatomic step of the substrate. b)-d) reproduced from ref. ⁹⁸.

Chemical etching is a more reliable method for STM tip fabrication in terms of reproducibility, and it is preferred in UHV experiments because of the hurdles associated with re-establishing the proper vacuum after the chamber has been opened to mount a tip (this is a long process

that can take as long as a few days). On the other hand, experiments in ambient conditions have an advantage that if the tip performance is not satisfactory, it can be easily replaced in a few seconds (the Pt/Ir wire is not too expensive: roughly 1.50\$ per tip). Surprisingly enough, mechanically cut tips can lead to resolution as high as that of etched tips. In the preparation of such tips, the Pt/Ir wire is cut with pliers applying simultaneously a pulling force. In such a way, the two sides of the wire are not separated by a sharp and straight cut, rather they are torn apart. Given the nature of the metal wire, which is ductile and malleable, this method leads to tips whose end is typically sharp enough for STM experiments.

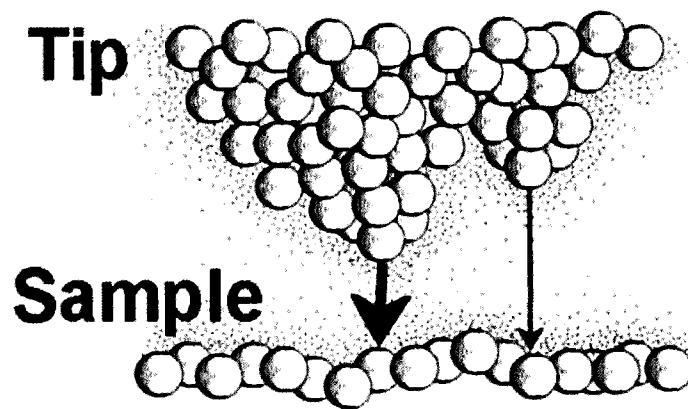


Figure 4.7: The tunneling transmittivity decreases exponentially with the tunneling distance, in vacuum about a factor of 10 for every Å. Therefore, assuming a tungsten tip, the current through the thicker arrow is approximately 40 times larger. Reproduced from ref. ⁸⁹.

Furthermore, thanks to the exponential dependence of the tunneling current with the tip-to-sample distance, even tips with multiple protrusions near the apex can perform well. In fact, assuming that the tunneling current decreases by a factor 10 every Å ⁸⁹, for the tungsten ($r^W = 1.39 \text{ \AA}^7$) tip of Figure 4.7 the current through the thicker arrow would be roughly 40 times larger than that through the thinner arrow. One drawback of this cheap and fast STM tip fabrication method is that the shape of the tip is never the same, which can be a problem in terms of reproducibility between different experiments. Although at first glance mechanically cut tips look less appropriate for delicate STM experiments compared to etched tips (Figure 4.5d,e vs. f), they perform very well despite the ease of the fabrication method. Note that etched tips may also be used for experiments in ambient conditions.

Chapter 5. THEORETICAL METHODS: DENSITY FUNCTIONAL THEORY

One of the main scientific achievements of last century was the advent of quantum mechanics (perhaps together with Einstein's theories of relativity), a completely new branch of physics that describes the laws of nature from the molecular to the subatomic scale. Despite the principles of quantum mechanics being counterintuitive from a classical perspective, this theory not only explains real phenomena that cannot be described by classical laws, but is also extremely accurate. Kohn-Sham (KS) density functional theory is an extremely successful approach developed in the 1960s that permits solving the fundamental equations that describe atoms and molecules^{29, 99-100}, namely the Schrödinger equation (already mentioned in Chapter 4, Eq.4.1), "generating information that would be essentially impossible to determine through experiments"¹⁰¹. The advantage of DFT over other quantum chemistry computational methods is that it allows calculation of the electronic structure of a material by transforming a computationally heavy many-electron problem into a simpler problem involving non-interacting electrons moving in a self-consistent field¹⁰² (see Section 5.1). In the past few decades, the application of DFT calculations has changed from being used only by scientists at the cutting edge of quantum mechanical theory to being a "standard tool" in diverse fields such as physics, chemistry, materials science and geology. A recent study of the papers published and cited in the Physical Review family of journals 1893-2003³⁰ shows that the three most-cited ones are all DFT papers^{29, 99, 103}. Similarly, four out of the five papers most cited by chemists in 2003¹⁰⁴, as well as the most-cited physics paper published since 1994¹⁰⁵, are also DFT papers. DFT has given important contributions to remarkable scientific advances, from ammonia synthesis by heterogeneous catalysis¹⁰⁶ and the embrittlement of metals by trace impurities¹⁰⁷ to models for planetary formation¹⁰⁸.

DFT calculations, together with other forms of computational chemistry, are tools that allow one to solve the Schrödinger equation of systems such as atoms, molecules and solids, therefore providing physical information such as bond distances and angles, energy and electron density. The simplest form of the 3D Schrödinger equation, *i.e.* time-independent and nonrelativistic, is $E\psi = H\psi$ (note that here we cannot use Eq.4.1 because this problem is not 1D). In this equation, H is the Hamiltonian operator that describes the physical system and ψ

is a set of solutions (*eigenstates*) of the Hamiltonian. In the case of a solid or a molecule, the Hamiltonian must include all the electrons interacting with all the nuclei:

$$\left[\frac{h^2}{2m} \sum_{i=1}^N \nabla_i^2 + \sum_{i=1}^N V(\mathbf{r}_i) + \sum_{i=1}^N \sum_{j<1}^N U(\mathbf{r}_i, \mathbf{r}_j) \right] \psi = E\psi. \quad 5.1$$

In this equation m is the electron mass, h is Planck's constant, \mathbf{r}_i and \mathbf{r}_j are the spatial coordinates of each of the N electrons and E_n is the eigenvalue associated with the specific ψ_n . This Hamiltonian, known as the *Born-Oppenheimer approximation*, treats electrons and nuclei separately given their huge difference in mass (each proton or neutron in a nucleus has more than 1800 times the mass of an electron). The first term in bracket defines the kinetic energy of each electron, the second term the attractive interaction energy between each electron and the collection of atomic nuclei and the third term the repulsive interaction energy between different electrons. The electronic wave function ψ is function of the 3 spatial coordinates of each of the N electrons, thus $\psi = \psi(\mathbf{r}_1, \dots, \mathbf{r}_N)$, which can be approximated as the product of individual electron wave functions, $\psi = \psi_1(\mathbf{r})\psi_2(\mathbf{r}), \dots, \psi_N(\mathbf{r})$. This approximation, known as *Hartree product*, does not reduce the variables on which the electronic wave function ψ depends, *i.e.* $3N$, however in some cases it is mathematically easier to handle. At this point it is clear that computations are realistically feasible only for fairly simple systems. For instance, the full wave function of a nanocluster of 100 Pt atoms would have more than 23000 dimensions. Furthermore, the situation is even more complicated considering that the Schrödinger equation is a many-body problem, this meaning that the individual electron wave function $\psi_i(\mathbf{r})$ cannot be found without considering at the same time all the other individual wave functions in the third term of the Hamiltonian in Eq.5.1, *i.e.* the electron-electron interaction term.

Density functional theory is a solution to these hurdles, being a fairly simple computational chemistry theory for which W. Kohn was awarded the Nobel Prize in chemistry in 1998, jointly with J. Pople "for his development of computational methods in quantum chemistry" ¹⁰⁹. Note that this was the first time ever that a Nobel Prize in physics or chemistry was awarded for the development of numerical methods. Although any quantum mechanical

system is entirely and solely defined by its wave function, this is not a physical observable that can be actually measured. These fundamental concepts are the foundations of quantum computing and quantum cryptography. Note that the 2012 Physics Nobel Prize was awarded to S. Haroche and D. J. Wineland "for ground-breaking experimental methods that enable measuring and manipulation of individual quantum systems", which broadly means measuring a wave function without causing its collapse ¹¹⁰.

Although the electronic wave function, solution of Eq.5.1, cannot be measured, one can measure the probability that the N electrons are at a given set of coordinates $\mathbf{r}_1, \dots, \mathbf{r}_N$. In quantum mechanics such probability is given by the complex conjugate of the wave function. A quantity that is closely related to this is the density of electrons at a particular position in space, $n(\mathbf{r})$, which can be expressed in terms of the individual electron wave functions:

$$n(\mathbf{r}) = 2 \sum_i \psi_i^*(\mathbf{r})\psi_i(\mathbf{r}). \quad 5.2$$

This summation goes over all the individual electron wave functions occupied by electrons, hence the term inside the summation is the probability that an electron in $\psi_i(\mathbf{r})$ is located at position \mathbf{r} . The great advantage of using the electron density is that this is function of only 3 coordinates, which give the position \mathbf{r} where the electron density is to be calculated. The electronic density (3 variables) contains less information than the full wave function ($3N$ variables), however it has great amount of the actually physically observable information contained in the full wave function (and considerably smaller computational effort).

The entire field of density functional theory is based on two fundamental mathematical theorems, proved by Kohn and Hohenberg, and a set of equations derived by Kohn and Sham in the mid-1960s. The first theorem reads:

"The ground-state energy from Schrödinger's equation is a unique functional of the electron density".

In other words, the ground-state energy (E) can be expressed as the functional $E[n(\mathbf{r})]$, which is the reason why this field is known as density functional theory. Note that DFT does not

necessarily imply *electron* density functional theory. In fact, the theory can be based on functionals of electron density, spin density, kinetic energy density, and so on – see Section 5.1. A functional is a mathematical entity similar to a function, however instead of taking the value of one or more variables it takes the value of a function and defines a single number of the function:

$$f(x) = x^2 + 1 \quad \text{function}$$

$$F[f] = \int_{-1}^1 f(x) dx. \quad \text{functional}$$

The importance of this theorem is that it allows one to solve the Schrödinger equation. The ground-state energy can be found by using a function of 3 spatial variables, *i.e* $n(\mathbf{r})$, rather than of $3N$ variables (ψ). This is valid for any system, even the nanocluster of 100 Pt atoms with its 23000 variables.

The first Hohenberg-Kohn (HK) theorem, however, does not provide any information of the actual functional to be used, which is instead included in the second theorem:

“The electron density that minimizes the energy of the overall functional is the true electron density corresponding to the full solution of the Schrödinger equation”.

Given that the single-electron wave functions $\psi_i(\mathbf{r})$ define the electron density (Eq.5.2), it is useful to express the energy functional in function of these:

$$E[\{\psi_i\}] = E_{\text{known}}[\{\psi_i\}] + E_{\text{XC}}[\{\psi_i\}], \quad 5.3$$

where the functional was split into a known term (E_{known}), which can be written in a simple analytical form, and in another term (E_{XC}) known as the exchange-correlation (XC) functional, which includes all the quantum mechanical effects not included in E_{known} . The known term includes the electron kinetic energy, the Coulomb attractive interactions between the

electrons and nuclei, the repulsive Coulomb interactions between pairs of electrons and between pairs of nuclei:

$$E_{known}[\{\psi_i\}] = \frac{\hbar^2}{m} \sum_i \int \psi_i^* \nabla^2 \psi_i d^3\mathbf{r} + \int V(\mathbf{r})n(\mathbf{r})d^3\mathbf{r} + \frac{e^2}{2} \iint \frac{n(\mathbf{r})n(\mathbf{r}')}{|\mathbf{r} - \mathbf{r}'|} + E_{ion}. \quad 5.4$$

So far the HK theorems were used to approach the problem of solving the Schrödinger equation from another perspective, namely searching the ground-state energy in terms of the electron density rather than in terms of the wave functions (1st HK theorem). The electron density that minimizes the energy of the overall functional (variational principle) is the true electron density of the full solution of the Schrödinger equation (2nd HK theorem). However, this does not indicate that solving the Schrödinger equation by searching for the electron density instead of the wave functions is actually simpler. It was Kohn and Sham who showed that this was indeed true, demonstrating that the right electron density can be found by solving a set of equations where each equation involves only a single electron:

$$\left[\frac{\hbar^2}{2m} \nabla^2 + V(\mathbf{r}) + V_H(\mathbf{r}) + V_{XC}(\mathbf{r}) \right] \psi_i(\mathbf{r}) = \epsilon_i \psi_i(\mathbf{r}) \quad 5.5$$

Kohn – Sham equations

The solution of each KS equation is a single-electron wave function $\psi_i(\mathbf{r})$, which depends only on three spatial variables. The first potential V in Eq.5.5 is the attractive Coulomb potential between the electrons and the nuclei, the same as in Eqs.5.1 and 5.4. The second potential V_H , called *Hartree potential*, describes the repulsion between the electron of the specific KS equation being considered and all the other electrons of the problem (*i.e.* the total electron density).

$$V_H(\mathbf{r}) = e^2 \int \frac{n(\mathbf{r}')}{|\mathbf{r} - \mathbf{r}'|} d^3\mathbf{r}' \quad 5.6$$

This potential also includes a self-interaction contribution due to the fact that the electron being considered is at the same time part of the total electron density. Therefore, the Hartree potential includes an unphysical interaction of the electron with itself, whose correction is included in the third potential V_{XC} .

$$V_{XC}(\mathbf{r}) = \frac{\delta E_{XC}(\mathbf{r})}{\delta n(\mathbf{r})} \quad 5.7$$

The right-hand side of Eq.5.7 is the derivative of a functional, for which reason it is written with the symbol δ rather than d , typically used for derivatives of functions. It should be noted that in order to solve the KS equations we must define the Hartree potential, which depends on the electron density: however, the electron density is the quantity we wish to calculate, ultimately giving the ground state of the Schrödinger equation. The problem is tackled by using an iterative approach (self-consistent method): first a trial electron density is chosen; this is used to define V_H and V_{XC} and therefore to solve the KS equations, which give the single-particle wave functions $\psi_i(\mathbf{r})$; the wave functions are then used to calculate the electron density with Eq.5.2, which is then compared to the trial one. If the two densities are equal then this is the ground-state electron density (which is used to compute the total energy); if not, the trial electron density must be updated, and the process is repeated.

Being this chapter only an introduction to DFT, we do not discuss in further detail important aspects such as how the trial electron density is chosen, how is it updated or how convergence criteria are chosen.

5.1 THE EXCHANGE-CORRELATION FUNCTIONALS USED: B3LYP, M06-L AND M06-2X

We have not defined yet the density functional for the exchange-correlation energy (E_{XC}), which is necessary to solve the KS equations. The true form of this functional is not known, which is why it is written separately in Eq.5.3, however we know it exists thanks to the 1st HK theorem. Levy has shown that the exact XC functional can be in principle determined¹⁰⁰, however this involves the satisfying of many exact constraints that would make the problem intractable¹⁰². Therefore, the XC functional is typically expressed in simplified approximations. The exchange-correlation energy is due to the fact that the electrons do not move randomly through the electron density but avoid one another, an effect that lowers the expectation value of the electron-electron Coulomb interaction¹⁰². The XC energy has three contributions: the first one is the *potential energy of exchange* (which includes self-exchange and self-correlation correction); the second one is the *potential energy of correlation* (due to the Coulomb repulsion on the interacting wave functions); the third one is a small *kinetic energy* due to the extra swerving motion of the electrons avoiding one another¹⁰². The first two terms are both negative because they reduce the expectation value of the repulsive electron-electron Coulomb interaction. On the other hand, the third (smaller) term is positive. According to the analogy of Tran and Perdew, “the motion of electrons through the electron density is like the motion of shoppers through a crowded mall”¹¹¹. As each shopper is surrounded by his/her “personal space”, each electron is surrounded by its so-called exchange-correlation *hole density*. Similarly to the fact that each shopper cannot bump into him/herself, an electron never interacts with itself. The exact XC energy provides a self-interaction correction to the Hartree electrostatic energy – Eq. 5.5.

Although the exchange-correlation energy is typically a relatively small part of the total energy of a given system¹⁰², it is the largest part of “Nature’s glue” that binds atoms together¹¹². Therefore, the type of approximation of the XC functional makes the difference between poor and accurate ground-state DFT calculations (we specify “ground-state” because DFT is known to be inaccurate for excited states¹⁰²). This section describes in detail the classes of

XC functionals used in DFT calculations. For clarity, we first describe the different classes of quantum chemistry calculations.

Quantum chemistry calculations can be classified according to the quantity that is to be calculated. We have so far described *DFT calculations*, whose goal is to compute the electron density to then find the ground-state energy. There is another class of calculations known as *wave function theory (WFT) calculations*, which can converge to the exact wave function describing the physical system (*wave-function-based methods*). An example of these kinds of calculations is the *Hartree-Fock (HF)* method, which is a self-consistent method similar to the procedure described above to solve the KS equations. In the HF method the total wave function is formed from the *Slater determinant* of the N lowest energy spin orbitals, where the spin orbitals are expanded in a finite set of functions, known as *basis set* (see Section 5.2). The main difference between HF and DFT methods is that the former ones do not describe electron correlations, although in principle treat the exchange part of the problem exactly.

Another way of classifying quantum chemistry calculations is according to which types of mathematical functions are used to represent their solutions, namely the electron density for DFT calculations or the full wave function for WFT methods. *Spatially-localized functions*, which tend to zero for large values of the spatial variable, are used in calculations with isolated atoms or molecules, given that in these physical systems the wave functions really do decay to zero far away. On the other hand, *periodic spatially-extended functions* are used for calculations with bulk materials, given that in the ideal defect-free case the wave functions of these systems are spatially periodic functions (*plane-wave methods*).

With the main classes of quantum chemistry calculations described, we may describe the different kinds of exchange-correlation functionals used in DFT methods. First of all, functionals can be *nonempirical* or *empirical* (the latter are also referred to as *semiempirical*). These two classes of XC functionals also define two classes of developers of functionals for DFT: traditional functional developers such as Perdew, Tao, Staroverov and Scuseria prefer using few or no empirical parameters, being against the “anything that works” attitude¹¹³. Nonempirical functionals are designed to satisfy the theoretical physical constraints imposed by the true KS functional, while empirical functionals are fitted to selected experimental data or *ab initio* calculations (as many as 21 fit parameters can be included in empirical

functionals)¹¹³. Nonempirical functionals are expected, generally speaking, to be more accurate than empirical functionals as more constraints are satisfied (with consequent higher computational effort). However, even though empirical functionals often violate known properties of the true KS functional, they can be very accurate in those problems that are closely related to the systems included in the training set (and fail badly in systems considerably different from these¹¹³). Empirical high-level functionals can be far less accurate for bulk and surface properties of simple metals than even the lowest-level non-empirical functionals¹¹⁴ (one of the reasons is that the latter typically satisfy the *uniform electron gas* (UEG) *limit* – see below). Therefore, empirical functionals are known to lack broad applicability.

The other important property of functionals is *locality*. Many functionals in DFT calculations with spatially-localized basis functions mix approximations for the correlation part with exact results for the exchange part, typically known from the HF method¹¹⁵ (the mixing is allowed by the *adiabatic connection theory*¹¹⁵). For these functionals, known as *hybrid* or *nonlocal*, the exact exchange part is typically expressed as a percentage (e.g. the functional M05 has 28% of HF exchange¹¹⁶), whereas the correlation part is derived from other sources, such as *ab initio* or empirical. All the other functionals are said to be *local* or *semilocal* (0% of HF exchange), namely when their electronic density or spin densities at a single spatial point depends only on the behavior of the electronic density and kinetic energy at and near that point¹¹⁷ (therefore intrinsically satisfying the UEG limit). In general, hybrid functionals perform better than local ones for main-group thermochemistry, whereas local functionals are more accurate for transition metals thermochemistry¹¹⁸. It is worth noting that the exact description of the exchange can only be implemented in calculations using spatially-localized functions but not periodic ones, given that solving the KS equations in a plane-wave basis set already considerably increases the numerical burden. Therefore, functionals in plane-wave DFT calculations usually do not include contributions from the exact exchange result.

The simplest approximation of the KS functional is the *local density approximation* (LDA), which uses only the local density to define the approximate exchange-correlation functional (hence the name *local functionals*). In the LDA, the local V_{XC} in the KS equations

5.5 is approximated by the exchange potential for the spatially uniform electron gas with the same density as the local electron density:

$$V_{XC}^{LDA}(\mathbf{r}) = V_{XC}^{electron\ gas}[n(\mathbf{r})]. \quad 5.8$$

In this case the electron density is constant at all points in space, and although this may seem limiting for the description of real materials (where bonds occur because of variations in electron density), it is a practical way to solve the KS equations. Note that the uniform electron gas is the only case where the exchange-correlation functional can be derived exactly, typically with careful *Monte Carlo calculations*¹¹³ (a computationally expensive technique that can converge to the exact solution of the Schrödinger equation). An important feature of local functionals is that they are exact in the UEG, the most fundamental constraint of the true KS functional, the limit meaning that *the exchange-correlation energy should be the exact energy of the uniform electron gas at that density*. As a general rule of thumb, local functionals perform well for bulk solids, where the valence electron density varies slowly, but are not desirable for atoms or molecules, where the electron density in general can change abruptly. Furthermore, they are expected to be accurate for closed systems near equilibrium but to fail for open systems of fluctuating electron number¹⁰². Note that LDA functionals do not necessarily depend on the electron density, but may also depend on the local spin density, its gradient or Laplacian, or even spin kinetic energy density of KS spin-orbitals¹¹⁹ (in absence of magnetic fields, the spin densities are a better choice than electron density¹⁰²). For instance, when LDA functionals are extended to spin-polarized systems, they are designed in the *local-spin-density approximation* (LSDA), in which density functionals depend only on the up- and down-spin local spin densities¹¹⁸. LSDA functionals are known to give accurate predictions in solid-state physics, however they are not (in principle) suitable for chemical systems given that they underestimate barrier heights and overestimate chemical bond energies¹¹⁸.

A higher-level approximation of the KS functionals is the *generalized gradient approximation* (GGA), which uses information about the local electron density and the local gradient in the electron density. This makes GGA functionals more flexible than LDA ones,

given that including information on the spatial variation in the electron density better describes real materials (whose electron density is not uniform).

$$V_{XC}^{GGA}(\mathbf{r}) = V_{XC}[n(\mathbf{r}), \nabla n(\mathbf{r})]. \quad 5.9$$

Although GGA functionals use more information than LDA ones, they do not necessarily provide more accurate calculations (despite being more computationally demanding). Similarly to LDA functionals, non-empirical GGA functionals satisfy the UEG limit. Two widely used nonempirical functionals used in calculations involving solids are the Perdew-Wang functional (PW91) and the Perdew-Burke-Ernzerhof functional (PBE).

According to J. Perdew's classification of DFT functionals (Figure 5.1), the next higher class of functionals is defined by *meta-GGA functionals*, which include information from the electronic density, its gradient and its Laplacian. The Tao-Perdew-Staroverov-Scuseria (TPSS) functional is an example of a non-empirical meta-GGA functional. The M06-L and M06-2X functionals, used in the DFT calculations reported in this work, are also empirical meta-GGA functionals¹¹⁹ (Section 5.1.2 and 5.1.3).

The fourth, and last, rung of the ladder in Figure 5.1 is the class of functionals typically used in quantum chemistry calculations with localized basis sets. In these kinds of functionals the exact exchange energy is derived from the exchange energy density, which can be expressed as a function of the KS orbitals. It is worth noting that the exchange energy density is *nonlocal*, which creates new numerical complications in solving the KS equations that would not be present if a local functional were used.

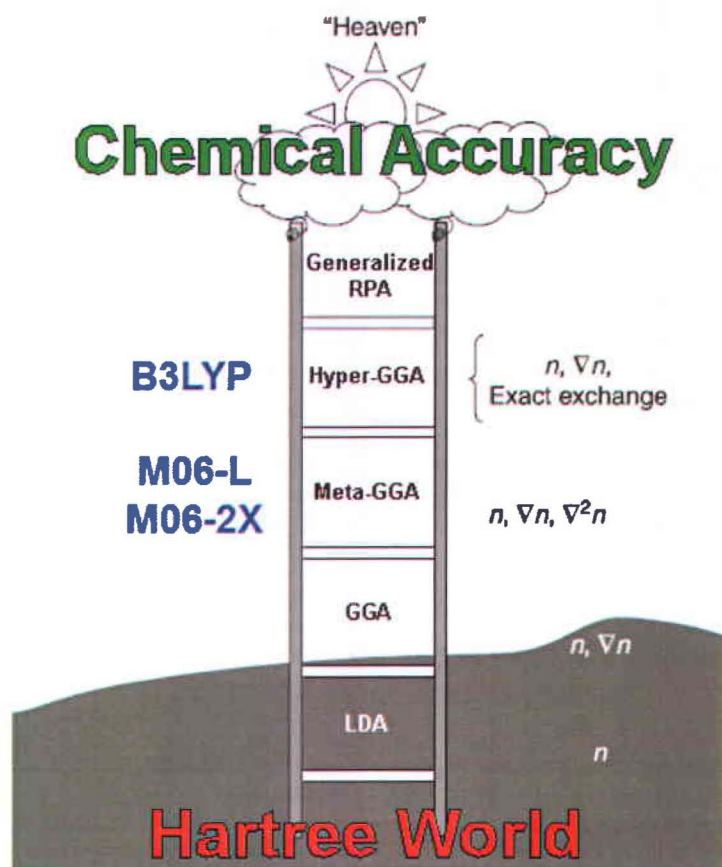


Figure 5.1: Illustration of J. Perdew's classification of DFT functionals, starting from the Hartree world of unrealistically weak or missing bonding to the five steps to the heaven of chemical accuracy. The physical ingredients included in the functionals from each rung are summarized on the right. Reproduced from ref. ¹⁰¹.

These functionals, known as *hyper-GGA functionals*, describe the overall exchange using a mixture of the exact exchange and a GGA exchange functional (*i.e.* they are *nonlocal* or *hybrid*). B3LYP, the other functional used in this work, belongs to this class. Note that also higher-rung functionals exist, *e.g.* the fifth-rung semiempirical functional B2-PLYP recently proposed by Grimme ¹²⁰, which add the unoccupied orbitals through the *random-phase approximation* (RPA) ¹²¹. The main advantage of these functionals is that they bring in vdW interactions ¹²² (although there are other simpler ways to do so ¹⁰²), however they require huge basis sets and thus they are not yet practical for general use ¹¹³.

Computational times increase modestly for the first three rungs of functionals and much more steeply after that ¹⁰² (especially the fifth ¹¹³). Despite the fact that the first three

rungs and the fifth require no fitting, empiricism seems unavoidable for the fourth rung functionals¹²³. All the functionals used in this work are empirical.

It should be emphasized that it is not always reasonable to expect higher-level functionals to perform better than lower ones, especially if the higher-level functional is empirical. Furthermore, using functionals with more information inevitably leads to the introduction of additional systematic errors between DFT and experimental results. Knowing if a functional is appropriate to describe a particular problem depends on the specific property of the physical system being described. For instance, a functional can describe better covalent bonds vs. non-covalent interactions, predict well bond lengths while underestimating barrier heights or describe main-group elements better than transition metals (main-group elements belong to the groups, *i.e.* columns, in the periodic table whose lighter elements are hydrogen, beryllium, boron, carbon, nitrogen, oxygen, fluorine and helium). Ideally, a functional that works well for any property of any physical system is desirable.

5.1.1 THE B3LYP FUNCTIONAL

The B3LYP is the most widely used functional for localized basis sets calculations, that is to say for systems typically involving molecules. This semiempirical, hyper-GGA (hybrid) functional was designed in 1993 by Becke (B) ^{115, 124-125}, who worked on the exchange part of the problem, and Lee, Yang and Parr (LYP) ¹²⁶, who developed the correlation part of the functional. The number 3 in the name of the functional describes the particular way the results are mixed together.

The B3LYP functional combines the standard local exchange LSDA functional (E_X^{LSDA}) with relative Becke's 1988 gradient correction (ΔE_X^{B88}), a contribution of exact HF exchange (E_X^{HF}) and the Lee-Yang-Parr correlation functional (E_C^{LYP}) ¹²⁶. Given that the LYP correlation functional contains both a local and non-local (*i.e.* gradient-dependent) part, it is typically implemented with another local correlation functional ¹²⁷. In this work DFT calculations were performed using the *Gaussian09* software package ¹²⁸, developed by Pople and co-workers. In this package the local Vosko-Wilk-Nusair correlation functional III (E_C^{VWN3}) ¹²⁹ is added to the LYP correlation functional of B3LYP, hence providing the local correlation excess required ¹³⁰. The expression of the exchange-correlation B3LYP functional used in *Gaussian09* is ¹³⁰:

$$\begin{aligned} E_{XC}^{B3LYP} &= E_X^{B3LYP} + E_C^{B3LYP} \\ &= [(1 - 0.2) E_X^{LSDA} + 0.2 E_X^{HF} + 0.72 \Delta E_X^{B88}] \\ &\quad + [0.81 E_C^{LYP} + (1 - 0.81) E_C^{VWN3}]. \end{aligned} \tag{5.10}$$

The parameters 0.2, 0.72 and 0.81 are three *semiempirical coefficients* (from here the number 3 in B3LYP) optimized by Becke to fit atomization energies, ionization potentials, proton affinities and the 10 first-row total atomic energies ¹¹⁵, in reference to the Gaussian-1 (G1) database defined by Pople and co-workers ¹³¹. The B3LYP functional implemented in *Gaussian09* uses the same semiempirical parameters suggested by Becke in 1993 ^{115, 130}. From Eq.5.10 it turns out that B3LYP is a hybrid functional with 20% of exact HF exchange ($0.2 E_X^{HF}$).

Despite this being the most popular exchange-correlation functional for molecular systems, the B3LYP is not widely applicable because it is an empirical functional (it has eight fit parameters: one empirical in its Becke exchange, four in its LYP correlation and three in the hybridization with exact exchange ¹¹³). This means that it is not expected to perform well for systems considerably different from those of the fitting set (*i.e.* the G1 database) ¹¹⁵. Furthermore, similarly to many other empirical functionals ¹¹³, B3LYP does not satisfy the UEG limit, therefore it does not perform well for periodic bulk materials (especially metals ¹²⁷, whose valence electrons can be approximated as a uniform or slowly-varying electron gas). Moreover, hybrid functionals are rarely applied to bulk systems because of the computational effort required to evaluate the Fock exchange term under periodic boundary conditions ¹²⁷. Note that the original three-parameter hybrid proposed by Becke, the B3PW91 functional, was a semiempirical functional designed to be exact in the UEG ¹³². Additional drawbacks of the B3LYP functional include poor performance for transition metal chemistry, underestimation of barrier heights (ascribed to the unphysical self-interaction error) and inaccuracy in describing medium-range correlation-energy interactions (*e.g.* vdW interaction and π - π stacking) ¹¹⁸.

5.1.2 THE M06-L FUNCTIONAL

The M06-L is a local (L) density functional designed by D. G. Truhlar and Y. Zhao from University of Minnesota (M) in 2006 (06). It belongs to a suite of four M06 functionals, the other three being the M06, the M06-2X and the M06-HF¹³³. The M06-L functional depends on spin-up and spin-down electron densities, spin density gradients and spin kinetic energy densities (from which the name *meta*)¹¹⁸. M06-L is a meta-GGA functional¹¹⁹ and it is an extension of the nonlocal M05 functional¹¹⁶, which is itself based on previous works by Becke^{117, 132}, Perdew *et. al.*¹³⁴⁻¹³⁵ and others¹³⁶.

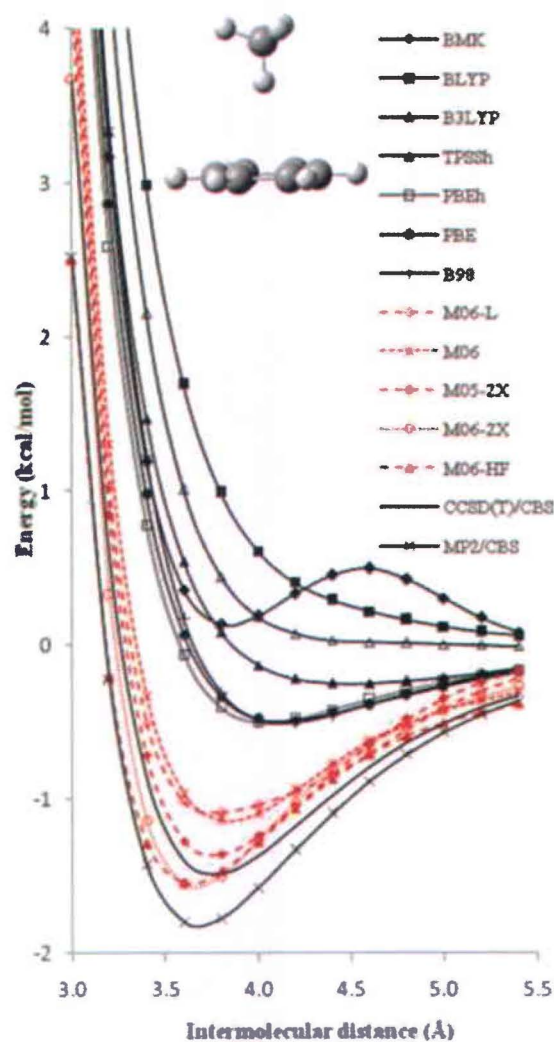


Figure 5.2: Binding energy curves for the C₆H₆...CH₄ complex with the 6-311+G(2df,2p) basis as functions of the distance between the carbon atom in CH₄ and the C₆H₆ plane. Reproduced from ref.¹¹⁸.

The M05 is a hybrid functional designed to have a high percentage of HF exchange ¹¹⁶, and it is not flexible enough to provide a local functional with broad accuracy ¹¹⁹. For this reason, the M06-L was obtained by combining some features of the M05 with others of the local VSXC ¹³⁷ functional, built by Van Voorhis and Scuseria in 1998 (this functional is also known as VS98).

M06-L performs well simultaneously for main-group and transition element thermochemistry, thermochemical kinetics and non-covalent interactions (these being relevant for the systems discussed in this work) ¹¹⁹. Figure 5.2 shows the binding energy of the C₆H₆⋯CH₄ complex computed with several functionals in DFT and WFT methods (WFT methods are the best methods for non-covalent interactions ¹¹⁸, e.g. the Møller-Plesset second-order perturbation theory ¹³⁸ (MP2), although typically more computationally demanding ¹²⁵). These results indicate that the M06-L functional accurately describes intermolecular non-covalent interactions. Therefore, given that the M06-L is particularly suitable for molecular solids and molecular recognition problems (e.g. supramolecular chemistry) ¹¹⁹, it was used in the present work (see also Section 8.1).

The main difference with the B3LYP functional is that the M06-L is local, which not only has the advantage of satisfying the fundamental exact constraint of the UEG limit (and consequently better description of periodic systems), but also makes calculations tens or hundreds of times faster (very important for moderate-sized and large systems) ¹¹⁹. It is also worth noting that the M06-L functional is free of the unphysical self-correlation energy ¹¹⁸. Moreover, calculations including the exact HF exchange (*i.e.* with nonlocal functionals such as B3LYP) are impractical for many solids, unless specific techniques are used ¹¹⁵. The fast computational time of M06-L is due to the fact that this functional scales as N^3 , N being the size of a system, whereas for instance the nonlocal fifth-rung B2-LYP functional scales as N^5 , despite having fewer parameters than M06-L ¹¹⁹.

5.1.3 THE M06-2X FUNCTIONAL

The M06-2X is also a meta-GGA exchange-correlation functional of the suite of M06 functionals, similar to M06-L, however it is hybrid and not local. M06-2X is a high-nonlocality functional with twice the amount of nonlocal exchange (2X) of the M06 functional, and it is parametrized only for non-metals. The local parts of the M06-2X functional depend on three variables: spin density, reduced spin density gradient and spin kinetic energy density. The correlation part of the functional is the same as the functional form of the M06-L functional, while the exchange part is slightly different¹³³. The hybrid exchange-correlation energy can be written as:

$$E_{XC}^{hyb} = \frac{X}{100} E_X^{HF} + \left(1 - \frac{X}{100}\right) E_X^{DFT} + E_C^{DFT}, \quad 5.11$$

where E_X^{HF} is the nonlocal HF exchange energy, X is the percentage of HF exchange in the hybrid functional, E_X^{DFT} is the local DFT exchange energy and E_C^{DFT} is the local DFT correlation energy. The optimization of all the six parameters of the M06-2X functional was done in a self-consistent way, by fitting them to the data used in the training set and enforcing the UEG limit. The optimized percentage of HF exchange is 54% ($X = 54$), more than twice that of B3LYP.

After testing its performance on several databases, the developers of the M06-2X functional recommend it for applications involving main-group thermochemistry, kinetics, non-covalent interactions and electronic energies to valence and Rydberg states¹³³. The M06-2X functional performs considerably better than B3LYP for non-covalent interactions, and it is also preferred over the M06-L functional (Figure 5.2)¹³³.

5.2 THE BASIS SET

In quantum chemistry the *basis set* refers to the set of non-orthogonal one-particle functions, *i.e.* atomic orbitals (AOs), used to construct the electron density, the full wave function or the molecular orbitals (MOs). This technique is known as the *linear combination of atomic orbitals (LCAO) method*. Slater-type orbitals (STOs) were originally used to represent the solution of the Schrödinger equation, however since the 1950s quantum chemists nearly universally use Gaussian-type orbitals (GTOs), introduced first by F. Boys, because they are easier to compute. Physicists typically prefer using plane-wave basis sets. The expressions for STOs and GTOs are given below:

$$\phi_{abc}^{STO}(x, y, z) = N x^a y^b z^c e^{-\zeta r}, \quad 5.12$$

$$\phi_{abc}^{GTO}(x, y, z) = N x^a y^b z^c e^{-\zeta r^2}. \quad 5.13$$

In Eqs.5.12 and 5.13 N is a normalization constant, a , b and c are parameters related to the angular momentum ($a = b = c = 0$ for 1s orbitals), ζ (zeta) controls the width of the orbital and r is the distance from the point where the AO is centered, which is taken to be the origin, which coincides with the center of the nucleus. A large ζ gives tight functions whereas a small ζ gives diffuse functions. The main disadvantage of STOs is that although they are more accurate, they are computationally intensive. A linear combination of GTO primitives can also be used to mimic a STO. These basis sets are referred to as contracted-GTOs (CGTOs) or STO-nG, where n indicates the number of GTOs used to mimic the STO, and are given as:

$$\phi_{abc}^{CGTO}(x, y, z) = N \sum_{i=1}^n c_i x^a y^b z^c e^{-\zeta_i r^2}. \quad 5.14$$

Figure 5.3 shows the comparison between the 1s STO and the approximated Gaussian STO-nGs of different value of n . Combining GTOs has also the advantage of removing the cusp of STOs for $r \rightarrow 0$, which misrepresents the electron density close to the nucleus (Figure 5.3).

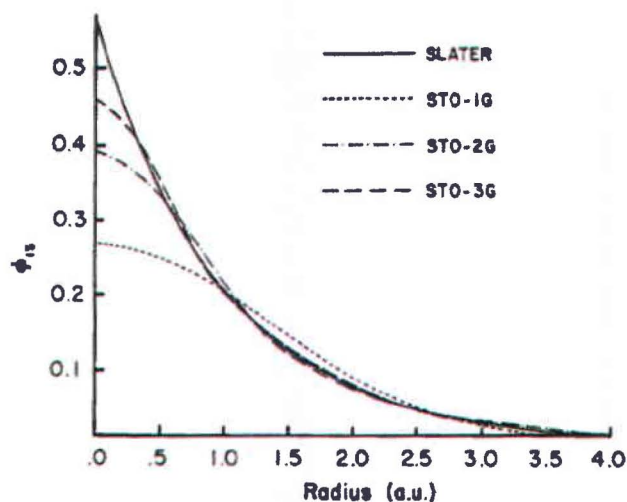


Figure 5.3: Comparison of the quality of the least-squares fit of a 1s Slater function ($\zeta = 1.0 \text{ \AA}^{-2}$) obtained at the STO-1G, STO-2G and STO-3G levels. Reproduced from ref. ¹³⁹.

Different classes of basis sets exist. A *minimal basis set* is built including one basis function of each atomic orbital type of the atoms that comprise a molecule. If at least one p- or d-type orbital is occupied in an atom of the molecule, then the complete set of 3 p-type or 5 d-type functions must be included in the basis set. For instance, the minimal basis set necessary to describe the methane molecule (CH_4) would require 9 basis functions, 5 for the 1s orbitals of the single carbon atom and the four hydrogens, another function for the 2s orbital of carbon and 3 more for carbon $2p_x$, $2p_y$ and $2p_z$. This example for the simple methane molecule shows how the size of the basis sets increases quickly as both the number and size of the atoms that compose a molecule increases.

The next class is the *Double-Zeta (DZ) basis sets*, which uses two functions for each type of orbital of each atom, making DZ basis sets twice as large as minimal sets. The advantage of using a larger basis set is that it allows the electronic energy of a molecule to decrease and approach the exact value more closely (due to the Variational Principle). The two basis functions used for each type of orbital are not identical, but have different orbital exponents (*i.e.* different values of ζ , hence the name *double-zeta*). Even though the orbital exponent is known for isolated atoms, the electron density of atoms in a molecule differs from that of isolated atoms due to the perturbation introduced by chemical bonds. Therefore, the orbital coefficient of atoms in molecules is not exactly known. Using two basis functions with

different orbital exponents (which determine the orbital size and width) allows a better description of variations in the electron density due to bonding or other interactions. Note that *Triple-Zeta* (TZ), *Quadruple-Zeta* (QZ) and higher basis sets exist, each comprising successively more basis functions.

Given that the core electrons in atoms are less affected by the external chemical environment (e.g. bonds) than the valence electrons are, they can be described with a minimal basis set while using a larger higher-level set (e.g. DZ) for the valence electrons. These basis sets, known as *split-valence basis set*, can considerably accelerate DFT calculations involving large molecules.

Polarized basis sets, which have a larger size than the split-valence sets, include polarization functions that are normally unoccupied in the isolated atom (these are functions with higher angular momentum than any occupied molecular orbitals)¹⁴⁰⁻¹⁴¹. In the case of hydrogen this would mean adding p-type and d-type functions, for first-row elements d-type and f-type functions and for transition metals only f-type orbitals. Polarization functions are useful because they improve the flexibility of the basis set, particularly to represent electron density in bonding regions. Consider the spherical 1s orbital of hydrogen in the isolated state. When hydrogen binds to carbon in methane, for instance, its electronic density is no longer spherical but shifted (polarized) along the C–H bond. Adding the polarized p-type (pseudo) orbital to the (real) s-type orbital of hydrogen gives a better representation of the electron density at the C–H bonding region (Figure 5.4).

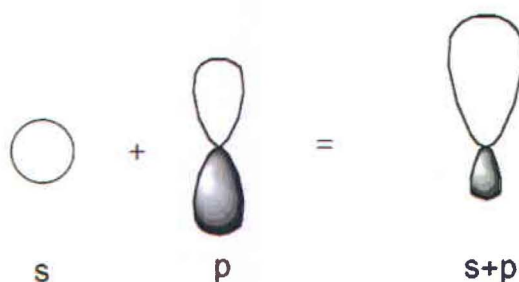


Figure 5.4: The addition of s-type and p-type basis functions is used to allow for polarization of the real electron density of the s-type orbital along the direction imposed by the polarization p-type orbital. Reproduced from ref. ¹⁴².

The last class is *diffuse basis functions*. These are extra functions (usually s- or p-type) added to the basis set in order to represent very broad electron distributions (they have very small orbital exponents ζ). It is strongly suggested to include diffuse functions in basis sets for the description of the electron density in anions or intermolecular complexes (where bonds as long as a few Angstroms may be spread over a large region).

A good database for basis sets can be found in ref. ¹⁴³, however it is always useful to refer to the manual of the software package used (Gaussian09 in our case ¹³⁰).

5.2.1 ALL-ELECTRONS POPLER BASIS SETS: 6-31G AND 3-21G

In this work the 6-31G and 3-21G *Pople basis sets* were used. The basis functions of Pople basis sets are made of linear combinations of Gaussian primitives in order to resemble STOs (Section 5.2). The nomenclature of Pople basis sets is either N - M 1G or N - M 11G, where N and M are integers. The first class of Pople basis sets is double zeta and the second one is triple zeta, both being split-valence basis sets. The G in the name indicates that GTOs are used to mimic STOs, whereas the integers N and M represent the number of GTOs used in the linear combination to represent a STO. N is the number of Gaussian primitives used to construct the core orbital basis functions, while M and 1 are the number of Gaussian primitives used to describe the valence orbital basis functions (M and 1 refer to the valence orbitals of ζ_1 and ζ_2 , respectively, ζ_1 and ζ_2 due to the fact that the basis set is a double-zeta, *i.e.* it uses two functions to describe the atomic orbitals).

Polarization functions can also be added to Pople basis sets. Writing 6-31G(d) (or 6-31G*) means that one set of d-type polarization functions is added to each non-hydrogen atom in the molecule, while writing 6-31G(d,p) (or 6-31G**) means that one set of d-type polarization functions is added to each non-hydrogen atom in the molecule and one set of p-type polarization functions is added to hydrogens.

The use of diffuse functions in Pople basis sets is indicated by the notation + or ++. The + notation, as in 6-31+G(d), means that one set of sp-type diffuse basis functions is added to non-hydrogen atoms (4 diffuse basis functions per atom). The ++ notation, as in 6-31++G(d), means that one set of sp-type diffuse function is added to each non-hydrogen atom and one s-type diffuse function is added to hydrogen atoms.

5.2.2 EFFECTIVE CORE POTENTIAL BASIS SETS: LanL2DZ

When calculations involving heavy atoms like iodine are performed, one can choose between either all-electrons basis sets (discussed in the previous section) or effective core potential (ECP) basis sets (also known as electron core potential). In the Gaussian 09 program iodine is included only in 3-21G but not in 6-31G, hence imposing the use of lower quality basis sets for molecules with heavy iodine atoms. Another possible choice is the ECP basis set LanL2DZ. This basis set uses the full DZ basis set D95V¹⁴⁴⁻¹⁴⁵ for first-row elements and includes an ECP¹⁴⁶⁻¹⁴⁸ for the innermost electrons plus a DZ basis for other elements. In this work, no polarization functions were added to LanL2DZ, which in its original form already includes polarization and diffuse functions for Br.

Chapter 6. THE INVESTIGATED MOLECULES

In this project we investigated 2D self-assembly on surfaces using halogenated molecules and molecules containing the diacetylene moiety (Figure 3.2c). The work with the halogenated molecules was done in collaboration with Prof. D. F. Perepichka's group of the Department of Chemistry at McGill University, whereas the work with the diacetylenes was done in collaboration with Prof. J.-F. Morin's group of the Department of Chemistry at Université Laval. The collaborators contributed to this work by performing the chemical synthesis of the molecules.

Solutions of the molecular precursors were prepared in heptanoic acid (Sigma-Aldrich, 96%), 1-phenyloctane (Sigma-Aldrich, 98%) and 1,2,4-trichlorobenzene (TCB) (Sigma-Aldrich, $\geq 99\%$); 2-propanol (Sigma-Aldrich, $\geq 99\%$) was used to rinse the samples when needed. All solvents were used as purchased, without further purification. These solvents (apart from 2-propanol), have low volatility and ensured a consistent experimental environment over the period of a typical experiment (*i.e.* a few hours). Prior each experiment, solutions were sonicated for 10 – 20 minutes.

6.1 HALOGENATED PRECURSORS

2D self-assembly of the halogenated molecules 2,4,6-tris(4-bromophenyl)-1,3,5-triazine (TBPT) and 2,4,6-tris(4-iodophenyl)-1,3,5-triazine (TIPT) was studied at the liquid-solid interface (Figure 6.1a,c). These are halogenated aromatic molecules with C₃ symmetry, incorporating a triazine core with three halophenyl functional side groups. The goal of this project was to investigate the role of the triazine core in driving the assembly process, comparing our results with those from two other molecules whose surface self-assembly is widely reported in the literature, namely 1,3,5-tri(4-bromophenyl)benzene (TBPB)^{31, 56, 149-152} and 1,3,5-tri(4-iodophenyl)benzene (TIPB)^{26, 32, 153-154} (Figure 6.1b,d). TBPT and TIPT are also interesting because they may be used to build 2D covalent polymers following Ullmann coupling on the Au(111) surface (see Chapter 3 and Section 7.2).

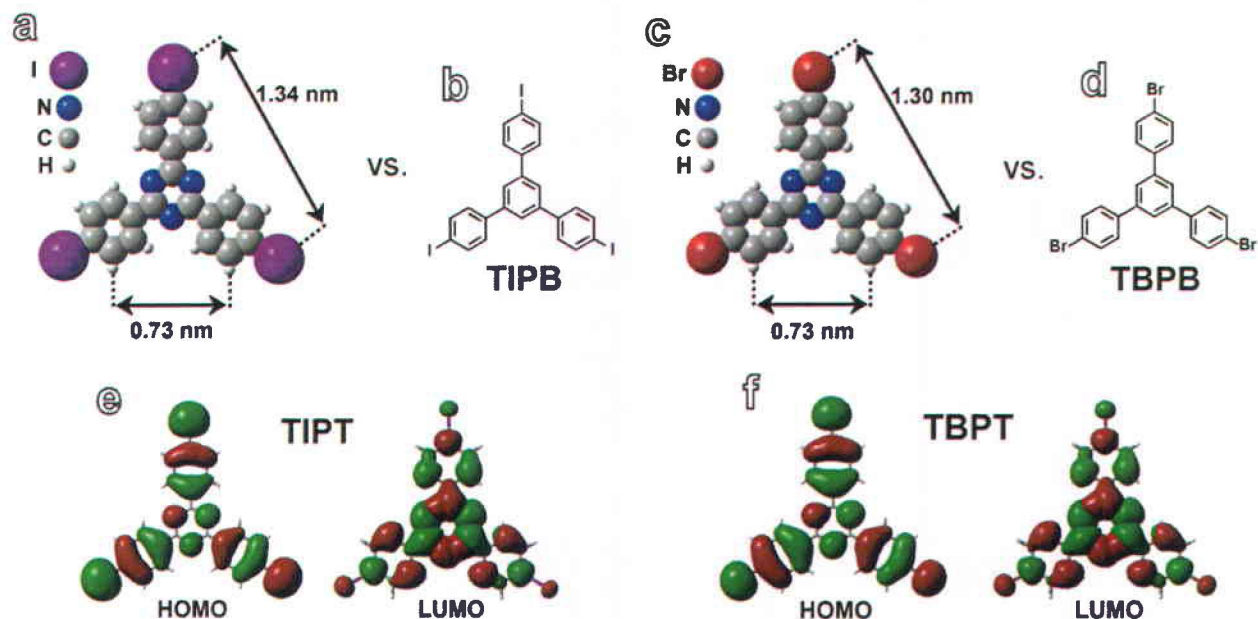


Figure 6.1: Molecular structure of a) TIPT and c) TBPT optimized in gas-phase DFT. The structure of b) TIPB and d) TBPB is reported for comparison. Highest occupied molecular orbital (HOMO) and lowest unoccupied molecular orbital (LUMO) of e) TIPT and f) TBPT were computed at the 0.015 electrons Bohr⁻³ isodensity surface. Green and red isosurfaces are, respectively, positive and negative phases of the orbitals. Calculations performed at the B3LYP/LanL2DZ level of theory.

6.2 DIACETYLENE PRECURSORS

2D self-assembly of the diacetylene molecules was also investigated at the liquid-solid interface. The goal of this project was to find an optimal molecular packing that might lead to polymerization of diacetylenes in two dimensions (see Chapter 3). Polymerization of diacetylenes on surfaces, in fact, typically leads to 1D polymeric chains but not to extended 2D covalent networks, which are desirable for possible applications in electronics. We first studied the molecule Maude-2-041 (Figure 6.2a), which has a diacetylene core and side functional groups consisting of a phenyl ring and 14 carbons alkyl chains. In a second stage of the project we moved on two other precursors, namely the molecules SR-10-134 and SR-10-152 (Figure 6.2b,c). These, in contrast with the first molecule, have two nitrogen atoms in the aryl rings that can be exploited to achieve different adsorption configurations. Other differences are also present in the molecular side groups, however these should have a minor effect in the adsorption geometry of the molecules, *i.e.* they only play a role in the lateral stabilization of the assembly. Odd-even effects can make pronounced difference in molecular packing on the surface, nevertheless both precursors have alkyl chains made of an even number of carbon atoms.

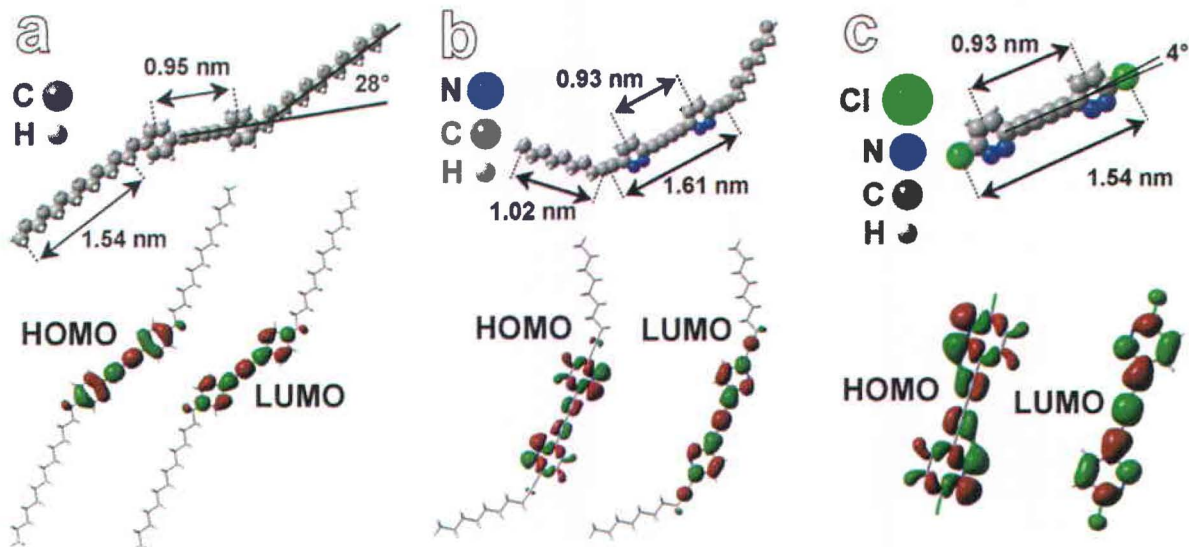


Figure 6.2: Molecular structure, HOMO and LUMO of a) Maude-2-041, b) SR-10-134 and c) SR-10-152 optimized and computed, respectively, in gas-phase DFT at the B3LYP/6-31G** level of theory. Molecular orbitals computed at the 0.02 electrons Bohr⁻³ isodensity surface; green and red isosurfaces are, respectively, positive and negative phases of the orbitals.

Chapter 7. SUBSTRATES

SAMNs of the molecules presented in Chapter 6 were studied at the liquid-solid interface on HOPG and on Au(111) thin films. Thanks to their low reactivity, these are the substrates typically used in STM experiments in ambient conditions. Molybdenum disulfide (MoS_2) crystals are also stable enough to be used in ambient ¹⁵⁵, but are less commonly reported on. The data from HOPG allow us to comparatively explore the intermolecular interactions thanks to weak molecular adsorption, whereas the experiments on gold provide insights into molecule-substrate interactions. Furthermore, experiments on Au(111) also allow us to investigate surface polymerization of the halogenated precursors, which would take place through aryl-aryl coupling after the dehalogenation been catalyzed by the more reactive metal surface (Ullmann reaction - Chapter 3).

7.1 HOPG

Graphite is the most stable allotrope of carbon at RT and ambient pressure (Figure 7.1a). Other allotropes include carbon nanotubes (CNTs), Buckminsterfullerene (C_{60}), graphene and diamond (Figure 7.1b-f). HOPG differs from mineral graphite in that its graphite sheets, *i.e.* graphene layers, are oriented within a very small angular spread, and it has a lower density of structural and substitutional defects.

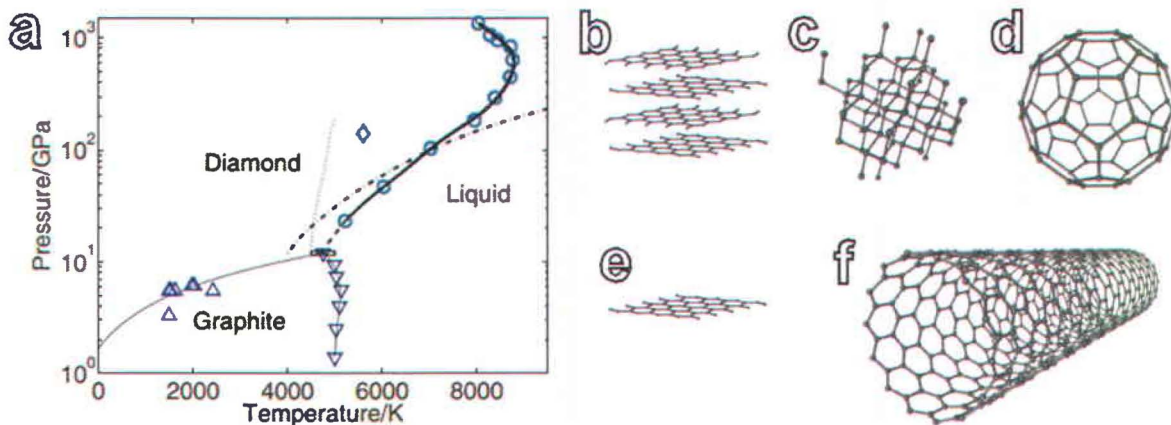


Figure 7.1: a) Carbon phase diagram from *ab initio* molecular dynamics. Allotropes of carbon include b) graphite, c) diamond, d) C_{60} , e) graphene and f) carbon nanotubes. Reproduced from a) ref. ¹⁵⁶ and b)-f) ref. ⁷.

Graphite is a lamellar material, made of one-atom-thick carbon-atoms sheets stacked in parallel layers along the *c*-axis. Within each graphene layer carbon atoms are covalently bonded by conjugated C–C bonds ($d^{C-C} = 1.42 \text{ \AA}$) ¹⁵⁷ – sp^2 hybridization. Parallel layers are bonded together by weak vdW interactions, which results in the ease of cleaving of graphite ($d^{\text{interplanar}} = 3.35 \text{ \AA}$) ¹⁵⁷. The exfoliation energy of graphite, extrapolated from experimental temperature programmed desorption (TPD) data, is $52 \pm 5 \text{ meV/atom}$ ¹⁵⁸. The carbon atoms within each graphene layer are arranged in a hexagonal 2D lattice, with each atom involved in three C–C bonds (Figure 7.2a). Consecutive layers are arranged in an ABAB fashion, which gives graphite its *hcp* crystal structure (Figure 7.2b). In HOPG the *c*-axis is vertical to the (macroscopic) surface of the substrate, where the (0001) basal plane lies. Therefore, HOPG substrates have 3-fold symmetry. On the other hand, mineral graphite is composed of small-

size crystals that are randomly oriented in space. HOPG is typically used for scientific research rather than for industrial applications.

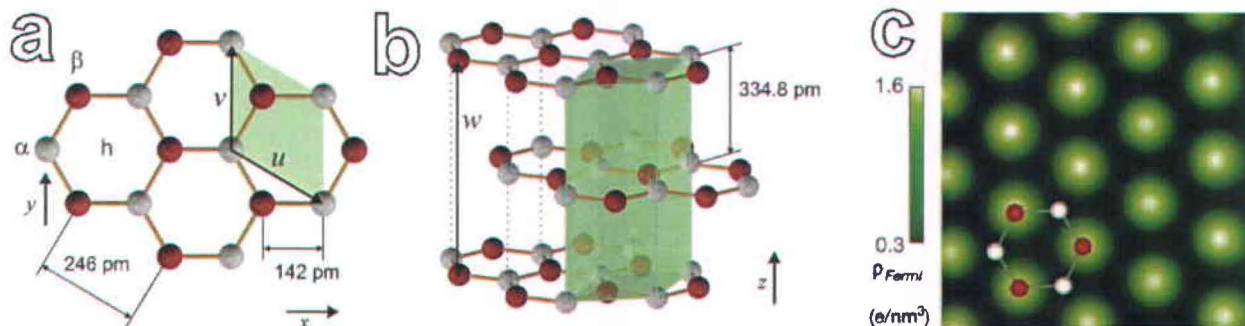


Figure 7.2: a) Top view and b) perspective view of a graphite crystal. c) Calculated charge density of graphite at the Fermi level ρ_{Fermi} at a height of 200 pm over the surface plane, ranging from 0.3 to 1.6 electrons per nm^3 . The maxima are at the β atom positions. Reproduced from ref. ¹⁵⁷.

In STM not all the atoms of the first atomic layer of graphite appear as bright protrusions. Due to an overlap of DOS between the first two layers, only one of the two carbon atoms per unit cell of the first layer is observed in the STM image (Figure 7.2c). The distance between each protrusion is of 2.46 Å, the value used for the lattice correction of the STM data from distortions introduced by the piezoelectric transducers and/or thermal drift. HOPG substrates are typically inert in terms of molecular adsorption, given that the electrons in the first atomic layer are either well localized (strongly bonded) in covalent C–C bonds or spread over the whole surface (π -conjugated system). The most common interactions that molecules experience on HOPG is the π stacking, which is why planar aromatic molecules adsorb well on this substrate. For the experiments reported in this work, HOPG substrates (Structure Probe Inc.) were freshly cleaved on the (0001) basal plane with adhesive tape before each experiment. This technique, known as *scotch-tape micromechanical cleavage*, was pioneered for the production of graphene by Novoselov, Geim and co-workers (2010 Nobel Prize in Physics) ⁸⁰.

7.2 Au(111)

Gold is a metallic element that crystallizes in a single-atom basis *fcc* Bravais lattice, a close-packed crystal structure (bulk interatomic distance $d^{\text{bulk}} = 2.88 \text{ \AA}$ ¹⁵⁹). The (111) crystallographic plane of gold is the highest density plane, where each atom has six in-plane neighbors, three neighbors in the upper plane and three other neighbors in the lower plane (coordination number $N_{\text{bulk}} = 12$). When a solid is split to form a surface, the atoms on the exposed facets are less stable than those in the bulk, and the surface may undergo a process called *reconstruction*, by which an energy minimum is reached by reorganizing these surface atoms. In a reconstructed surface the topmost layers have a crystal structure different from that of the same crystallographic plane in the bulk. If the energy penalty associated with the creation of a surface is not very high the system stabilizes with a process called *surface relaxation*, in which only the interlayer distance of the outer planes change without otherwise affecting the crystal structure. Metallic solids typically exhibit surface relaxation, whereas covalent solids such as silicon typically undergo surface reconstruction. Close-packed (111) surfaces of metals typically do not undergo surface reconstructions, thanks to the non-directionality of the metallic bond and to the fact that (111) close-packed surfaces have the smallest number of missing atoms coordinated with the top layer ($N_{\text{surface}} = 9$). However, Au(111) is an exception, and gains energy while introducing surface strain in a complicated structure known as *herringbone reconstruction* (Figure 7.3a and Figure 7.4a,b) ¹⁶⁰. Pt is the only other example of an *fcc* metal whose (111) surface reconstructs, however this occurs only in specific conditions (e.g. at high temperature or in presence of a saturated Pt vapor) ¹⁶¹⁻¹⁶². The strain is introduced by a compression of the topmost atomic layer along the [1-10] crystallographic direction of approximately 4% ¹⁶³, which results in the insertion of an extra gold atom every 22 atoms along this direction. Hence the herringbone reconstruction is also known as $22 \times \sqrt{3}$ – Figure 7.3a.

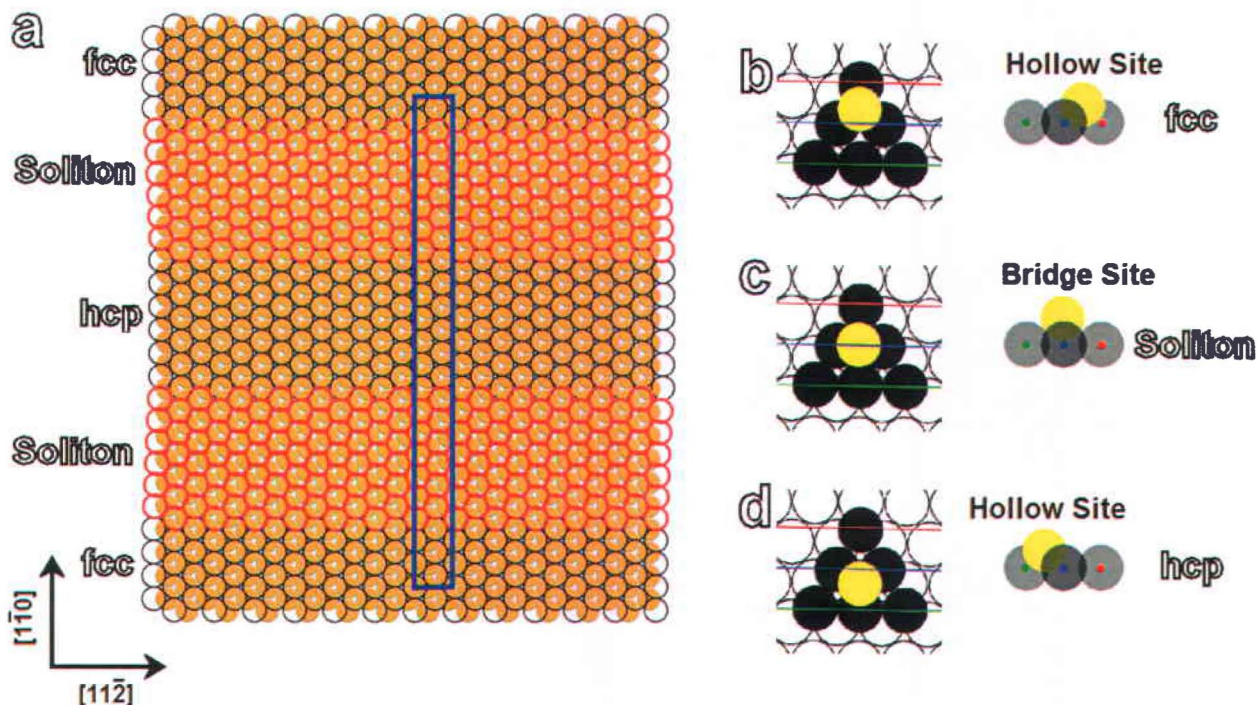


Figure 7.3: a) Model of the herringbone reconstruction. Atoms of the topmost layer are drawn as empty circles (black circles refer to the *fcc* and *hcp* regions whereas the red atoms refer to the faulted solitons). Atoms of the second layer are indicated by full orange circles. The unit cell of the reconstruction is indicated by the blue rectangle. b)-d) Top- and side-views of the model for the transition from *fcc* to *hcp* structure. Yellow, black and white circles represent gold atoms of the 1st, 2nd and 3rd layer, respectively. Note that in a) the two layers were not superimposed according to the actual *fcc* stacking structure of the unreconstructed Au(111) surface, but in a way that shows the relative displacement with respect to the *fcc* structure. This displays more clearly the effect of the compression.

The extra atom along the $[1-10]$ direction leads to a topmost layer that is more dense along $[1-10]$ than the bulk-terminated Au(111) surface¹⁵⁹. The reconstructed Au(111) surface has two different lattice constants: the compressed $d^{[1-10]}$ equal to 2.75 Å and the uncompressed $d^{[11-2]}$ equal to that of the bulk, *i.e.* 2.88 Å^{159, 164} (note that $d^{[1-10]} = (2.88 \cdot 22)/23 = 2.755$ Å). The compression along $[1-10]$ causes a buckling in the topmost layer, where certain atoms are slightly lifted off the surface to accommodate the extra atom. This process does not occur uniformly over the whole 22 atom-unit cell, rather the compression along $[1-10]$ leads to periodic alternating *fcc*- and *hcp*-stacked regions (Figure 7.3a). The boundaries between the *fcc* and *hcp* regions are referred to as *bridges* or *solitons*, and have stacking structure intermediate between *fcc* and *hcp*¹⁵⁹ (Figure 7.3b-d). The periodicity solitons pairs along $[1-10]$ is 6.3 nm¹⁵⁹, whereas the distance between the lines within each pair is 2.2 nm¹⁶⁵ –

Figure 7.4e. On a larger scale, strain is introduced with rotational domains (15 – 25 nm period¹⁵⁹⁻¹⁶⁰) in the form $\pm 120^\circ$ turns commensurate with the 3-fold symmetric Au(111) surface, which give rise to the typical zigzag pattern (*i.e.* herringbone reconstruction)¹⁵⁹ – Figure 7.4a. These rotational domains are believed to be due to long-range elastic forces¹⁶⁶.

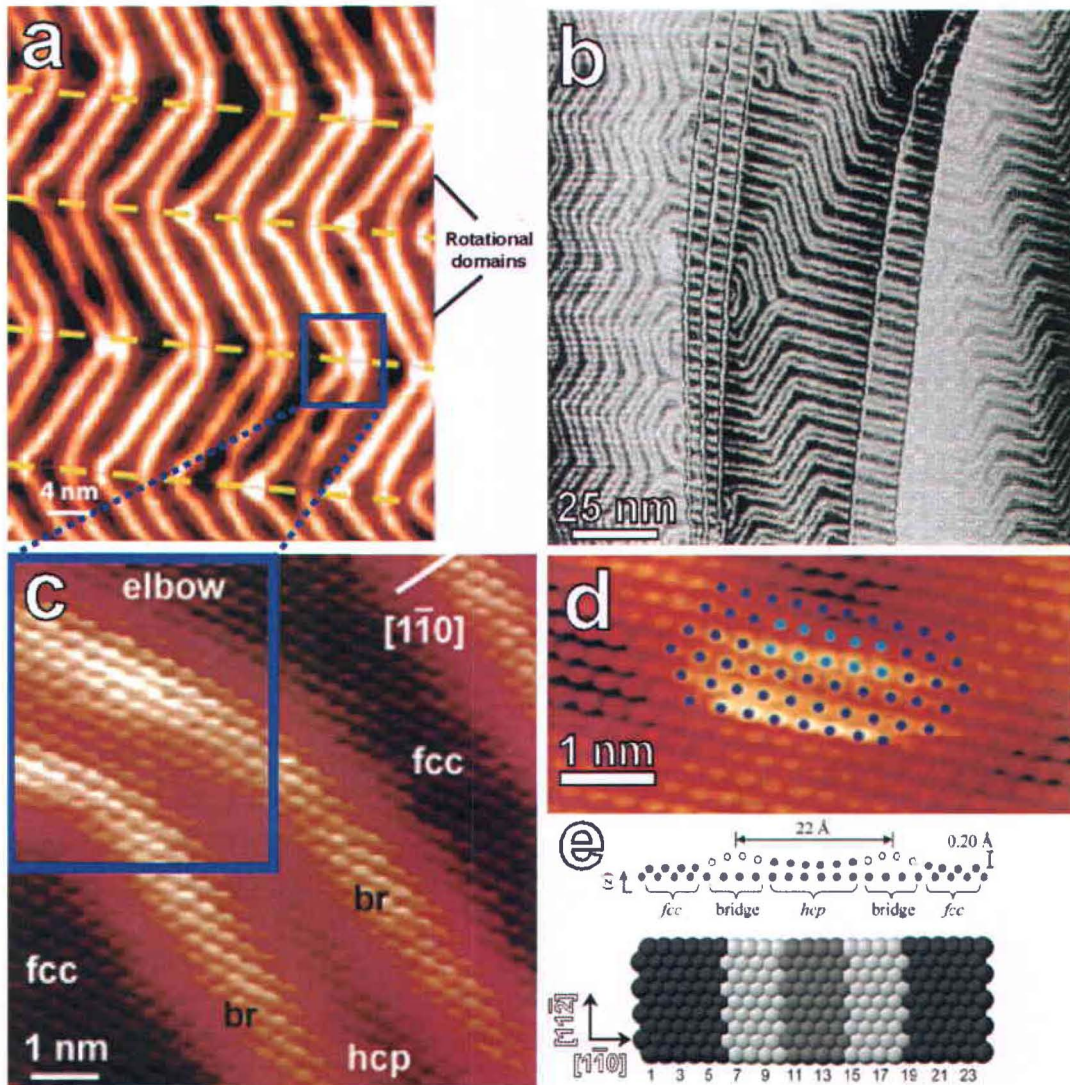


Figure 7.4: a),b) STM images of the $(22 \times \sqrt{3})$ herringbone reconstruction of the Au(111) surface. c) Magnification of an elbow, imaged with atomic resolution in d). In d) the blue circles mark the apparent centers of the underlying Au atoms, while the light blue color corresponds to the coordinatively unsaturated atoms, which exhibit increased reactivity. e) Model of the herringbone reconstruction. Reproduced from a) ref.¹⁶⁷, b) ref.⁹¹, c) ref.¹⁶⁸, d) ref.¹⁵⁹ and e) ref.¹⁶⁵.

The points where the solitons rotate by 120° have a missing gold atom and are referred to as *elbows*. Due to their defective structure, these are preferential nucleation centers in heteroepitaxy of metals ¹⁶⁹⁻¹⁷⁰ (Figure 7.5a-c) and preferential adsorption sites for molecules ¹⁵⁹ (Figure 7.5d).

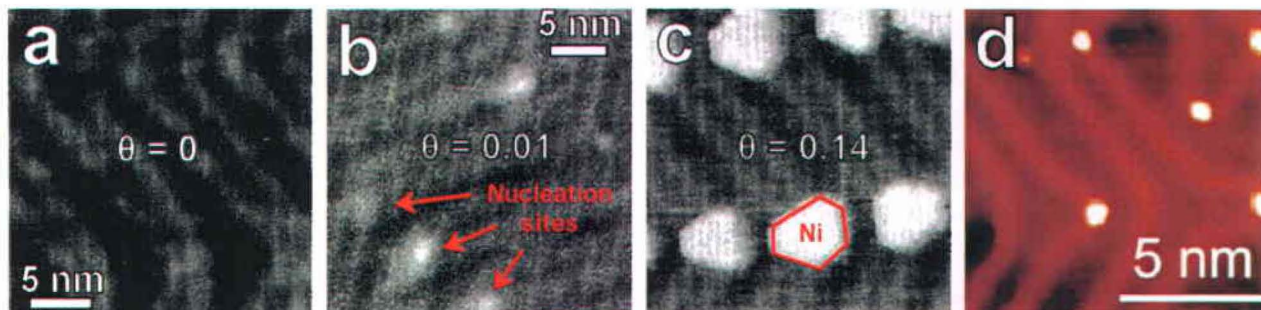


Figure 7.5: a)-c) Growth stages of Ni islands on Au(111); a) clean reconstructed Au(111) surface, b) nucleation of Ni islands at elbows at Ni coverage (θ) 0.01 monolayer (ML); c) completed nucleation and polygonal shape of Ni islands at $\theta = 0.014$ ML. a) and c) have same scale bar. d) STM image at 77 K of the reconstructed Au(111) surface with 0.01 ML of CH_3SH molecules, imaged as bright protrusions. The image shows preferential adsorption of CH_3SH on the elbow sites. a)-c) Reproduced from ref. ¹⁷⁰, d) from ref. ¹⁵⁹.

The herringbone reconstruction is easily discerned in STM images, where the solitons between *fcc* and *hcp* regions appear as bright, parallel lines with a large vertical corrugation ($0.20 \pm 0.05 \text{ \AA}$ ¹⁶⁰). Regions with *fcc* and *hcp* structure appear darker than the solitons, and the *fcc* region is wider than the *hcp* (Figure 7.4c). This indicates that *fcc*-stacked regions, which have the same structure of pristine bulk-terminated Au(111) surfaces, are more stable than the *hcp* ones. Furthermore, theoretical works have shown that the STM contrast associated with the herringbone reconstruction mostly arises from the topography of the surface and not from electronic effects. Figure 7.6 shows that the electronic states associated with the top layer are relatively uniform across the *fcc* and *hcp* regions of the reconstruction. Therefore, the measured height profile in a STM image similar to that in Figure 7.4a is almost entirely due to the physical perturbation of the surface.

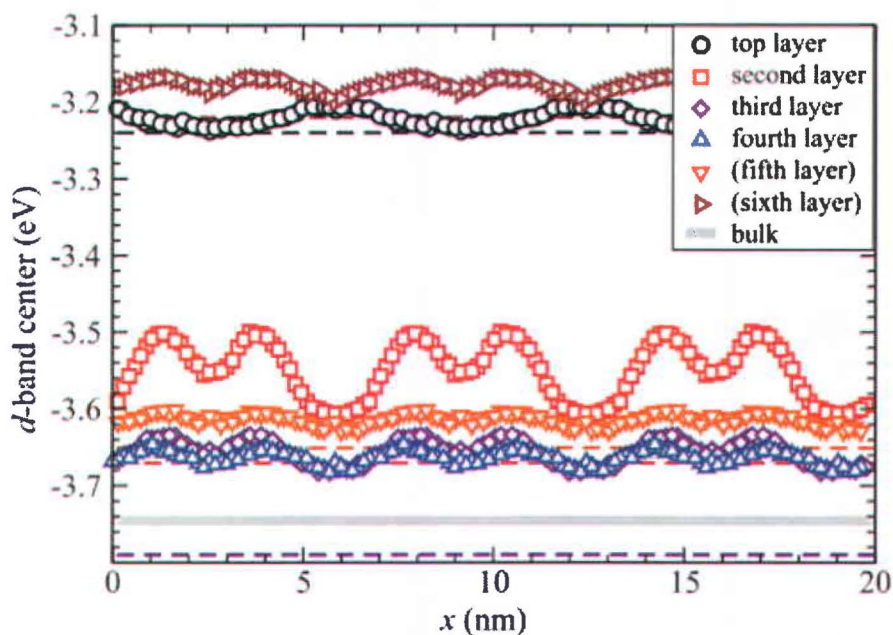


Figure 7.6: Integrated d -band centers with respect to the Fermi level for all atoms in the six-layer Au $22 \times \sqrt{3}$ unit cell. Reproduced from ref. ¹⁶³.

In this project, Au(111) thin films were grown on mica substrates by molecular beam epitaxy (MBE). Mica is a silicate, with formula $H_2KAl_3(SiO_4)_3$, that occurs naturally in the form *muscovite* or *phlogopite*. Muscovite is typically ruby, green or white, and can be processed up to 500 – 600 °C. Phlogopite is typically amber, yellow or silver, and has a maximum temperature of 800 – 900 °C ¹⁷¹. Medium quality (V5) muscovite mica substrates were purchased from Electron Microscopy Sciences ¹⁷¹. Muscovite, also known as *granitic mica*, is the best mica in terms of dielectric strength, transparency and cleavage, which is of particular interest for thin film deposition ¹⁷¹. Muscovite is composed of 45.5% silica, 37.5% alumina, 12% potash and 5% water ¹⁷¹.

Mica substrates were cleaved on the basal plane with a sharp blade, exposing pristine. Gold films were deposited on mica using optimal evaporation parameters reported in the literature ¹⁷², in a vacuum environment with a base pressure of 10^{-6} mbar and a peak value of 10^{-5} mbar during film growth. The pristine mica substrates were degassed at 200 °C for 2 hours and then kept at 360 °C during gold (ESPI Metals) deposition, which led to (111)-oriented thin films (Figure 7.7). Once the deposition was completed, at a film thickness of

approximately 40 nm (see below), the gold samples were annealed in nitrogen (N₂) at 400 °C for 1 hour, which led to atomically flat terraces hundreds of nm large. The quality of the gold films was verified by using STM to discern the presence of the 22×√3 herringbone reconstruction. Prior to each experiment, the Au(111) samples were rinsed with deionized water, dried with N₂ and passed a few times over a propane flame. With this procedure it was possible to remove any molecules and macroscopic dust particles adsorbed on the surface

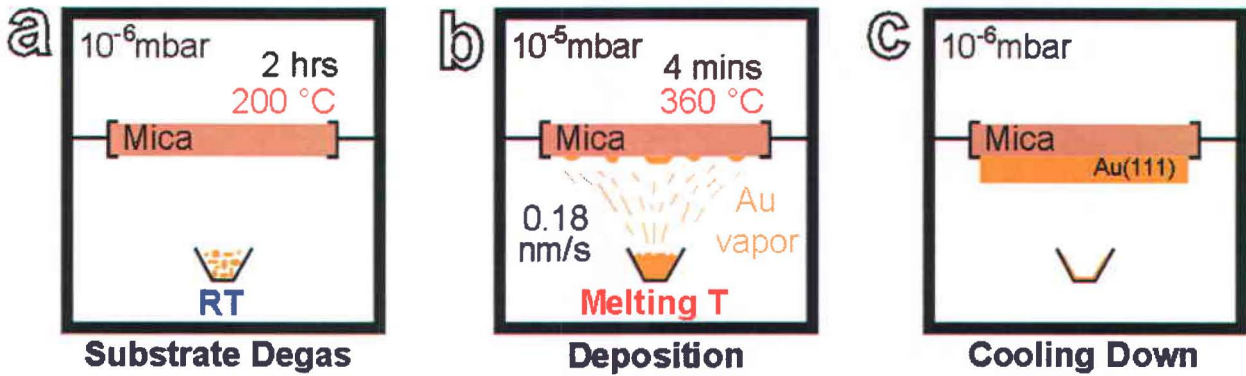


Figure 7.7: Steps involved in the deposition of thin Au(111) films on mica.

The Au(111) film thickness of 40 nm is estimated and not actually measured. The evaporation rate was measured by a quartz balance positioned closer to the gold crucible than to the mica substrate (Figure 7.8). Hence, the average deposition rate (R_d) measured by the balance (0.55 nm/s) is an overestimation of the actual deposition rate. Given that the deposition rate decreases quadratically with the distance¹⁷³, the geometry of the setup allows us to calculate the actual deposition rate at the substrate:

$$R_d(a) = \frac{K}{a^2} = 0.55 \frac{\text{nm}}{\text{s}} \xrightarrow{\text{yields}}$$

$$R_d(1.75a) = \frac{K}{(1.75a)^2} = \frac{K}{(1.75)^2 a^2} = \frac{R_d(a)}{(1.75)^2} = 0.18 \frac{\text{nm}}{\text{s}}, \quad 7.1$$

where the constant K includes parameters that do not depend on the distance, such as source dimension and temperature as well as the atomic weight and density of the element

being evaporated (gold in this case) ¹⁷³. Therefore, an evaporation of four minutes at the deposition rate of Eq.7.1 gives a film thickness of 43 nm.

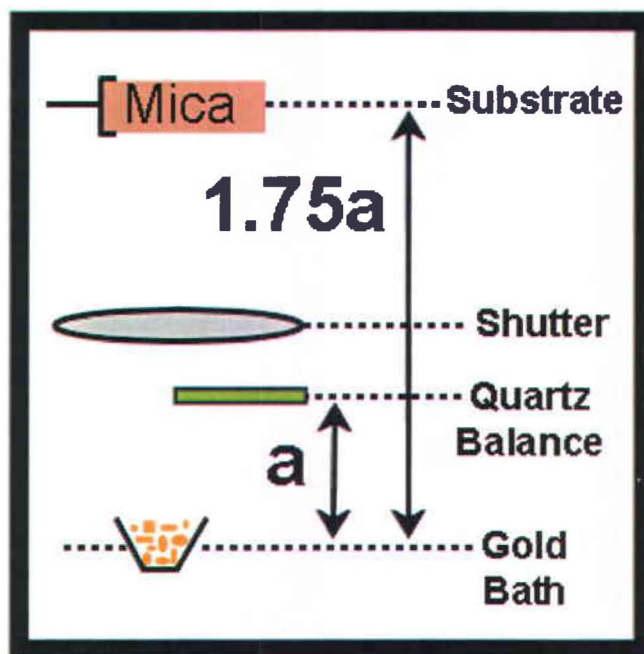


Figure 7.8: Scheme of the evaporation setup used for the growth of thin Au(111) films. The evaporation rate measured with the quartz balance overestimates the actual deposition rate at the mica substrate (quadratic dependence with the distance). The evaporation was performed using a shutter, which allowed for precise control over the deposition duration.

Chapter 8. RESULTS AND DISCUSSION

In this chapter we will discuss the computational and experimental results of the halogenated molecules first and of the diacetylene precursors after. In all cases self-assembly was investigated at the liquid-solid interface. For the halogenated molecules surface polymerization was attempted using the Ullmann-reaction approach, whereas UV light irradiation was used for the diacetylenes (Chapter 3).

DFT Calculations were performed with the Grex SGI Altix XE 1300 cluster system, which is part of the WestGrid installation located at University of Calgary, using 8 processors and 15 GB of RAM per processor. This cluster system consists of 316 compute nodes, each with two 6-core Intel Xeon X5650 2.66 GHz processors (Intel Westmere architecture). 24 compute nodes of the cluster have 96 GB of memory and the remaining 292 nodes have 48 GB of memory ¹⁷⁴.

8.1 THE CHOICE OF THE FUNCTIONAL

The B3LYP functional was used for single-molecule calculations, given that it is the best for non-periodic molecular systems. However, to calculate the net binding energy of 2D extended systems, single-molecule energies must be computed using the same functional and basis set used in the calculations with periodic boundary conditions (PBCs). Net binding energies were computed subtracting the single-molecule energy of each molecule in the unit cell from the total energy of the optimized 2D lattice.

Another way to calculate the net BE uses a further term that is subtracted from the total energy (*counterpoise correction*, introduced by Boys in 1970) ¹⁷⁵. The counterpoise (CP) correction accounts for the basis-set superposition effect (BSSE) due to the truncation of the basis set in the construction of the atomic and molecular orbitals of interacting systems. The major effects of the truncation act against one another: *i*) lowering the calculated interaction energy because of BSSE and *ii*) raising the interaction energy because of the incompleteness

of the basis for describing the perturbation of the subsystems (also referred to as *monomers* or *fragments*)¹⁷⁶. For practical basis sets, the BSSE effect *i*) is the most dominant component, therefore the CP-corrected net binding energy is typically lower (*i.e.* less bonded) than the non-corrected energy. However, in this work the CP correction was not used because of its problems in calculations with PBCs.

The performance of the three functionals presented in Sections 5.1.1, 5.1.2 and 5.1.3 was systematically addressed for calculations of extended 2D molecular lattices. A summary of the properties of these functionals is reported in Table 8.1 (local functionals require less computational effort, which increases with the HF exchange percentage; functionals exact in the UEG limit are suitable for periodic systems).

Table 8.1: Summary of the tested functionals.

	Year	Local	Hybrid	HF Exchange %	UEG ^{Exchange}	UEG ^{Correlation}
B3LYP	1994	No	Yes	20	Yes	No
M06-L	2006	Yes	No	0	Yes	Yes
M06-2X	2008	No	Yes	54	Yes	Yes

This systematic study was done for one of the investigated polymorphs of TBPT on HOPG (TBPT² in Table 8.5), given that it is less computationally expensive than calculations involving TIPT molecules with iodine atoms. The 6-31G** basis set was used (see next section for details of the basis sets). We find that the two M06 functionals give roughly the same results in terms of binding energy and interatomic distances. The B3LYP functional gives Br...H and Br...Br distances slightly larger than the other two functionals, hence leading to a SAMN approximately 30% less stable (Table 8.2).

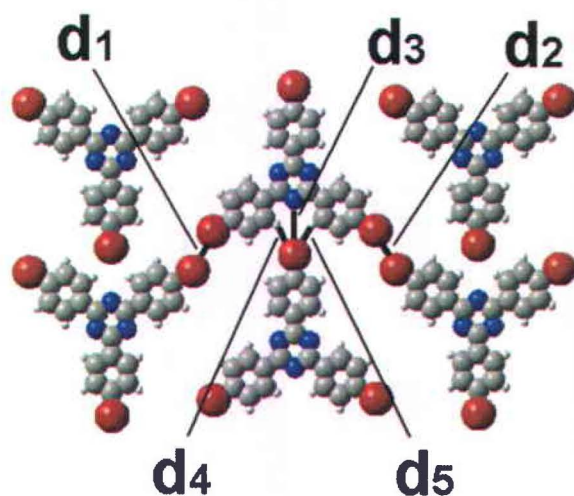


Figure 8.1: Interatomic distances in the assembly TBPT² of Table 8.5.

Table 8.2: Performance of the tested functionals for the TBPT² polymorph of Table 8.5, using the 6-31G** basis set. See Figure 8.1 for labels. The central processing unit (CPU) times were normalized to the number of iterations of the optimization.

	CPU Time	d1 (Å)	d2 (Å)	d3 (Å)	d4 (Å)	d5 (Å)	BE (kcal/mol)
M06-2X	162 ^h 12 ^m	3.47	3.47	4.35	2.79	2.79	-15.8
B3LYP	19 ^h 19 ^m	3.55	3.55	4.47	2.92	2.91	-9.8
M06-L	5 ^h 35 ^m	3.47	3.48	4.30	2.76	2.78	-14.8

The two M06 functionals are known to be more accurate for periodic systems, given that the B3LYP functional is not exact in the UEG limit (Table 8.1)¹¹³, and for systems stabilized by non-covalent interactions^{119, 133}. Furthermore, the M06-L, being local (*i.e.* HF = 0%), is much less computationally expensive than the M06-2X functional (HF = 54%). Plotting the CPU time as a function of the percentage of exact HF exchange in the functional (Figure 8.2) shows a larger than squared dependence on the HF term. Therefore, given that for halogen-bonded systems the two M06 functionals give similar results in terms of interatomic distances and BE, and given the difference in their CPU time, the M06-L was chosen for calculations of extended 2D molecular lattices.

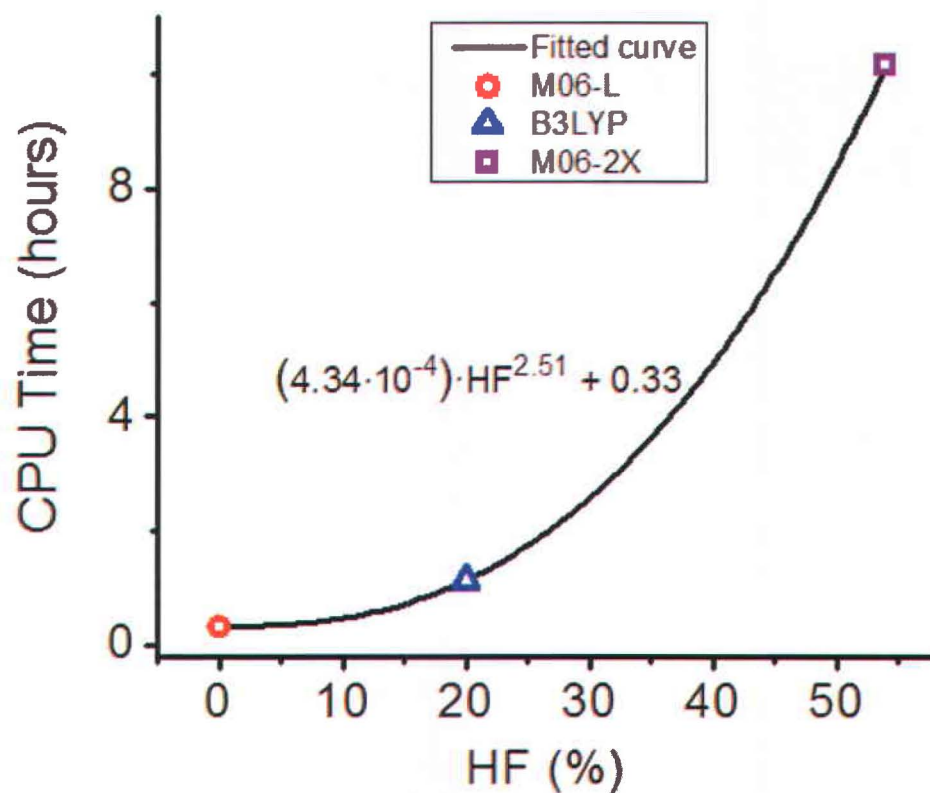


Figure 8.2: Plot of the CPU time in function of the HF percentage of exact exchange of the used functionals. The fitted curve is a power law of the HF percentage, with exponent equal to 2.51 (data from Table 8.2).

8.2 THE CHOICE OF THE BASIS SET

The choice of the basis set is as important as the choice of the exchange-correlation functional. Using a functional that does not describe accurately the physics of a system typically gives unphysical results. Similarly, if a small basis set is used to represent the results (*i.e.* the atomic orbitals) obtained from a DFT calculation with an appropriate functional, the results can be completely wrong. To assess which is the best form of the 6-31G basis set, the effect of polarization functions was systematically investigated. Diffuse functions could not be included in the basis set because they lead to problems in calculations with periodic boundary conditions. Figure 8.3 shows that given the same starting geometry, the CPU time increases with a power law when polarization functions are added. On the other hand, from Table 8.3 it is clear that the intermolecular distances do not change much by varying polarization functions. In all cases, d_1 , d_2 , d_4 and d_5 are smaller than the sum of the vdW radii of the atoms involved in the bonds ($2r^{\text{Br}} = 3.70 \text{ \AA}$, $r^{\text{Br}} + r^{\text{H}} = 3.05 \text{ \AA}$ ¹⁷⁷). As a trade-off between accuracy and CPU time, we ultimately chose the 6-31G(d,p), *i.e.* 6-31G**, basis set for all the calculations not involving heavy iodine atoms.

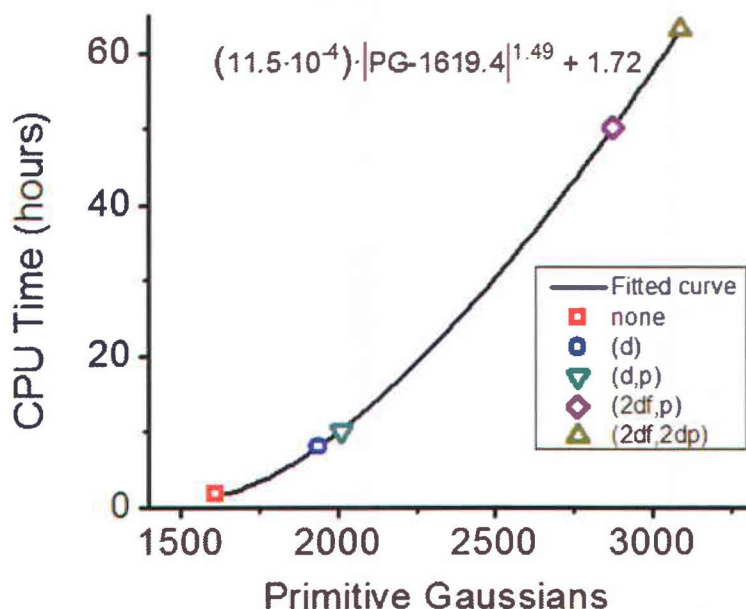


Figure 8.3: Plot of the CPU time in function of the primitive gaussians (PG) of the basis set, *i.e.* in function of the polarized functions added to the 6-31G basis set (data from Table 8.3). The CPU time increases with a power law in function of the number of primitive gaussians.

Table 8.3: Effect of polarized functions on the 6-31G basis set. Calculations for the 2D SAMN of TBPT molecules of Figure 8.1, using the M06-2X functional. Note that this functional is the most computationally expensive of Table 8.2. See Figure 8.1 for labels. The CPU times were normalized to the number of iterations of the optimization.

Polarized Functions	CPU Time	d1 (Å)	d2 (Å)	d3 (Å)	d4 (Å)	d5 (Å)
none	1 ^h 43 ^m 52 ^m	3.39	3.39	4.08	2.61	2.61
d	8 ^h 4 ^m 14 ^m	3.47	3.47	4.34	2.79	2.79
d,p	10 ^h 8 ^m 15 ^m	3.47	3.47	4.35	2.79	2.79
2df,p	50 ^h 16 ^m 12 ^m	3.40	3.40	4.39	2.83	2.84
2df,2pd	63 ^h 12 ^m 22 ^m	3.40	3.40	4.37	2.82	2.81

6-31G could not be used for TIPT because iodine is not included in this basis set in Gaussian09¹⁷⁸. Calculations involving heavy atoms such as iodine are not trivial, given the large number of core electrons, and choosing the proper basis set is crucial to achieve reliable results¹⁷⁹. In the present work we computed systems with iodine atoms using either the 3-21G* or LanL2DZ basis set (discussed in Sections 5.2.1 and 5.2.2). In the numerous DFT studies in the literature¹⁸⁰⁻¹⁸⁵, heavy iodine atoms are also typically described with Dunning's correlation-consistent basis sets¹⁸⁶. The 3-21G and ECP basis sets are relatively low-quality. Furthermore, 3-21G is not suitable for calculations involving ions because it does not incorporate diffuse functions¹⁷⁹. To assess which is the best basis set between 3-21G* and LanL2DZ we investigated the trend of binding energies of molecular complexes made of two halo-benzene molecules, using chlorine, bromine and iodine. Our calculations show that LanL2DZ leads to a more accurate description of the energies of halogen-bonded systems than 3-21G*, *i.e.* with the binding energy of molecular complexes in the correct order $BE^{\text{iodo}} > BE^{\text{bromo}} > BE^{\text{chloro}}$ (Figure 8.4).¹⁸⁷ For this reason, LanL2DZ was preferred over 3-21G*, which provides similar results to LanL2DZ in terms of molecular packing but underestimates the interaction energy of TIPT network. This effect is not due to the used functional (M06-L), given that it properly reproduces the relative binding energy of bromine- and chlorine-containing halogen-bonded complexes. Note that calculations with 3-21G*, which has 1170 PGs, are faster than 6-31G** (2010 PGs) – Figure 8.3. The computational effort of calculations with LanL2DZ is similar to 3-21G*.

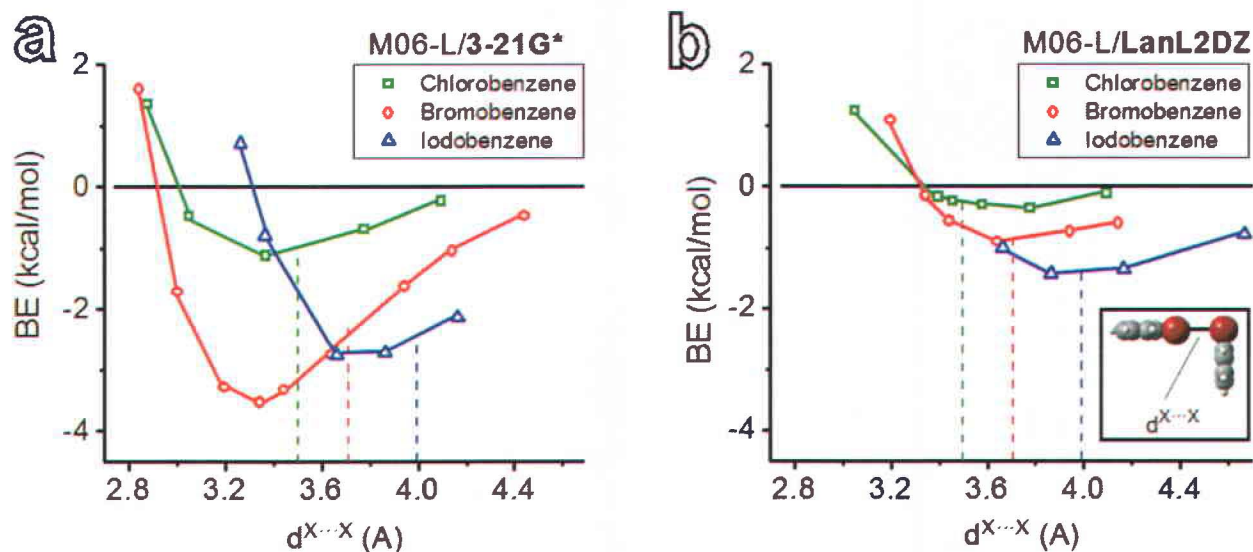


Figure 8.4: Single-point (SP) DFT-computed energies of complexes of two chlorobenzene, bromobenzene and iodobenzene molecules in function of the halogen-to-halogen distance ($d^{X...X}$), using the M06-L functional and the a) 3-21G* and b) LanL2DZ basis sets. The complexes are bonded in the geometry shown in the inset in b). The graphs show that the 3-21G* basis set underestimates the binding energy of iodobenzenes complexes, whereas the LanL2DZ basis sets accurately predicts the trend $BE^{\text{iodobenzene}} > BE^{\text{bromobenzene}} > BE^{\text{chlorobenzene}}$. The graphs also show that halogen bonding stabilizes the molecular complexes even for distances larger than the sum of the vdW of the involved halogens (vertical dotted lines).

8.3 HALOGENATED MOLECULES

In this section we will discuss the results obtained for both TIPT and TBPT, first on HOPG and then on Au(111).

8.3.1 TIPT ON HOPG

Following the application of a sessile drop (approximately 5 μl) of a solution of TIPT in TCB (10^{-2} M) on HOPG, a 2D self-assembled network of TIPT molecules spontaneously formed at the interface between the substrate and the solution (Figure 8.5a). Different domains, as large as 100 nm, are rotated from one another by 120° , commensurate with the underlying 3-fold symmetric graphite lattice (green lines in Figure 8.5a).

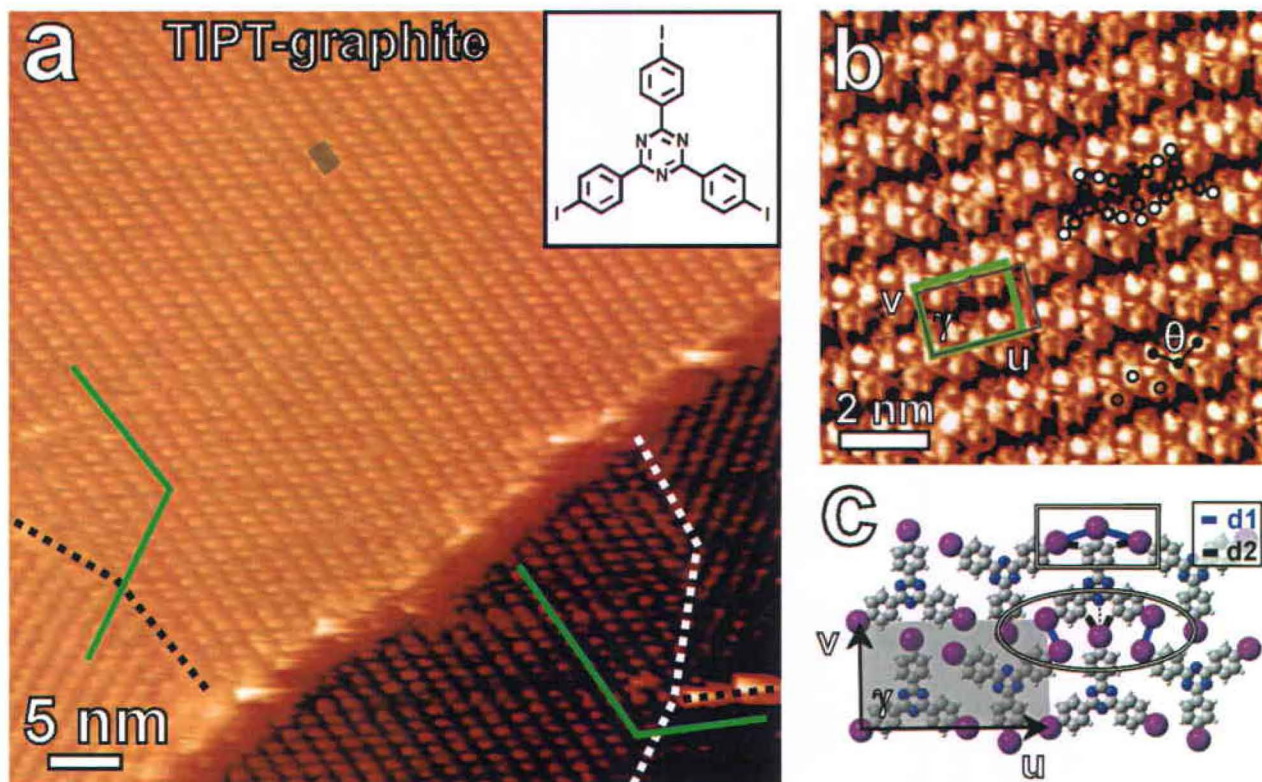


Figure 8.5: a) Large-scale STM image of TIPT (inset) molecules assembled at the TCB-HOPG interface ($56.8 \times 56.8 \text{ nm}^2$, $V_s = -1.75 \text{ V}$, $I_t = 200 \text{ pA}$). Dotted black and white lines indicate grain boundaries

between neighboring domains; the gray box indicates the molecular unit cell. b) High-resolution STM image of the molecular overlayer ($9.8 \times 9.8 \text{ nm}^2$, $V_s = -1.0 \text{ V}$, $I_t = 150 \text{ pA}$). TIPT molecules are shown schematically; full and empty circles indicate the iodine atoms of trimeric halogen-bonded motifs pointing down and up, respectively, which define the trimeric angle θ . The experimentally determined unit cell, with parameters $u = 2.04 \pm 0.09 \text{ nm}$, $v = 1.54 \pm 0.09 \text{ nm}$ and $\gamma = 90 \pm 5^\circ$, and the DFT-optimized cell (Table 8.4) are drawn in green and grey, respectively. c) DFT-calculated structure of SAMN (M06-L/LanL2DZ level); d1 and d2 are the iodine-to-iodine and iodine-to-hydrogen bonds, respectively. The rectangle and the circle highlight the intra-row and the inter-row interactions, respectively. The dotted line indicates the possible attractive interaction between iodine and nitrogen.

Table 8.4: Experimental and computed unit cell parameters and computed interatomic distances (see Figure 8.5c and Figure 8.15c for labels) of the TIPT and TBPT molecular network at the solution-HOPG interface (M06-L/LanL2DZ and 6-31G** levels of theory). Bold distances refer to intermolecular bonds shorter than the sum of the vdW radii of the atoms involved ($2r^I = 3.96 \text{ \AA}$, $r^I + r^H = 3.18 \text{ \AA}$, $r^I + r^N = 3.53 \text{ \AA}$, $2r^{Br} = 3.70 \text{ \AA}$, $r^{Br} + r^H = 3.05 \text{ \AA}$, $r^{Br} + r^N = 3.40 \text{ \AA}$).¹⁷⁷

	u (nm)	v (nm)	γ ($^\circ$)	θ ($^\circ$)	Intra-row contacts		Inter-row contacts		Energy (kcal/mol)
					d1 (\AA) X...X	d2 (\AA) X...H	d1 (\AA) X...X	d2 (\AA) X...H	
TIPT^{EXP}	2.04 \pm 0.09	1.54 \pm 0.09	90 \pm 5	141 \pm 6	N/A	N/A	N/A	N/A	N/A
TIPT^{DFT} (LanL2DZ)	2.41	1.38	91	139	5.43, 5.76	3.05 , 3.25	4.46, 4.58	3.17, 3.18	-2.9
TBPT^{EXP}	2.05 \pm 0.09	1.47 \pm 0.09	89 \pm 5	129 \pm 6	N/A	N/A	N/A	N/A	N/A
TBPT^{DFT} (LanL2DZ)	2.35	1.34	90	134	5.60, 5.75	2.99 , 3.17	4.43, 4.53	2.88 , 2.93	-5.6
TBPT^{DFT} (6-31G**)	2.25	1.32	90	146	5.04	2.73	3.82	2.82 , 2.89	-26.0

High-resolution STM images allow us to elucidate the molecular packing within the adlayer, as shown in Figure 8.5b where the halogen atoms appear as bright protrusions and the molecular core appears dark. In the 2D lattice TIPT molecules arrange in a parallel row structure, with a rectangular molecular unit cell containing two molecules ($u = 2.04 \pm 0.09 \text{ nm}$, $v = 1.54 \pm 0.09 \text{ nm}$, $\gamma = 90 \pm 5^\circ$). The protrusions ascribed to iodine atoms suggest the presence of halogen trimers along the u -vector direction (full and empty circles of Figure 8.5b). The angle defined by the trimers (θ) is equal to $141 \pm 6^\circ$. This assembly is packed differently from that of the counterpart molecule TIPB on HOPG reported in the literature (Figure 8.6a-c), however it is incidentally similar to that of TIPB on Au(111) and of THB on a boron-treated Si(111) surface (Figure 8.6d,e).^{32, 56, 153}

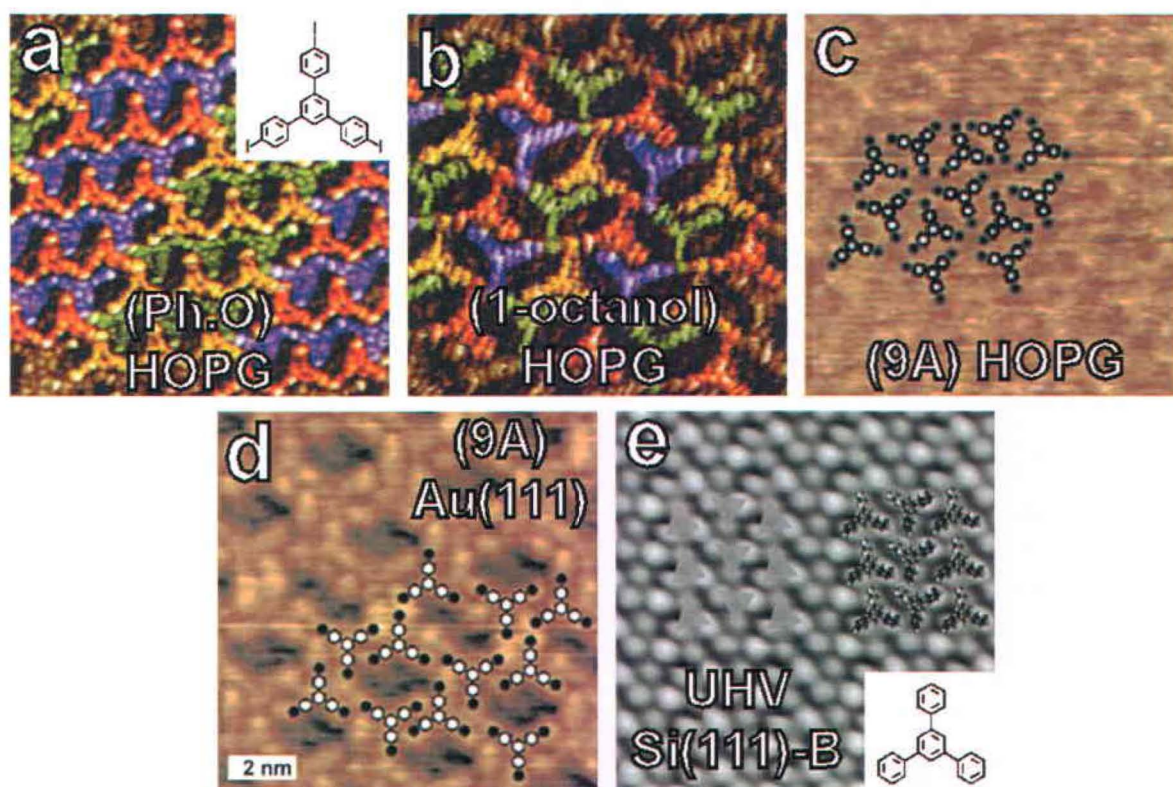


Figure 8.6: STM images of TIPB molecules on a) c) HOPG and d) on Au(111). In e) is reported a STM image of THB molecules assembled on a Si(111)-B surface in UHV at 100 K. The reported SAMNs were obtained in a) phenyloctane, b) 1-octanol and c), d) nonanoic acid (9A). Reproduced from a), b) ref. ³², c), d) from ref. ¹⁵³ and e) from ref. ⁵⁶.

The u vector is rotated by $94 \pm 5^\circ$ either clockwise (CW) or counter-clockwise (CCW) with respect to graphite $\langle 10\text{--}10 \rangle$, *i.e.* the *armchair* directions, as indicated by the 2D fast Fourier transform (FFT) of STM micrographs containing both the SAMN and the atomically-resolved HOPG substrate (Figure 8.7 and Figure 8.8). Combining this 2-fold degeneracy with the 3-fold degeneracy of Figure 8.5a, six different domains are in principle possible, however they were not simultaneously observed with the STM given that each domain extends over several tens of nm (Figure 8.5a). See also Figure 8.9 for the relation between the 2D FFT and the real-space high-symmetry directions of the HOPG substrate. Note that since the SAMN was observed only when single HOPG terraces were completely covered, imaging both the adlayer and the underlying substrate was only possible by changing the tunneling parameters halfway through image acquisition.

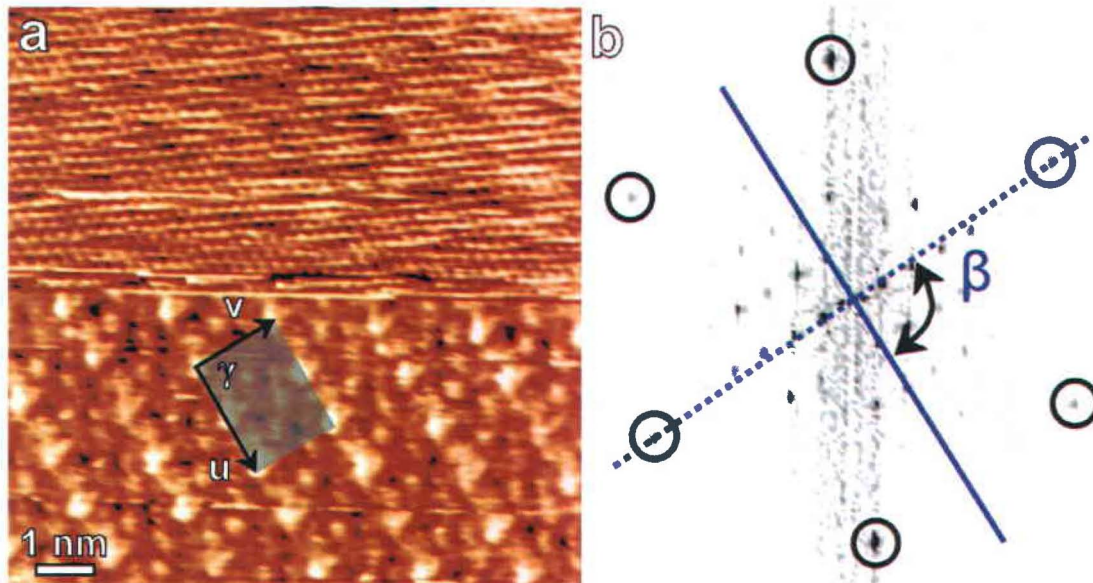


Figure 8.7: a) STM) image showing TIPT molecules assembled at the TCB-HOPG interface (lower part) and the underlying graphite lattice with atomic resolution (upper part) ($10.2 \times 10.2 \text{ nm}^2$, $I_t = 141 \text{ pA}$, $V_s^{\text{HOPG}} = -0.02 \text{ V}$ and $V_s^{\text{SAMN}} = -0.64 \text{ V}$) and b) corresponding 2D FFT. The spots of the HOPG lattice are highlighted by black circles, whereas the blue dotted and solid lines lie along one of the $\langle 10\text{--}10 \rangle$ armchair high-symmetry directions of graphite and along the u vector of the unit cell, respectively. The SAMN is rotated CW by an angle $\beta = 94 \pm 5^\circ$ with respect to the HOPG substrate. The unit cell vectors are $u = 2.04 \pm 0.09 \text{ nm}$, $v = 1.54 \pm 0.09 \text{ nm}$ and the angle between them is $\gamma = 90 \pm 5^\circ$.

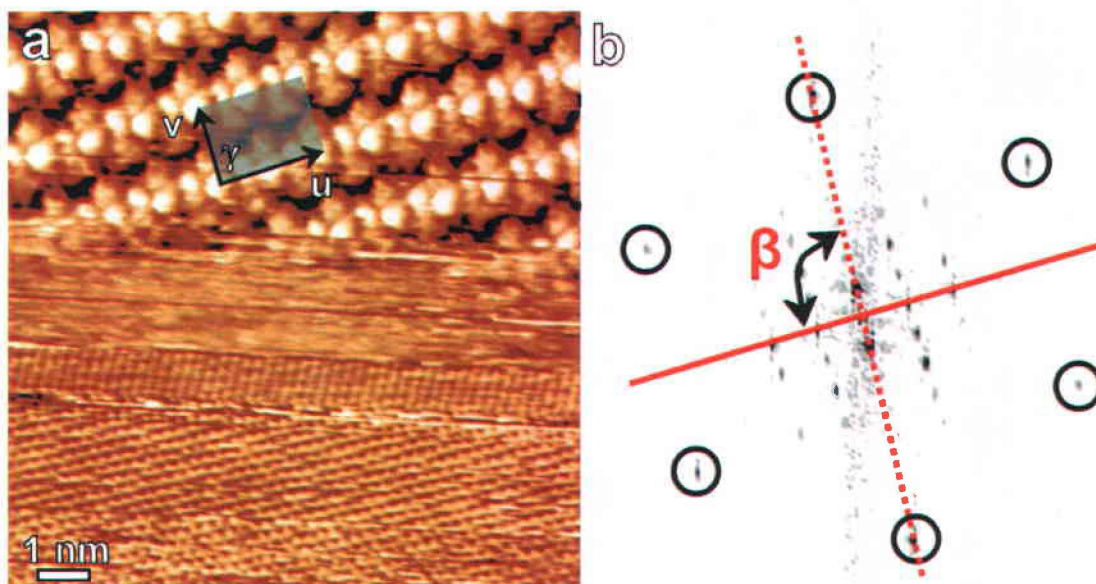


Figure 8.8: a) STM image showing TIPT molecules assembled at the TCB-HOPG interface (upper part) and the underlying graphite lattice with atomic resolution (lower part) ($11.1 \times 11.1 \text{ nm}^2$, $I_t = 133 \text{ pA}$, $V_s^{\text{HOPG}} = -0.02 \text{ V}$ and $V_s^{\text{SAMN}} = -1.61 \text{ V}$) and b) corresponding 2D-FFT. The spots originating from the HOPG lattice are highlighted by black circles, whereas the red dotted and solid lines lie along one of the $\langle 10-10 \rangle$ armchair high-symmetry directions of graphite and along the u vector of the unit cell, respectively. The SAMN is rotated CCW by an angle $\beta = 94 \pm 5^\circ$ with respect to the HOPG substrate. The unit cell vectors are $u = 2.04 \pm 0.09 \text{ nm}$, $v = 1.54 \pm 0.09 \text{ nm}$ and the angle between them is $\gamma = 90 \pm 5^\circ$.

Starting from the experimentally observed molecular structure (Figure 8.5b) we performed gas-phase DFT optimization of the SAMN. The geometry predicted by the DFT calculations is in agreement with the experimental STM images, namely with TIPT molecules arranged in consecutive rows along the direction specified by the v vector (Figure 8.5c). This molecular configuration is favorable for halogen bonding,¹⁸⁸⁻¹⁹¹ with the positively charged tip of the C–I bonds pointing toward the negatively charged belts of neighboring C–I bonds (d1), however the calculations show that the iodines are too far apart to engage in halogen-bonding (Table 8.4). Indeed, molecular rows (rectangle in Figure 8.5c) and neighboring rows (circle in Figure 8.5c) are mostly stabilized by I \cdots H hydrogen-bonds (Table 8.4), which despite being weaker than typical hydrogen bonds involving –OH and –NH donor groups have already shown to be important in driving pattern formation.¹⁹² Although the σ -hole of the iodine atoms points toward the nucleophilic nitrogen atom of the neighboring TIPT along the v vector (dotted line in Figure 8.5c), the approach to the triazine core is screened by the electrophilic hydrogens of the phenyl groups (Figure 8.10a,b). Therefore, the nitrogen does not participate

in the lateral stabilization of the assembly (Table 8.4). The computed net intermolecular binding energy is -2.9 kcal/mol per unit cell (*i.e.* -0.038 eV/nm²)

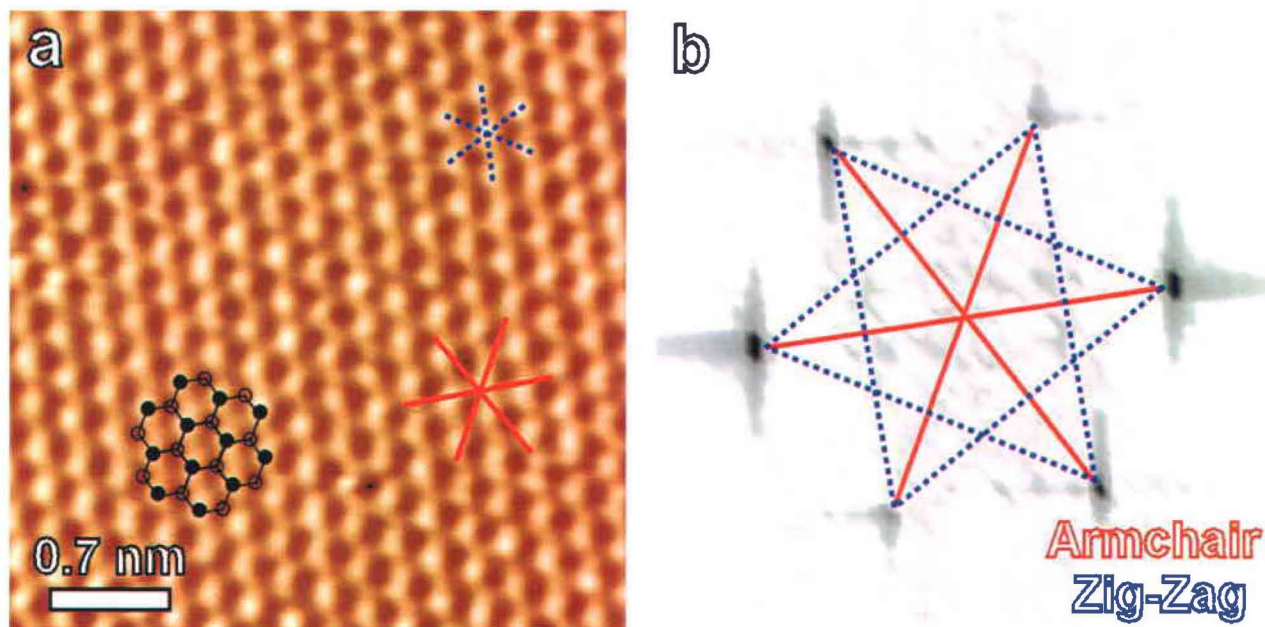


Figure 8.9: a) Only the β atoms (black full dots) of the graphite lattice are imaged in STM (see also Figure 7.2). b) The 2D FFT of the a STM image containing the HOPG lattice such as the one in a) provides information of the high-symmetry directions of the substrate. Red and blue lines indicate the armchair and zig-zag directions of the HOPG surface.

Since this value does not account for stabilizing substrate effects, the total binding energy of the system is in principle higher as it includes the attractive $\pi \cdots \pi$ interaction, which comprises both dispersive and electrostatic interactions,¹⁷ between the HOPG and the aromatic molecular core. TPD experiments show that the adsorption energy of polycyclic aromatic hydrocarbons (PAHs) on graphite is equal to 52 ± 5 meV/atom¹⁵⁸. This means that a single TIPT molecule would have adsorption energy on graphite of roughly -30 kcal/mol, which is one order of magnitude higher than the energy due to lateral intermolecular interactions obtained from our DFT calculations (Table 8.4). Similarly, theoretical works of PAHs on graphene, *i.e.* on a single sheet of graphite, show that the adsorption energy (E_{bind}) can be expressed in function of the number of carbon (N_C) and hydrogen atoms (N_H)¹⁷:

$$E_{bind} = N_C E_{CC} + N_H (E_{CH} - E_{CC}), \quad 8.1$$

where $E_{CC} = -49.2$ meV is the fitted adsorption energy per graphene-like carbon and $E_{CH} = -80.1$ meV is the fitted energy per benzene-like carbon and its adjoining hydrogen atom. Graphene-like carbon atoms feature three covalent bonds with neighboring carbons, whereas benzene-like carbons are covalently bonded to one hydrogen and two carbon atoms. For a PAH molecule similar to TIPT, *i.e.* the molecule reported in the inset of Figure 8.6e, equation 8.1 gives an adsorption energy of roughly -40 kcal/mol, not far from the experimental data discussed above.

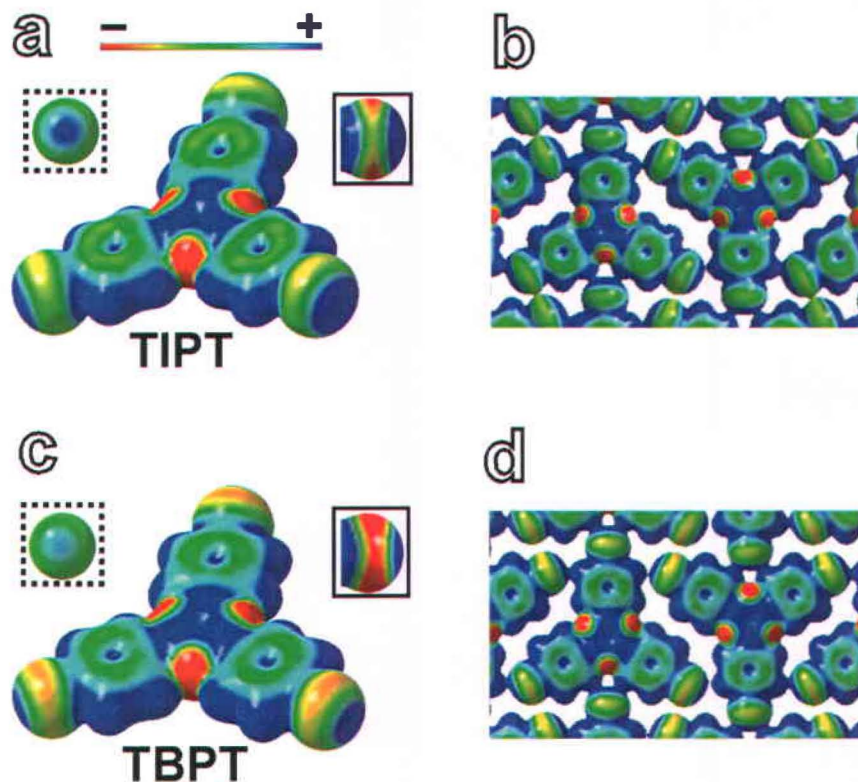


Figure 8.10: Molecular ESP map (M06-L/LanL2DZ) of a),b) TIPT and c),d) TBPT molecules in the a),c) isolated state (3D view) and b),d) in the assembly (top-view), expressed in a.u. at the 0.004 electrons Bohr^{-3} isodensity surface (blue and red areas of single molecules and of the SAMNs correspond to a potential of $\pm 2 \times 10^{-2}$ a.u., respectively). The dotted and solid black squares show the ESP map of the halogen atoms of TIPT and TBPT molecules in the isolated state, seen along (σ -hole) and orthogonal (negatively charged ring) to the C-X bond direction; blue and red areas of the σ -hole correspond to a potential of $\pm 6 \times 10^{-2}$ a.u., respectively; blue and red areas of the ring correspond to a potential of $\pm 1 \times 10^{-2}$ a.u., respectively.

We note that DFT optimization leads to a molecular unit cell slightly different from the experimental data (see Figure 8.5b and Table 8.4). We ascribe this to the effect of the substrate, which was not taken into account in the gas-phase calculations. We also considered different polymorphs for the optimization. In STM images the apparent molecular unit cell of TIPT on HOPG ($u = 1.02 \pm 0.09$ nm, $v = 1.54 \pm 0.09$ nm and $\gamma = 90 \pm 5^\circ$) is too small to accommodate one TIPT molecule (intramolecular $I \cdots I$ distance equal to 1.34 nm) (see grey rectangle in Figure 8.11). For this reason we considered other physically possible unit cells, made of multiples of the apparent unit cell (colored cells in Figure 8.11). DFT calculations show that the most stable polymorphs are those with unit cell 1 (Table 8.5). The geometries discussed in this work are those labeled “1”, which despite being slightly less stable than the SAMNs “1*” have a molecular arrangement that resembles the STM contrast (Figure 8.11).

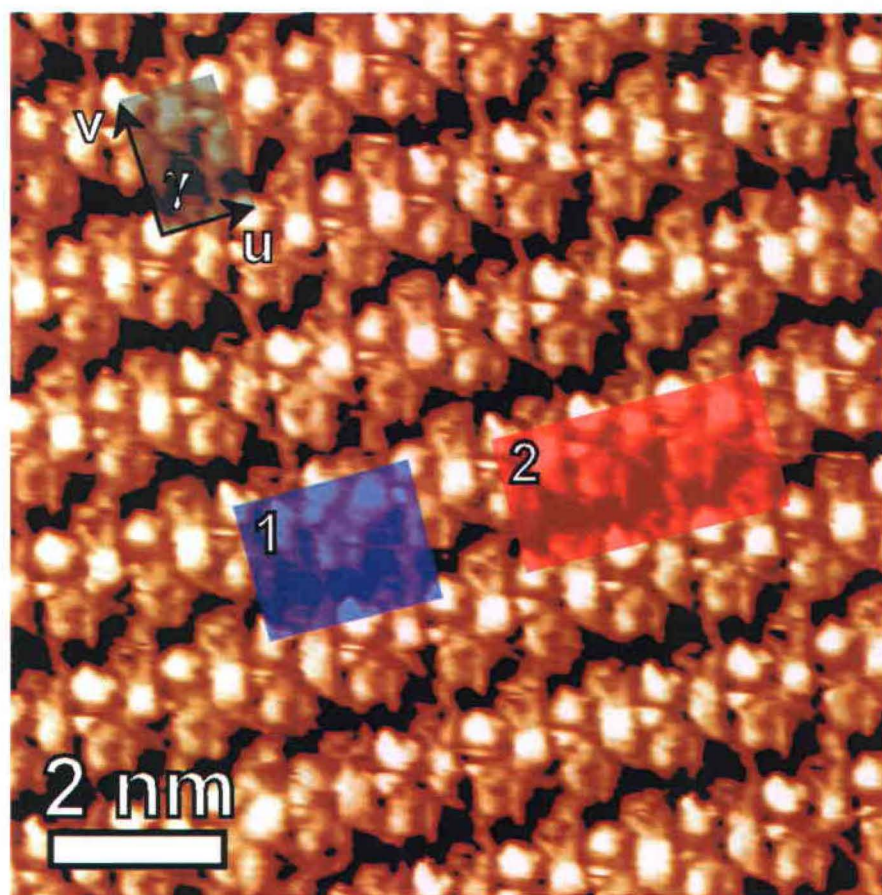


Figure 8.11: High-resolution STM image of the TIPT molecular overlayer at the TCB-HOPG interface (9.8×9.8 nm², $V_s = -1.0$ V, $I_t = 150$ pA). The apparent unit cell, with parameters $u = 1.02 \pm 0.09$ nm, $v = 1.54 \pm 0.09$ nm and $\gamma = 90 \pm 5^\circ$, is indicated in grey; the physically possible unit cells are indicated in color.

Table 8.5: DFT-optimized geometries of TIPT and TBPT SAMNs on HOPG (M06-L/LanL2DZ level of theory). Polymorphs labeled “1” and “1*” are two different geometries obtained from starting geometries with the unit cell 1 of Figure 8.11. Polymorphs labeled “2” refer to the unit cell 2 of Figure 8.11.

	u^{EXP} [u^{DFT}] (nm)	v^{EXP} [v^{DFT}] (nm)	γ^{EXP} [γ^{DFT}] (°)	Energy (eV/nm ²)	
TIPT ¹	2.04 ± 0.09 [2.41]	1.54 ± 0.09 [1.38]	90 ± 5	-0.038	
TIPT ^{1*}	2.04 ± 0.09 [2.19]	1.54 ± 0.09 [1.54]	90 ± 5	-0.072	
TIPT ²	3.06 ± 0.09 [3.06]	1.54 ± 0.09 [1.39]	90 ± 5	-0.022	
TBPT ¹	2.05 ± 0.09 [2.35]	1.47 ± 0.09 [1.34]	89 ± 5	-0.077	
TBPT ^{1*}	2.05 ± 0.09 [2.16]	1.47 ± 0.09 [1.52]	89 ± 5	-0.087	
TBPT ²	3.07 ± 0.09 [3.03]	1.47 ± 0.09 [1.32]	89 ± 5	-0.027	

The same long-range ordered self-assembly of TIPT molecules at the liquid-HOPG interface is obtained using phenyloctane as solvent, whereas no long-range order was observed with heptanoic acid. The stability of the SAMN was higher in TCB than in phenyloctane, given that using the latter it was quite difficult to probe the SAMN because of noise and instability (Figure 8.12).

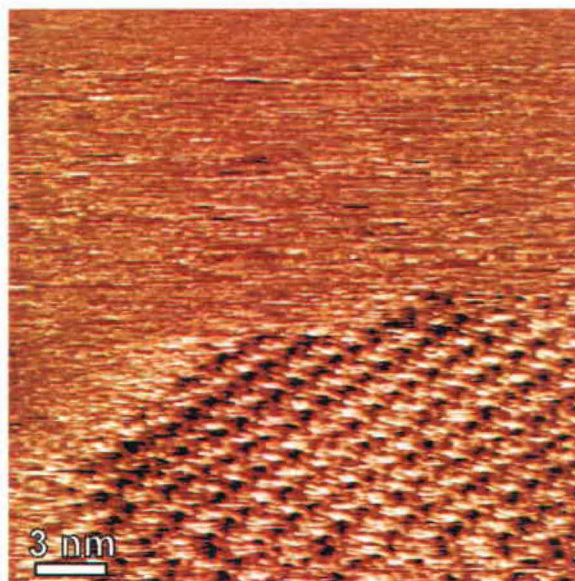


Figure 8.12: STM image of TIPT molecules assembled at the phenyloctane-HOPG interface ($25.0 \times 25.0 \text{ nm}^2$, $V_s = -1.15 \text{ V}$, $I_t = 66 \text{ pA}$).

From a chemical design point of view, having the triazine core in TIPT may be advantageous for achieving self-assembled structures. Figure 8.13 shows the energy associated with the rotation of the side groups of TBPT and its counterpart TBPB, reported elsewhere.^{31, 56, 149-152} This graph was obtained by plotting the energy of the DFT-optimized single-molecule configurations as a function of the (fixed) dihedral angle (δ) between the side groups and the molecular core (see inset in Figure 8.13). For each molecule, the energies are plotted relative to the least stable geometry. The calculations were performed for the brominated molecules, however a similar behavior is expected for TIPT vs. TIPB. Figure 8.13 shows that for TBPT the most stable conformation is planar ($\delta = 0^\circ$), whereas TBPB is most stable when $\delta \approx 40^\circ$. For TBPB the planar geometry is less stable (by 6 kcal/mol) because of repulsive interactions between the hydrogen atoms in the benzene core and at the ortho-positions of neighboring halo-phenyls (where the atomic positions are defined with respect to

the bond with the central core). From the diagram in Figure 8.13 we can conclude that TBPT is stiffer than TBPB. Therefore, from a fundamental perspective, self-assembly of TBPT is entropically more favorable than TBPB, given that the former allows for lower initial-entropy states (neglecting the effect of the solvent).⁵

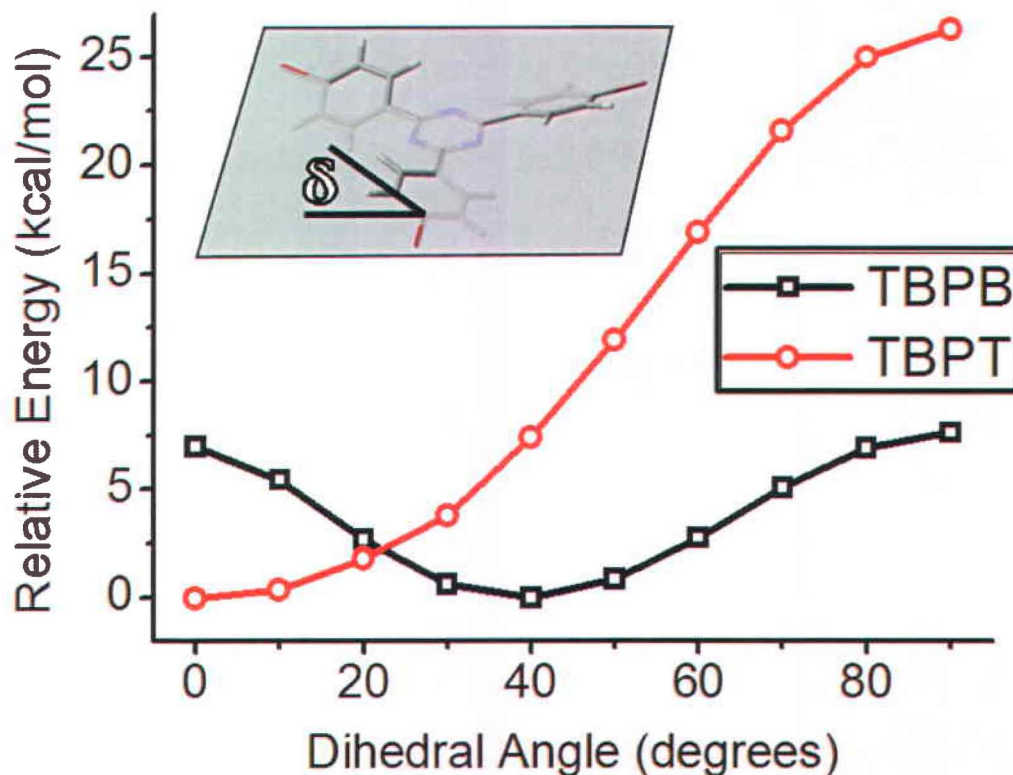


Figure 8.13: DFT computed energies for conformations of TBPT and TBPB with increasing dihedral rotation angle (δ) of the side groups (see TBPT molecule in the inset). For each molecule, energies are plotted relative to the least stable geometry. The diagram shows that TBPT is most stable when it is planar ($\delta = 0^\circ$), whereas for TBPB this occurs when $\delta \approx 40^\circ$. Calculations performed at the B3LYP/6-31G** level of theory.

Moreover, the non-planarity of TBPB in the isolated state may also lead to lower adsorption energy where the molecules are not fully planarized upon adsorption on the surface. The higher stiffness of TBPT arises from attractive intramolecular interactions between the nitrogen atoms in the triazine core and the hydrogen atoms at the ortho-positions of the halo-phenyl side groups ($d^{N \cdots H} = 2.46 \text{ \AA}$ vs. $r^N + r^H = 2.75 \text{ \AA}$ ¹⁷⁷), which bend the C–H bonds towards the central core. These considerations are valid for TIPT as well (Figure 8.14).

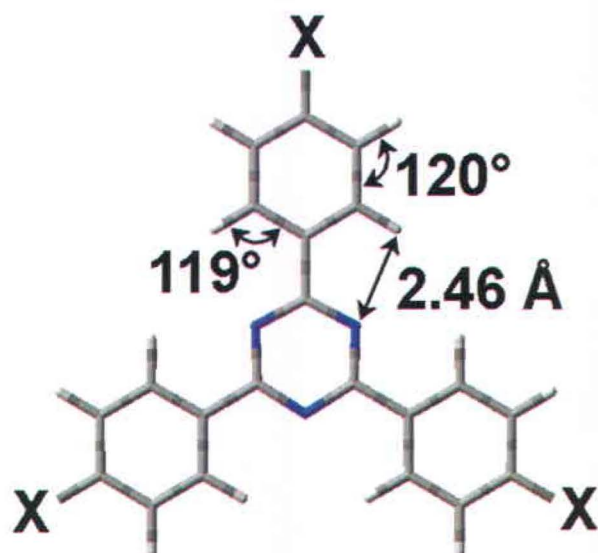


Figure 8.14: Both for TBPT (X = Br) and TIPT (X = I), intramolecular attractive interactions ($d^{N\cdots H} = 2.46 \text{ \AA}$ vs. $r^N + r^H = 2.75 \text{ \AA}$) take place between the nitrogen atoms of the triazine core and the hydrogen atoms at the ortho-positions of the halo-phenyl side groups (where the atomic positions are defined with respect to the bond with the central core). The C–H bonds at the ortho-positions are bent by 1° towards the electrophilic triazine core. These interactions render TXPT molecules more planar and stiffer precursors than TXPB molecules (namely molecules with the benzene core instead of the triazine core). Calculations performed at the B3LYP/6-31G** level.

8.3.2 TBPT ON HOPG

Following the application of one drop of a solution of the brominated molecule (TBPT) in TCB onto HOPG, with concentration varying from 10^{-2} M to 10^{-5} M, no SAMN was observed. On the other hand, when TBPT was dissolved in phenyloctane (10^{-2} M), a stable SAMN formed over tens of nanometers (Figure 8.15a). The molecular packing is similar to that in the SAMN obtained with the iodinated molecule (Figure 8.15b), *i.e.* with a rectangular unit cell hosting two molecules ($u = 2.05 \pm 0.09$ nm, $v = 1.47 \pm 0.09$ nm, $\gamma = 89 \pm 5^\circ$).

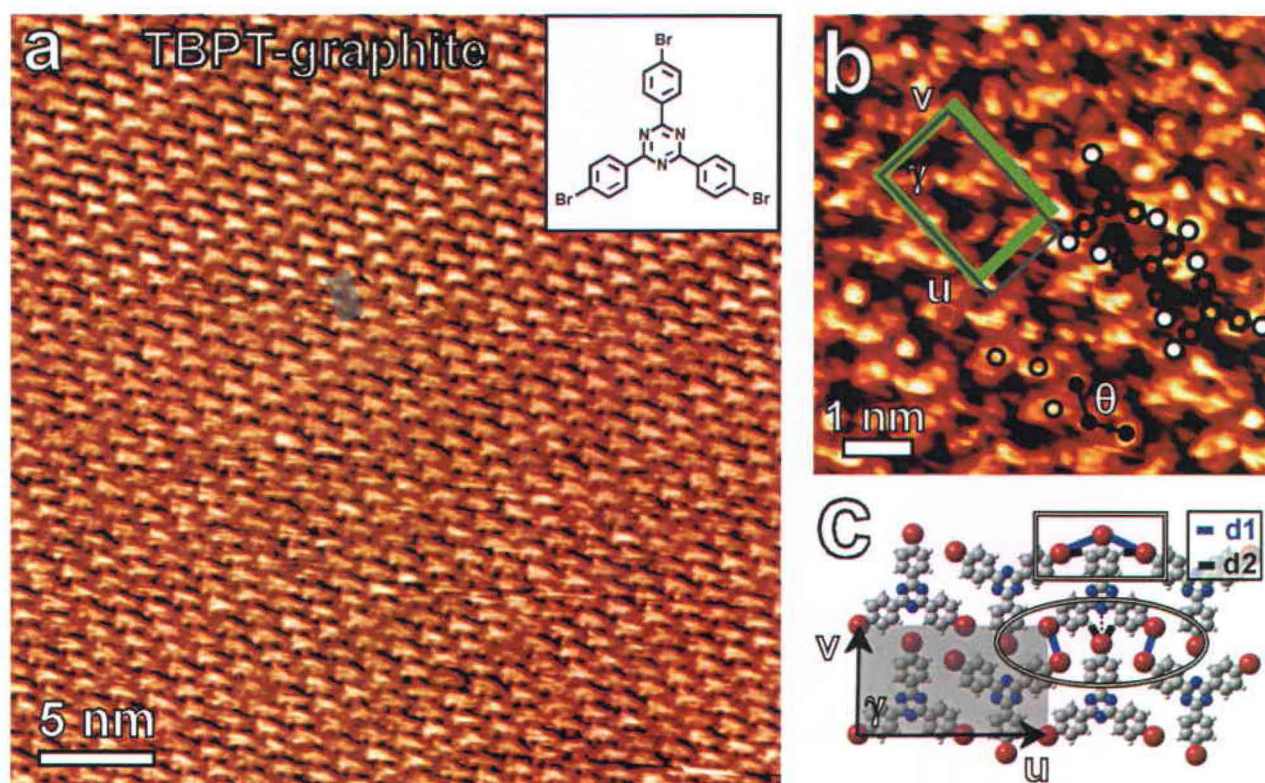


Figure 8.15: a) Large-scale and b) high-resolution STM image of TBPT molecules (inset) assembled at the phenyloctane-HOPG interface - a) 36.4×36.4 nm², $V_s = -1.20$ V, $I_t = 120$ pA, b) 6.6×6.6 nm², $V_s = -1.60$ V, $I_t = 117$ pA. TBPT molecules are schematically indicated in b); full and empty circles indicate the bromine atoms of trimeric halogen-bonded motifs pointing down and up, respectively, which define the trimeric angle θ . The experimentally determined unit cell, with parameters $u = 2.05 \pm 0.09$ nm, $v = 1.47 \pm 0.09$ nm and $\gamma = 89 \pm 5^\circ$, and the DFT-optimized cell (Table 8.4) are drawn in green and grey, respectively. b) SAMN computed with gas-phase DFT calculations at the M06-L/LanL2DZ level; d1 and d2 are the bromine-to-Bromine and bromine-to-hydrogen bonds, respectively. The rectangle and the circle highlight the intra-row and the inter-row interactions, respectively. The dotted line indicates the potential attractive interaction between bromine and nitrogen.

As suggested by the protrusions ascribed to the halogen atoms (circles in Figure 8.15b), TBPT molecules are arranged in rows stacked along the v vector ($\theta = 129 \pm 6^\circ$). Similar to the case of the iodinated molecule, the molecular framework is rotated with respect to the substrate with the u vector of the unit cell of the SAMN $93 \pm 5^\circ$ either clockwise or counter-clockwise with respect to the $\langle 10\text{--}10 \rangle$ armchair directions of the underlying HOPG surface (Figure 8.16 and Figure 8.17). As was the case with TIPT, the structure of Figure 8.15b is different from that reported in the literature for the analogous molecule TBPB on HOPG, which features an oblique unit cell (Figure 8.18).³¹

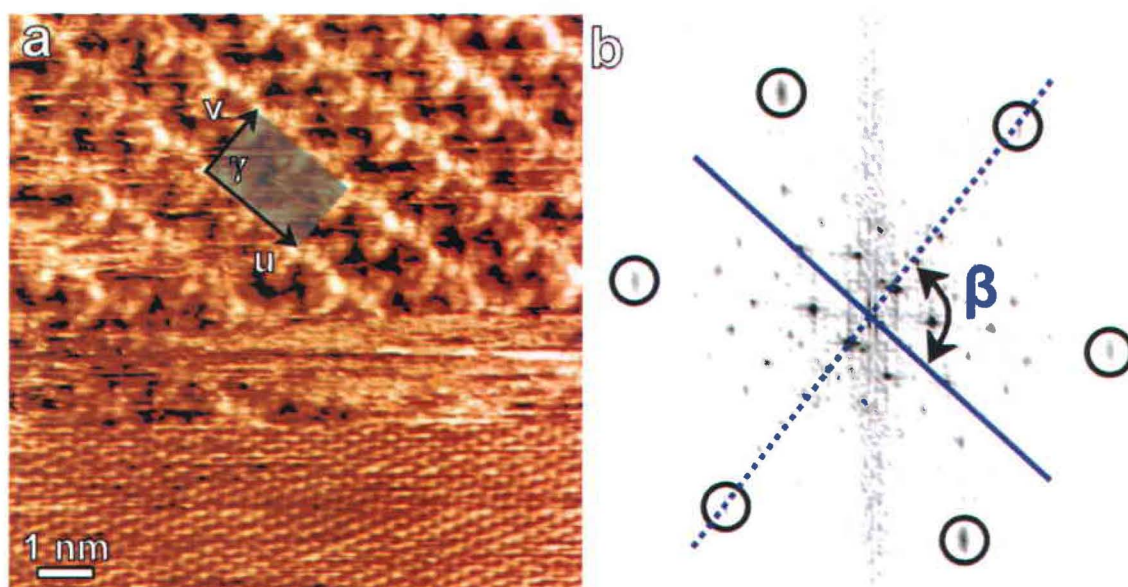


Figure 8.16: a) STM image showing TBPT molecules assembled at the phenyloctane-HOPG interface (upper part) and the underlying graphite lattice with atomic resolution (lower part) ($10.4 \times 10.4 \text{ nm}^2$, $I_t = 102 \text{ pA}$, $V_s^{\text{HOPG}} = -0.02 \text{ V}$ and $V_s^{\text{SAMN}} = -1.21 \text{ V}$) and b) corresponding 2D-FFT. The spots of the HOPG lattice are highlighted by black circles, whereas the blue dotted and solid lines lie along one of the $\langle 10\text{--}10 \rangle$ armchair high-symmetry directions of graphite and along the u vector of the unit cell, respectively. The SAMN is rotated CW by an angle $\beta = 93 \pm 5^\circ$ with respect to the HOPG substrate. The unit cell vectors are $u = 2.05 \pm 0.09 \text{ nm}$, $v = 1.47 \pm 0.09 \text{ nm}$ and the angle between them is $\gamma = 89 \pm 5^\circ$.

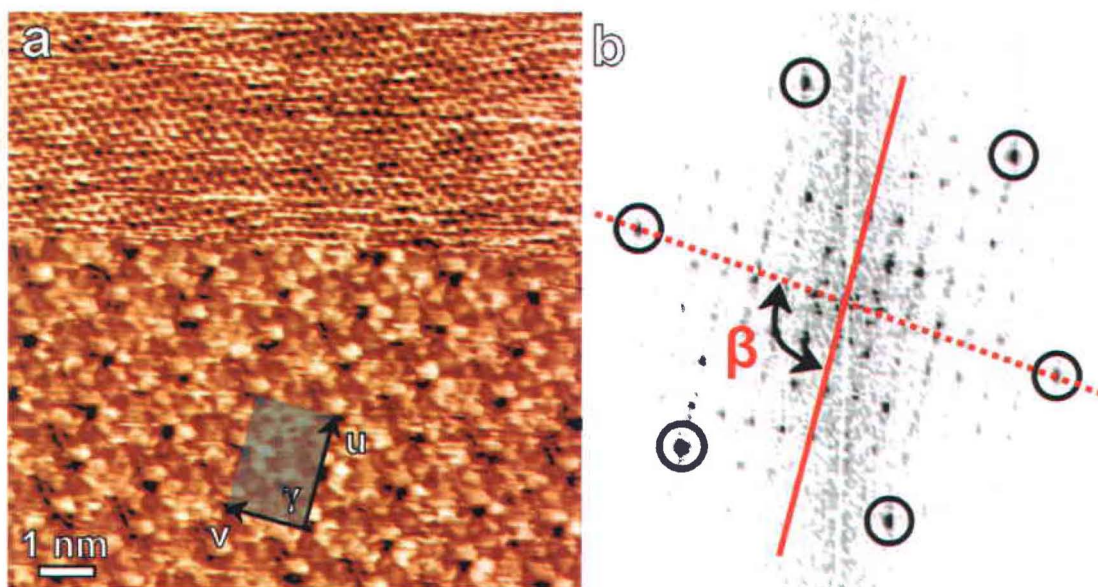


Figure 8.17: a) STM image showing TBPT molecules assembled at the phenyloctane-HOPG interface (lower part) and the underlying graphite lattice with atomic resolution (upper part) ($10.6 \times 10.6 \text{ nm}^2$, $I_t = 139 \text{ pA}$, $V_s^{\text{HOPG}} = -0.02 \text{ V}$ and $V_s^{\text{SAMN}} = -1.21 \text{ V}$) and b) corresponding 2D-FFT. The spots of the HOPG lattice are highlighted by black circles, whereas the blue dotted and solid lines lie along one of the $\langle 10-10 \rangle$ armchair high-symmetry directions of graphite and along the u vector of the unit cell, respectively. The SAMN is rotated CCW by an angle $\beta = 93 \pm 5^\circ$ with respect to the HOPG substrate. The unit cell vectors are $u = 2.05 \pm 0.09 \text{ nm}$, $v = 1.47 \pm 0.09 \text{ nm}$ and the angle between them is $\gamma = 89 \pm 5^\circ$.

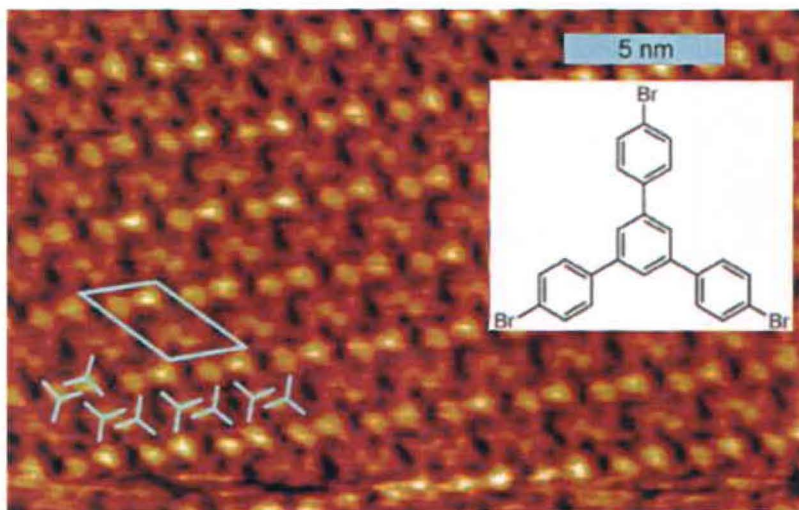


Figure 8.18: SAMN of TBPB molecules (inset) at the UHV-HOPG interface. Reproduced from ref. ³¹.

It is interesting to note that TIPT and TBPT networks on HOPG have same u vector despite the different size of the halogen atoms, which in turns leads to different v vectors and trimeric angles θ (Table 8.4). This may arise from a commensurability effect between the SAMNs and the substrate, which would also explain the discrepancies between the experimental and DFT-computed molecular unit cells (Figure 8.5b and Figure 8.15b).

As in the previous case, DFT optimization gives a molecular configuration with the halogens of each molecule participating in the stabilization of the SAMN *via* X \cdots H hydrogen bonds (Table 8.4). The halogen atoms are again oriented toward the nucleophilic triazine core of the neighboring TBPT molecule along the v vector (dotted line in Figure 8.15c), similarly to TIPT, but cannot engage in halogen bonding due to the electrostatic repulsion of the hydrogen atoms screening the nitrogen (Figure 8.10c,d). The calculations indicate that the X \cdots H contacts are closer for TBPT than for TIPT (Table 8.4). Therefore, in spite of the more pronounced σ -hole of iodine (Figure 8.10), the computed net intermolecular binding energy of TBPT (-5.6 kcal/mol per unit cell, -0.077 eV/nm²) is twice that of TIPT (Table 8.4). This is due to stronger Br \cdots H hydrogen bonds as a consequence of a more negative equatorial region at the C–Br bond (iodine is less electronegative) – Figure 8.10a,c.

In principle, by knowing the orientation of the adlayer with respect to the substrate it is possible to infer if the two are commensurate. However, both for the SAMNs of Figure 8.5 and Figure 8.15 it was not possible to unambiguously discern a unit cell commensurate with the substrate within the experimental uncertainty (Figure 8.19). Nonetheless, it seems that the longer (u) unit cell vectors lead to a similar adsorption site along this direction, *i.e.* on the same type of carbon atom of the HOPG substrate (see also Figure 7.2).

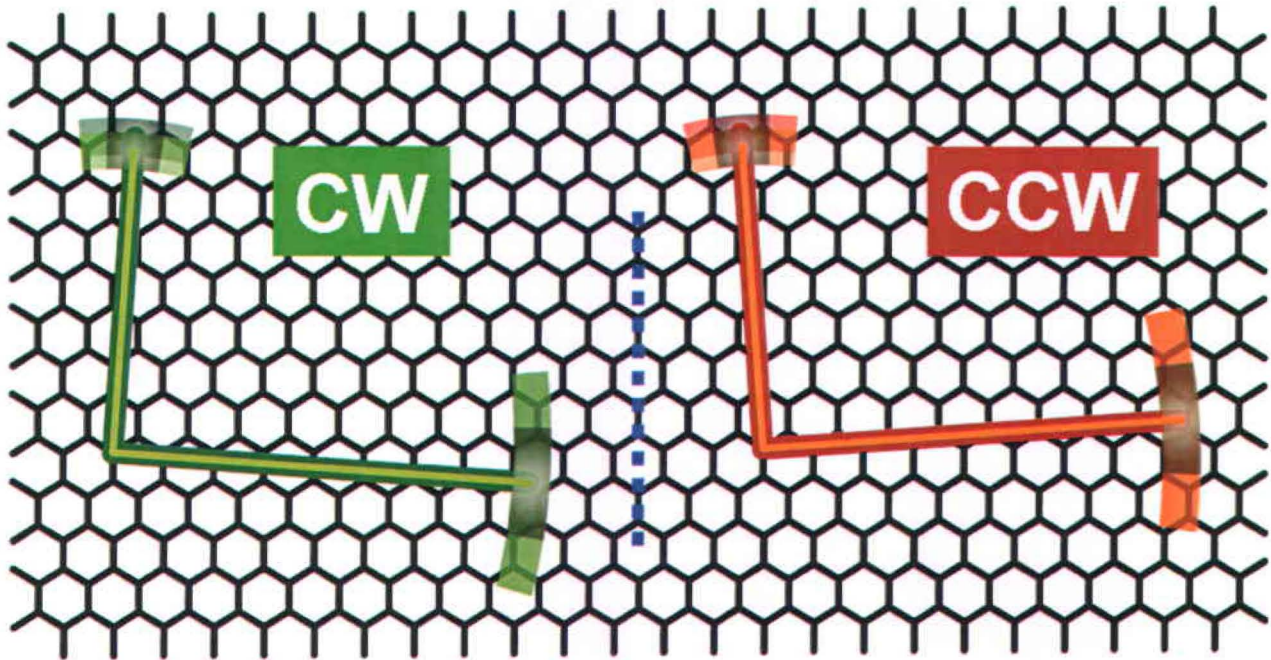


Figure 8.19: Model of the unit cells of the CW and CCW domains of the TIPT (darker green and red lines) and TBPT (lighter green and red lines) networks on HOPG. The dotted blue line indicates the armchair direction of the HOPG substrate to which the rotation of the u-vectors is referred to (see figures with FFTs). The semitransparent black regions represent the experimental uncertainty on the unit cell parameters, whereas the colored semitransparent regions represent the uncertainty on the rotation of the adlayer with respect to the substrate, measured on 2D FFTs. From the experimental data it is not possible to unambiguously infer the adlayer unit cell commensurate with the substrate.

8.3.3 TBPT-co-HEPTANOIC ON HOPG

Interestingly, when TBPT was dissolved in heptanoic acid (10^{-2} M) we observed a structure with completely different topology, as shown in the high-resolution STM images of Figure 8.20a,b. Protrusions consistent with the location of the bromine atoms of the building blocks are spaced by a distance of 1.3 ± 0.1 nm (two-headed arrow in Figure 8.20b), in agreement with DFT calculations (Figure 6.1c). In this polymorph, TBPT molecules are arranged in a 6-fold symmetric structure, with unit cell vectors $u = v = 2.7 \pm 0.1$ nm aligned along the $\langle 1-210 \rangle$ zig-zag high-symmetry directions of the graphite substrate (Figure 8.22) and angle $\gamma = 60 \pm 5^\circ$ (the large experimental uncertainty here is due to limited statistics).

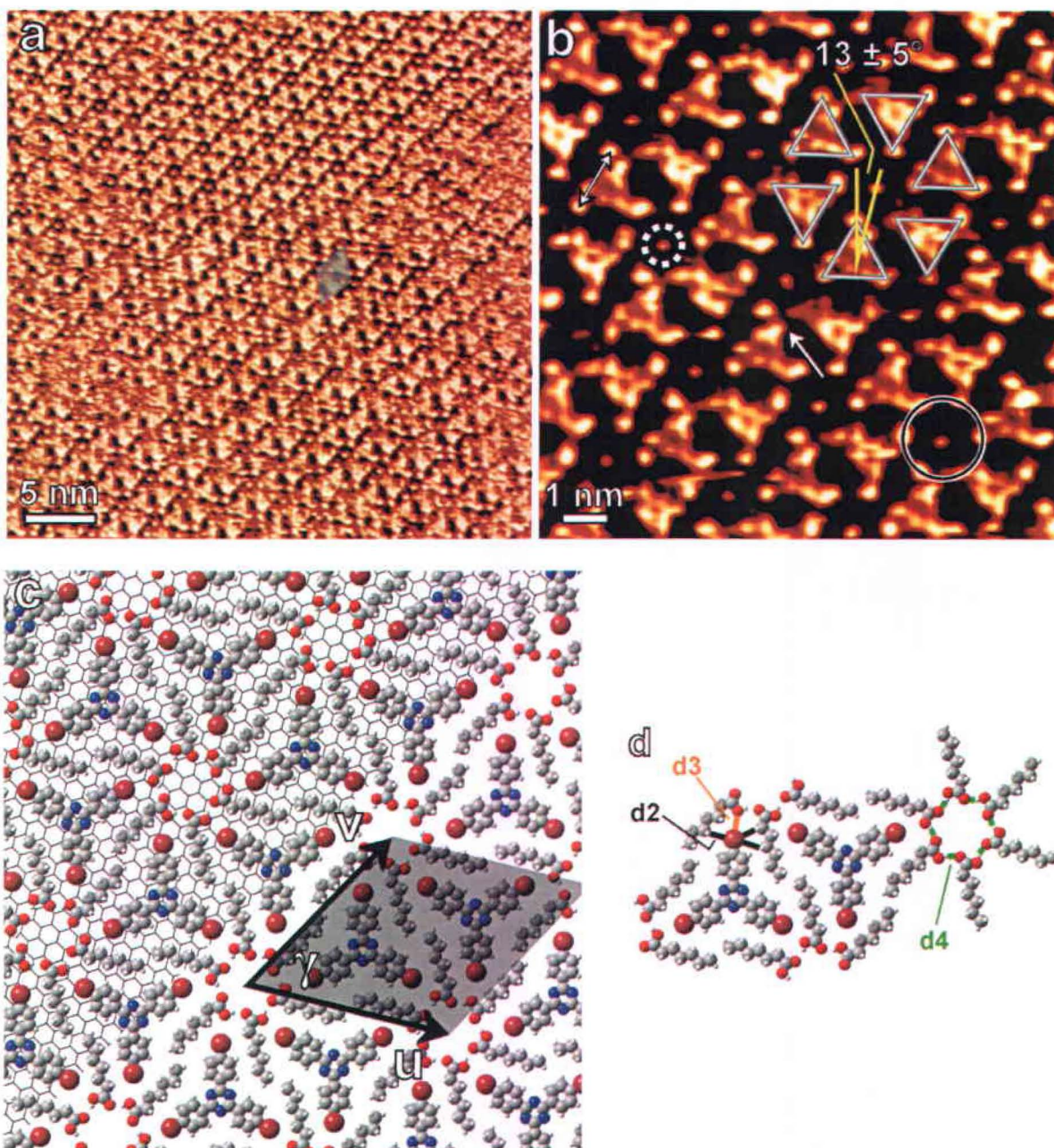


Figure 8.20. a) Large-scale and b) high-resolution STM image of TBPT molecules assembled at the heptanoic acid-HOPG interface – a) $38.5 \times 38.5 \text{ nm}^2$, $V_s = -1.40 \text{ V}$, $I_t = 50 \text{ pA}$, b) $11.2 \times 11.2 \text{ nm}^2$, $V_s = -1.40 \text{ V}$, $I_t = 50 \text{ pA}$. In a), the unit cell is indicated by the grey box. In b), the dotted and solid circles indicate a bright protrusion and a pore within the assembly (1.7 nm diameter, measured from X to X), respectively. The two-headed arrow indicates two bromine atoms, $1.3 \pm 0.1 \text{ nm}$ apart, of a TBPT molecule, whereas the single-headed arrow indicates the unusual internal contrast of TBPT molecules. Grey triangles superimposed to TBPT molecules highlight the chirality within the 2D lattice. c) DFT-computed bi-component SAMN at the M06-L/6-31G** level of theory (in the top-left part of the image the HOPG substrate is shown underneath the molecular network. d) Zoom of the computed network highlighting the stabilizing lateral interactions of the system. The experimentally determined unit cell is: $u = v = 2.7 \pm 0.1 \text{ nm}$, $\gamma = 60 \pm 5^\circ$.

In STM images this structure exhibits cavities 1.7 nm large (solid circle in Figure 8.20b), and hence it is less dense than that reported in Figure 8.15b (0.32 molecules/nm² vs. 0.67 molecules/nm² for TBPT(phenyloctane)-HOPG). This implies that TBPT molecules in the assembled network are too far apart to engage in Br \cdots Br halogen bonding ($d^{\text{Br}\cdots\text{Br}} = 8 \pm 1 \text{ \AA}$ vs. $2r^{\text{Br}} = 3.70 \text{ \AA}$),¹⁷⁷ suggesting that solvent molecules co-assemble in the SAMN. Our DFT calculations show that heptanoic acid molecules can arrange in cyclic hydrogen-bonded hexamers ($R_6^6(24)$), which provide a nearly perfect shape complementarity, thus co-assembling with TBPT molecules *via* vdW interactions (Figure 8.20c). This is remarkable because the $R_6^6(24)$ synthon of carboxylic groups is generally a metastable hydrogen bonding motif that is observed extremely rarely,¹⁹³ especially in 2D molecular crystals (Figure 8.21a,b),¹⁹⁴ and has never been reported to engage in multi-component self-assembly.

The structure of Figure 8.20 is topologically similar to those previously observed in mono-component halogen- and hydrogen-bonded SAMNs formed from C₃-symmetric organic building blocks at the liquid-HOPG interface^{19, 194} and in UHV (Figure 8.21).¹⁴⁹ We ascribe the bright protrusion located at the center of the TBPT hexamers (dotted white circle in Figure 8.20b) to an electronic effect arising from the co-assembled $R_6^6(24)$ synthons of solvent molecules.¹⁹⁵

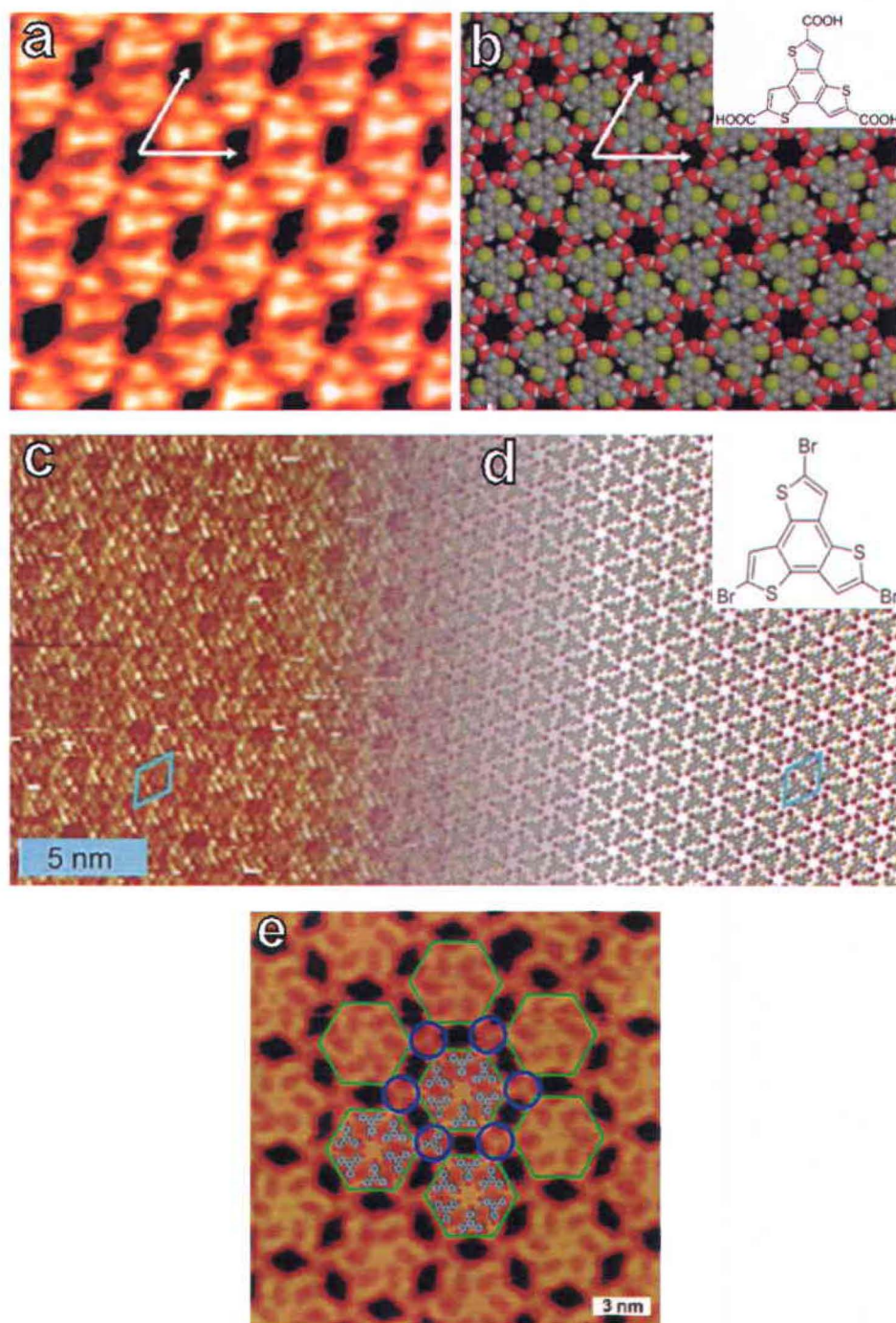


Figure 8.21: a) STM image and b) model of terthienobenzenetricarboxylic acid (TTBTA) molecules (inset) assembled at the heptanoic acid-HOPG interface. c) STM image and d) model of 2,5,8-tribromobenzo[1,2-*b*:3,4-*b'*:5,6-*b''*]trithiophene (inset) assembled at the TCB-HOPG interface. e) STM image of TBPB molecules assembled at the UHV-Ag(111) interface taken at 80 K. Hexameric synthons (grey hexagons) are linked between each other with a single TBPB molecule (blue circles). a),b) reproduced from ref. ¹⁹⁴, c),d) from ref. ¹⁹ and e) from ref. ¹⁴⁹.

The alignment of the molecular pattern along the <1-210> *zig-zag* directions of the substrate further corroborates the hypothesis of co-assembly of solvent molecules. In fact, this is consistent with a favorable adsorption geometry for each of the six heptanoic acid alkyl chains in each pore, if the chains are in a straight all-*trans* configuration¹⁹⁶ (*Groszek model*)¹⁹⁷ with the hydrogen atoms of the -CH₂- groups pointing down towards the center of the hexagons of the HOPG substrate (see Figure 8.20c). This is a phenomenon often observed for *n*-alkanes on graphite, thanks to the good registry between the alkyl chains (the -CH₂- groups have period of 2.51 Å) and the HOPG lattice (period of 2.46 Å along the zigzag directions).^{55, 198} In this configuration, in addition to lateral interactions at the hexameric hydrogen-bonded motif (d5 in Figure 8.20d, see discussion below), the co-adsorbed solvent molecules contribute to the stabilization of the system with relatively strong molecule...substrate interactions. TPD experiments have shown that the desorption barrier of straight-chain alkanes [H(CH₂)_NH, N = 5 – 60] from the surface of graphite has a nonlinear dependence on the chain length.¹⁹⁹ This surprising behavior is due to different mechanisms involved in the desorption of alkanes from graphite. The TPD data are well fit with the power law:

$$\Delta E_{des} = 29 - 42\sqrt{N} \text{ kJ/mol}, \quad 8.2$$

with *N* being the number of -CH₂- units in the alkyl chain. Therefore, neglecting the adsorption energy associated with the carboxylic group of the heptanoic acid molecules, equation 8.2 gives an adsorption energy of roughly -18 kcal/mol per solvent molecule.¹⁹⁹⁻²⁰⁰

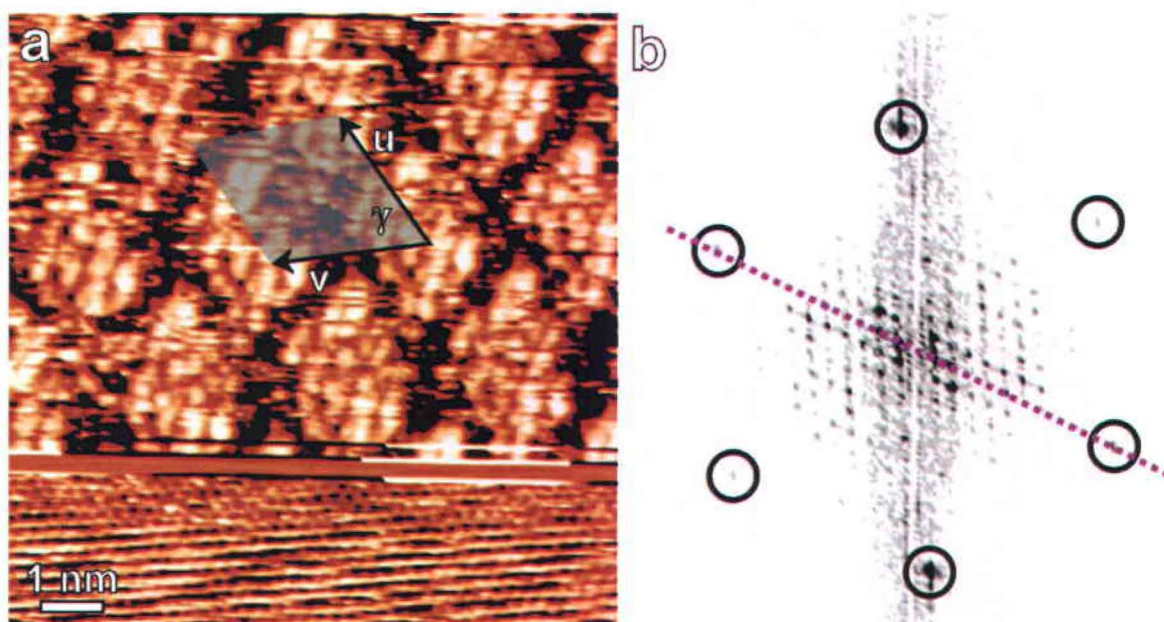


Figure 8.22: a) STM image showing TBPT molecules assembled at the heptanoic acid-HOPG interface (upper part) and the underlying graphite lattice with atomic resolution (lower part) ($9.8 \times 9.8 \text{ nm}^2$, $I_t = 57 \text{ pA}$, $V_s^{\text{HOPG}} = -0.02 \text{ V}$ and $V_s^{\text{SAMN}} = -1.89 \text{ V}$) and b) corresponding 2D-FFT. The spots of the HOPG lattice are highlighted by black circles, whereas the pink dotted line lies along one of the $\langle 10\text{--}10 \rangle$ armchair high-symmetry directions of graphite, which bisects the unit cell. The SAMN is rotated by an angle $\beta = 30 \pm 5^\circ$ with respect to the HOPG armchair directions, hence it is aligned along the zig-zag directions. The unit cell vectors are $u = v = 2.7 \pm 0.1 \text{ nm}$ and the angle between them is $\gamma = 60 \pm 5^\circ$.

Remarkably, Figure 8.20b clearly shows chirality within the TBPT-co-heptanoic acid SAMN, a phenomenon often observed in 2D molecular networks.^{194, 201-203} In this case, the chirality manifests itself through a counter-clockwise rotation of $13 \pm 5^\circ$ of TBPT molecules with respect to the center of the hexameric synthons (grey triangles in Figure 8.20b). Despite the intrinsic achirality of TBPT, enantiomorphism is introduced by the co-assembled prochiral $R_6^6(24)$ hexamers of heptanoic acid.

The alignment between the overlayer (C6 symmetric) and the substrate (C3 symmetric) is possibly due to the rotational commensurability between the two, which is consistent with the lack of moiré patterns in our experiments. Furthermore, the co-adsorption of solvent molecules along the zigzag directions necessarily implies also translational commensurability between the molecular overlayer and the substrate. As already mentioned above, the adlayer unit cell is aligned along the zigzag directions of the HOPG substrate, thus

the unit cell vectors must be expressed as integer multiples of the substrate periodicity along this direction (*i.e.* 0.246 nm). We find that only the integer number eleven gives a molecular unit cell that fits the experimental value within the uncertainty (*i.e.* $0.246 \cdot 11 = 2.706$ nm vs. 2.7 ± 0.1 nm).

Starting from the proposed bi-component geometry shown in Figure 8.20c, we performed gas-phase DFT-optimization of the molecular network. In the calculations we froze the atomic coordinates of the internal five carbon atoms of heptanoic acid chains and the molecular unit cell vectors to the value 2.706 nm, with angle between them of 60° . To some extent, these constraints allow the DFT calculations to account for the epitaxial matching with the substrate. Note that freezing the coordinates of the internal carbon atoms of solvent molecules is justified by the relatively strong molecule \cdots substrate interactions of *n*-alkanes on HOPG^{196, 198-200} (we left the 1 and 7 carbon atoms free to relax during the optimization to account for possible repulsions between the $-\text{CH}_3$ groups at the tails of heptanoic acid molecules and to achieve the optimal configuration of the hexameric hydrogen-bonded motif).

The optimization we performed did not converge to a value of forces gradient below the default threshold of the software used (Figure 8.23), however the configurations of the local minima still provide useful information (the lack of convergence is possibly due to the constraints imposed on the atomic coordinates of the solvent molecules, *e.g.* repulsion between the $-\text{CH}_3$ groups).

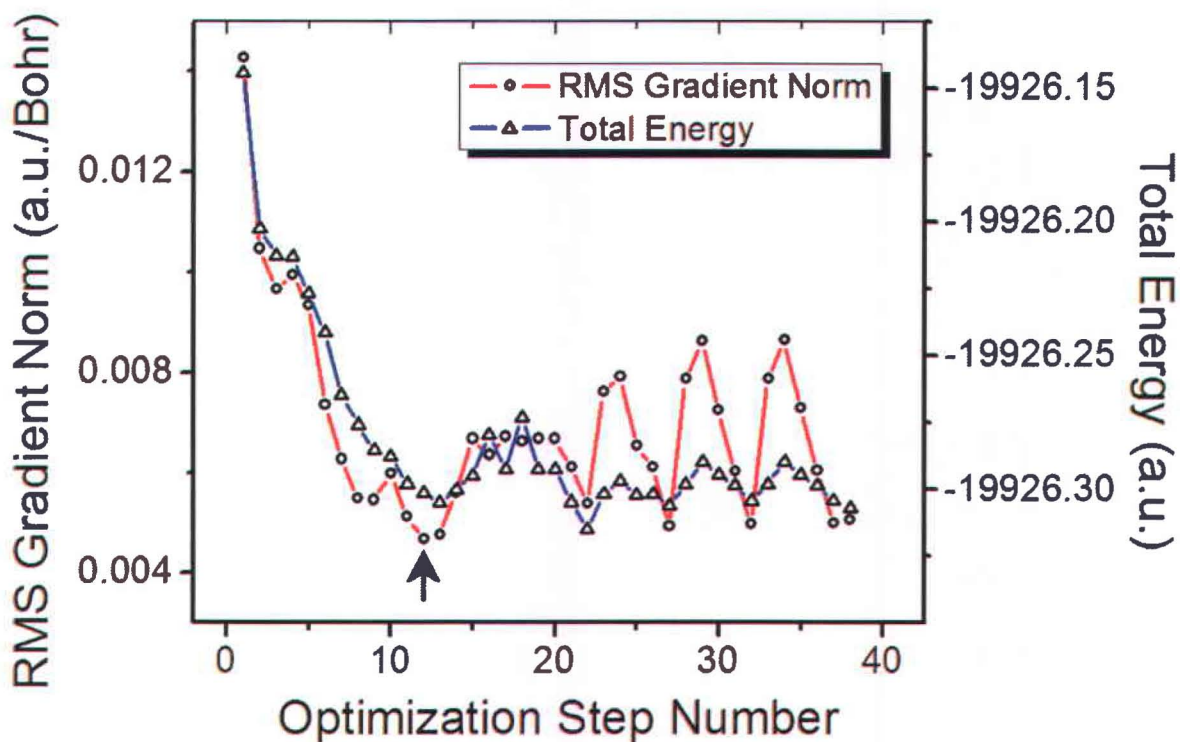


Figure 8.23: Plot of the forces gradient and total energy varying during the DFT optimization (M06-L/6-31G** level of theory) of the bi-component system TBPT + heptanoic acid. After the 15th iteration the optimized geometries oscillate around configurations of local minima. For the computational results of this system discussed in the MS we refer to the 12th iteration (black arrow), configuration with the lowest forces gradient (0.0047 a.u./Bohr vs. the Gaussian09 default threshold of 0.003 a.u./Bohr).

Our calculations show that the molecular network is laterally stabilized by hydrogen and halogen bonds. At the center of the pores made of TBPT molecules, heptanoic acid solvent molecules interact with attractive hydrogen bonds between their carboxylic groups, with intermolecular bond distances smaller than the sum of the vdW radii of hydrogen and oxygen ($r^O + r^H = 2.72 \text{ \AA}^{177}$ vs. $d_4 = 1.88 \text{ \AA}$ – Figure 8.20c and Table 8.6). Furthermore, each TBPT molecule, being surrounded by six solvent molecules, interacts with attractive halogen bonds between the positively charged tip of the bromine atoms and the nucleophilic oxygen atoms of the carboxylic groups of heptanoic acid molecules (d_3). Attractive $\text{Br} \cdots \text{H}$ interactions between TBPT and heptanoic acid molecules also stabilize the system (d_2). The computed net intermolecular binding energy of the bi-component SAMN is -74.3 kcal/mol (-0.510 eV/nm^2). Considering the value normalized per unit area it turns out that the bi-component system is 30% more stable than the structure in Figure 8.15. This is not only due to the larger

number of stabilizing interactions, but most importantly to the presence of considerably stronger hydrogen bonds (d4).

Table 8.6: Computed interatomic distances (see Figure 8.20d for labels) of the TBPT molecular network at the heptanoic acid-HOPG interface (M06-L/6-31G level of theory). Bold distances refer to intermolecular bonds shorter than the sum of the vdW radii of the atoms involved ($r^{\text{Br}} + r^{\text{H}} = 3.05 \text{ \AA}$, $r^{\text{Br}} + r^{\text{O}} = 3.37 \text{ \AA}$, $r^{\text{O}} + r^{\text{H}} = 2.72 \text{ \AA}$).¹⁷⁷**

d2 (Å)	d3 (Å)	d4 (Å)
Br...H	Br...O	O...H
3.28 – 3.83	3.83	1.88

The DFT calculations also provide some insight into the apparent chirality of the TBPT molecules in Figure 8.20a. STM images of 2,4,6-tris(2-pyridyl)-1,3,5-triazine (TPTZ) on Au(111), molecule with shape, size and symmetry similar to TBPT, display a similar intramolecular distortion, however in that case such effect is due to the intrinsic asymmetry of the pyridine side groups (Figure 8.24).²⁰⁴

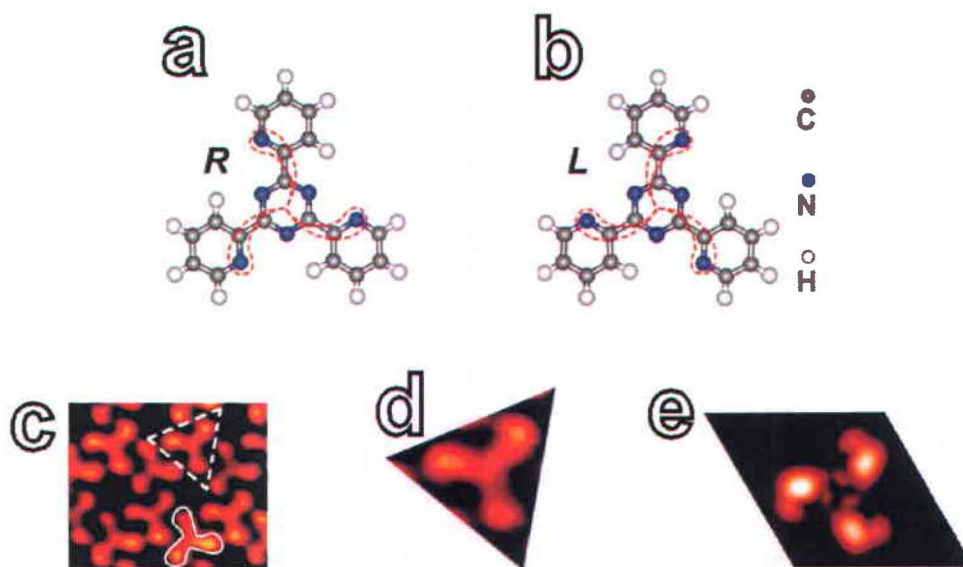


Figure 8.24: a),b) Schematic model of the two enantiomers of TPTZ. c) STM image of TPTZ molecules assembled at the UHV-Au(111) interface and magnified image of a molecule marked by the dashed triangle in c). e) Simulated STM image of a R-TPTZ molecule on Au(111) with a sample bias of 1.5 V at a constant height of 3 Å. Reproduced from ref. ²⁰⁴.

The contrast observed in Figure 8.20a suggests that the bromophenyl groups are rotated out-of-plane in such a way that their right side appears brighter (single-headed arrow in Figure 8.20b). Although in the gas phase TBPT molecules are most stable in the planar geometry (Figure 8.13), the DFT optimization of the bi-component system reported in Figure 8.20c confirms that the bromophenyl groups are indeed rotated out of plane, by an angle in the range $17 \pm 3^\circ$. This molecular distortion implies a destabilization of the system of roughly 1 kcal/mol per TBPT molecule (Figure 8.13), however it prevents unfavorable repulsive interactions between the hydrogen atoms of the bromophenyl groups and of the $-\text{CH}_2-$ groups of heptanoic acid molecules. The out-of-plane rotation of the side groups of TBPT molecules may contribute to the chiral contrast discussed above. For similar systems it has been shown that simulated STM images display a distortion similar to the one in Figure 8.20b when the functional groups are rotated off the mirror plane by specific angles with respect to the central core (Figure 8.25).¹⁵²

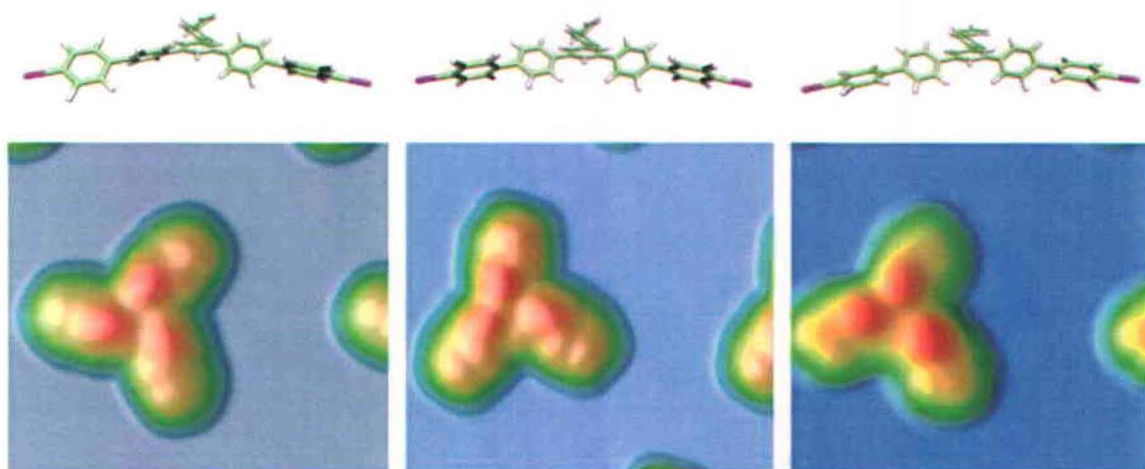


Figure 8.25: Simulated STM images (blue squares) indicate different apparent in-plane rotations by varying the molecular side groups out-of-plane rotation (reported on top of each square). Reproduced from ref. ¹⁵².

We also investigated the self-assembly process in the presence of guest molecules such as coronene and C_{60} . Considering that the cavities in Figure 8.20b are 1.7 nm in diameter, one coronene or multiple C_{60} molecules may be included into a single pore,¹⁹⁴ however no guest-stabilized networks were observed. In fact, in the experiments with guest

molecules we did not observe the assembly of Figure 8.20, this suggesting that the competition in the adsorption of different guest molecules, *i.e.* heptanoic acid vs. coronene or C₆₀, may in some way affect the stability of the SAMN and/or the kinetics of film formation. We also tried to blend different solvents (TCB+heptanoic acid, TCB+phenyloctane and heptanoic acid+phenyloctane), but no stable networks were found. The fact that the hexameric structure was only witnessed when TBPT was dissolved in heptanoic acid, but not when TIPT was, shows that the energetics involved in the stabilization of the SAMN *via* the possible coadsorption of solvent molecules is extremely subtle. We do not ascribe this to the different size of the halogen atoms, given that a difference in the vdW radii of bromine and iodine of merely 0.13 Å¹⁷⁷ is unlikely to be critical to the SAMN formation. Rather, the lateral interactions between heptanoic acid and TIPT within the overlayer may be unfavorable. For instance, the more positive σ -hole of iodine may lead to stronger repulsive forces between the halogens of TIPT molecules and the hydrogens of the heptanoic acid chains. This would require more pronounced rotations of the side groups, with consequent higher destabilization (Figure 8.13). Furthermore, different solvent effects may take place for the two halogenated precursors in solution (*e.g.* a stronger solvation enthalpy of TIPT in heptanoic acid may be unfavorable for self-assembly to occur).

8.3.4 TBPT ON Au(111)

In the experiments carried out on gold surfaces self-assembly was observed using solutions of much lower concentration, because of the higher reactivity of the substrate. This can be explained considering the gold and graphite electronic band structures. In the bulk, the valence and conduction bands of gold overlap, whereas in graphite they are separated by a small, yet finite, gap (40 meV). For these reasons, gold is regarded as a metal and graphite as a semimetal (and not as a semiconductor, whose band gaps are typically hundreds of meV). Therefore, given that in gold electrons are free to move from the valence to the conduction band and *vice versa*, they are “more prone” to interact with other systems, hence making gold more reactive than graphite. Note that these considerations refer to bulk materials, however they are also valid for surfaces (which is relevant for the experiments here reported). Note that surfaces are in principle more reactive than bulk materials (see Section 7.2). In fact, the concept of “reactivity” is typically associated with chemical reactions, which by definition take place at surfaces and not in the bulk.

By applying a sessile drop ($\approx 5 \mu\text{l}$) of a $5 \cdot 10^{-5}$ M solution of TBPT in phenyloctane onto a freshly cleaned gold substrate we observed the formation of molecular networks. The calibration of the data obtained on Au(111) was trickier than on HOPG due to the difficulties encountered in imaging the gold substrate with atomic resolution. For this reason we attempted to lattice correct the STM images using the contrast modulation associated with the $22 \times \sqrt{3}$ (herringbone) reconstruction of the underlying substrate (Figure 8.26a). With proper filtering, it is possible to suppress the contrast due to the molecular features and thus enhance that of the substrate periodicity. Once an image similar to the one in Figure 8.26b is obtained, it is possible to correct it to the known parameters of the $22 \times \sqrt{3}$ reconstruction of Au(111) – the period of the double ridge along the $[1-10]$ direction is of 6.3 nm.^{160, 205}

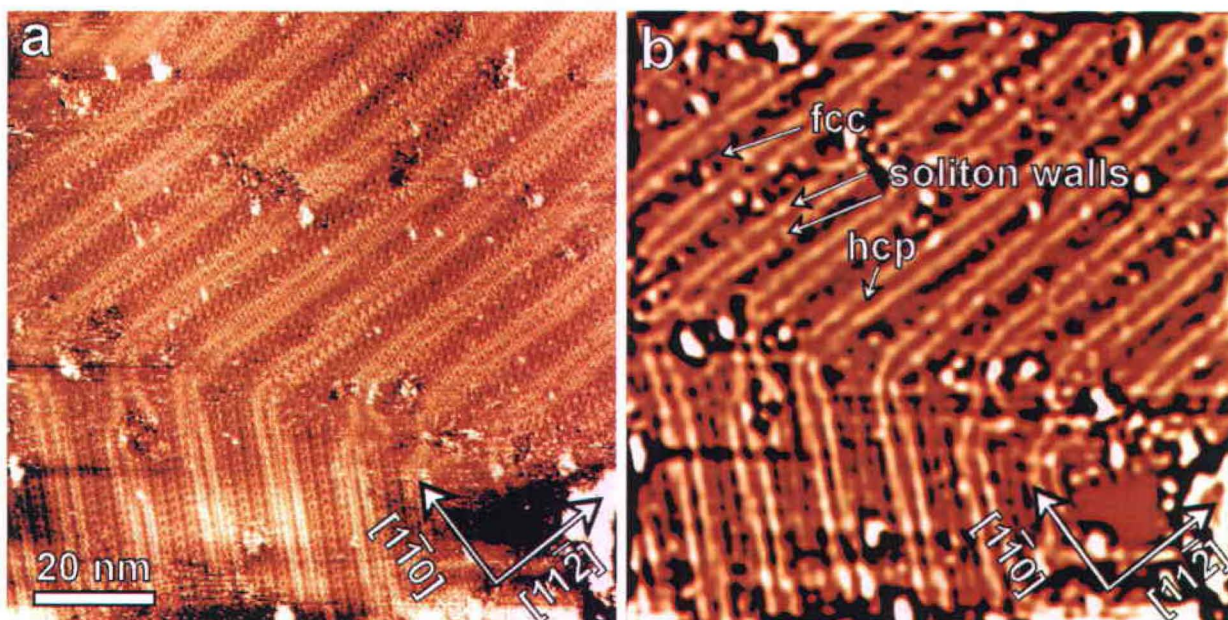


Figure 8.26: a) STM image of TBPT molecules assembled at the phenyloctane-Au(111) interface, showing the SAMN modulated by the underlying reconstructed surface ($100 \times 100 \text{ nm}^2$, $V_s = -0.40 \text{ V}$, $I_t = 200 \text{ pA}$); b) wavelet filtering of image a) enhancing the $22 \times \sqrt{3}$ reconstruction of the gold substrate underlying the adlayer. The features typical of the reconstructed Au(111) surface, *i.e* the *fcc*- and *hcp*-stacked regions as well as the soliton walls bridging them, are indicated by the arrows.

Experimentally, two molecules per unit cell were observed (see discussion below – Figure 8.31), however using the lattice correction to the $22 \times \sqrt{3}$ reconstruction produced unit cell dimensions too small to accommodate two intact TBPT molecules. One possible hypothesis is that the C–Br bonds of TBPT molecules were cleaved off upon adsorption on the gold surface (dotted circles in Figure 8.27), which can act as a catalyst for dehalogenation although for the similar system TBPB-Au(111) annealing at $200 \text{ }^\circ\text{C}$ is necessary to break the C–Br bonds.¹⁵¹ On the other hand, the C–I bonds of TIPB on Au(111) in vacuum are known break at room temperature¹⁵⁴, although for other systems temperatures as high as $300 \text{ }^\circ\text{C}$ have been reported²⁰⁶.

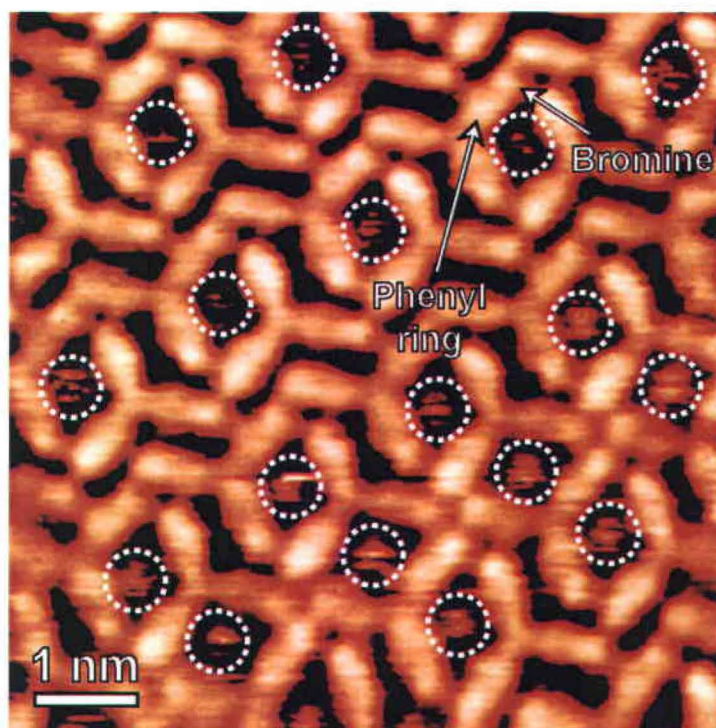


Figure 8.27: STM image of TBPT molecules assembled at the phenyloctane-Au(111) interface ($7.6 \times 7.6 \text{ nm}^2$, $V_s = +0.15 \text{ V}$ $I_t = 400 \text{ pA}$); dotted white circles highlight the bright protrusions possibly due to the bromine atoms cleaved from TBPT molecules and adsorbed on the Au(111) surface, whereas the arrows indicate the phenyl ring and the halogen atom of a sub-molecularly resolved TBPT molecule.

To address this issue we performed X-ray photoelectron spectroscopy (XPS) on the same sample. XPS was performed in a UHV chamber with base pressure of 10^{-9} torr, with a commercial system (VG ESCALab 200i) using a monochromated aluminum K_α source. The overall energy resolution in the high-resolution spectra was approximately 600 meV, using an analyzer pass energy of 20 eV. Prior to XPS experiments the samples were rinsed for one minute in a 2-propanol bath and left to dry in ambient conditions, followed by transfer into the UHV system. The XPS spectrum shows one doublet due to the spin orbit split 3d core level of bromine, whose components are centered at binding energies $BE_{\text{Br}}^{3d\ 5/2} = 69.9 \text{ eV}$ and $BE_{\text{Br}}^{3d\ 3/2} = 71.0 \text{ eV}$ (Figure 8.28). These peaks arise from intact C–Br bonds, given that chemisorbed Br atoms would exhibit considerably lower BE, thus excluding the hypothesis of dehalogenation of TBPT molecules at room temperature.^{86, 207}

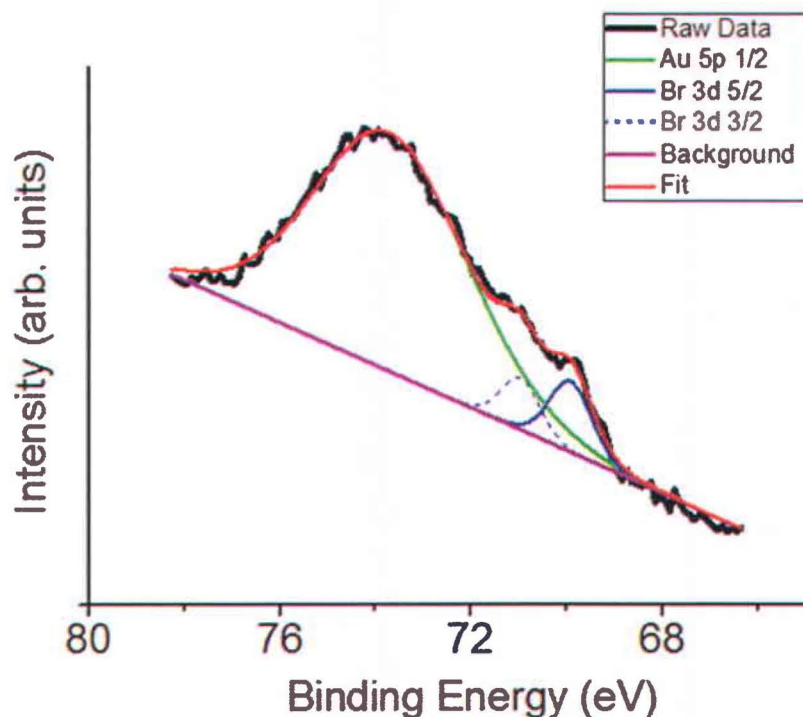


Figure 8.28: XPS spectrum of one monolayer of TBPT molecules assembled on Au(111).

Since the XPS investigation confirms the integrity of TBPT molecules upon adsorption on the gold substrate, we can infer that the parameters of typically reconstructed Au(111) surfaces employed to correct the micrograph in Figure 8.26a do not apply to our system. Although the filtered STM image in Figure 8.29b has features that resemble those of a typically reconstructed Au(111) surface, *i.e.* lines arranged in pairs orthogonal to $\langle 1-10 \rangle$ with characteristic 'elbows', we note that the herringbone periodicity along $\langle 1-10 \rangle$ before and after molecular adsorption is different. Figure 8.29a shows a STM image of the pristine Au(111) surface, whereas Figure 8.29b shows a version of the STM image in Figure 8.26a where frequencies related to the herringbone reconstruction have been enhanced through FFT filtering. These images demonstrate that the ratio between the width of the *fcc* regions (labeled B) and the *hcp* regions (labeled A) increases by approximately 25% upon molecular adsorption (Table 8.7), hence showing that the surface reconstruction is partially lifted as consequence of molecule-substrate interactions. Similar to the cases reported in the literature, only the *fcc* regions become wider after molecular adsorption, whereas the *hcp* regions stay constant (Table 8.7). Note that to compare the data before and after molecular

adsorption we assumed a similar lattice distortion in the two STM images shown in Figure 8.29, which is reasonable given that they were acquired during the same experiment. The specified uncertainties are due to the number of pixels of the STM image, however by assuming the parameters of the unperturbed reconstruction (Figure 8.29a) equal to those reported in the literature for pristine gold, from Table 8.7 one can estimate the uncertainty due to thermal drift and the piezoelectric response. The herringbone periodicity measured in the non-corrected STM image prior molecular deposition is 8.3 ± 0.3 nm, which is enlarged with respect to the value of 6.3 nm that is reported in the literature.¹⁶⁰ Therefore, by comparing the two values we can estimate that the experimental data overestimate distances and angles by approximately 32%.

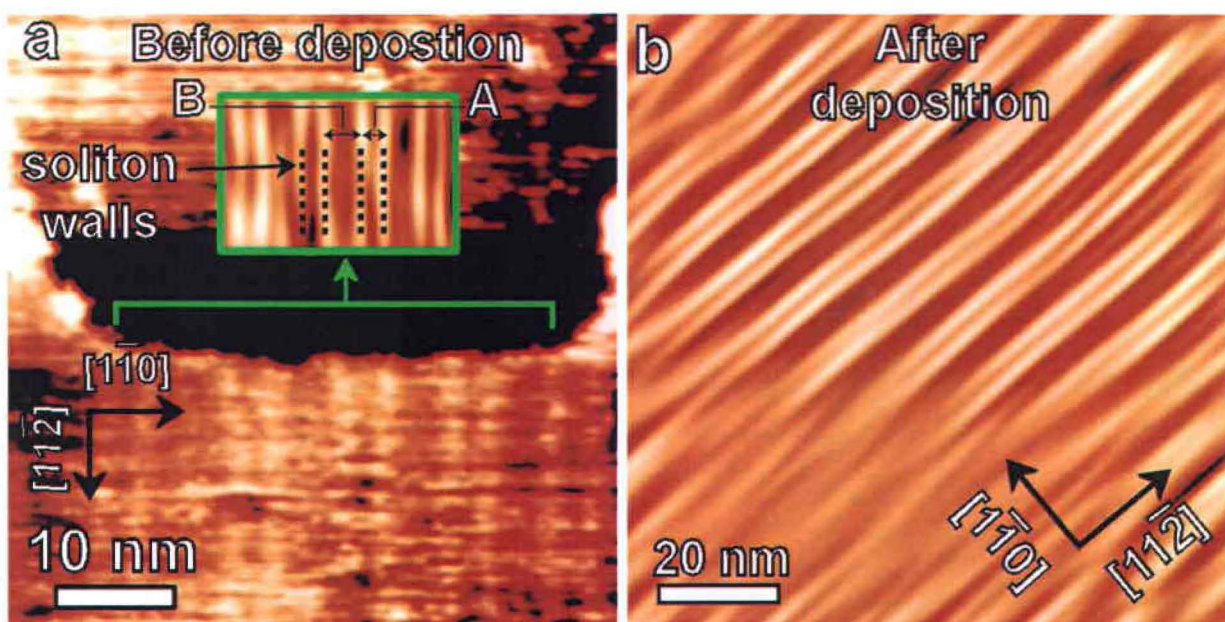


Figure 8.29: a) STM image of the clean reconstructed Au(111) surface prior deposition of TBPT molecules (47.3×47.3 nm², $V_s = -0.64$ V $I_t = 70$ pA). The inset is a FFT filtering of the STM image, with the *fcc* regions labeled B and the *hcp* regions labeled A. b) FFT filtering of the STM image in Figure 8.26a, enhancing the periodicity of the upper rotational domain of the herringbone reconstruction. The herringbone periodicity before and after molecular deposition is, respectively, 8.3 ± 0.3 nm and 9.7 ± 0.3 nm. Hence, molecular adsorption causes a partial lifting of the surface reconstruction, which enlarges by 17%.

Table 8.7: Width of the hcp regions (A), the fcc regions (B) and their ratio (B/A) for pristine gold as reported in the literature and for the experiments reported in this work before and after deposition (see Figure 8.29).

	A (nm)	B (nm)	B/A
<i>Pristine Gold Reported in the Literature</i>	2.20	4.10	1.86
This Work <u>Before Deposition</u>	3.17 ± 0.2	5.13 ± 0.2	1.62 ± 0.12
This Work <u>After Deposition</u>	3.20 ± 0.2	6.49 ± 0.2	2.03 ± 0.14

As a consequence of the partial reconstruction lifting we were not ultimately able to correct the STM data on gold from either thermal drift or any other distortion introduced by the piezoelectric motors of the instrument, hence all the measurements of distances or angles are affected by a large experimental uncertainty (on the order of 32%).

The partial lifting of the herringbone reconstruction has been observed for other molecular overlayers on Au(111),²⁰⁸⁻²¹² due to molecule-substrate interactions that cause gold atoms to be ejected from the surface, hence relieving the compression along [1–10] with consequent widening of the *fcc* regions (*i.e.* larger herringbone periodicity).⁵³ The widening of the herringbone periodicity can be directly related to the strength of the molecule-substrate interactions.²¹³⁻²¹⁶ Triphenylphosphine (PPh₃) molecules, for instance, produce an average herringbone separation 50% larger than pristine gold (Figure 8.30).²¹⁷ In this case the molecular building blocks in the SAMN interact with the gold atoms through the unshared electron pair of the phosphorous atom. This interaction is stronger than the π - π stacking expected for planar TBPT molecules on Au(111), in agreement with the narrower herringbone separation found for this system (17% vs. 50%).

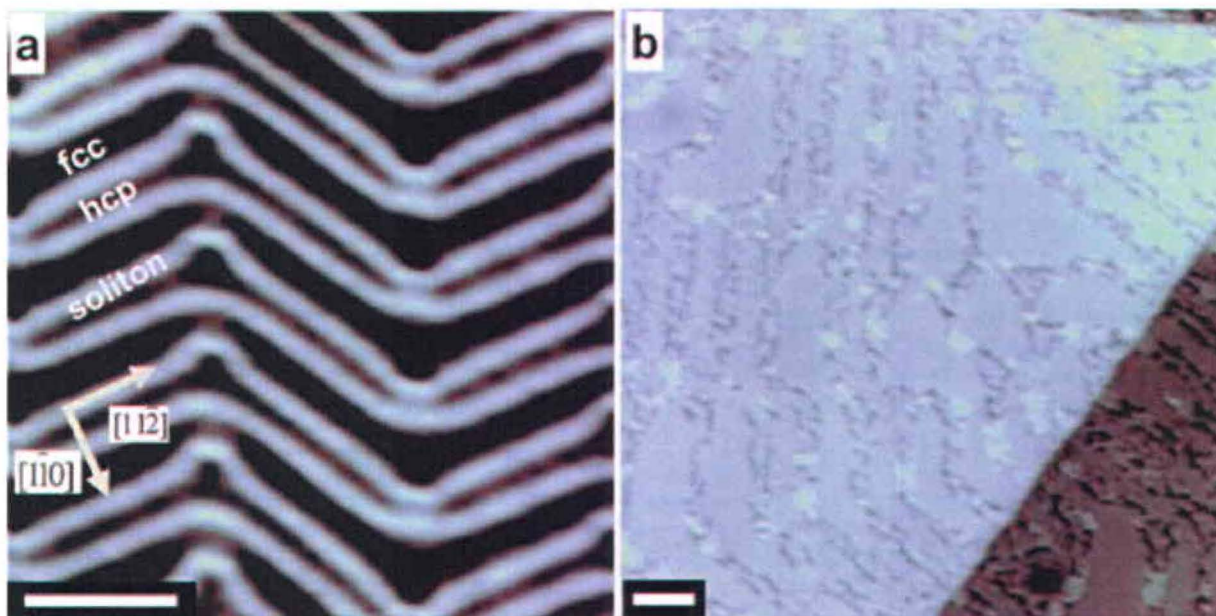


Figure 8.30: STM images of a) clean Au(111) and b) high-coverage PPh₃ on Au(111) after annealing at 220 K. The fcc, hcp, and soliton regions of the surface are indicated, as are the surface lattice vectors. b) The large-scale image shows that PPh₃ forms molecular domains confined by the soliton walls of the herringbone reconstruction. Scale bars = 10 nm. Reproduced from ref. ²¹⁷.

The TBPT molecular network formed at the solvent-Au(111) interface exhibits two phases, labeled α and β , made of rows of interdigitated TBPT molecules aligned just off the [11–2] herringbone direction (Figure 8.31a) – *i.e.* along the u vector in the α phase and the u' vector in the β phase. The u vectors are rotated by roughly 10° with respect to [11–2]. The molecular packing within each row of the two phases is the same, *i.e.* the u vector in the α phase and the u' vector in the β phase are equal. The main difference between the two phases is the relative molecular arrangement between neighboring rows: α phase has a (nearly) rectangular unit cell, whereas β phase has an oblique cell. This leads to different bonding motifs between neighboring rows in the two phases (see red and yellow circles of Figure 8.31a). In both phases TBPT molecules within each row are oriented parallel to the v direction of the α -phase unit cell (Figure 8.31a). A phase boundary exists along the v -vectors, where α and β polymorphs share one molecular row between the two different regions (cyan molecules with black contour in Figure 8.31a). The transition occurs *via* a sliding of the neighboring molecular row along the u directions. The v vector in the α phase and the v' vector in the β phase are rotated clockwise by $12 \pm 6^\circ$ and $26 \pm 6^\circ$, respectively, from [1–10]

(Figure 8.32). In contrast to the systems studied on HOPG, no 3-fold symmetric rotational domains were observed, probably due to the symmetry breaking associated with the reconstruction of the Au(111) surface.

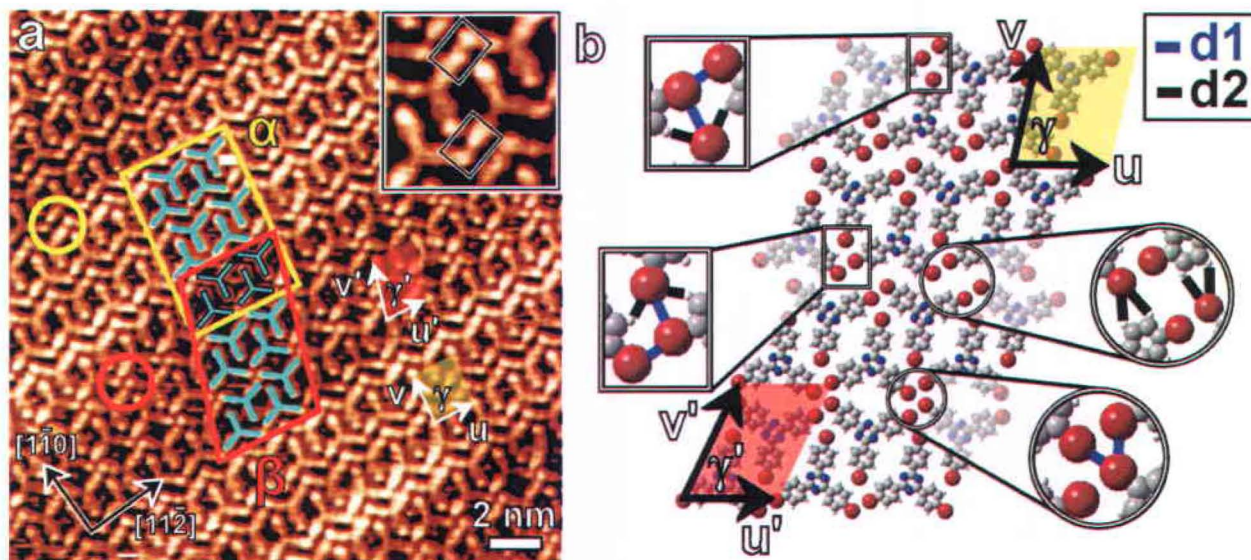


Figure 8.31: a) STM image of TBPT molecules assembled at the phenyloctane-Au(111) interface ($20.7 \times 20.7 \text{ nm}^2$, $V_s = +0.10 \text{ V}$, $I_t = 200 \text{ pA}$), showing the SAMN modulated by the reconstructed underlying substrate whose crystallographic directions are indicated by the black arrows. The α phase ($u = 1.7 \pm 0.2 \text{ nm}$, $v = 2.2 \pm 0.2 \text{ nm}$, $\gamma = 82 \pm 8^\circ$) is highlighted by the yellow rectangle while the β phase ($u' = 1.7 \pm 0.2 \text{ nm}$, $v' = 2.3 \pm 0.2 \text{ nm}$, $\gamma' = 72 \pm 8^\circ$) by the red rectangle. The two phases share one common molecular row (phase boundary), highlighted by the cyan molecules with black contour. The inset is a zoom of a high resolution STM image ($3.5 \times 3.5 \text{ nm}^2$, $V_s = +0.10 \text{ V}$, $I_t = 200 \text{ pA}$), with the black and white rectangles highlighting the closest contacts between the substituent end groups. The circles indicate the different bonding motifs in the two phases. b) DFT model of SAMN (M06-L/6-31G**); the two polymorphs were computed separately, constraining two intermolecular angles to account for the experimentally observed effect of the substrate (yellow and red circles superimposed to TBPT molecules). Rectangles and circles highlight intermolecular interactions within each row and between neighboring rows, respectively.

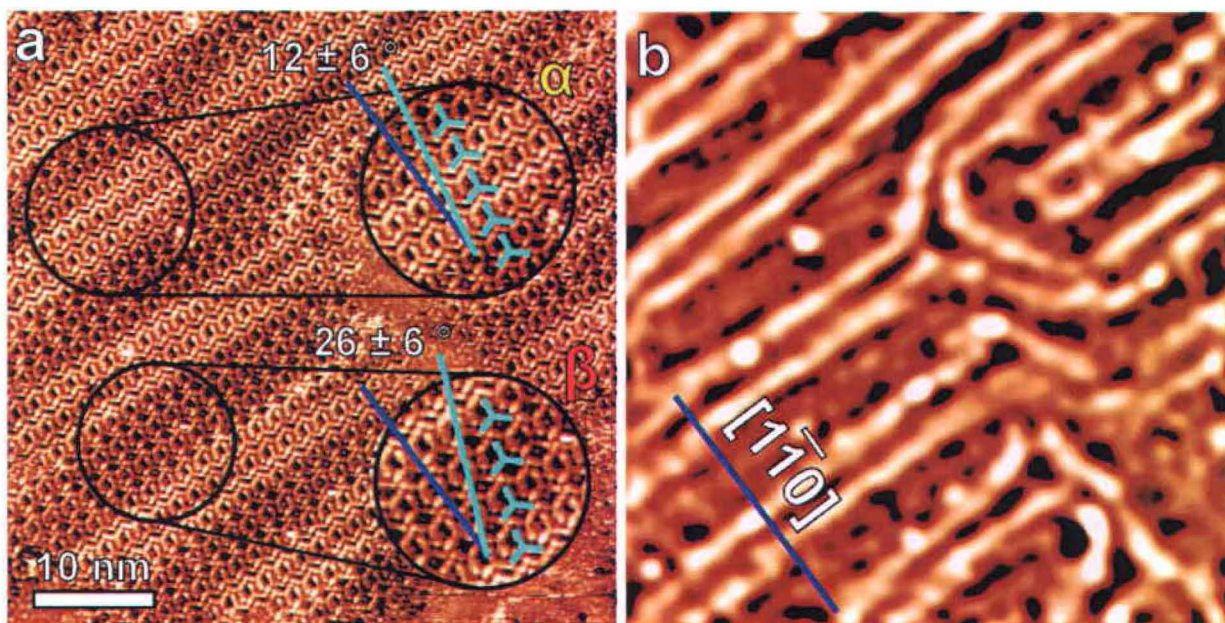


Figure 8.32: a) STM image of TBPT molecules assembled at the phenyloctane-Au(111) interface, showing the SAMN modulated by the underlying reconstructed surface ($50 \times 50 \text{ nm}^2$, $V_s = -0.10 \text{ V}$, $I_t = 200 \text{ pA}$); b) wavelet filtering of image a) enhancing the reconstruction of the gold substrate underlying the adlayer. The blue line in a) and b) indicates the $[1\bar{1}0]$ direction of the substrate. The v vector in the α and β phases is rotated CW by $12 \pm 6^\circ$ and $26 \pm 6^\circ$, respectively, with respect to the $[1\bar{1}0]$ crystallographic direction of the substrate.

Even though we could not rigorously lattice-correct the STM data, high-resolution micrographs provide insights into the molecular configuration. Unit cell vectors of the SAMN in both the α and β phase were obtained as averages over several STM images. Starting from these we performed gas-phase DFT calculations with PBCs. DFT optimization of the two TBPT polymorphs on Au(111) show that the intermolecular binding motifs experimentally observed (Figure 8.33a,b) are not properly reproduced if no constraints are applied (Figure 8.33c,d). For this reason we computed the α polymorph constraining all the intermolecular angles, allowing the unit cell parameters to relax (Figure 8.33e). Starting from this geometry we computed the β polymorph, constraining the intermolecular angles and the u -vector length, given the similarity between the two phases – Figure 8.33f. The unit cell parameters of the computed geometries are reported in Table 8.8.

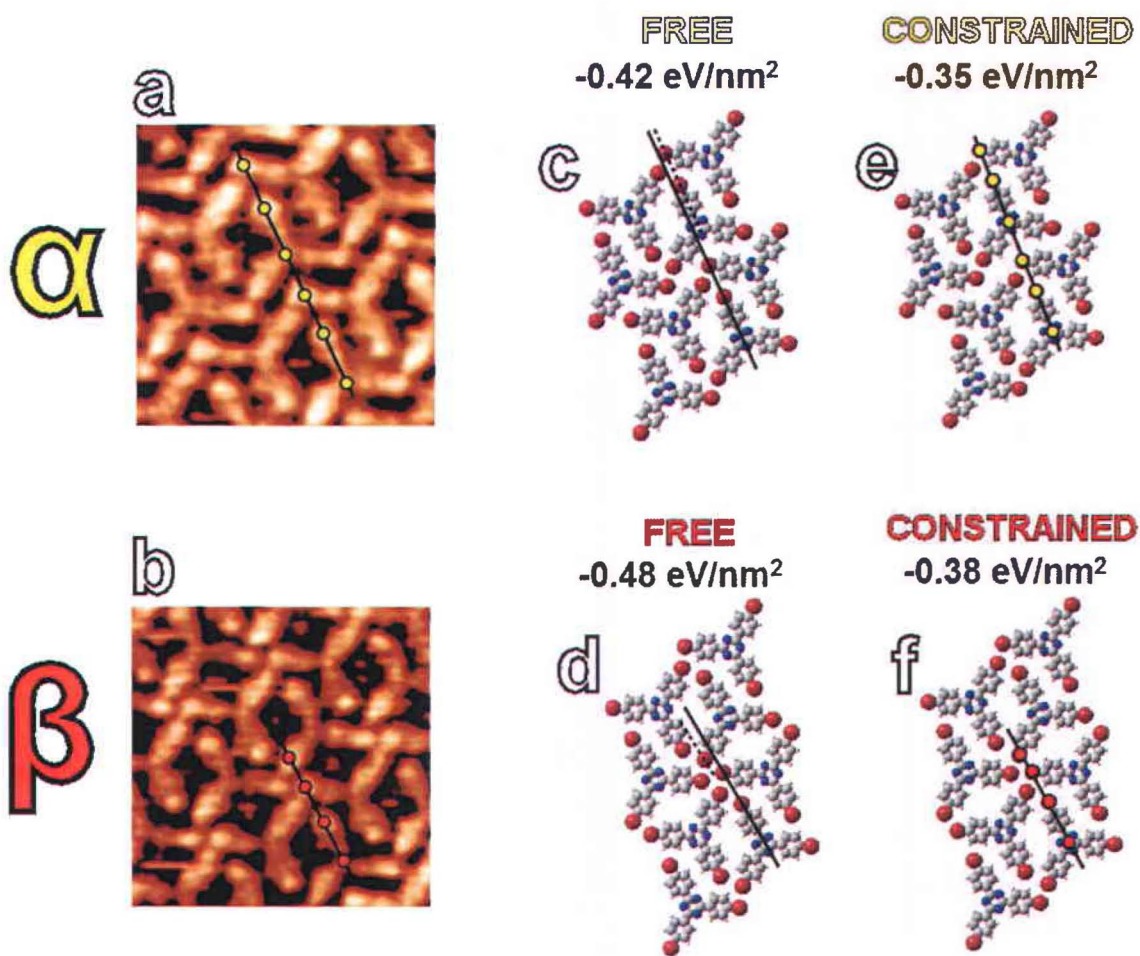


Figure 8.33: Zoomed regions of STM images containing a) the α and b) β TBPT polymorphs on Au(111). DFT optimized geometries c),d) without and e),f) with constraints.

Table 8.8: Experimental and computed unit cell parameters and energy (see Figure 8.33 for labels).

	u (nm)	v (nm)	γ (°)	Energy (kcal/mol)
α^{EXP}	1.7 ± 0.2	2.2 ± 0.2	82 ± 8	N/A
α^{FREE}	1.53	1.94	77	-27.8
$\alpha^{\text{CONSTRAINED}}$	1.54	1.98	78	-24.0
β^{EXP}	1.7 ± 0.2	2.3 ± 0.2	72 ± 8	N/A
β^{FREE}	1.51	2.10	66	-32.2
$\beta^{\text{CONSTRAINED}}$	1.54	2.14	65	-25.9

DFT calculations confirm a favorable configuration for hydrogen and halogen bonding, for both phases. All the three bromine atoms are involved in attractive interactions through electrostatic $\text{-Br}\cdots\text{Br-}$ and/or $\text{-Br}\cdots\text{H-}$ contacts (Figure 8.31b).

Table 8.9: Experimental and computed unit cell parameters and computed interatomic distances (see Figure 8.31b for labels) of the α and β phase in the TBPT molecular network at the phenyloctane-Au(111) interface – M06-L/6-31G** level of theory.¹⁷⁷

	u (nm)	v (nm)	γ (°)	Intra-row contacts		Inter-row contacts		Energy (kcal/mol)
				d1 (Å) Br \cdots Br	d2 (Å) Br \cdots H	d1 (Å) Br \cdots Br	d2 (Å) Br \cdots H	
α EXP	1.7 \pm 0.2	2.2 \pm 0.2	82 \pm 8	N/A	N/A	N/A	N/A	N/A
α DFT	1.54	1.98	78	3.40 – 3.88	2.71 – 2.96	N/A	3.62 – 3.77	-24.0
β EXP	1.7 \pm 0.2	2.3 \pm 0.2	72 \pm 8	N/A	N/A	N/A	N/A	N/A
β DFT	1.54	2.14	65	3.32 – 4.26	2.74 – 3.00	3.52 – 3.54	N/A	-25.9

For the α and β phase, a net intermolecular binding energy per unit cell of -24.0 kcal/mol (*i.e.* -0.35 eV/nm²) and -25.9 kcal/mol (*i.e.* -0.38 eV/nm²) was found, respectively. These values are similar to the energy found for TBPT assembly on graphite (Table 8.4). The intermolecular bonds within each row are similar in the two phases (see rectangles in Figure 8.31b and *intra-row contacts* in Table 8.9), hence the difference between the binding energies in the two phases is ascribed to the larger number of intermolecular bonds between neighboring rows in the α phase (see circles in Figure 8.31b and *inter-row contacts* in Table 8.9).

Figure 8.35 shows the network of assembled TBPT molecules (schematically drawn as cyan tripods) with contrast modulated in bright and dark stripes by the reconstructed underlying gold surface. While the α phase (yellow lines) is only observed on the *hcp*-stacked zones (*i.e.* on the wide, bright stripes), the β phase (red lines) is found only on the *fcc*-stacked zones (*i.e.* on the dark stripes). The implication from Figure 8.35 is that the two different polymorphs occur as a consequence of substrate effects, and in particular the difference

between the *fcc*- and *hcp*-stacked regions. The two differently stacked areas of the reconstructed substrate have the same lattice constant and symmetry. In other words, the molecular packing cannot be attributed to a lattice mismatch, but must instead arise from the difference in surface potential resulting from the different stacking structure of the topmost atomic layers in the *fcc* and *hcp* regions. The similar system TBPB-Au(111) also exhibits different polymorphs, however in that case no sensitivity to the reconstructed surface was observed.¹⁵¹ The different polymorphs were not a direct consequence of a template effect but merely distinct phases (Figure 8.35).

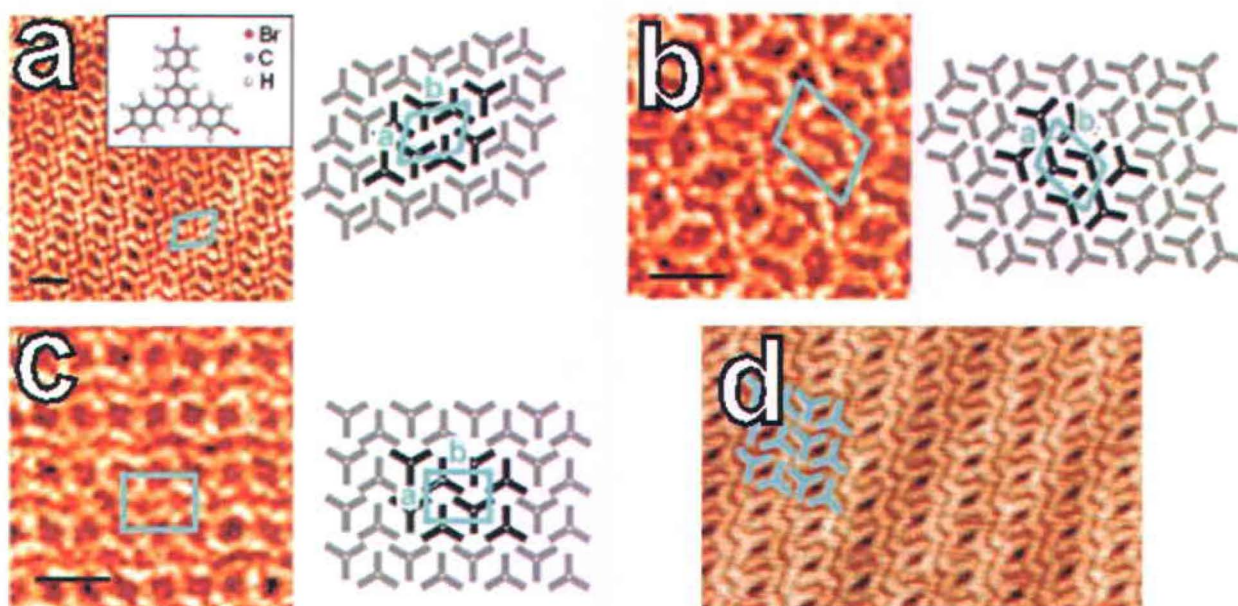


Figure 8.34: STM images of a)-c) three different phases of TBPB molecules (inset) at the liquid-Au(111) interface and d) at the UHV-Au(111) interface. The molecular layers are not sensitive to the *fcc* and *hcp* regions of the substrate. Reproduced from a)-c) ref.¹⁵¹ and d) ref.¹⁵⁰.

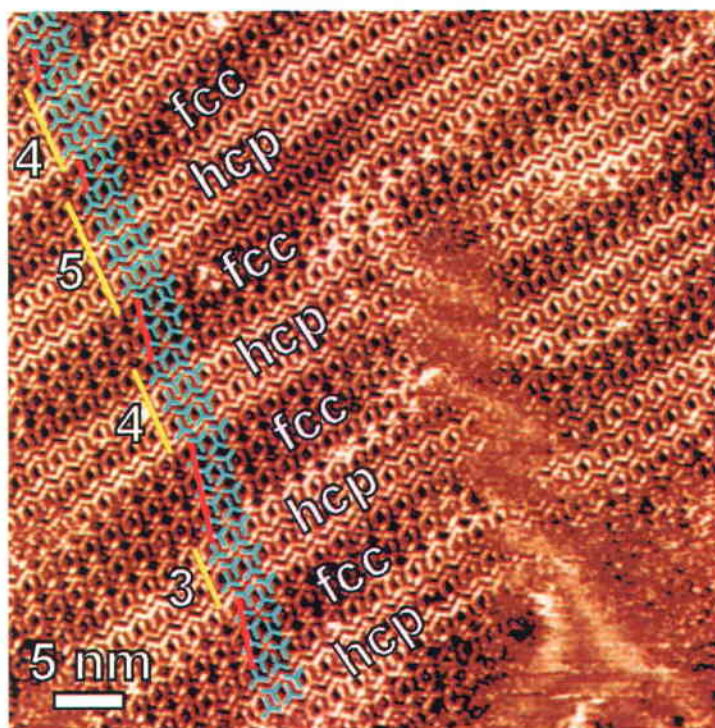


Figure 8.35. STM image of TBPT molecules assembled at the phenyloctane-Au(111) interface ($50 \times 50 \text{ nm}^2$, $V_s = +0.10 \text{ V}$, $I_t = 200 \text{ pA}$), showing the SAMN modulated by the reconstructed underlying substrate with TBPT molecules superimposed (cyan tripods) to highlight the α (yellow lines) and β phase (red lines) occurring in the assembly process. The labels on the right indicate different stacking structures of the underlying gold substrate as a consequence of the 4.34% compression of the topmost atomic layer along $[1-10]$.¹⁶³ The numbers on the left of the yellow lines indicate how many molecular rows are present in sets of aligned TBPT rows in the α phase. Each set of molecular rows (yellow lines) share one molecular row with the two neighboring phases, hence neglecting the shared phase boundaries the actual number of molecular rows would be the one reported minus two.

In addition, Figure 8.35 shows that the number of molecular rows in the α and β phase of the SAMN (numbers on the left) does not follow a recursive periodicity, at least not on the scale of this image ($\approx 50 \text{ nm}$). We attribute this to the fact that phase boundaries do not occur exactly at the faulted soliton walls (see below), whose size is comparable to that of the molecular unit cell.

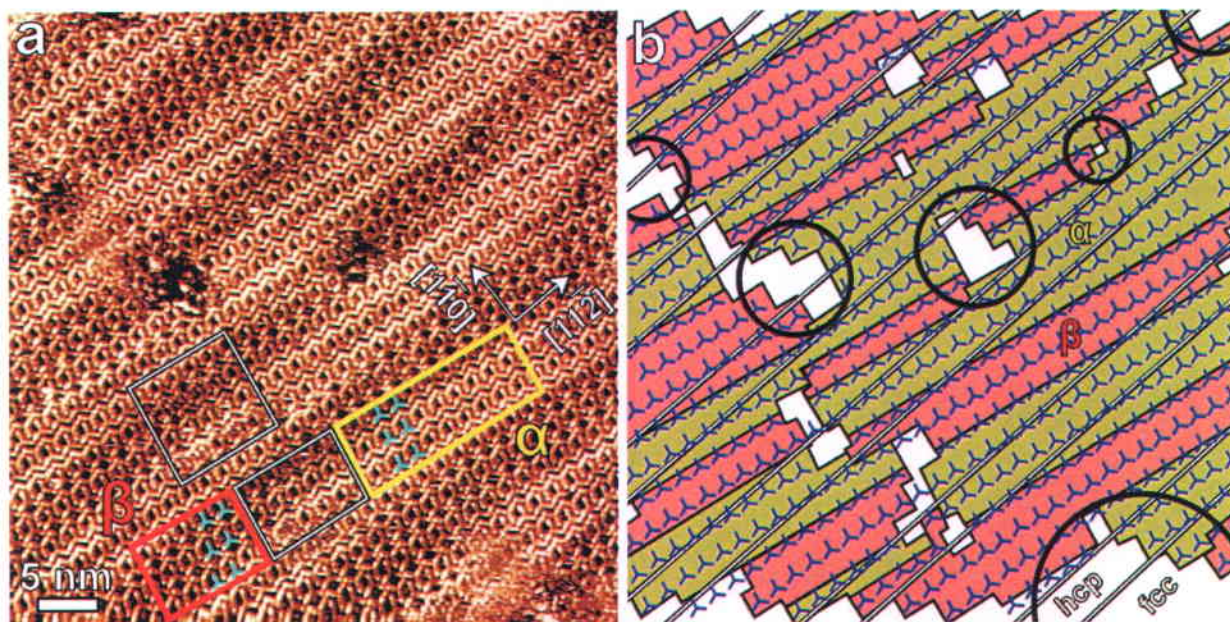


Figure 8.36. a) STM image of TBPT molecules assembled at the phenyloctane-Au(111) interface ($50 \times 50 \text{ nm}^2$, $V_s = +0.10 \text{ V}$, $I_t = 200 \text{ pA}$), showing the SAMN modulated by the reconstructed underlying substrate whose crystallographic directions are indicated by the black and white arrows. Cyan TBPT molecules have been superimposed on the micrograph to highlight the α (yellow rectangle) and β phase (red rectangle) occurring in the assembly process. The angle between $[1\bar{1}-2]$ and that aligned along the rows of TBPT molecules (*i.e.* the u vector in the α phase and the u' vector in the β phase) measured in the non-corrected image is approximately 10° . b) α (yellow) and β (red) domains of image a) with respect to the reconstructed Au(111) surface, whose faulted soliton walls are indicated by solid black and white lines. In this diagram, half of each shared molecular rows has been assigned to the α phase and the other half to the β phase. White regions indicate defective areas of the SAMN (the regions circled in black are due to defects of the underlying gold substrate rather than to the transition between two different phases).

Figure 8.36a allows us to infer that the transition between the α and β phase does not occur sharply at the bridges between the *fcc*- and *hcp*-stacked regions of the gold substrate. Instead, molecules in the α (β) phase can be observed to extend for a small distance onto the darkly (brightly) modulated stripes of the micrograph, in some cases for more than one unit cell. Larger β phase domains of TBPT molecules are expected both in terms of lateral stabilization energy (larger net BE) and because the *fcc* regions of the reconstructed Au(111) surface, which host the β phase, are wider than the *hcp* regions. However, Figure 8.36b shows that instead the area of α domains is 20% larger than the β domains. This can be ascribed to stronger molecule...substrate interactions of TBPT molecules on *hcp* regions of the substrate,¹⁶³ where the α phase is stable. Under this hypothesis TBPT molecules would have a higher adsorption probability on *hcp* regions in the very early stages of film growth,

which in turn leads to larger α domains. Moreover, Figure 8.36b suggests that the molecular overlayer grows with the Volmer-Weber mechanism, namely with the formation of islands at low coverage on *fcc* and *hcp* regions of the substrate up to one single monolayer. In the case of TBPT on Au(111), in the early stages of film growth α and β domains nucleate on *hcp* and *fcc* regions of the reconstructed Au(111) surface, respectively. The film growth proceeds as more molecules from the solution adsorb at the edges of the domains, expanding until they encounter unfavorable regions of the substrate. This “patchwork” growth leads to domain boundaries along the v vectors of the unit cells (Figure 8.31a), as well as along the u vectors. These are defective regions of the molecular network, where single TBPT molecules are not clearly resolved with the STM (black and white rectangles in Figure 8.36a and white regions in Figure 8.36b).

Previous work has shown that TPTZ molecules, which, like TBPT, have a triazine core, 3-fold symmetry, and similar size and aryl side groups, tend to adsorb with the triazine core and side groups (referred to as lobes) on *hollow sites* of the Au(111) surface (Figure 8.37).²⁰⁴ Similarly, for halo-benzenes on Au(111) the most favorable adsorption site is with the aryl ring on a hollow site.²¹⁸⁻²¹⁹ By assuming a similar behavior for TBPT molecules it is possible to infer the adsorption site of TBPT molecules on Au(111). Geometrical considerations indicate that favorable adsorption configurations of TBPT on Au(111), *i.e.* with core and lobes on hollow sites, are achieved for specific rotations of the molecule with respect to the substrate (Figure 8.37). As already mentioned above, in the TBPT network on Au(111) all the molecules in both phases are aligned parallel to the v vector of the α phase, which is rotated by $12 \pm 6^\circ$ clockwise with respect to $[1-10]$ (see Figure 8.38c and Figure 8.32). One of the two molecules in the unit cell (labeled Y) of both phases has one lobe pointing toward this direction, in agreement with the 10° rotation predicted by geometrical considerations (Figure 8.37). The other molecule in the unit cell (Z) is rotated in both phases by 180° with respect to Y, a configuration that also puts the lobes on hollow sites of the substrate (see Figure 8.38c and Figure 8.37). These considerations indicate, therefore, that the two molecules in the unit cell of both phases of the TBPT network on Au(111) can adsorb with the stable configurations reported for TPTZ, namely with core and lobes on hollow sites of the Au(111) surface. Note that given its molecular structure, when the core of TBPT molecules is adsorbed on *fcc* (*hcp*) hollow sites of Au(111), the molecular lobes are adsorbed on *hcp* (*fcc*) sites.

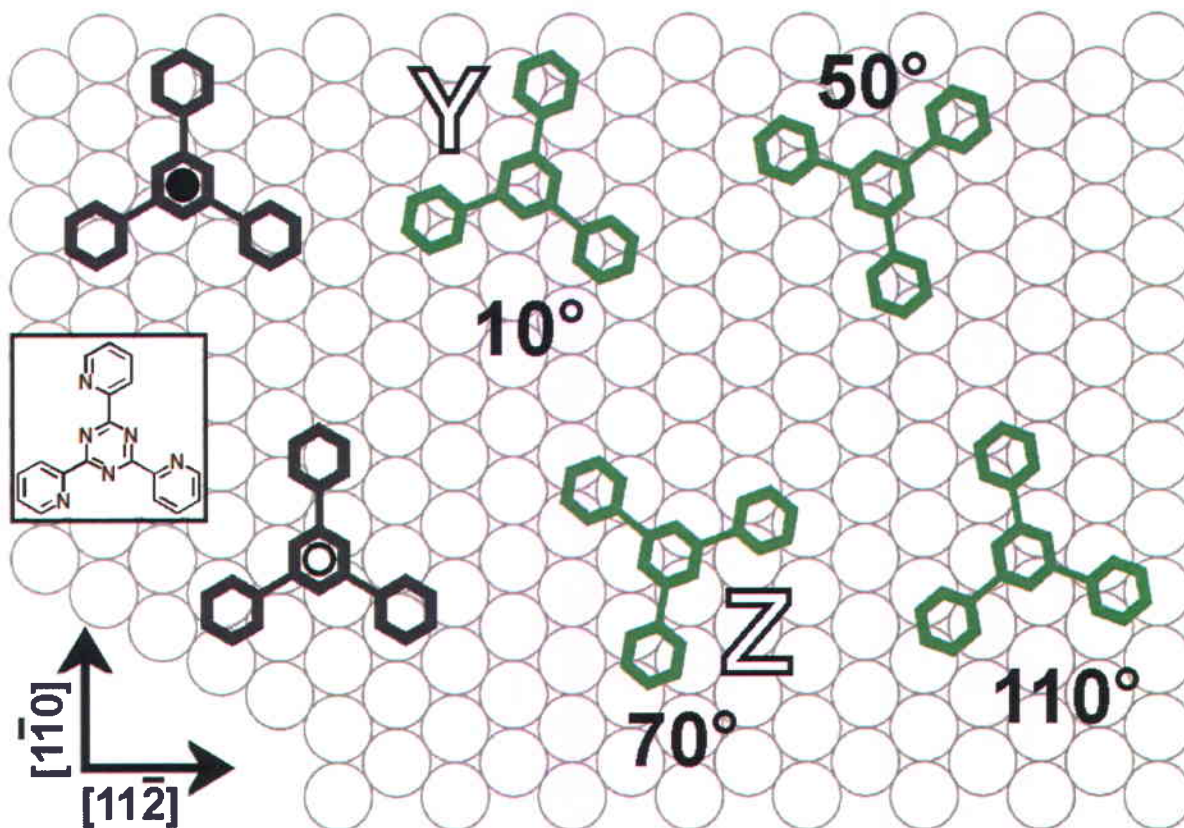


Figure 8.37: Theoretical calculations have shown that the most stable adsorption configuration of TPTZ (inset) on a fcc Au(111) surface is with the triazine core and molecular side groups on hollow sites.²⁰⁴ Such configurations are achieved for specific rotations of the molecular side groups with respect to the substrate. White and black circles indicate different hollow sites (we do not specify here the type of hollow site). Note that when the core is adsorbed on an fcc hollow site the aryl side groups are adsorbed on a hcp site (and *vice versa*). Labels Y and Z indicate the molecular configurations observed for TBPT on Au(111) – see Figure 8.38.

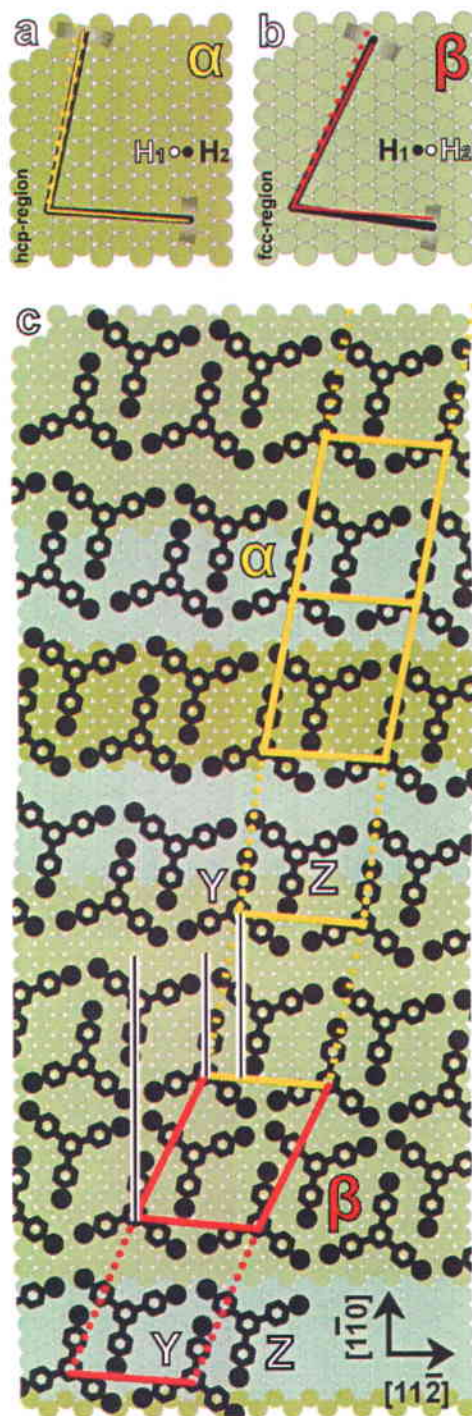


Figure 8.38. a),b) Experimentally determined unit cell vectors (solid black lines) with the experimental uncertainty (semitransparent regions). The unit cell vectors that account for an adlayer commensurate with the substrate (solid, dashed and dotted red and yellow lines) are within the experimental uncertainty (yellow vectors are for the α phase and red vectors for the β phase). The two types of hollow sites of the top layer are represented by white and black circles (fcc vs. hcp sites depend on how the three top layers of the gold crystal are stacked with respect to each other). In the fcc and hcp regions of the substrate the type of hollow sites is inverted. c) Model in scale of the TBPT network on gold

featuring the two phases on the different regions of the substrate (whose crystallographic directions are indicated by the black arrows). In reference to the text, the two molecules Y and Z per unit cell are also indicated. In the model, the lattice constant of the substrate in the unfaulted wider fcc (darker green atoms) and narrower hcp regions (brighter green atoms) is equal to that in the bulk (2.88 Å). In the soliton walls (light blue atoms), six gold atoms were “squeezed” and shifted along [11–2] to account for the $22\times\sqrt{3}$ herringbone reconstruction. TBPT molecules are drawn in scale with the substrate, with intramolecular distances obtained from gas-phase DFT optimization (Figure 6.1). The aryl rings are drawn as hexagons with dimensionless atoms, whereas the bromine atoms are drawn with size equal to 80% of their actual vdW radius.

Figure 8.38c shows the top layer of the reconstructed Au(111) surface with the two phases of the TBPT network (yellow and red unit cells). Our model demonstrates that if Y and Z molecules always adsorb on hollow sites, the (longer) *v*-vectors in both phases vary slightly within the adlayer (dotted and dashed vs. solid vectors of Figure 8.38). These slight variations would not be evident in the experimental data because they are smaller than the resolution of STM. Two kinds of hollow sites can be distinguished in close-packed (111) surfaces. Fcc- and hcp-hollow sites sit on a hollow and top site of the second layer, respectively. In Figure 8.38 these two kinds of hollow sites are found along [11–2] (H1 and H2). In this model the Y and Z molecules in each unit cell of the β phase (fcc regions of the substrate) are adsorbed with the triazine core on a H2 and H1 hollow site, respectively. In the α phase (hcp regions of the substrate) Y and Z are still respectively adsorbed on H2 and H1 sites, however given the different fcc and hcp stacking structures of the substrate these two types of hollow sites are inverted (namely, if in the fcc regions of the substrate H1 is a fcc (white) and H2 a hcp (black) hollow site, in the hcp regions they are a hcp (black) and fcc (white) site, respectively – Figure 8.38a,b). According to our model, therefore, TBPT molecules adsorb with the triazine core either on fcc or hcp hollow sites, as long as the molecular orientation allows the side groups to be adsorbed on hcp or fcc hollow sites, respectively. This is consistent with calculations of TPTZ on Au(111), which, for molecular configurations with core and lobes on hollow sites, indicate similar adsorption energy regardless the type of adsorption site for the triazine core.²⁰⁴ However, the relative coverage of α and β domains in Figure 8.36b suggests that the adsorption energy is higher in *hcp* regions. It is also conceivable that if Y and Z in the β phase (fcc regions) are adsorbed on H2 and H1 sites, respectively, in the α phase (*hcp* regions) they shift to H₁ and H2 hollow sites, in order to keep the same kind of adsorption site. However, we exclude this hypothesis because it would imply that TBPT molecules in one of the two

domains would no longer have the aryl side groups adsorbed on hollow sites, which is a less favorable adsorption configuration.²⁰⁴

The model in Figure 8.38c indicates that for both phases, the Y and Z molecules adsorb on the H2 and H1 sites, respectively, however the nature of the adsorption hollow site changes because of the different stacking structure of the substrate in *fcc* and *hcp* regions. However, such model does not explain the presence of the two phases, i.e. the shifting along the *u*-vector of the unit cells (see vertical black and white lines in Figure 8.38c). The simple model presented in Figure 8.38c is based only on considerations of molecular adsorption sites on *fcc* and *hcp* regions, hence neglecting other phenomena that may occur at the soliton walls. For instance, the relative shift of the two phases may be influenced by anisotropic standing waves in the Fermi-level surface-state electron density, which are particularly enhanced along the pairwise soliton walls (Figure 8.39a).²²⁰⁻²²¹ Furthermore, the long-range herringbone reconstruction acts as a superlattice for surface-state electrons, which in turns affects the band structure of the Au(111) surface and leads to higher density of low-energy electrons in *hcp* regions and of higher energy electrons in *fcc* regions (Figure 8.39c,d).²²²⁻²²³ Furthermore, molecular adsorbates are known to perturb the electronic potential of surfaces,²²⁴⁻²²⁵ even in cases of weak molecule-substrate interactions.²²⁶ When molecule-substrate interactions are strong enough they can change the substrate geometry and lead to surface reconstruction.²²⁷ Such substrate-mediated interactions can drive pattern formation with intermolecular interactions mediated by the molecular perturbation of the surface.²²⁵ A typical example of this effect is that observed for benzene molecules adsorbed at step edges of Cu(111) surfaces, which perturb the electronic structure of the adjacent terrace providing adsorption sites for additional molecular rows (Figure 8.39b).²²⁸ Therefore, the occurrence of two phases in the TBPT network on reconstructed Au(111), which cannot be addressed considering only the molecular adsorption site, may be due to different intermolecular interactions dictated by the different molecular perturbation of the surface potential in *fcc* and *hcp* regions of the substrate, as well as at the soliton walls.

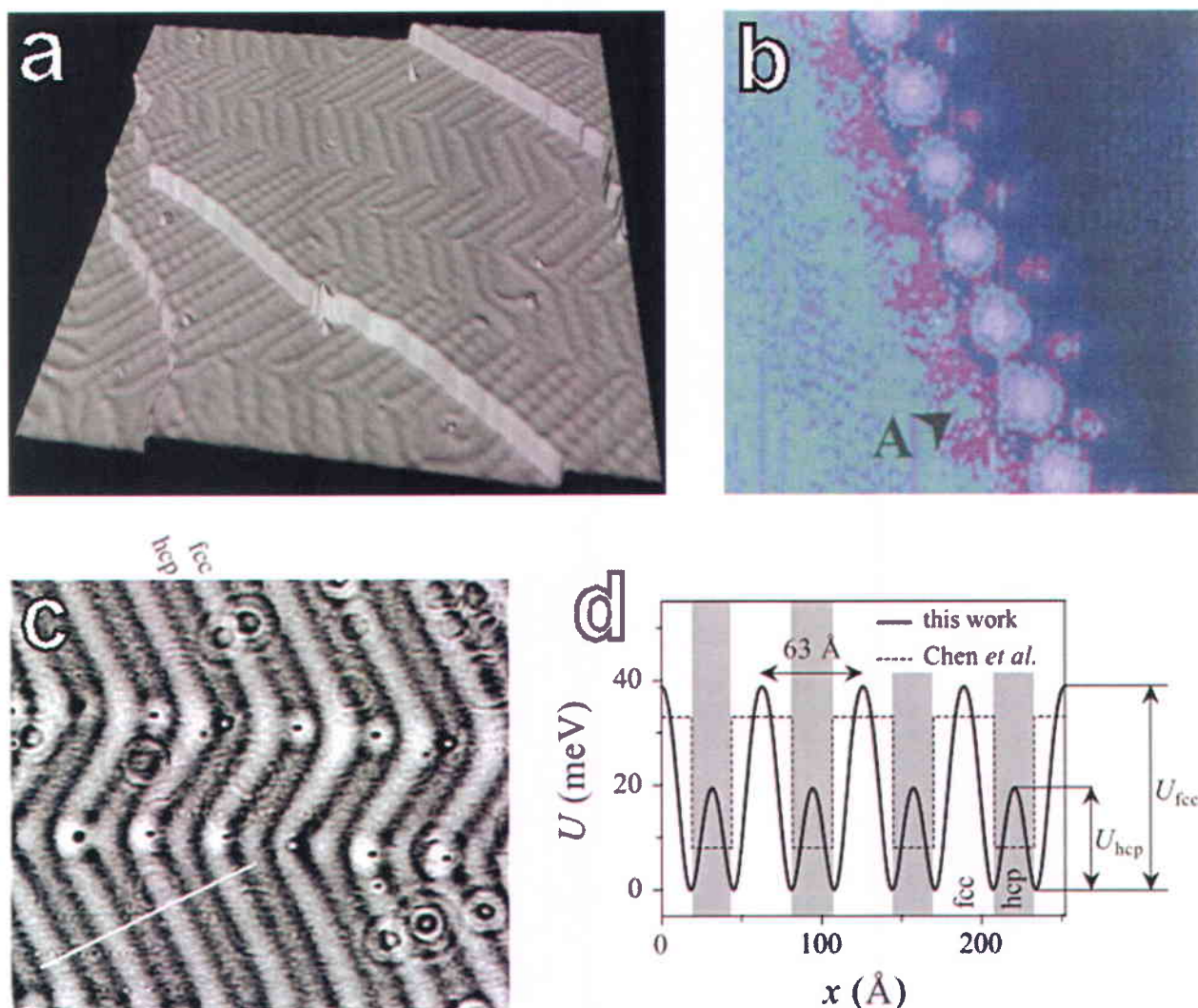


Figure 8.39: a) STM image of the Au(111) surface at 4 K. The herringbone reconstruction and surface-state standing waves are clearly visible. b) STM image of benzene molecules at 77 K along a monoatomic step edge on Cu(111) perturb the electronic structure of the adjacent surface thereby setting up adsorption sites for subsequent rows of molecules. The arrow A indicates the empty surface electronic states above the step edge. c) External potential map of the reconstructed Au(111) surface derived from the density map acquired with STM. d) Electronic potential perpendicular to the Au(111) reconstruction white line in c). Reproduced from a) ref. ²²², b) ref. ²²⁴ and c),d) ref. ²²³.

Clearly, the existence of two different phases as a function of the surface reconstruction is a consequence of molecule···substrate interactions. Since TBPB does not show this behavior (Figure 8.34) on Au(111) we hypothesize that these substrate effects are due to the triazine core in the building blocks of the assembly, which makes TBPT molecules planar (Figure 8.13) and thus leads to a stronger molecule···substrate adsorption energy,

assuming similar behavior in the physisorption of the benzene and triazine core on the gold surface. The more negative charge distribution compared to a benzene core may also play a role in this, however there cannot be any electronic coupling between the gold surface states and the unshared electrons of the nitrogen atoms given that these are delocalized in the molecular mirror plane (in addition to being screened - Figure 8.10c). In other words, the planar adsorption configuration of TBPT molecules prevents any form of interaction similar to that observed for pyridine-terminated molecules²²⁹ or phosphines^{209, 217} on Au(111), which manifests with the carbon-nitrogen bonds vertical to the surface (see Figure 8.48). Dibromianthraquinones (DBAQs), which are another kind of halogenated molecule with an anthracene core, form long-range defect-free SAMNs on reconstructed Au(111) similar to TBPB (Figure 8.40a,b).²³⁰ In this case, however, despite the molecules being flat, a smaller size accounts for a smaller adsorption energy and therefore a smaller coupling with the reconstructed gold surface. The similar precursor TPTZ does not assemble in different phases on the *hcp* and *fcc* regions of the Au(111) surface at monolayer coverage (Figure 8.40c). In this case the molecules are flat in the gas phase as well as upon adsorption on the gold surface,²⁰⁴ therefore they should display a behavior similar to TBPT. However, the reported assembly of TPTZ is laterally stabilized by CH \cdots N hydrogen bonds, which are stronger than the halogen bonds of the TBPT network on Au(111) and hence may overcome the template effect of the surface.²⁰⁴

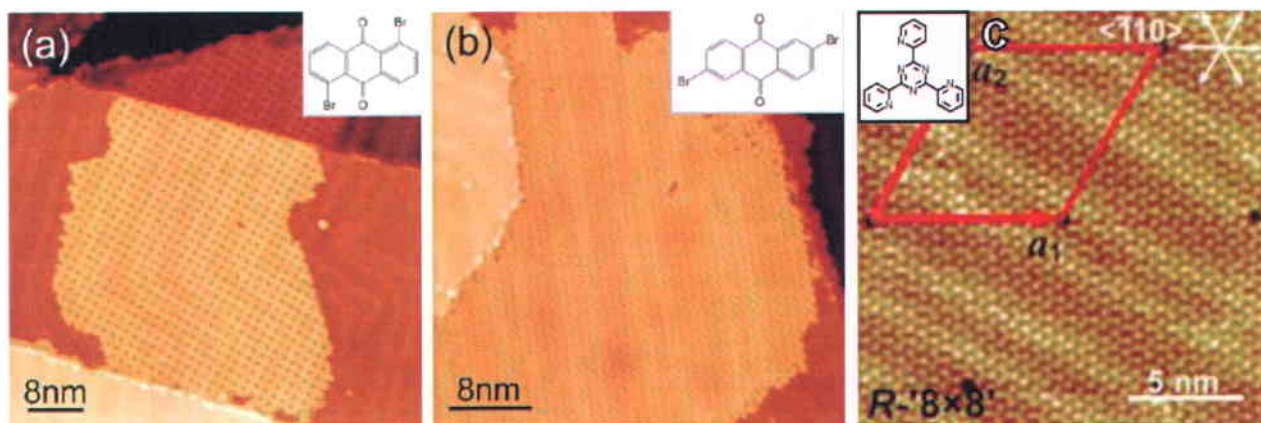


Figure 8.40: STM images of a),b) DBAQs and c) TPTZ at the UHV-Au(111) interface. In both systems the adlayer is not sensitive to the differently reconstructed regions of the Au(111) substrate. Reproduced from a),b) ref. ²³⁰ and c) ref. ²⁰⁴.

Different behaviors of molecular species adsorbed on the *fcc* vs. *hcp* regions of the Au(111) surface have already been reported for benzene (Figure 8.41e,f),^{98, 231-232} azobenzene (Figure 8.41c)²³³ and iron(II) phthalocyanine (FePc) (Figure 8.41a,b,d),²³⁴⁻²³⁵ but in these cases the effect is only observed at low coverage.^{231, 233-235}

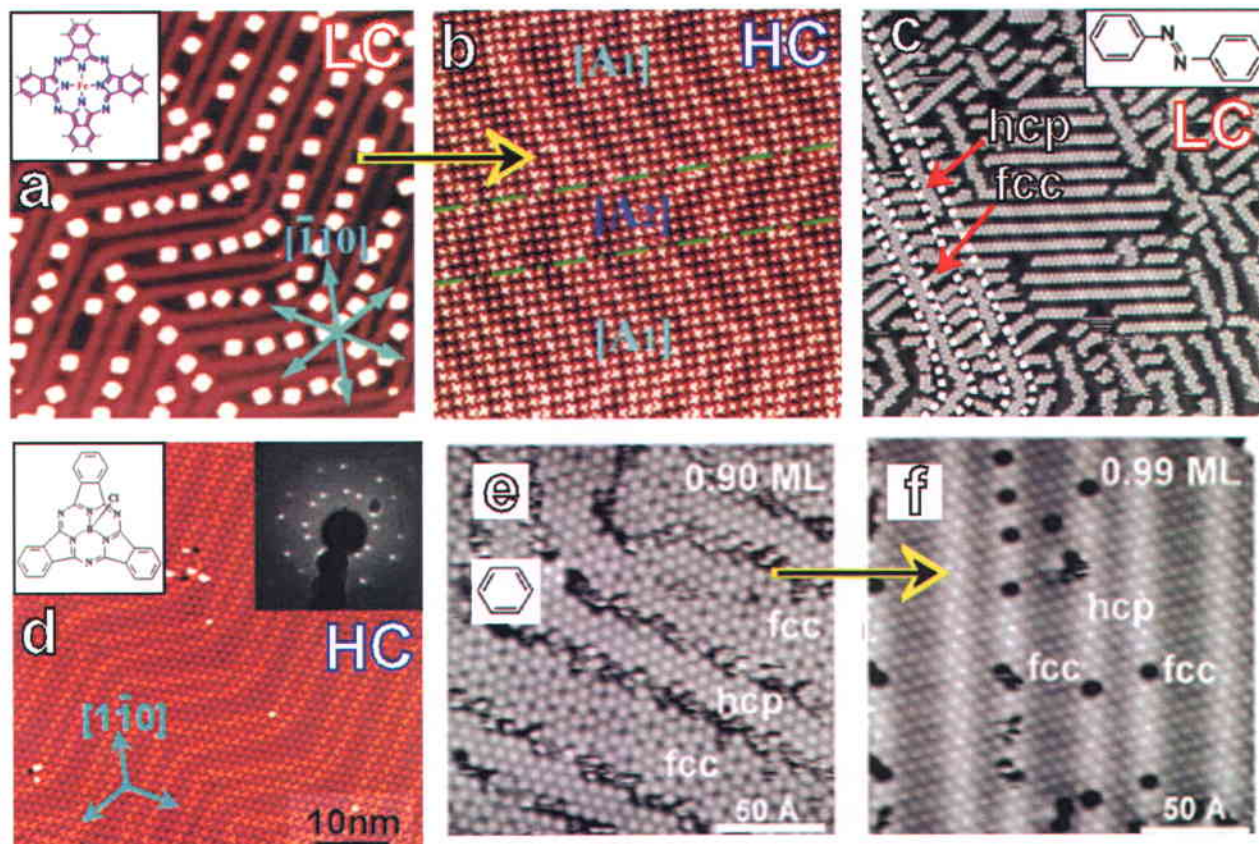


Figure 8.41: STM images of a),b) FePc, c) azobenzene, d) subphthalocyanine (SubPc) and e),f) benzene on Au(111). Reproduced from a),b) ref.²³⁵, c) ref.²³³, d) ref.²³⁶ and e),f) ref.⁹⁸.

The bi-component system melamine and 3,4,9,10-perylenetetracarboxylic diimide (PTCDI) SAMN contains mere stacking faults commensurate with the surface reconstruction, but not the extended single-phase domains as we report here (Figure 8.42b).²⁰⁵ We ascribe the surface-reconstruction sensitivity of TBPT-Au(111) to stronger adsorption energy than TBPB-Au(111) and to the similarity between the α and β polymorphs, in terms of phase boundaries in the form of shared molecular rows along the *v*-vectors of the unit cells.

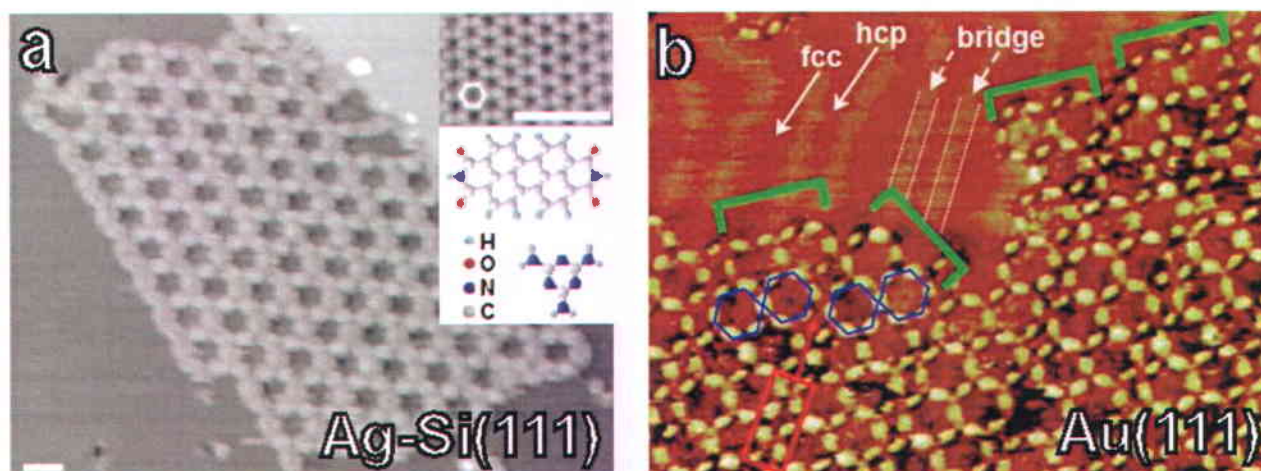


Figure 8.42: STM images of the bi-component system melamine and PTCDI on a) $\sqrt{3} \times \sqrt{3} R30^\circ$ Ag/Si(111) and b) $22 \times \sqrt{3}$ Au(111). In b) the sub-ML adlayer is sensitive to the *fcc* and *hcp* regions of the substrate. Reproduced from a) ref. ²³⁷ and b) ref. ²⁰⁵.

We also attempted surface polymerization of TBPT molecules on Au(111) to compare our results with the covalent organic frameworks (COFs) of TBPB and TIPB monomers at the liquid solid-interface reported in the literature. These experiments proved to be extremely challenging. Drops of TBPT-phenyloctane solutions of concentration between 10^{-2} M and 10^{-6} M were deposited on the Au(111) substrate held at temperatures between 100 °C and 200 °C. After drop deposition, the systems were allowed to stabilize on the hot plate for between 2 and 10 minutes. One of the problems in these experiments was that after solvent evaporation macroscopic molecular aggregates were left on the surface, which obstructed the STM tip during image acquisition. A possible solution could be to rinse the surface with 2-propanol, which would help removing macroscopic adsorbates without affecting the COFs or the single molecules physisorbed on the surface. All of the experimental methodologies described above were attempted, however only one TBPT dimer was ever found on Au(111) (Figure 8.43).

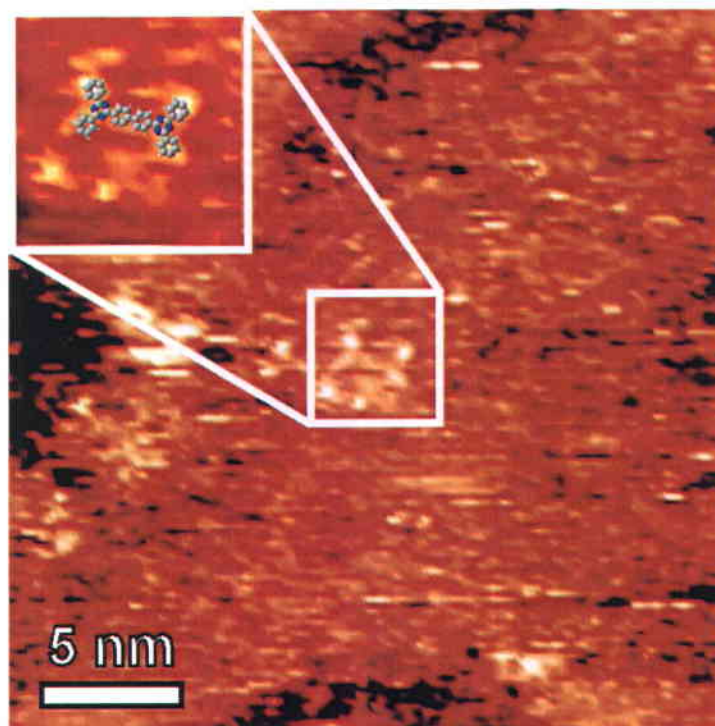


Figure 8.43: STM image of a dimer of TBPT molecules at the air-Au(111) interface ($25 \times 25 \text{ nm}^2$, $V_s = -0.4 \text{ V}$, $I_t = 194 \text{ pA}$). The inset shows a zoom of the dimer with the model superimposed.

Despite being challenging, solution preparation of COFs on Au(111) is in principle possible. In fact, for the similar precursors TBPB and TIPB covalent networks obtained at the liquid-solid interface have already been reported (Figure 8.44).

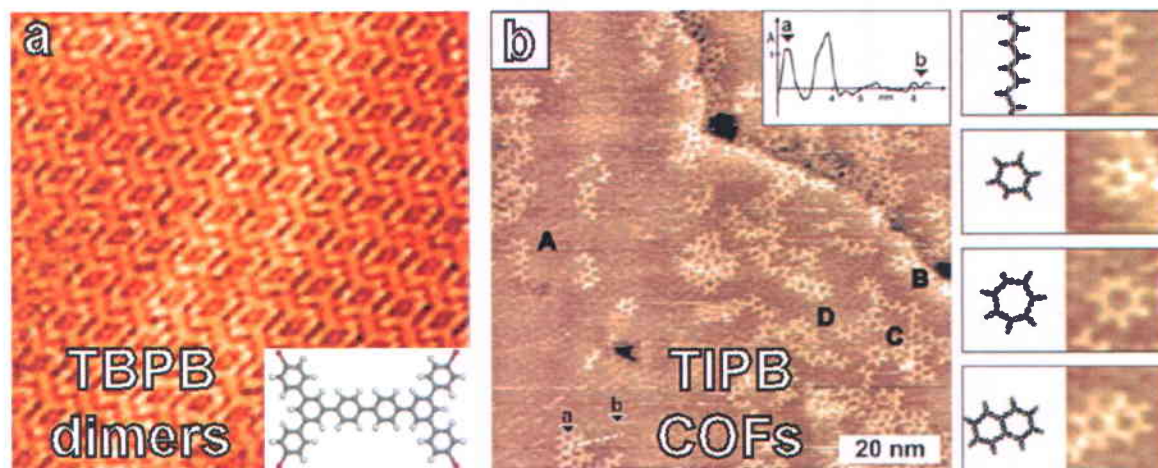


Figure 8.44: STM images of a) TBPB dimers (inset) and b) COFs of various shapes obtained from TIPB monomers. Reproduced from a) ref. ¹⁵¹ and b) ref. ¹⁵³.

8.3.5 TIPT ON Au(111)

Probing the assembly of TIPT molecules on Au(111) was more challenging than for the brominated molecule. Using similar drop volumes and concentrations only small domains of assembled molecules (up to ≈ 10 nm) were observed. The domains were rotated between themselves and lacked long-range order (Figure 8.45a). The tip-sample interaction was quite strong, making image acquisition difficult (see Figure 8.46).

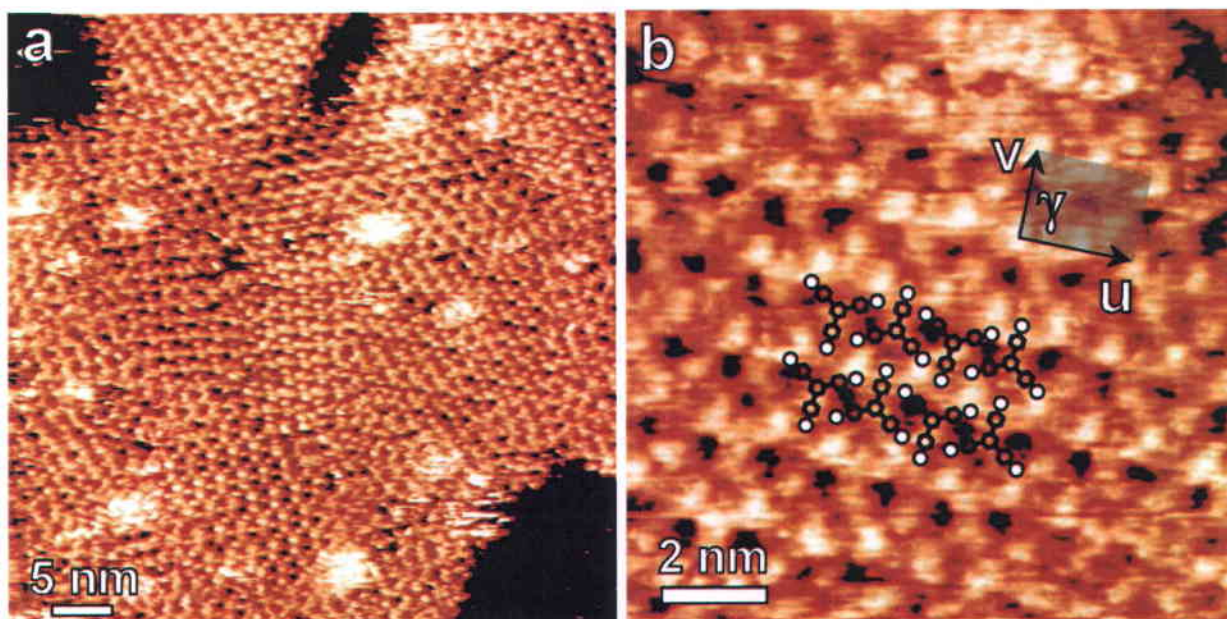


Figure 8.45: a),b) STM images of TIPT molecules (schematically superimposed) assembled at the TCB-Au(111) interface a) (50.0×50.0 nm², $V_s = -0.62$ V, $I_t = 177$ pA), b) (11.7×11.7 nm², $V_s = -0.79$ V, $I_t = 231$ pA). The experimentally determined unit cell parameters are $u = 2.2 \pm 0.2$ nm, $v = 1.6 \pm 0.2$ nm and $\gamma = 90 \pm 8^\circ$.

However, the experimental data still allow for a limited comparison between this system and TBPT assembly on Au(111). For instance, as opposed to the previous case, the STM micrographs do not show the presence of different phases sensitive to *fcc* and *hcp* regions nor any contrast modulation due to the underlying surface reconstruction. The latter may be a consequence of the adsorbed molecules perturbing the surface reconstruction,²⁰⁸⁻²¹² although we cannot exclude an influence of the tunneling parameters used for imaging.

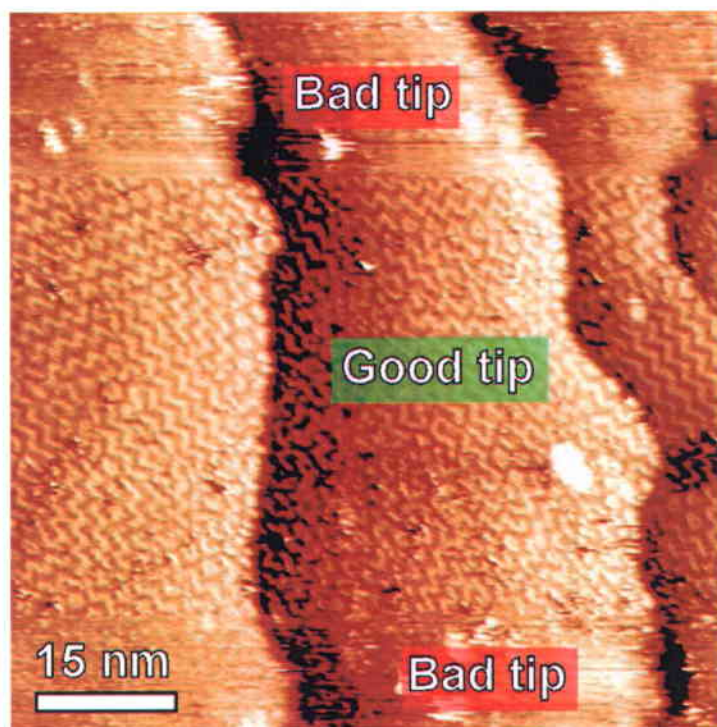


Figure 8.46: STM image of TIPT molecules assembled at the TCB-Au(111) interface, showing STM tip instability – central part vs. upper and lower parts ($72.9 \times 72.9 \text{ nm}^2$, $V_s = +0.10 \text{ V}$, $I_t = 200 \text{ pA}$).

High-resolution images (Figure 8.45b) suggest that the assembly of TIPT on Au(111) is similar to that on HOPG (Figure 8.5b), and closely resembles the assembly of TIPB on Au(111)¹⁵³ – *i.e.* with a rectangular unit cell that hosts two molecules (Figure 8.6d). In some cases, however, small domains with packing similar to that of TBPT on Au(111) were also observed (Figure 8.47). Overall, the molecule···substrate interactions appear to be quite different from those in the TBPT-Au(111) system. The nature of halogen atoms not only affects the lateral stabilization of the overlayer *via* halogen bonding, but also modulates molecule-substrate interactions with Au(111).

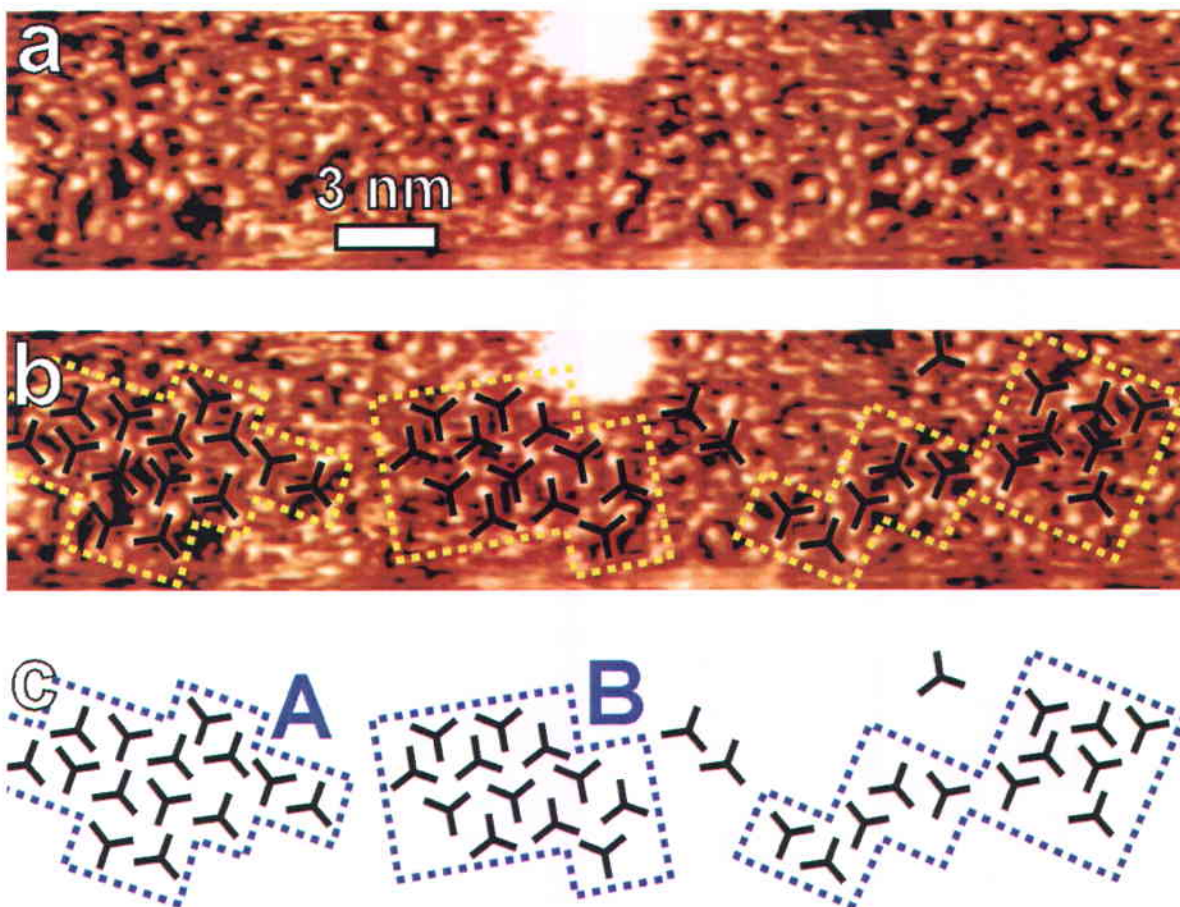


Figure 8.47: a) Molecularly resolved STM image of TIPT molecules adsorbed on Au(111) with b) model of the structures superimposed (molecules drawn as black tripods, $37.2 \times 8.1 \text{ nm}^2$, $V_s = +0.05 \text{ V}$ $I_t = 400 \text{ pA}$). c) Reports the model of b) without the background STM image; the domain A is similar to TIPT-HOPG and the domain B similar to the structure of TBPT on Au(111).

8.4 DIACETYLENE MOLECULES

In this section we will discuss the results obtained for Maude-2-041 first and then for SR-10-152 and SR-10-134 (Section 6.2). The self-assembly of Maude-2-041 on HOPG revealed that the phenyl rings introduce steric hindrance within the 2D molecular lattice, hence preventing an optimal packing for diacetylene polymerization (Chapter 3). This motivated us to investigate the other two precursors, whose aryl rings contain nitrogen atoms (Section 6.2). The goal was to achieve a more favorable adsorption geometry with these two precursors on Au(111), through a coupling between the unshared electron pair of the nitrogen atoms and the gold surface atoms, similar to that observed for pyridine-terminated molecules on Au(111)²²⁹. Namely, a vertical adsorption of the aryl rings (*edge-on*) is desired over the planar configuration (*flat-on*) – Figure 8.48. A similar geometry for a nitrogen-containing molecule adsorbed on Au(111) has been reported recently, although in that case the edge-on geometry was only observed at high molecular coverage, where it allows a more dense, hence more favorable, packing with respect to the flat-on configuration observed at low coverage²³⁸.

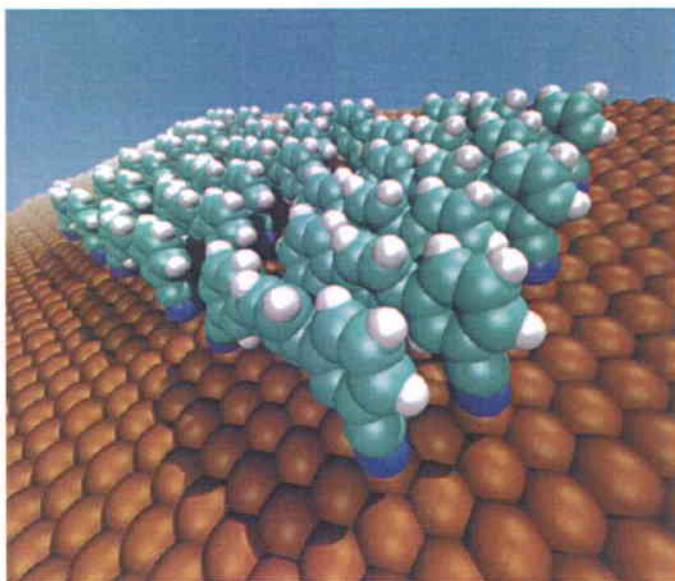


Figure 8.48: Edge-on adsorption geometry of nitrogen-containing molecules on Au(111). Reproduced from ref. ²³⁸.

8.4.1 MAUDE-2-041 ON HOPG

After applying a $\approx 5 \mu\text{l}$ drop of Maude-2-041 dissolved in heptanoic acid (10^{-2} M) on a freshly cleaved HOPG substrate, a SAMN spontaneously formed. Large-scale STM images show that three different domains are present within the adlayer, rotated by multiples of 120° (Figure 8.49b). The adlayer is therefore commensurate with the 3-fold symmetric HOPG substrate.

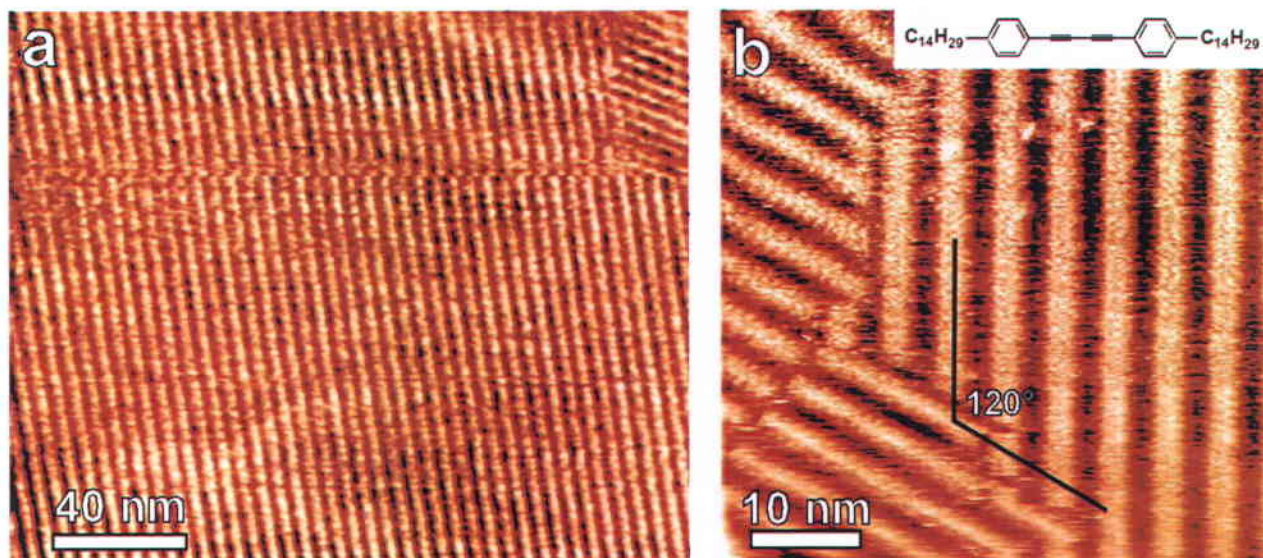


Figure 8.49: Large-scale STM images of Maude-2-041 molecules (inset) assembled at the heptanoic acid-HOPG interface ($200.0 \times 161.3 \text{ nm}^2$, $V_s = -1.40\text{V}$ $I_t = 670 \text{ pA}$; $50.0 \times 50.0 \text{ nm}^2$, $V_s = -0.95 \text{ V}$ $I_t = 200 \text{ pA}$). The adlayer comprises three symmetrically equivalent domains, rotated by 120° between each other.

High-resolution STM images show that the molecules within the SAMN are arranged with interdigitated alkyl chains, a configuration typical of long-chain molecules on HOPG (Figure 8.50)⁵⁵. As already observed for similar systems²³⁹, also the rigid diacetylene cores arrange in a lamellar structure with the aryl subunits, dictating the spacing between neighboring molecules (Figure 8.50). The assembled network is laterally stabilized by vdW interactions between the tightly-packed alkyl chains. Although weaker than other intermolecular interactions, vdW forces (0.02 – 0.1 eV) can lead to strong lateral interactions as the length of the alkyl chains increases⁵⁵. The lateral stabilization energy is on the order of 25 meV per pair of methylene ($-\text{CH}_2-$) groups²⁴⁰. According to the molecular models in

Figure 8.50 each alkyl chain has approximately 10 interacting CH₂ groups with each of the two neighboring molecules. Given that each Maude-2-041 molecule has two chains, we estimate $2 \cdot (2 \cdot 10) \cdot 25 = 1000 \text{ meV} = 23 \text{ kcal/mol}$ of lateral stabilization energy. Furthermore, as already discussed in Section 8.3.2, *n*-alkanes typically adsorb along $\langle 100 \rangle$ of the basal plane of graphite (*Groszek model*¹⁹⁷)^{55, 198}. In the system reported in Figure 8.50 the alkyl chains are in fact aligned along the zig-zag directions (see discussion below, Figure 8.54). Maude-2-041 has two alkyl chains of 14 carbon atoms, therefore according to Eq.8.2 we can estimate an adsorption energy due to the alkyl chains of -57.5 kcal/mol . Note that this value neglects the adsorption energy of the aryl rings and the diacetylene core. According to the discussion of Section 8.3.1, each phenyl ring of Maude-2-041 contributes with additional -7 kcal/mol to the total adsorption energy¹⁷.

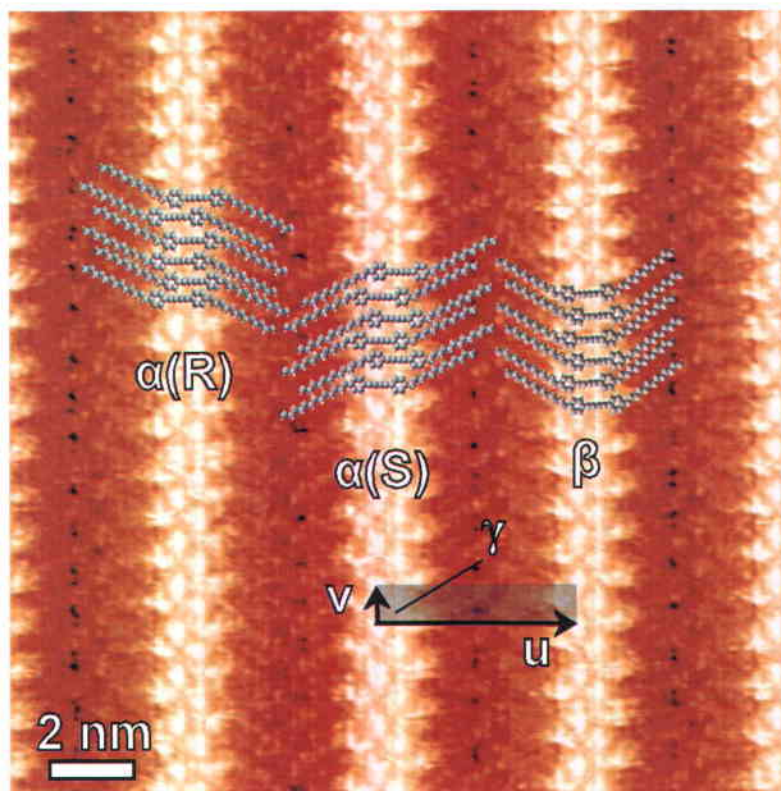


Figure 8.50: High-resolution STM image of Maude-2-041 molecules assembled at the heptanoic acid-HOPG interface ($18.6 \times 18.6 \text{ nm}^2$, $V_s = -0.85 \text{ V}$, $I_t = 150 \text{ pA}$), with the packing model for the different phases superimposed. The unit cell is also reported ($u = 4.85 \pm 0.08 \text{ nm}$, $v = 1.06 \pm 0.08 \text{ nm}$ and $\gamma = 90 \pm 2^\circ$). Note that the molecules in the $\alpha(R)$ and $\alpha(S)$ phase constitute a pair of enantiomers, since one is the mirror image of the other.

From Figure 8.50 it is evident that different phases, defined by the arrangement of the alkyl chains, are present in the SAMN. However, assuming that the spacing and the orientation of the diacetylene moiety between the two phenyl rings of Maude-2-041 molecules does not vary for different phases, the unit cell of the molecular structures can be defined. In all the STM images the aryl rings typically appear with bright contrast, while it was much more challenging to achieve sub-molecular resolution of the alkyl chains.

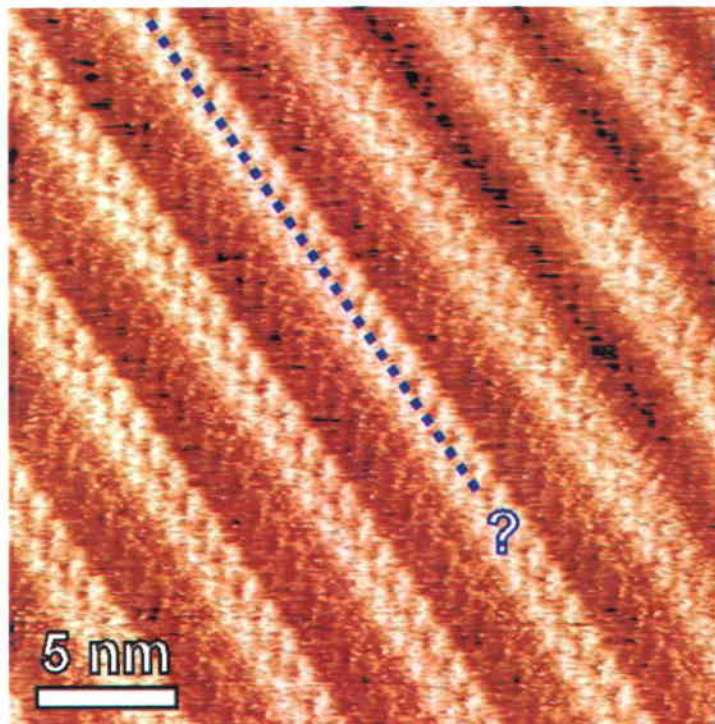


Figure 8.51: STM image of Maude-2-041 molecules assembled at the heptanoic acid-HOPG interface after 50 minutes of UV-light irradiation ($25 \times 25 \text{ nm}^2$, $V_s = 0.51 \text{ V}$, $I_t = 260 \text{ pA}$). The lack of a bright line along the dotted blue line suggests that the polymerization has not occurred.

Since the goal of this work was to study the chain-reaction that leads to polydiacetylene molecules starting from diacetylene monomers, the presence of different phases within the adlayer was not investigated further. Instead, we used the same unit cell for all the phases, an assumption that is valid for the rigid backbones, since these rigid rods exhibit similar packing in all phases (Figure 8.50). After a stable SAMN was obtained, the sample was irradiated with UV light (254 nm) with the same wavelength used for the 3D polymerization of similar molecules achieved in the liquid state by our collaborators²⁴¹. The

SAMN was illuminated for a minimum of 1 minute up to one hour, however polymerization was never achieved.

Figure 8.51 shows a SAMN after 50 minutes of UV-light irradiation. When polymerization occurs, a change in the contrast (brighter lines) of the STM image is expected due to the change in the electronic and topographic molecular structure (Figure 3.2a,b). However, even though the resolution of Figure 8.51 is not ideal, it is clear that this distinct feature is not present, hence we can conclude that no polymerization has occurred. Because the UV radiation used in our experiments is similar to that used in the 3D case in terms of photon energy and intensity, we believe that in our 2D case polydiacetylenes were not obtained for topochemical reasons⁸³. It is known that to activate the polymerization starting from monomers with diacetylene units, specific geometrical conditions must be fulfilled. The reaction progresses through 1,4-addition of adjacent units for very specific rotations of the monomers (Chapter 3)⁸³. In particular, apart from a few exceptions, reactivity is only observed if the separation (R) between the reacting atoms (1,4-carbon atoms) is less than a limiting distance of approximately 4 Å, as shown in Figure 8.52 where reactivity is achieved only for structures with distance $R < 4$ Å (full black circles). In addition to this, the maximal reactivity is achieved when the stacking distance of the monomers in the array (d) is ≈ 5 Å and the angle between the diacetylene rods and the stacking axis (φ) is $\approx 45^\circ$ (see Figure 3.2d for labels).

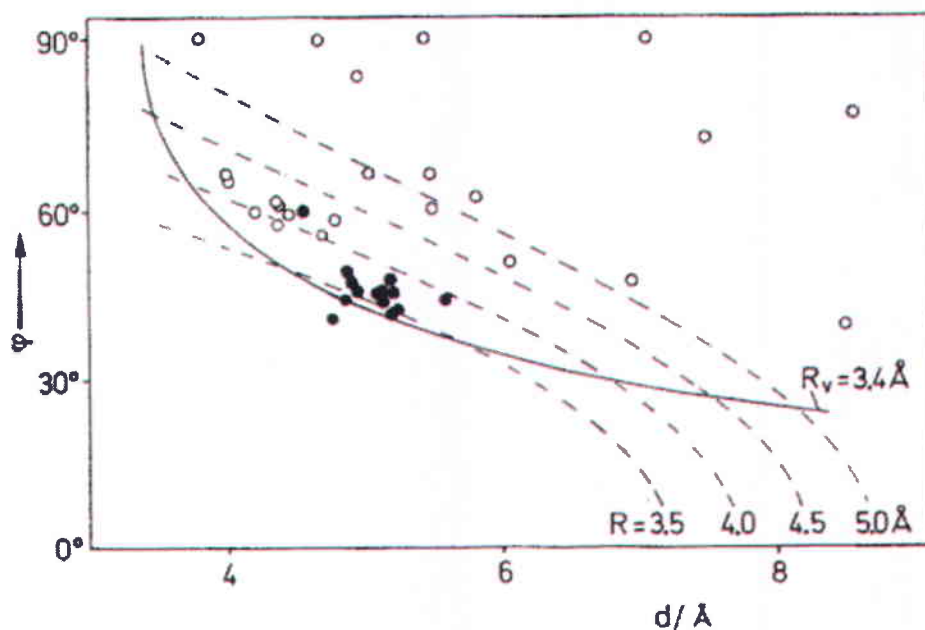


Figure 8.52: Plot of the angle φ between the stacking axis and the rigid backbone vs. the stacking distance d . The dashed lines refer to constant values of the distance R between the 1,4-carbon atoms. Empty and full circles represent inactive and active structures, respectively. Therefore, only structures with $R < 4 \text{ Å}$ can essentially lead to topochemical polymerization. Reproduced from ref. ⁸³.

Our results show that the interspacing distance between the diacetylene rods is $\approx 5 \text{ Å}$, in agreement with the topochemical requirement, however the large distance between the 1,4-carbon atoms ($\approx 5 \text{ Å}$ instead of less than 4 Å) as well as the high-angle orientation of the diacetylene moieties ($85 \pm 5^\circ$ for the three different phases instead of $\approx 45^\circ$) likely prevent the polymerization (Figure 8.53a). Furthermore, the alternated packing of the diacetylene backbones rather than the ideal packing reported in Figure 3.2d may be an additional reason to the lack of polymerization.

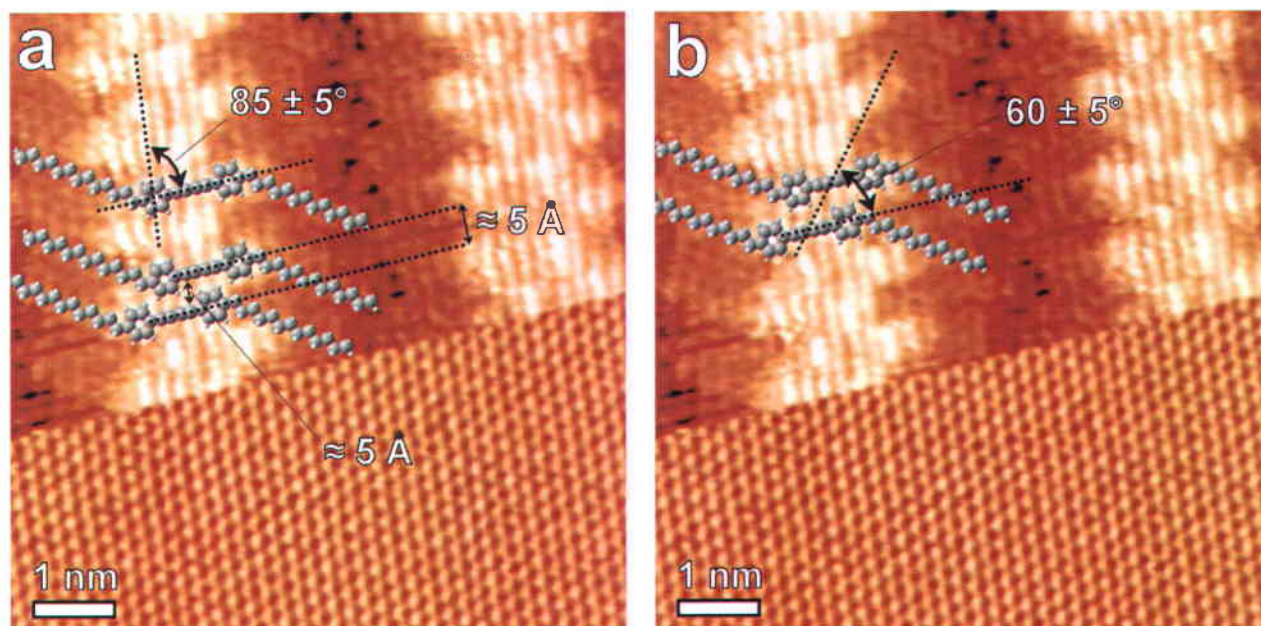


Figure 8.53: High-resolution STM image of Maude-2-041 molecules assembled at the heptanoic acid-HOPG interface (upper part) and the underlying HOPG substrate (lower part) ($8.4 \times 8.4 \text{ nm}^2$, $V_s^{\text{HOPG}} = -0.02 \text{ V}$ and $V_s^{\text{SAMN}} = -0.85 \text{ V}$, $I_t = 150 \text{ pA}$). The packing model has been superimposed to highlight the experimental topochemical parameters.

In spite of these considerations, by focusing only on the two molecules of a single unit cell one can see that there could be the possibility of the formation of dimers. According to Figure 8.53b it is evident that, in this case, an angle closer to the required 45° is achieved, however the dimerization is not observed because also in this case the distance between the reacting carbon atoms as well as the orientation angle are too large. Moreover, dimers are unlikely to form because they would introduce stress within the adlayer, given the geometrical rearrangement of the monomers upon topochemical polymerization (Figure 3.2b,d)⁸³.

This is the same reason why the topochemical polymerization is also referred to as a *chain reaction*, due to the fact that when the reaction is activated and the first two monomers polymerize, the geometrical rearrangement is “transferred” to neighboring monomers which therefore polymerize as well⁸³. The steps involved in this geometrical rearrangement are still not well understood⁸³.

The reason for studying the adsorption of Maude-2-041 on HOPG is that this substrate is rather inert, that is to say it should not affect the intermolecular interactions driving the self-

assembly process. However, Figure 8.54 shows that there is an epitaxial matching between the molecular adlayer and the HOPG substrate (as already mentioned above, this is typical for *n*-alkanes on HOPG⁵⁵).

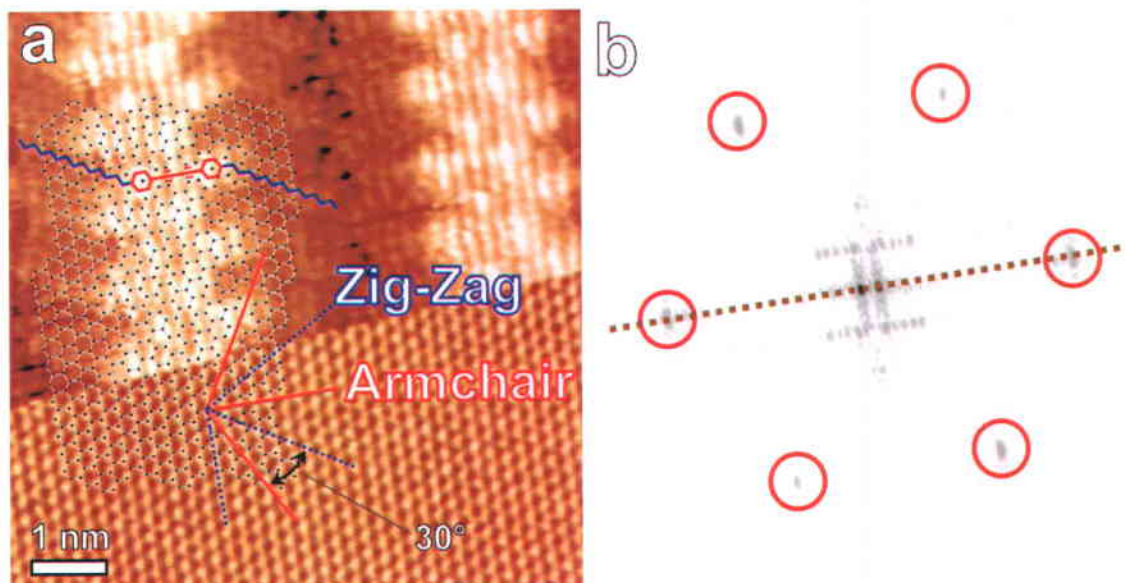


Figure 8.54: a) High-resolution STM image of Maude-2-041 molecules assembled at the heptanoic acid-HOPG interface (upper part) and the underlying HOPG substrate (lower part) ($8.4 \times 8.4 \text{ nm}^2$, $V_s^{\text{HOPG}} = -0.02 \text{ V}$ and $V_s^{\text{SAMN}} = -0.85 \text{ V}$, $I_t = 150 \text{ pA}$). The packing model and the graphite top-layer lattice have been superimposed. The side alkyl chains and the diacetylene core are aligned along the *zig-zag* and *armchair* directions of the HOPG substrate, respectively. b) 2D FFT of the image in a).

Similar to the system discussed in Section 8.3.2, the alkyl chains are aligned along the zig-zag directions of the graphite substrate, a geometry in which the system minimizes its energy thanks to the registry between the alkyl chains and the substrate⁵⁵. Also the rigid backbone of each molecule is aligned along one of the symmetry axes of HOPG, along a so-called *armchair* direction. This implies that the intramolecular angle between the alkyl chains and the diacetylene core of Maude-2-041 molecules must be $\approx 30^\circ$. Single-molecule DFT calculations indicate this angle is 28° , thus confirming that minimal intramolecular strain is introduced to achieve this angle (Figure 6.2a). The 2D FFT in Figure 8.54b confirms that the molecular rigid cores are aligned along one of the armchair directions. In principle, the FFT should also display the alignment of the alkyl chains along the zig-zag direction, however this is not observed in Figure 8.54b because of the poor contrast of the side groups in the STM image (Figure 8.54a). Furthermore, the model in Figure 8.54 suggests that the molecules

adsorb on the surface with their phenyl rings aligned with the *ABAB* layered structure of crystalline graphite, *i.e.* with a graphite carbon atom directly below the center of the phenyl rings of the molecular layer (Section 7.1). Theoretical works show that this is the most stable adsorption geometry for PAH molecules¹⁷. Gas-phase DFT calculations for the extended 2D molecular lattice were not performed because density functional theory is known to not perform well for weakly bonded vdW systems¹⁰¹, although recently there have been improvements in this respect¹⁷. These calculations typically require high-level exchange-correlation functionals (Chapter 5)¹¹³.

In conclusion, two of the three topochemical requirements to activate polymerization between the diacetylene groups were not achieved, namely the molecular rigid backbone orientation as well as the distance between the reacting carbon atoms. This is likely the cause for the lack of polymerization upon UV-light absorption. The excessive distance between the 1,4-carbon atoms could be reduced by removing the phenyl rings, which introduce steric hindrance due to their flat adsorption geometry by forcing the diacetylene moieties far apart. The orientation of the rigid backbones with respect to the lamellar axis, on the other hand, may be addressed by modifying the side groups. The major role of the long alkyl chains is to stabilize the SAMN, however themselves may be responsible for high-angle orientations. In fact, it has been observed that linear molecules with phenyl rings adjacent to the diacetylene moiety self-assemble with higher orientation angles when alkyl chains are added as end groups²³⁹. The introduction of one alkyl group only changes the orientation of the rigid cores with respect to the lamellar direction rather than changing their alignment, thus playing a key role for topochemical polymerization. For instance, the molecular packing in Figure 8.55a is topochemically favorable for polymerization, with the angle between the rigid rods and the packing axis (51°) quite close to the $\approx 45^\circ$ required. However, when an alkyl chain is added as an end group to one side of the diacetylene moiety, higher angles are obtained (Figure 8.55b,c), result similar to what we have experimentally found (Figure 8.53). Since the number of unsaturated units within the diacetylene moiety does not affect the lamellar arrangement of the rigid backbones (Figure 8.55b,c), changing the characteristics of the end-group of the alkyl chains may be the one way to achieve the diacetylene polymerization. For instance, alkyl chains with different parity in the number of carbon atoms can be introduced on the two sides of the rigid rod, as well as polar groups such as the carboxyl or the hydroxyl group at

the end of one or both the functional groups linked to the diacetylene moiety. Nevertheless, we also believe that though this may be a solution for one of the hurdles, the large distance between the 1,4-carbon atoms will still likely be a barrier for the polymerization, unless the phenyl rings are removed.

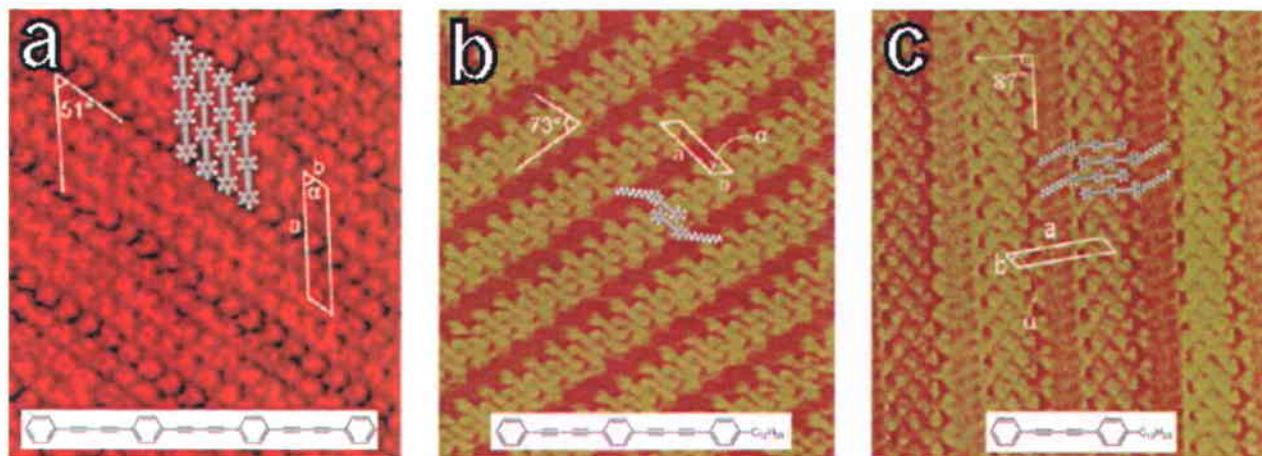


Figure 8.55: Different molecular arrangements in SAMNs of diacetylene monomers on HOPG. a) Without alkyl chains the molecules self-assemble with an angle favorable for topochemical polymerization, but b),c) if an alkyl chain is added to the rigid backbone very high angles are achieved, regardless the number of unsaturated repeat units. Reproduced from ref. ²³⁹.

8.4.2 SR-10-152 ON HOPG

Given the unsuccessful topochemical polymerization of Maude-2-041 molecules on HOPG (Section 8.4.1) we investigated the self-assembly process of another precursor, namely SR-10-152 (Figure 6.2c). As already mentioned at the beginning of this chapter, the idea of this project is to exploit the unshared electron pair of the nitrogen atoms in the aryl rings to achieve an edge-on adsorption configuration (Figure 8.48). In this configuration the aryl rings do not introduce steric hindrance, as it was the case for the flat-on adsorption geometry of Maude-2-041 molecules on HOPG (Section 8.4.1), rather they participate in the lateral stabilization of the assembly through π - π stacking²³⁸. Note that in the case of edge-on adsorption the molecules are no longer merely physisorbed on the surface, but are anchored to the surface with stronger bonds through the nitrogen atoms (*e.g.* organometallic or covalent bonds).

We first studied the system on HOPG to find the optimal experimental conditions for the self-assembly process, in terms of type of solvent and solution concentration. SAMNs of SR-10-152 were obtained both in heptanoic acid and TCB with solutions in the concentration range $10^{-2} - 10^{-3}$ M (Figure 8.56a,c). Both solvents lead to the same molecular packing, however whereas for heptanoic acid the adlayer is rotated clockwise by an angle $\beta = 2 \pm 1^\circ$ with respect to the armchair directions of the substrate, for TCB this angle is $\beta' = 23 \pm 1^\circ$, as indicated in the 2D FFT of STM micrographs containing both the SAMN and the atomically-resolved HOPG substrate (Figure 8.56b,d). Pairs of bright protrusions, at a distance of approximately 1 nm within each pair, are resolved in the micrographs. Given the molecular structure of SR-10-152 (Figure 6.2c), we tentatively ascribe these protrusions to the contrast of the aromatic rings of adsorbed molecules (Figure 8.56a).

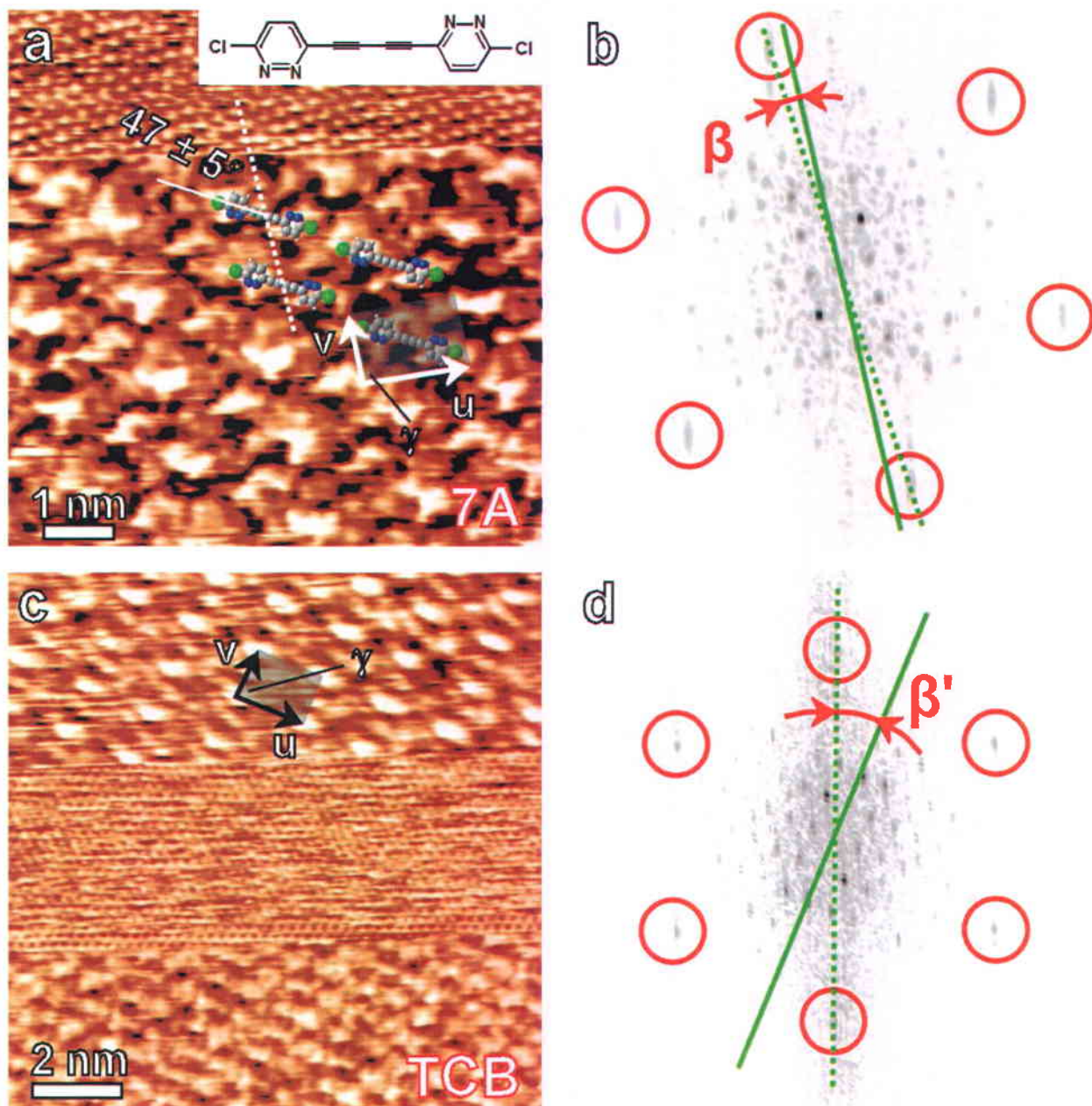


Figure 8.56: a),c) STM images of SR-10-152 molecules (inset) assembled at the heptanoic acid- and TCB-HOPG interface, respectively. The underlying graphite lattice is also resolved with atomic resolution ($7.7 \times 7.7 \text{ nm}^2$, $I_t = 89 \text{ pA}$, $V_s^{\text{HOPG}} = -0.02 \text{ V}$ and $V_s^{\text{SAMN}} = -0.92 \text{ V}$; $12.1 \times 12.1 \text{ nm}^2$, $I_t = 151 \text{ pA}$, $V_s^{\text{HOPG}} = -0.02 \text{ V}$ and $V_s^{\text{SAMN}} = -0.90 \text{ V}$). Note that the different imaging of the adlayer in the upper and lower part of c) is not due to a change in the polarity of the bias voltage, rather to a change in the tip state as a consequence of the scanning of the HOPG lattice during image acquisition. b),d) 2D-FFTs of a) and c), respectively. The spots of the HOPG lattice are highlighted by red circles. The green dotted and solid lines lie along one of the $\langle 10\bar{1}0 \rangle$ armchair high-symmetry directions of graphite and along the v vector of the unit cell, respectively. The SAMN is rotated clockwise by an angle $\beta = 2 \pm 1^\circ$ with respect to the HOPG substrate when heptanoic acid is used as solvent, while in TCB this angle is $\beta' = 23 \pm 1^\circ$. The unit cell vectors are $u = 1.57 \pm 0.02 \text{ nm}$, $v = 1.18 \pm 0.03 \text{ nm}$ and the angle between them is $\gamma = 89 \pm 2^\circ$.

Since the goal of this work is to investigate the possible role of the nitrogen atoms driving the assembly of SR-10-152 molecules on a gold surface, we did not attempt surface polymerization of the SAMN on HOPG nor did we study this system more thoroughly. Note that as opposed to the case of Maude-2-041, the angle between the stacking axis and the diacetylene moiety of SR-10-152 molecules within the assembly is favorable for topochemical polymerization at $47 \pm 5^\circ$ – Figure 8.56a. The model proposed in Figure 8.56a has not been validated with higher resolution STM images nor with DFT calculations. Given the polarization at the carbon-halogen bond, which manifests as a positively charged tip (σ -hole) and a negative ring-like charge distribution at the halogen atom (Chapter 2), we expect the assembly to be stabilized by Coulombic donor-acceptor interactions in the form of attractive $\text{Cl}\cdots\text{Cl}$ and/or $\text{Cl}\cdots\text{H}$ intermolecular bonds (halogen bonding). We note, however, that among the elements of the seventh group, chlorine exhibits the smallest σ -hole since fluorine does not have it at all¹⁸. Therefore, chlorine atoms may play a minor role in the stabilization of the system, which may be mostly stabilized by π - π stacking between the molecular aryl rings and the graphite substrate. Attractive $\text{N}\cdots\text{H}$ bonds may also be involved in the lateral stabilization of the 2D molecular network.

Self-assembly on Au(111) was investigated with solutions of considerably lower concentration. By applying a drop of a SR-10-152/TCB 10^{-7} M solution, single molecules were not discernible on the Au(111) substrate with the STM (Figure 8.57a). Although we did not succeed in achieving ordered and extended SAMNs on Au(111), the data presented in Figure 8.57 show a remarkable result. Sub-ML coverage was achieved using diluted solutions (the dotted path in Figure 8.57a is a region of the substrate with no molecules adsorbed), which is an unexpected result for experiments at the liquid-solid interface. In fact, SAMNs at the liquid-solid interface typically exhibit full-ML coverage because of the large amount of solute molecules present in solution. Using very dilute solutions may be problematic for creating SAMNs, given that if not enough molecules are provided to fill entire terraces SAMNs may not form at all due to the instability of low-coordination weakly bonded molecules as well as the competition with solvation energy. In UHV conditions, on the other hand, sub-ML coverage is possible thanks to the controllable evaporation rate as well as the “cleaner” environment. Furthermore, the absence of solvents molecules stabilizing the initial disassembled state is favorable for molecular adsorption.

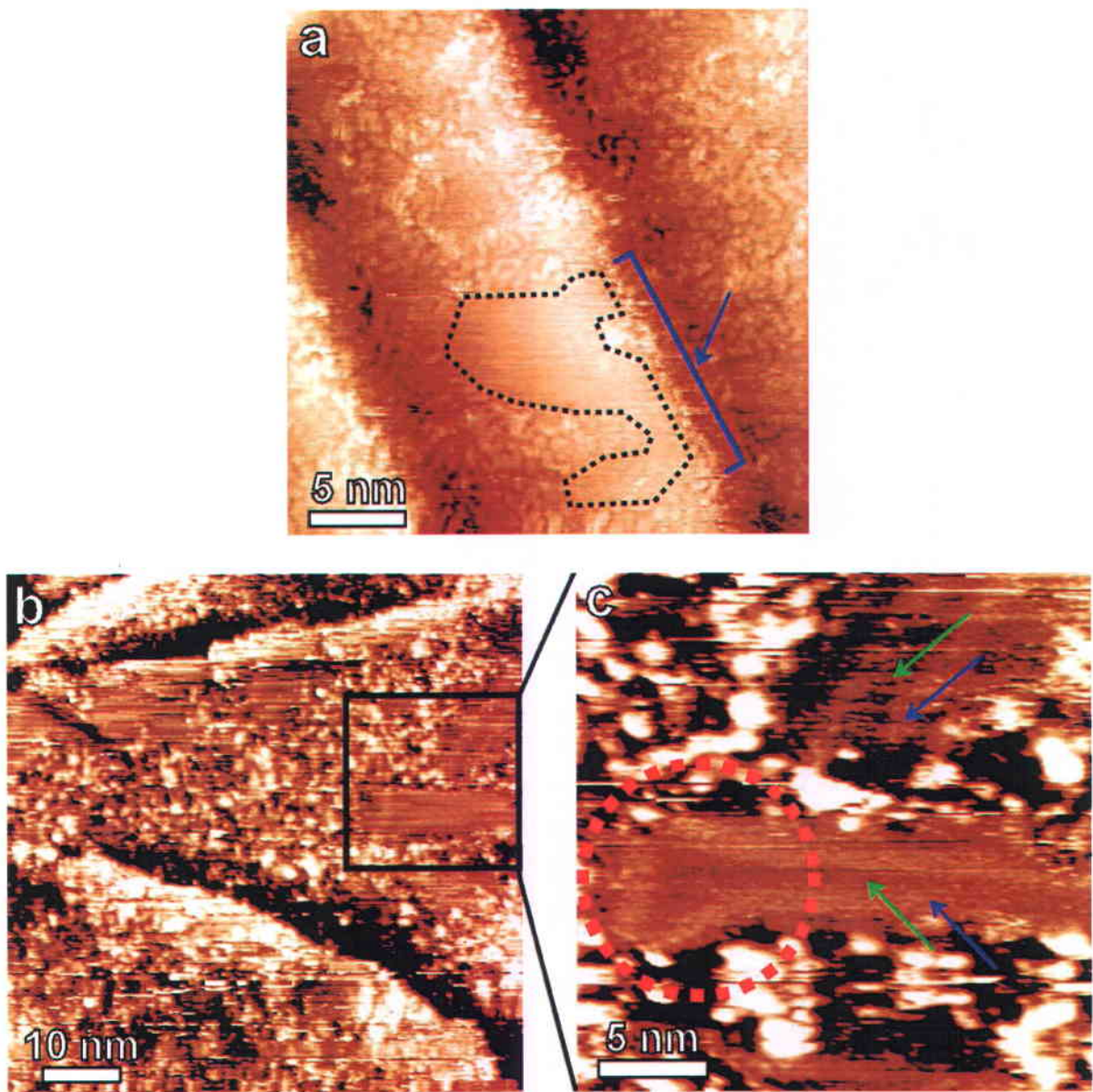


Figure 8.57: STM images of SR-10-152 molecules assembled at the TCB-Au(111) interface. The dotted path in a) highlights an uncovered region of the substrate. The blue arrow indicates the step-edge of a Au(111) terrace with adsorbed molecules. c) Is a zoom of the square in b); the blue arrows indicate the boundaries (solitons) between *fcc*- and *hcp*-stacked (green arrows) regions of the Au(111) substrate. The red circle indicates a U-turn defect typical of reconstructed Au(111) surfaces. a) $27.4 \times 27.4 \text{ nm}^2$, $V_s = -0.43 \text{ V}$, $I_t = 168 \text{ pA}$; b) $66.4 \times 66.4 \text{ nm}^2$, $V_s = -1.30 \text{ V}$, $I_t = 123 \text{ pA}$; c) $22.7 \times 22.7 \text{ nm}^2$, $V_s = -1.43 \text{ V}$, $I_t = 32 \text{ pA}$.

From Figure 8.57a it is clear that although some regions of the substrate are uncovered, molecules tend to adsorb at step-edges of terraces (blue arrow in Figure 8.57a). This is a typical effect due to the fact that step-edges are low-coordinated high-energy

defective sites of surfaces, to which molecules easily bind (see also the higher sticking probability at the elbows of reconstructed Au(111) surfaces, Figure 7.5a-c). Furthermore, SR-10-152 are expected to preferentially adsorb with their nucleophilic nitrogen atoms above step edges. This is due to the fact that the filled electronic state density is decreased above step edges while it is increased at the lower edge of the steps (*Smoluchowski effect*, inset of Figure 8.58a)²⁴². The empty surface electronic states are affected in the opposite way. This smoothing of the surface electron density affects molecular adsorption, namely nucleophilic molecules (e.g. benzene²²⁵) adsorb more favorably above the step edges (Figure 8.58a) and electrophilic molecules adsorb more favorably below step edges (Figure 8.58b).

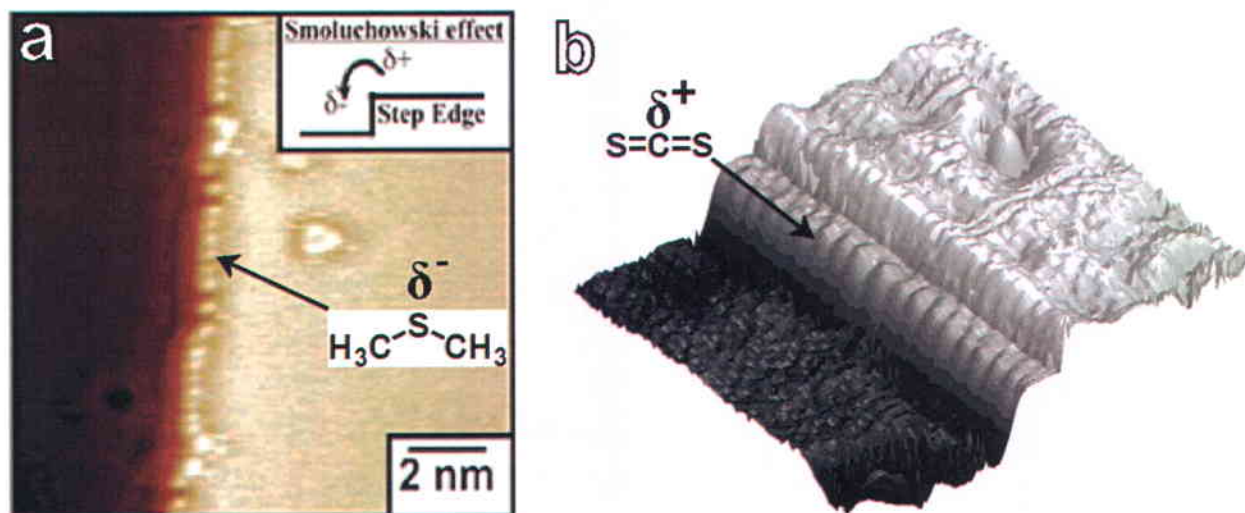


Figure 8.58: a) Dimethyl sulfide molecules adsorb with their nucleophilic sulphur atom above step edges of a Cu(111) surface. b) Carbon disulfide molecules, on the other hand, adsorb with their electrophilic carbon atom below step edges of a Au(111) surface. Reproduced from refs.²⁴³ and ²²⁶.

Note that in some cases, features typical of reconstructed Au(111) surfaces were resolved in the uncovered regions of the substrate. These images reveal that the molecules preferentially adsorb on the *fcc* regions of the reconstructed substrate (Figure 8.57c), an effect widely discussed in Section 8.3.4.

These findings suggest that SR-10-152 molecules interact strongly with the surface, plausibly through the nitrogen atoms, hence suggesting that the edge-on adsorption geometry desirable for polymerization at the diacetylene moiety of SR-10-152 molecules has been achieved. The strong interaction between single building blocks and the substrate may be the

cause of the lack of ordered, extended self-assembled domains. We therefore attempted the self-assembly process at 50 °C, the idea being to provide additional surface mobility to the adsorbed molecules through thermal energy, however this was not successful (drop of solutions were deposited on Au(111) samples on a hot plate). Using higher concentration solutions was not successful either. Nevertheless, we note that this type of experiments are very subtle and thus require further and more complete investigation.

Another cause for the lack of ordered 2D SAMNs is that SR-10-152 likely adsorbs on the substrate only *via* one of the two nitrogen-containing aromatic groups. Indeed, single-molecule DFT calculations indicate that in the isolated state the system is most stable when the nitrogen atoms of the two aromatic groups point in opposite directions (Figure 6.2c). This would prevent the ideal adsorption configuration required for diacetylene polymerization, involving all the nitrogen atoms at the adsorption site (Figure 8.59a). We note, however, that substrate-molecule interactions are typically several times higher than this activation barrier²⁰⁴, meaning that the surface most likely drives the molecules to achieve the configuration of Figure 8.59a, which is the most stable (Figure 8.58b). Although the geometry of Figure 8.59a incorporates attractive π - π stacking interactions between the aromatic rings, neighboring chlorine atoms may experience destabilizing repulsive forces at the negatively charged belt around the C–Cl bond (Figure 8.59a).

Given the subtlety of this system at the liquid-solid interface, self-assembly of SR-10-152 is being currently investigated in our group in UHV conditions. Hopefully, combining the results from the two different environments may give insights on the adsorption geometry of this precursor on Au(111).

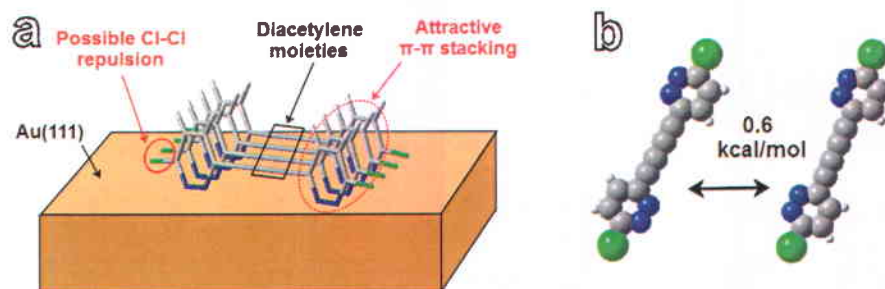


Figure 8.59: a) Scheme of the ideal edge-on adsorption geometry of SR-10-152 molecules on Au(111), favorable for polymerization at the diacetylene moieties. b) Energy competition between the two configurations of SR-10-152 (left most stable), computed in DFT at the B3LYP/6-31G**.

8.4.3 SR-10-134 ON HOPG

Self-assembly of SR-10-134 was observed on HOPG using TCB, heptanoic acid and phenyloctane (Figure 8.60). In all cases the packing within the adlayer is similar. Six equivalent domains are observed, rotated between each other by multiples of 30° (Figure 8.60c).

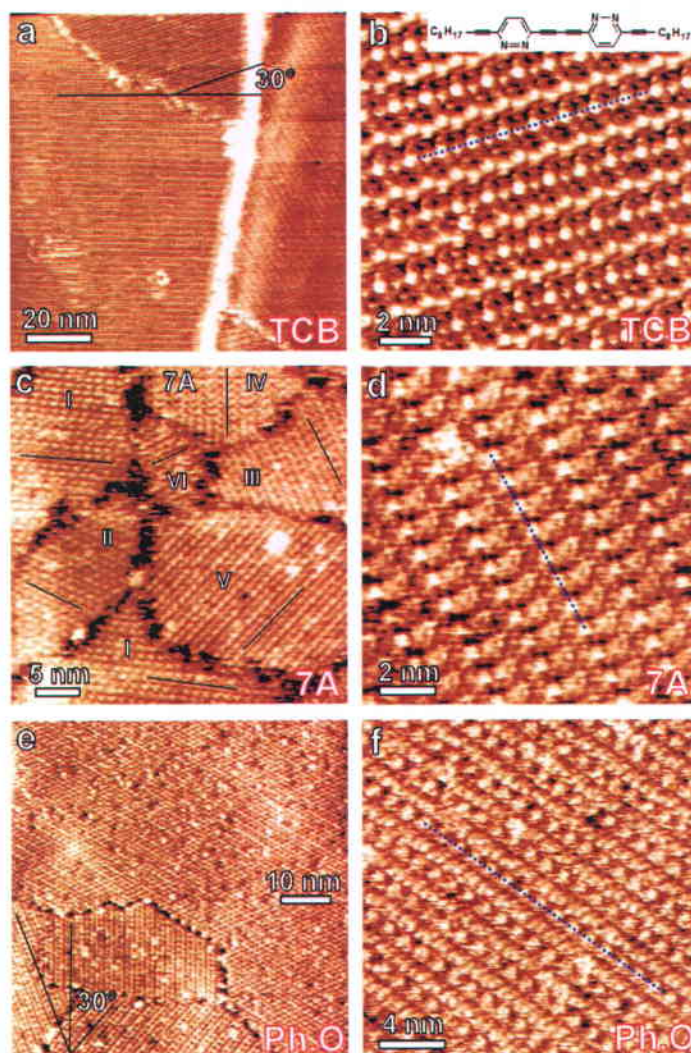


Figure 8.60: Large-scale and high-resolution STM images of SR-10-134 molecules (inset) assembled at the a),b) TCB-, c),d) heptanoic acid- and e),f) phenyloctane-HOPG interface. Black solid lines in large-scale images and dotted blue lines in high-resolution images indicate the molecular stacking axis. Six equivalent domains are observed within the adlayer, rotated by multiples of 30° between each other - see image c). a) $100 \times 100 \text{ nm}^2$, $V_s = -0.89 \text{ V}$, $I_t = 100 \text{ pA}$; b) $12.7 \times 12.7 \text{ nm}^2$, $V_s = -0.55 \text{ V}$, $I_t = 80 \text{ pA}$; c) $42.7 \times 42.7 \text{ nm}^2$, $V_s = -1.17 \text{ V}$, $I_t = 47 \text{ pA}$; d) $12.0 \times 12.0 \text{ nm}^2$, $V_s = -1.06 \text{ V}$, $I_t = 78 \text{ pA}$; e) $68.8 \times 68.8 \text{ nm}^2$, $V_s = -1.00 \text{ V}$, $I_t = 39 \text{ pA}$; f) $19.5 \times 19.5 \text{ nm}^2$, $V_s = -1.16 \text{ V}$, $I_t = 34 \text{ pA}$.

Similar to the case of SR-10-152, we tentatively ascribe pairs of bright protrusions to the aryl rings of SR-10-134 molecules, given their molecular structure and given that no DOS is found in the LUMO on the alkyl chains (Figure 6.2c). This interpretation is supported by STM micrographs obtained at positive and negative bias polarity, which hence are a map of the convolution of occupied and unoccupied electronic states of the adsorbate, respectively, and the LDOS of the substrate (Figure 8.61). Note that in the model in Figure 8.61 it was not possible to define the packing of the side group $R = C_8H_{17}$ because of the poor resolution of the STM data. Similar to the SR-10-152 case, the angle between the stacking axis and the diacetylene moiety is favorable for topochemical polymerization, as opposed to the SAMN of Maude-2-041 molecules. However, we did not attempt to polymerize the system in Figure 8.61 because the goal of this project is to exploit the nitrogen atoms to achieve the edge-on adsorption geometry favorable for polymerization. Experiments in this respect are still ongoing in our group.

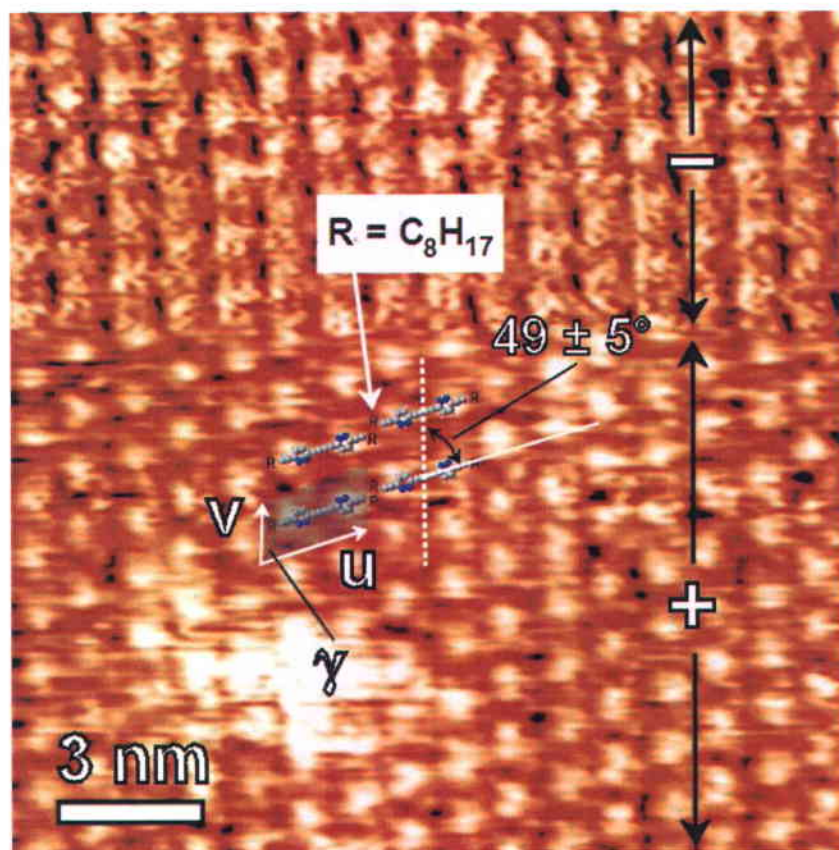


Figure 8.61: STM image of SR-10-134 molecules assembled at the TCB-HOPG interface, obtained at both positive and negative bias polarity ($17.8 \times 17.8 \text{ nm}^2$, $V_s = \pm 1.0 \text{ V}$, $I_t = 372 \text{ pA}$). The unit cell vectors are $u = 2.00 \pm 0.10 \text{ nm}$, $v = 1.20 \pm 0.05 \text{ nm}$ and the angle between them is $\gamma = 90 \pm 2^\circ$.

Chapter 9. CONCLUSIONS AND PERSPECTIVES

We performed a STM and DFT study of 2D self-assembled supramolecular networks at the liquid-solid interface. The systematic study of the two halogenated precursors TIPT and TBPT revealed that on HOPG the molecular packing does not change substantially by varying the halogen atoms (Figure 8.5 and Figure 8.15). However, these structures are different from those reported in the literature for the similar molecules TIPB and TBPB on HOPG (Figure 8.6 and Figure 8.18). DFT calculations show that the molecular building blocks are laterally stabilized by $X\cdots H$ weak hydrogen bonds, with X being the halogen atoms (Table 8.4). Moreover, the triazine core of the investigated molecules renders these precursors stiffer than the counterpart molecules TIPB and TBPB (Figure 8.13). From an entropic point of view, this minimizes the initial accessible states hence making self-assembly of TIPT and TBPT more favorable than TIPB and TBPB. Interestingly, varying solvents revealed that TBPT forms a bi-component polymorph not observed for TIPT (Figure 8.20), emphasizing the subtlety of the energetics involved in the formation of such weakly bonded SAMNs.

TIPT and TBPT exhibit different behaviors on Au(111). Whereas the former assembles with some domains similar to its counterpart TIPB (Figure 8.45), as reported in the literature, the pattern obtained with TBPT exhibits interesting features due to substrate effects (Figure 8.31). TBPT molecules assemble in two different phases on the two differently reconstructed regions of the surface (*i.e.* *fcc* vs. *hcp*). This molecule is the first reported to form a monolayer SAMN at the liquid-solid interface that is sensitive to the differently reconstructed regions of the Au(111) surface. Given that such behavior is not observed for TBPB on Au(111), we ascribe this effect to the presence of the triazine core in the molecular building blocks. This feature, which makes TBPT molecules planar, perhaps leads to stronger molecule \cdots substrate interactions therefore causing the observed sensitivity to the *hcp*- and *fcc*-stacked regions of the substrate. The occurrence of the two phases is also due to the similarity between the two polymorphs, which allows stable phase boundaries.

The investigation of the diacetylene precursors revealed that the molecular packing of Maude-2-041 molecules on HOPG is unfavorable for polymerization. In the specific, the reacting 1,4-carbon atoms are too far apart as a consequence of the steric hindrance

introduced by the phenyl rings (Figure 8.53). Despite the fact that weak molecule-substrate interactions are expected on HOPG, we found that the alkyl chains of the molecules within the adlayer align along the high-symmetry zig-zag directions of the substrate (Figure 8.54). This is due to the registry between substrate periodicity along such direction and the periodicity of the methylene groups of the chains (Groszek model). Given the unfavorable packing of Maude-2-041 on HOPG we investigated nitrogen-containing molecules on Au(111), namely SR-10-152 and SR-10-134. The goal was to achieve a vertical adsorption configuration (edge-on) of the aryl groups, through a stronger coupling between the unshared electron pair of their nitrogen atoms and the surface, which would be favorable for polymerization. Our data demonstrate that such stronger interaction is perhaps achieved, given that we were able to image adsorbates at sub-ML coverage (Figure 8.57). However, long-range ordered SAMNs that could potentially lead to surface polymers were not ultimately achieved.

Possible future works for the halogenated molecules may focus on the sub-ML investigation of TBPT networks on Au(111) in UHV. This could elucidate insights in the balance between molecule···molecule and molecule···substrate interactions and perhaps address more quantitatively the occurrence of the two phases at ML coverage reported in this work. DFT calculations that also account for the effect of the substrate could be very helpful in this respect. Regarding surface polymerization at the liquid-solid interface much still needs to be done both for TBPT and TIPT. Different approaches for this type of experiments include: i) heating the substrate before or after deposition; ii) heating the solution before deposition; iii) tuning the concentration of the solution to avoid macroscopic aggregates after solvent evaporation; iv) rinsing the substrate after molecular deposition or v) varying the nature of the solvent. Several of these potentially successful approaches were attempted in this work, but none succeeded. We believe that particular effort must be put in understanding the process of molecular adsorption when the solutions are deposited on a hot substrate.

Achieving the edge-on adsorption configuration of the nitrogen-containing precursors for diacetylene polymerization at the liquid-Au(111) interface is considerably more challenging than the experiments on HOPG. Performing experiments in UHV may be a solution to these hurdles, given the more controlled environment and hence the fewer variables to take into account. A temperature-dependent study may address potential activation barriers that inhibit the formation of long-range ordered networks with the required adsorption geometry.

LIST OF PUBLICATIONS

R. Gatti, J.M. MacLeod, J.A. Lipton-Duffin, A. Moiseev, D.F. Perepichka, F. Rosei, Substrate, Molecular Structure and Solvent Effects in 2D Self-Assembly *via* Hydrogen and Halogen Bonding. *J. Phys. Chem. C* **2014** – submitted.

L.E. Dinca, F. De Marchi, J.M. MacLeod, J.A. Lipton-Duffin, **R. Gatti**, D. Ma, D.F. Perepichka, F. Rosei, Pentacene on Ni(111): Room-Temperature Molecular Packing and Temperature-Activated Conversion to Graphene. *Langmuir* **2014** – in preparation.

LIST OF ATTENDED CONFERENCES

Materials Science & Technology (MS&T), 27th–31st October 2013, Montréal, QC, Canada –
Oral Contribution

Canadian Association of Physicists (CAP), 27th–31st May 2013, Montréal, QC, Canada – **Oral
Contribution**

Joint Workshop on Functional Materials and Surfaces, 23rd May 2013, Montréal, QC, Canada
– **Poster Contribution**

REFERENCES

1. Moore, G. E., Cramming More Components onto Integrated Circuits. *Electronics* **1965**, *38*.
2. Wagner, C.; Harned, N., Euv Lithography: Lithography Gets Extreme. *Nat. Photonics* **2010**, *4*, 24-26.
3. Thompson, S.; Parthasarathy, S., Moore's Law: The Future of Si Microelectronics. *Mater. Today* **2006**, *9*, 20-25.
4. Whitesides, G. M.; Mathias, J. P.; Seto, C. T., Molecular Self-Assembly and Nanochemistry - a Chemical Strategy for the Synthesis of Nanostructures. *Science* **1991**, *254*, 1312-1319.
5. Palma, C. A.; Cecchini, M.; Samorì, P., Predicting Self-Assembly: From Empirism to Determinism. *Chem. Soc. Rev.* **2012**, *41*, 3713-30.
6. Lehn, J.-M., Toward Complex Matter: Supramolecular Chemistry and Self-Organization. *Proc. Natl. Acad. Sci. U.S.A.* **2002**, *99*, 4763-4768.
7. Wikipedia. <http://en.wikipedia.org/>.
8. Nahmad-Molinari, Y.; Ruiz-Suárez, J., Epitaxial Growth of Granular Single Crystals. *Phys. Rev. Lett.* **2002**, *89*, 264302(4).
9. Clark, T. D.; Tien, J.; Duffy, D. C.; Paul, K. E.; Whitesides, G. M., Self-Assembly of 10-Um-Sized Objects into Ordered Three-Dimensional Arrays. *J. Am. Chem. Soc.* **2001**, *123*, 7677-7682.
10. He, Y.; Ye, T.; Su, M.; Zhang, C.; Ribbe, A. E.; Jiang, W.; Mao, C., Hierarchical Self-Assembly of DNA into Symmetric Supramolecular Polyhedra. *Nature* **2008**, *452*, 198-201.
11. Sun, Q. F.; Iwasa, J.; Ogawa, D.; Ishido, Y.; Sato, S.; Ozeki, T.; Sei, Y.; Yamaguchi, K.; Fujita, M., Self-Assembled M24I48 Polyhedra and Their Sharp Structural Switch Upon Subtle Ligand Variation. *Science* **2010**, *328*, 1144-1147.
12. Adisoejoso, J.; Tahara, K.; Okuhata, S.; Lei, S.; Tobe, Y.; De Feyter, S., Two-Dimensional Crystal Engineering: A Four-Component Architecture at a Liquid-Solid Interface. *Angew Chem Int Ed Engl* **2009**, *48*, 7353-7.
13. Barth, J. V.; Costantini, G.; Kern, K., Engineering Atomic and Molecular Nanostructures at Surfaces. *Nature* **2005**, *437*, 671-679.
14. Mali, K. S.; Lava, K.; Binnemans, K.; De Feyter, S., Hydrogen Bonding Versus Van Der Waals Interactions: Competitive Influence of Noncovalent Interactions on 2d Self-Assembly at the Liquid-Solid Interface. *Chem. - Eur. J.* **2010**, *16*, 14447-58.
15. Macleod, J. M.; Ivasenko, O.; Perepichka, D. F.; Rosei, F., Stabilization of Exotic Minority Phases in a Multicomponent Self-Assembled Molecular Network. *Nanotechnology* **2007**, *18*, 424031-424039.
16. Gutzler, R.; Ivasenko, O.; Fu, C.; Brusso, J. L.; Rosei, F.; Perepichka, D. F., Halogen Bonds as Stabilizing Interactions in a Chiral Self-Assembled Molecular Monolayer. *Chem. Commun.* **2011**, *47*, 9453-5.
17. Björk, J.; Hanke, F.; Palma, C.-A.; Samorì, P.; Cecchini, M.; Persson, M., Adsorption of Aromatic and Anti-Aromatic Systems on Graphene through π - π Stacking. *J. Phys. Chem. Lett.* **2010**, *1*, 3407-3412.
18. Clark, T.; Hennemann, M.; Murray, J. S.; Politzer, P., Halogen Bonding: The Sigma-Hole. Proceedings of "Modeling Interactions in Biomolecules II", Prague, September 5th-9th, 2005. *J. Mol. Model.* **2007**, *13*, 291-6.
19. Gutzler, R.; Fu, C.; Dadvand, A.; Hua, Y.; MacLeod, J. M.; Rosei, F.; Perepichka, D. F., Halogen Bonds in 2d Supramolecular Self-Assembly of Organic Semiconductors. *Nanoscale* **2012**, *4*, 5965-71.
20. Bieri, M.; Blankenburg, S.; Kivala, M.; Pignedoli, C. A.; Ruffieux, P.; Mullen, K.; Fasel, R., Surface-Supported 2d Heterotriangulene Polymers. *Chem Commun (Camb)* **2011**, *47*, 10239-41.
21. Lafferentz, L. E., V.; Dri, C.; Africh, C.; Comelli, G.; Esch, F.; Hecht, S.; Grill, L., Controlling on-Surface Polymerization by Hierarchical and Substrate-Directed Growth. *Nature Chemistry* **2012**, *4*.
22. Okawa, Y. A., M., Nanoscale Control of Chain Polymerization. *Nature* **2001**, *409*.

23. Sakaguchi, H.; Matsumura, H.; Gong, H., Electrochemical Epitaxial Polymerization of Single-Molecular Wires. *Nature materials* **2004**, *3*, 551-7.
24. Okawa, Y.; Aono, M., Linear Chain Polymerization Initiated by a Scanning Tunneling Microscope Tip at Designated Positions. *J. Chem. Phys.* **2001**, *115*, 2317-2322.
25. Binnig, G.; Rohrer, H.; Gerber, C.; Weibel, E., 7×7 Reconstruction on Si(111) Resolved in Real Space. *Phys. Rev. Lett.* **1983**, *50*, 120-123.
26. Makoudi, Y.; Baris, B.; Jeannoutot, J.; Palmino, F.; Grandidier, B.; Cherioux, F., Tailored Molecular Design for Supramolecular Network Engineering on a Silicon Surface. *Chemphyschem : a European journal of chemical physics and physical chemistry* **2013**, *14*, 900-4.
27. Crommie, M. F.; Lutz, C. P.; Eigler, D. M., Confinement of Electrons to Quantum Corrals on a Metal Surface. *Science* **1993**, *262*, 218-220.
28. Wiesendanger, R., Spin Mapping at the Nanoscale and Atomic Scale. *Rev. Mod. Phys.* **2009**, *81*, 1495-1550.
29. Hohenberg, P.; Kohn, W., Inhomogeneous Electron Gas. *Phys. Rev.* **1964**, *136*, B864-B871.
30. Redner, S., Citation Statistics from More Than a Century of Physical Review. *Bull. Am. Phys. Soc.* **2005**.
31. Gutzler, R.; Walch, H.; Eder, G.; Kloft, S.; Heckl, W. M.; Lackinger, M., Surface Mediated Synthesis of 2d Covalent Organic Frameworks: 1,3,5-Tris(4-Bromophenyl)Benzene on Graphite(001), Cu(111), and Ag(110). *Chem. Commun.* **2009**, 4456-8.
32. Silly, F., Selecting Two-Dimensional Halogen-Halogen Bonded Self-Assembled 1,3,5-Tris(4-Iodophenyl)Benzene Porous Nanoarchitectures at the Solid-Liquid Interface. *J. Phys. Chem. C* **2013**, *117*, 20244-20249.
33. The Nobel Prize in Physics 1956. http://www.nobelprize.org/nobel_prizes/physics/laureates/1956/.
34. Tanenbaum, M.; Valdes, L. B.; Buehler, N. B., *J. Appl. Phys.* **1955**, *26*, 686-692.
35. Kilby, J. S.; Keonjian, E., Design of a Semiconductor-Solid-Circuit Adder. *Tech. Dig. IEDM* **1959**, *5*, 76-78.
36. Dawon, K. 1963.
37. Gates, B. D. X., Q.; Stewart, M.; Ryan, D.; Willson, C. G.; Whitesides, G. M., New Approaches to Nanofabrication: Molding, Printing, and Other Techniques. *Chem. Rev.* **2005**, *105*, 1171-1196.
38. De Feyter, S.; De Schryver, F. C., Two-Dimensional Supramolecular Self-Assembly Probed by Scanning Tunneling Microscopy. *Chem. Soc. Rev.* **2003**, *32*, 139-150.
39. Burroughes, J. H.; Bradley, D. D. C.; Brown, A. R.; Marks, R. N.; Mackay, K.; Friend, R. H.; Burns, P. L.; Holmes, A. B., Light-Emitting Diodes Based on Conjugated Polymers. *Nature* **1990**, *347*, 539-541.
40. Chua, L.-L.; Zaumseil, J.; Chang, J.-F.; Ou, E. C.-W.; Ho, P. K.-K.; Sirringhaus, H.; Friend, R. H., General Observation of N-Type Field-Effect Behaviour in Organic Semiconductors. *Nature* **2005**, *434*, 194-199.
41. Mutolo, K. L.; Mayo, E. I.; Rand, B. P.; Forrest, S. R.; Thompson, M. E., Enhanced Open-Circuit Voltage in Subphthalocyanine/C₆₀ Organic Photovoltaic Cells. *J. Am. Chem. Soc.* **2006**, *128*, 8108.
42. Whitesides, G. M.; Grzybowski, B., Self-Assembly at All Scales. *Science* **2002**, *295*, 2418-2421.
43. Kushner, D. J., *Bacteriol. Rev.* **1969**, *33*, 302-345.
44. Shen, Y.-T. Z., N.-B.; Zhang, X.-M.; Lei, S.; Wei, Z.; Li, M.; Zhao, D.; Zeng, Q.-D.; Wang, C., Assemblies, at the Liquid-Solid Interface: Chirality Expression from Molecular Conformers. *Chemphyschem : a European journal of chemical physics and physical chemistry* **2013**, *14*.
45. Lim, J.; Lee, W.; Kwak, D.; Cho, K., Evaporation-Induced Self-Organization of Inkjet-Printed Organic Semiconductors on Surface-Modified Dielectrics for High-Performance Organic Transistors. *Langmuir* **2009**, *25*, 5404-10.
46. Langmuir, I., The Mechanism of the Surface Phenomena of Flotation. *Trans. Faraday Soc.* **1920**, *15*.
47. Ciesielski, A.; Palma, C. A.; Bonini, M.; Samori, P., Towards Supramolecular Engineering of Functional Nanomaterials: Pre-Programming Multi-Component 2d Self-Assembly at Solid-Liquid Interfaces. *Adv Mater* **2010**, *22*, 3506-20.
48. Kudernac, T.; Lei, S.; Elemans, J. A.; De Feyter, S., Two-Dimensional Supramolecular Self-Assembly: Nanoporous Networks on Surfaces. *Chemical Society reviews* **2009**, *38*, 402-21.

49. Macleod, J. M.; Ben Chaouch, Z.; Perepichka, D. F.; Rosei, F., Two-Dimensional Self-Assembly of a Symmetry-Reduced Tricarboxylic Acid. *Langmuir* **2013**, *29*, 7318-24.
50. Gutzler, R.; Cardenas, L.; Rosei, F., Kinetics and Thermodynamics in Surface-Confined Molecular Self-Assembly. *Chem. Sci.* **2011**, *2*, 2290-2300.
51. Hof, F. R., J. Jr., Molecules within Molecules: Recognition through Self-Assembly. *PNAS* **2002**, *99*.
52. Kühnle, A. L., T. R.; Hammer, B.; Besenbacher, F., Chiral Recognition in Dimerization of Adsorbed Cysteine Observed by Scanning Tunneling Microscopy. *Nature* **2002**, *415*.
53. Maksymovych, P.; Sorescu, D.; Yates, J., Gold-Adatom-Mediated Bonding in Self-Assembled Short-Chain Alkanethiolate Species on the Au(111) Surface. *Phys. Rev. Lett.* **2006**, *97*.
54. Nath, K. G.; Ivasenko, O.; MacLeod, J. M.; Miwa, J. A.; Wuest, J. D.; Nanci, A.; Perepichka, D. F.; Rosei, F., Crystal Engineering in Two Dimensions: An Approach to Molecular Nanopatterning. *J. Phys. Chem. C* **2007**, *111*, 16996-17007.
55. Bléger, D.; Bocheux, A.; Kreher, D.; Mathevet, F.; Attias, A.-J.; Metgé, G.; Douillard, L.; Fiorini-Debuisschert, C.; Charra, F., An Optimized Alkyl Chain-Based Binding Motif for 2d Self-Assembly: A Comprehensive Crystallographic Approach. *Nanoscale* **2013**, *5*, 1452-1455.
56. Baris, B.; Luzet, V.; Duverger, E.; Sonnet, P.; Palmino, F.; Cherioux, F., Robust and Open Tailored Supramolecular Networks Controlled by the Template Effect of a Silicon Surface. *Angew. Chem., Int. Ed.* **2011**, *50*, 4094-8.
57. Grimme, S., Do Special Noncovalent Pi-Pi Stacking Interactions Really Exist? *Angew. Chem. Int. Ed.* **2008**, *47*, 3430-4.
58. Lackinger, M. G., S.; Heckl, W. M.; Hietschold, M.; Flynn, G. W., Self-Assembly of Trimesic Acid at the Liquid-Solid Interface - a Study of Solvent-Induced Polymorphism. *Langmuir* **2005**, *21*.
59. Stepanow, S.; Lin, N.; Barth, J. V.; Kern, K., Surface-Template Assembly of Two-Dimensional Metal-Organic Coordination Networks. *J. Phys. Chem. B* **2006**, *110*, 23472-23477.
60. Di Giovannantonio, M. E. G., M.; Lipton-Duffin, J.; Meunier, V.; Cardenas, L.; Revurat, Y. F.; Cossaro, A.; Verdini, A.; Perepichka, D. F.; Rosei, F.; Contini, G., Insight into Organometallic Intermediate and Its Evolution to Covalent Bonding in Surface-Confined Ullmann Polymerization. *ACS Nano* **2013**, *7*, 8190-8198.
61. Desiraju, G. R.; Ho, P. S.; Kloo, L.; Legon, A. C.; Marquardt, R.; Metrangolo, P.; Politzer, P.; Resnati, G.; Rissanen, K., Definition of the Halogen Bond (Iupac Recommendations 2013). *Pure Appl. Chem.* **2013**, *85*, 1711-1713.
62. El Garah, M.; Lipton-Duffin, J.; Macleod, J. M.; Gutzler, R.; Palmino, F.; Luzet, V.; Cherioux, F.; Rosei, F., Self-Assembly of a Halogenated Molecule on Oxide-Passivated Cu(110). *Chem. - Asian. J.* **2013**, *8*, 1-6.
63. Müller, T.; Werblowsky, T. L.; Florio, G. M.; Berne, B. J.; Flynn, G. W., Ultra-High Vacuum Scanning Tunneling Microscopy and Theoretical Studies of 1-Halohexane Monolayers on Graphite. *Proc. Natl. Acad. Sci. U.S.A.* **2005**, *102*, 5315-22.
64. Florio, G. M.; Werblowsky, T. L.; Ilan, B.; Müller, T.; Berne, B. J.; Flynn, G. W., Chain-Length Effects on the Self-Assembly of Short 1-Bromoalkane and N-Alkane Monolayers on Graphite. *J. Phys. Chem. C* **2008**, *112*, 18067-18075.
65. Yoon, J. K. S., W.-j., Chung, K.-H.; Kim, H.; Han, S.; Kahng, S.-J., Visualizing Halogen Bonds in Planar Supramolecular Systems. *J. phys. Chem. C* **2011**, *115*.
66. Bui, T. T. T.; Dahaoui, S.; Lecomte, C.; Desiraju, G. R.; Espinosa, E., The Nature of Halogen•••Halogen Interactions: A Model Derived from Experimental Charge-Density Analysis. *Angew. Chem. Int. Ed.* **2009**, *48*, 3838-3841.
67. Reddy, C. M.; Kirchner, M. T.; Gundakaram, R. C.; Padmanabhan, K. A.; Desiraju, G. R., Isostructurality, Polymorphism and Mechanical Properties of Some Hexahalogenates Benzenes: The Nature of Halogen•••Halogen Interactions. *Chem. - Eur. J.* **2006**, *12*, 2222-2234.
68. Metrangolo, P.; Meyer, F.; Pilati, T.; Resnati, G.; Terraneo, G., Halogen Bonding in Supramolecular Chemistry. *Angew. Chem. Int. Ed.* **2008**, *47*, 6114-27.

69. Forrest, S. R., The Path to Ubiquitous and Low-Cost Organic Electronic Appliances on Plastic. *Nature* **2004**, *428*, 911-918.
70. Grim, P. C. M. D. F., S.; Gesquière, A.; Vanoppen, P.; Rücker, M.; Valiyaveetil, S.; Moessner, G.; Müllen, K.; De Schryver, F. C.;, Submolecularly Resolved Polymerization of Diacetylene Molecules on the Graphite Surface Observed with Scanning Tunneling Microscopy. *Angew. Chem. Int. Ed. Engl.* **1997**, *36*.
71. D. F. Perepichka, F. R., Extending Polymer Conjugation into the Second Dimension. *Science* **2009**, *323*.
72. El Garah, M. M., J. M.; Rosei, F.;, Covalently Bonded Networks through Surface-Confined Polymerization. *Surf. Sci.* **2013**, *613*.
73. Lackinger, M. H., W. M.;, A Stm Perspective on Covalent Intermolecular Coupling Reactions on Surfaces. *J. Phys. D: Appl. Phys.* **2011**, *44*.
74. Grill, L. D., M.; Lafferentz, L.; Persson, M.; Peters, M. V.; Hecht, S., Nano-Architectures by Covalent Assembly of Molecular Building Blocks. *Nature* **2007**, *2*.
75. Treier, M. P., C. A.; Laino, T.; Rieger, R.; Mullen, K.; Passerone, D.; Fasel, R., Surface-Assisted Cyclodehydrogenation Provides a Synthetic Route Towards Easily Processable and Chemically Tailored Nanographenes. *Nat. Chem.* **2011**, *3*.
76. Kertesz, M. C., C. H.; Yang, S.;, Conjugated Polymers and Aromaticity. *Chem. Rev.* **2005**, *105*.
77. Zaumseil, J. S., H.;, Electron and Ambipolar Transport in Organic Field-Effect Transistors. *Chemical Reviews* **2007**, *107*.
78. Bieri, M., et al., Porous Graphenes: Two-Dimensional Polymer Synthesis with Atomic Precision. *Chem Commun (Camb)* **2009**, 6919-21.
79. Cai, J., et al., Atomically Precise Bottom-up Fabrication of Graphene Nanoribbons. *Nature* **2010**, *466*, 470-3.
80. Novoselov, K. S.; Geim, A. K.; Morozov, S. V.; Jiang, D.; Zhang, Y.; Dubonos, S. V.; Grigorieva, I. V.; Firsov, A. A., Electric Field Effect in Atomically Thin Carbon Films. *Science* **2004**, *306*, 666-9.
81. Novoselov, K. S.; Jiang, D.; Schedin, F.; Booth, T. J.; Khotkevich, V. V.; Morozov, S. V.; Geim, A. K., Two-Dimensional Atomic Crystals. *Proceedings of the National Academy of Sciences of the United States of America* **2005**, *102*, 10451-3.
82. Ullmann, F. M., G.; Loewenthal, O.; Gilli, E.;, *Justus Liebigs Ann. Chem.* **1904**, *3332*.
83. Enkelmann, V., Structural Aspects of the Topochemical Polymerization of Diacetylenes. *Adv. Pol. Sci.* **1984**, *63*, 91-136.
84. Lipton-Duffin, J. A.; Ivasenko, O.; Perepichka, D. F.; Rosei, F., Synthesis of Polyphenylene Molecular Wires by Surface-Confined Polymerization. *Small* **2009**, *5*, 592-7.
85. Lipton-Duffin, J. A. M., J. A.; Kondratenko, M.; Cicoira, F.; Sumpter, B. G.; Meunier, V.; Perepichka, D. F.; Rosei, F.;, Step-by-Step Growth of Epitaxially Aligned Polythiophene by Surface-Confined Reaction. *PNAS* **2010**, *107*.
86. Cardenas, L., et al., Synthesis and Electronic Structure of a Two Dimensional Π -Conjugated Polythiophene. *Chem. Sci.* **2013**, *4*, 3263.
87. Schlickum, U., et al., Metal-Organic Honeycomb Nanomeshes with Tunable Cavity Size. *Nano Letters* **2007**, *7*, 3813-3817.
88. Saywell, A.; Greñ, W.; Franc, G.; Gourdon, A.; Bouju, X.; Grill, L., Manipulating the Conformation of Single Organometallic Chains on Au(111). *J. Phys. Chem. C* **2014**, *118*, 1719-1728.
89. Binnig, G.; Rohrer, H., Scanning Tunneling Microscopy — from Birth to Adolescence. *Rev. Mod. Phys.* **1987**, *59*, 615-625.
90. Binnig, G.; Rohrer, H.; Gerber, C.; Weibel, E., Tunneling through a Controllable Vacuum Gap. *Applied Physics Letters* **1982**, *40*, 178-180.
91. Chen, C. J., *Introduction to Scanning Tunneling Microscopy*; Oxford University Press: New York, 1993; Vol. 227.
92. Stroscio, J. A.; Eigler, D. M., Atomic and Molecular Manipulation with the Scanning Tunneling Microscope. *Science* **1991**, *254*, 1319-1326.

93. Eigler, D. M.; Schweizer, E. K., Positioning Single Atoms with a Scanning Tunnelling Microscope. *Nature* **1990**, *344*, 524-526.
94. Stipe, B. C.; Rezaei, M. A.; Ho, W., Single-Molecule Vibrational Spectroscopy and Microscopy. *Science* **1998**, *280*, 1732-1735.
95. Lambe, J.; McCarthy, S., Light Emission from Inelastic Electron Tunneling. *Phys. Rev. Lett.* **1976**, *37*, 923-925.
96. Derycke, V.; Soukiassian, P. G.; Amy, F.; Chabal, Y. J.; D'Angelo M, D.; Enriquez, H. B.; Silly, M. G., Nanochemistry at the Atomic Scale Revealed in Hydrogen-Induced Semiconductor Surface Metallization. *Nat. Mater.* **2003**, *2*, 253-258.
97. Horcas, I.; Fernandez, R.; Gomez-Rodriguez, J. M.; Colchero, J.; Gomez-Herrero, J.; Baro, A. M., Wsxm: A Software for Scanning Probe Microscopy and a Tool for Nanotechnology. *Rev. Sci. Instrum.* **2007**, *78*, 013705.
98. Sykes, E. C. H.; Mantooh, B. A.; Han, P.; Donhauser, Z. J.; Weiss, P. S., Substrate-Mediated Intermolecular Interactions: A Quantitative Single Molecule Analysis. *J. Am. Chem. Soc.* **2005**, *127*, 7255-7260.
99. Kohn, W.; Sham, L. J., Self-Consistent Equations Including Exchange and Correlation Effects. *Phys. Rev.* **1965**, *140*, A1133-A1138.
100. Levy, M., Universal Variational Functionals of Electron Densities, First-Order Density Matrices, and Natural Spin-Orbitals and Solution of the V-Representability Problem. *Proc. Natl. Acad. Sci. U.S.A.* **1979**, *76*, 6062-6065.
101. Sholl, D. S.; Steckel, J. A., *Density Functional Theory: A Practical Introduction*; John Wiley & Sons: Hoboken, New Jersey, 2009.
102. Perdew, J. P.; Ruzsinszky, A.; Constantin, L. A.; Sun, J.; Csonka, G. I., Some Fundamental Issues in Ground-State Density Functional Theory: A Guide for the Perplexed. *J. Chem. Theory Comput.* **2009**, *5*, 902-908.
103. Perdew, J. P.; Zunger, A., Self-Interaction Correction to Density-Functional Approximations for Many-Electron Systems. *Phys. Rev. B* **1981**, *23*, 5048-5079.
104. Dft Papers Citation from Chemists. <http://www.cas.org/spotlight/bchem03/bchem03.html>.
105. Perdew, J. P.; Burke, K.; Ernzerhof, M., Generalized Gradient Approximation Made Simple. *Phys. Rev. Lett.* **1996**, *77*, 3865-3868.
106. Honkala, K.; Hellman, A.; Remediakis, I. N.; Logadottir, A.; Carlsson, A.; Dahl, S.; Christensen, C. H.; Norskov, J. K., Ammonia Synthesis from First-Principles Calculations. *Science* **2005**, *307*, 555-558.
107. Schweinfest, R.; Paxton, A. T.; Finnis, M. W., Bismuth Embrittlement of Copper Is an Atomic Size Effect. *Nature* **2004**, *432*, 1008-1011.
108. Umemoto, K.; Wentzcovitch, R. M.; Allen, P. B., Dissociation of MgSiO₃ in the Cores of Gas Giants and Terrestrial Exoplanets. *Science* **2006**, *311*, 983-986.
109. Kohn Pople Nobel Prize 1998. http://www.nobelprize.org/nobel_prizes/chemistry/laureates/1998/advanced.html.
110. Physics Nobel Prize 2012. http://www.nobelprize.org/nobel_prizes/physics/laureates/2012/.
111. Tran, H. T.; Perdew, J. P., How Metals Bind: The Deformable-Jellium Model with Correlated Electrons. *Am. J. Phys.* **2003**, *71*, 1048-1061.
112. Kurth, S.; Perdew, J. P., Role of the Exchange–Correlation Energy: Nature’s Glue. *Int. J. Quantum Chem.* **2000**, *77*, 814-818.
113. Perdew, J. P.; Ruzsinszky, A.; Tao, J.; Staroverov, V. N.; Scuseria, G. E.; Csonka, G. I., Prescription for the Design and Selection of Density Functional Approximations: More Constraint Satisfaction with Fewer Fits. *J. Chem. Phys.* **2005**, *123*, 62201(9).
114. Kurth, S.; Perdew, J. P.; Blaha, P., Molecular and Solid-State Tests of Density Functional Approximations: Lsd, Ggas, and Meta-Ggas. *Int. J. Quantum Chem.* **1999**, *75*, 889-909.
115. Becke, A. D., Density-Functional Thermochemistry. Iii. The Role of Exact Exchange. *J. Chem. Phys.* **1993**, *98*, 5648-5652.
116. Zhao, Y.; Schultz, N. E.; Truhlar, D. G., Exchange-Correlation Functional with Broad Accuracy for Metallic and Nonmetallic Compounds, Kinetics, and Noncovalent Interactions. *J. Chem. Phys.* **2005**, *123*, 161103(4).

117. Becke, A. D., A New Inhomogeneity Parameter in Dft. *J.Chem. Phys.* **1998**, *109*, 2092–2098.
118. Zhao, Y.; Truhlar, D. G., Density Functionals with Broad Applicability in Chemistry. *Acc. Chem. Res.* **2008**, *41*, 157-167.
119. Zhao, Y.; Truhlar, D. G., A New Local Density Functional for Main-Group Thermochemistry, Transition Metal Bonding, Thermochemical Kinetics, and Noncovalent Interactions. *J. Chem. Phys.* **2006**, *125*, 194101(18).
120. Grimme, S., Semiempirical Hybrid Density Functional with Perturbative Second-Order Correlation. *J. Chem. Phys.* **2006**, *124*, 034108(16).
121. Constantin, L. A.; Pitarke, J. M.; Dobson, J. F.; Garcia-Lekue, A.; Perdew, J. P., High-Level Correlated Approach to the Jellium Surface Energy, without Uniform-Electron-Gas Input. *Phys. Rev. Lett.* **2008**, *100*, 036401(4).
122. Dion, M.; Rydberg, H.; Schröder, E.; Langreth, D. C.; Lundqvist, B. I., Van Der Waals Density Functional for General Geometries. *Phys. Rev. Lett.* **2004**, *92*, 246401(4).
123. Perdew, J. P.; Staroverov, V. N.; Tao, J.; Scuseria, G. E., Density Functional with Full Exact Exchange, Balanced Nonlocality of Correlation, and Constraint Satisfaction. *Phys. Rev. A* **2008**, *78*, 052513(13).
124. Becke, A. D., Density-Functional Exchange-Energy Approximation with Correct Asymptotic Behavior. *Phys. Rev. A* **1988**, *38*, 3098-3100.
125. Stephens, P. J.; Devlin, F. J.; Chabalowski, C. F.; Frisch, M. J., Ab Initio Calculation of Vibrational Absorption and Circular Dichroism Spectra Using Density Functional Force Fields. *J. Phys. Chem.* **1994**, *98*, 11623-11627.
126. Lee, C.; Yang, W.; Parr, R. G., Development of the Colle-Salvetti Correlation-Energy Formula into a Functional of the Electron Density. *Phys. Rev. B* **1988**, *37*, 785-789.
127. Paier, J.; Marsman, M.; Kresse, G., Why Does the B3lyp Hybrid Functional Fail for Metals? *J. Chem. Phys.* **2007**, *127*, 024103(10).
128. Frisch, M. J., et al., *Gaussian 09*, Revision B.01; Gaussian, Inc.: Wallingford CT, 2009.
129. Vosko, S. H.; Wilk, L.; Nusair, M., Accurate Spin-Dependent Electron Liquid Correlation Energies for Local Spin Density Calculations: A Critical Analysis. *Can. J. Phys.* **1980**, *58*, 1200-1211.
130. Gaussian09 Functionals. http://www.gaussian.com/g_tech/g_ur/k_dft.htm.
131. Pople, J. A.; Head-Gordon, M.; Fox, D. J.; Raghavachari, K.; Curtiss, L. A., Gaussian-1 Theory: A General Procedure for Prediction of Molecular Energies. *J. Chem. Phys.* **1989**, *90*, 5622-5629.
132. Becke, A. D., Density-Functional Thermochemistry. Iv. A New Dynamical Correlation Functional and Implications for Exact-Exchange Mixing. *J. Chem. Phys.* **1996**, *104*, 1040-1046.
133. Zhao, Y.; Truhlar, D. G., The M06 Suite of Density Functionals for Main Group Thermochemistry, Thermochemical Kinetics, Noncovalent Interactions, Excited States, and Transition Elements: Two New Functionals and Systematic Testing of Four M06-Class Functionals and 12 Other Functionals. *Theor. Chem. Acc.* **2008**, *120*, 215-241.
134. Perdew, J. P.; Ernzerhof, M.; Burke, K., Rationale for Mixing Exact Exchange with Density Functional Approximations. *J. Chem. Phys.* **1996**, *105*, 9982-9985.
135. Perdew, J. P.; Wang, Y., Accurate and Simple Analytic Representation of the Electron-Gas Correlation Energy. *Phys. Rev. B* **1992**, *45*, 13244–13249.
136. Stoll, H.; Pavlidou, C. M. E.; Preuss, H., On the Calculation of Correlation Energies in the Spin-Density Functional Formalism. *Theor. Chim. Acta* **1978**, *49*, 143-149.
137. Van Voorhis, T.; Scuseria, G. E., A Novel Form for the Exchange-Correlation Energy Functional. *J. Chem. Phys.* **1998**, *109*, 400-410.
138. Møller, C.; Plesset, M. S., Note on an Approximation Treatment for Many-Electron Systems. *Phys. Rev.* **1934**, *46*, 618-622.
139. Szabo, A.; Ostlund, N. S., *Modern Quantum Chemistry: Introduction to Advanced Electronic Structure Theory.* ; Dovers Publications: Chicago, 1989.
140. Hariharan, P. C.; Pople, J. A., The Influence of Polarization Functions on Molecular Orbital Hydrogenation Energies. *Theor. Chim. Acta* **1973**, *28*, 213-222.

141. Francl, M. M.; Pietro, W. J.; Hehre, W. J.; Binkley, S.; Gordon, M. S.; DeFrees, D. J.; Pople, J. A., Self-Consistent Molecular Orbital Methods. Xxiii. A Polarization-Type Basis Set for Second-Row Elements. *J. Chem. Phys.* **1982**, *77*, 3654-3665.
142. Basis Sets 460. <http://chemistry.illinoisstate.edu/standard/che460/handouts/460basissets.pdf>.
143. Basis Sets Database Website. <https://bse.pnl.gov/bse/portal>.
144. Dunning Jr., T. H.; Hay, P. J., *Modern Theoretical Chemistry*: Plenum, New York, 1977; Vol. 3.
145. Wong, M. W.; Gill, P. M. W.; Nobes, R. H.; Radom, L., 6-311g(Mc)(D,P): A Second-Row Analogue of the 6-311g(D,P) Basis Set. Calculated Heats of Formation for Second-Row Hydrides. *J. Phys. Chem.* **1988**, *92*, 4875-4880.
146. Hay, P. J.; Wadt, W. R., Ab Initio Effective Core Potentials for Molecular Calculations - Potentials for K to Au Including the Outermost Core Orbitals. *J. Chem. Phys.* **1985**, *82*, 299-310.
147. Wadt, W. R.; Hay, P. J., Ab Initio Effective Core Potentials for Molecular Calculations - Potentials for Main Group Elements Na to Bi. *J. Chem. Phys.* **1985**, *82*, 284-298.
148. Hay, P. J.; Wadt, W. R., Ab Initio Effective Core Potentials for Molecular Calculations - Potentials for the Transition-Metal Atoms Sc to Hg. *J. Chem. Phys.* **1985**, *82*, 270-283.
149. Walch, H.; Gutzler, R.; Sirtl, T.; Eder, G.; Lackinger, M., Material- and Orientation-Dependent Reactivity for Heterogeneously Catalyzed Carbon-Bromine Bond Homolysis. *J. Phys. Chem. C* **2010**, *114*, 12604-12609.
150. Blunt, M. O.; Russell, J. C.; Champness, N. R.; Beton, P. H., Templating Molecular Adsorption Using a Covalent Organic Framework. *Chem. Commun.* **2010**, *46*, 7157-9.
151. Russell, J. C.; Blunt, M. O.; Garfitt, J. M.; Scurr, D. J.; Alexander, M.; Champness, N. R.; Beton, P. H., Dimerization of Tri(4-Bromophenyl)Benzene by Aryl-Aryl Coupling from Solution on a Gold Surface. *J. Am. Chem. Soc.* **2011**, *133*, 4220-3.
152. Baris, B.; Jeannoutot, J.; Luzet, V.; Palmino, F.; Rochefort, A.; Chérioux, F., Noncovalent Bicomponent Self-Assemblies on a Silicon Surface. *ACS Nano* **2012**, *6*, 6905-6911.
153. Eder, G.; Smith, E. F.; Cebula, I.; Heckl, W. M.; Beton, P. H.; Lackinger, M., Solution Preparation of Two-Dimensional Covalently Linked Networks by Polymerization of 1,3,5-Tri(4-Iodophenyl)Benzene on Au(111). *ACS Nano* **2013**, *7*, 3014-3021.
154. Schlögl, S.; Heckl, W. M.; Lackinger, M., On-Surface Radical Addition of Triply Iodinated Monomers on Au(111)—the Influence of Monomer Size and Thermal Post-Processing. *Surf. Sci.* **2012**, *606*, 999-1004.
155. Kaneda, Y.; Stawasz, M. E.; Sampson, D. L.; Parkinson, B. A., Stm Investigations of the Two-Dimensional Ordering of Perylenetetracarboxylic Acid N-Alkyl-Diimides on HOPG and MoS₂ Surfaces. *Langmuir* **2001**, *17*, 6185-6195.
156. Wang, X.; Scandolo, S.; Car, R., Carbon Phase Diagram from Ab Initio Molecular Dynamics. *Phys. Rev. Lett.* **2005**, *95*, 185701(4).
157. Hembacher, S.; Giessibl, F. J.; Mannhart, J.; Quate, C. F., Revealing the Hidden Atom in Graphite by Low-Temperature Atomic Force Microscopy. *Proc. Natl. Acad. Sci. U.S.A.* **2003**, *100*, 12539-12542.
158. Zacharia, R.; Ulbricht, H.; Hertel, T., Interlayer Cohesive Energy of Graphite from Thermal Desorption of Polyaromatic Hydrocarbons. *Phys. Rev. B* **2004**, *69*, 155406(8).
159. Maksymovych, P. S.; D. C.; Dougherty, D.; Yates Jr., J. T., Surface Bonding and Dynamical Behavior of the CH₃SH Molecule on Au(111). *J. Phys. Chem. B* **2005**, *109*.
160. Barth, J. V.; Brune, H.; Ertl, G.; Behm, R. J., Scanning Tunneling Microscopy Observations on the Reconstructed Au(111) Surface: Atomic Structure, Long-Range Superstructure, Rotational Domains, and Surface Defects. *Phys. Rev. B* **1990**, *42*, 9307-9318.
161. Sandy, A.; Mochrie, S.; Zehner, D.; Grübel, G.; Huang, K.; Gibbs, D., Reconstruction of the Pt(111) Surface. *Phys. Rev. Lett.* **1992**, *68*, 2192-2195.
162. Pushpa, R.; Narasimhan, S. V., D., Reconstruction of Pt(111) and Domain Patterns on Close-Packed Metal Surfaces. *Phys. Rev. B* **2003**, *67*, 205418(6).
163. Hanke, F.; Björk, J., Structure and Local Reactivity of the Au(111) Surface Reconstruction. *Phys. Rev. B* **2013**, *87*, 235422(6).

164. Goyhenex, C.; Bulou, H., Theoretical Insight in the Energetics of Co Adsorption on a Reconstructed Au(111) Substrate. *Phys. Rev. B* **2001**, *63*, 235404(5).
165. Schneider, K. S. N., K. T.; Fosnacht, D. R.; Orr, B. G.; Holl, M. M. B., Effect of Surface Reconstruction on Molecular Chemisorption: A Scanning Tunneling Microscopy Study of H₈Si₈O₁₂ Clusters on Au(111) 23X3. *Langmuir* **2002**, *18*, 8116.
166. Bach, C. E.; Giesen, M.; Ibach, H.; Einstein, T. L., Stress Relief in Reconstruction. *Phys. Rev. Lett.* **1997**, *78*, 425-428.
167. Maksymovych, P.; Dougherty, D. B., Molecular Self-Assembly Guided by Surface Reconstruction: Ch₃sh Monolayer on the Au(111) Surface. *Surface Science* **2008**, *602*, 2017-2024.
168. Rzeznicza, I. I. L., J.; Maksymovych, P.; Yates Jr., J. T., Nondissociative Chemisorption of Short Chain Alkanethiols on Au(111). *J. Phys. Chem. B* **2005**, *109*.
169. Meyer, J. A.; Baikie, I. D.; Kopatzki, E.; Behm, R. J., Preferential Island Nucleation at the Elbows of the Au(111) Herringbone Reconstruction through Place Exchange. *Surf. Sci.* **1996**, *365*, L647-L651.
170. Chambliss, D.; Wilson, R.; Chiang, S., Nucleation of Ordered Ni Island Arrays on Au(111) by Surface-Lattice Dislocations. *Phys. Rev. Lett.* **1991**, *66*, 1721-1724.
171. Mica. <http://www.emsdiasum.com/microscopy/products/preparation/mica.aspx>.
172. Levlin, M.; Laakso, A.; Niemi, H. E.-M.; Hautojärvi, P., Evaporation of Gold Thin Films on Mica: Effect of Evaporations Parameters. *Appl. Surf. Sci.* **1997**, *115*, 31-38.
173. Plummer, J. D.; Deal, M. D.; Griffin, P. B., *Silicon Vlsi Technology Fundamentals, Practice and Models*; Prentice Hall, 2000.
174. Cluster. <https://www.westgrid.ca/support/systems/Grex>.
175. Boys, S. F.; Bernardi, F., The Calculation of Small Molecular Interactions by the Differences of Separate Total Energies. Some Procedures with Reduced Errors. *Mol. Phys.* **1970**, *19*, 553-566.
176. Schwenke, D. W.; Truhlar, D. G., Systematic Study of Basis Set Superposition Errors in the Calculated Interaction Energy of Two Hf Molecules. *J. Chem. Phys.* **1985**, *82*, 2418-2426.
177. Bondi, A., Van Der Waals Volumes and Radii. *J. Phys. Chem.* **1964**, *68*, 441-451.
178. Basis Sets Gaussian. http://www.gaussian.com/g_tech/g_ur/m_basis_sets.htm.
179. Kim, C. K.; Yoon, S. H.; Won, J.; Kim, C. K., Examination of Gaussian-Type Basis Sets on Alkali Metal Iodides. *Bull. Korean Chem. Soc.* **2006**, *27*, 1219-1221.
180. Zhao, C.; Wang, D.; Phillips, D. L., Density Functional Theory Investigation of the Remarkable Reactivity of Geminal Dizinc Carbenoids (Rzn)₂chi (R) Et or I) as Cyclopropanation Reagents with Olefins Compared to Mono Zinc Carbenoids Rznchi₂, Etchiznr (R) Et or I). *J. Am. Chem. Soc.* **2002**, *124*, 12903-12914.
181. Nakamura, M.; Hirai, A.; Nakamura, E., Reaction Pathways of the Simmons-Smith Reaction. *J. Am. Chem. Soc.* **2003**, *125*, 2341-2350.
182. Zhang, Q.; Carpenter, C. J.; Kemper, P. R.; Bowers, M. T., On the Dissolution Processes of Na₂i+ and Na₃i₂ + with the Association of Water Molecules: Mechanistic and Energetic Details. *J. Am. Chem. Soc.* **2003**, *125*, 3341-3352.
183. Tsao, M.-L.; Hadad, C. M.; Platz, M. S., Computational Study of the Halogen Atom-Benzene Complexes. *J. Am. Chem. Soc.* **2003**, *125*, 8390-8399.
184. Deubel, D. V., From Evolution to Green Chemistry: Rationalization of Biomimetic Oxygen-Transfer Cascades. *J. Am. Chem. Soc.* **2004**, *126*, 996-997.
185. Marten, J.; Seichter, W.; Weber, E.; Böhme, U., Crystalline Packings of Diketoarylhydrazones Controlled by a Methyl for Trifluoromethyl Structural Change. *Cryst. Eng. Comm.* **2008**, *10*, 541-547.
186. Dunning, T. H., Gaussian Basis Sets for Use in Correlated Molecular Calculations. I. The Atoms Boron through Neon and Hydrogen. *J. Chem. Phys.* **1989**, *90*, 1007-1023.
187. Lu, Y.; Zou, J.; Wang, H.; Yu, Q.; Zhang, H.; Jiang, Y., Triangular Halogen Trimers. A Dft Study of the Structure, Cooperativity, and Vibrational Properties. *J. Phys. Chem. A* **2005**, *109*, 11956-11961.
188. Politzer, P.; Murray, J. S.; Clark, T., Halogen Bonding: An Electrostatically-Driven Highly Directional Noncovalent Interaction. *PhysChemChemPhys* **2010**, *12*, 7748-57.

189. Wang, F. F.; Hou, J. H.; Li, Z. R.; Wu, D.; Li, Y.; Lu, Z. Y.; Cao, W. L., Unusual Halogen-Bonded Complex $\text{Fbr}^{\delta+} \cdots \Delta^+ \text{Brf}$ and Hydrogen-Bonded Complex $\text{Fbr}^{\delta+} \cdots \Delta^+ \text{Hf}$ Formed by Interactions between Two Positively Charged Atoms of Different Polar Molecules. *J. Chem. Phys.* **2007**, *126*, 144301(5).
190. Wu, J.; Yan, H.; Cao, W., Study on the Nature of Unusual Hydrogen-Bonded Complexes Fclhx and Halogen-Bonded Complexes Fclclf . *J. Mol. Struct.: THEOCHEM* **2009**, *893*, 93-97.
191. Li, Q.; Li, R.; Zhou, Z.; Li, W.; Cheng, J., $\text{S} \cdots \text{X}$ Halogen Bonds and $\text{H} \cdots \text{X}$ Hydrogen Bonds in $\text{H}_2\text{cs-Xy}$ ($\text{Xy} = \text{Ff, Clf, Clcl, Brf, Brcl, and Brbr}$) Complexes: Cooperativity and Solvent Effect. *J. Chem. Phys.* **2012**, *136*, 014302(8).
192. Fourmigué, M.; Batail, P., Activation of Hydrogen- and Halogen-Bonding Interactions in Tetrathiafulvalene-Based Crystalline Molecular Conductors. *Chem. Rev.* **2004**, *104*, 5379-5418.
193. Ivasenko, O.; Perepichka, D. F., Mastering Fundamentals of Supramolecular Design with Carboxylic Acids. Common Lessons from X-Ray Crystallography and Scanning Tunneling Microscopy. *Chem. Soc. Rev.* **2011**, *40*, 191-206.
194. Macleod, J. M.; Ivasenko, O.; Fu, C.; Taerum, T.; Rosei, F.; Perepichka, D. F., Supramolecular Ordering in Oligothiophene-Fullerene Monolayers. *J. Am. Chem. Soc.* **2009**, *131*, 16844-16850.
195. Bartels, L.; Meyer, G.; Rieder, K.-H., Controlled Vertical Manipulation of Single Co Molecules with the Scanning Tunneling Microscope: A Route to Chemical Contrast. *Appl. Phys. Lett.* **1997**, *71*, 213-215.
196. Askadskaya, L.; Rabe, J. P., Anisotropic Molecular Dynamics in the Vicinity of Order-Disorder Transitions in Organic Monolayers. *Phys. Rev. Lett.* **1992**, *69*, 1395-1398.
197. Groszek, A. J., Selective Adsorption at Graphite/Hydrocarbon Interfaces. *Proc. R. Soc. Lond. A* **1970**, *314*, 473-498.
198. Rabe, J. P.; Buchholz, S., Commensurability and Mobility in 2-Dimensional Molecular Patterns on Graphite. *Science* **1991**, *253*, 424-426.
199. Paserba, K. R.; Gellman, A. J., Kinetics and Energetics of Oligomer Desorption from Surfaces. *Phys. Rev. Lett.* **2001**, *86*, 4338-4341.
200. Gellman, A. J.; Paserba, K. R., Kinetics and Mechanism of Oligomer Desorption from Surfaces: N-Alkanes on Graphite. *J. Phys. Chem. B* **2002**, *106*, 13231-13241.
201. Ernst, K.-H., Molecular Chirality at Surfaces. *Phys. Status Solidi B* **2012**, *249*, 2057-2088.
202. Ortega Lorenzo, M.; Baddeley, C. J.; Muryn, C.; Raval, R., Extended Surface Chirality from Supramolecular Assemblies of Adsorbed Chiral molecules. *Nature* **2000**, *404*.
203. Ronci, F., et al., Organizational Chirality Expression as a Function of the Chirality Measure of Simple Amino Alcohols on Cu(100). *Surf. Sci.* **2014**, 10.1016/j.susc.2014.02.006.
204. Zhang, J.; Li, B.; Cui, X.; Wang, B.; Yang, J.; Hou, J. G., Spontaneous Chiral Resolution in Supramolecular Assembly of 2,4,6-Tris(2-Pyridyl)-1,3,5-Triazine on Au(111). *J. Am. Chem. Soc.* **2009**, *131*, 5885-5890.
205. Silly, F.; Shaw, A. Q.; Briggs, G. A. D.; Castell, M. R., Epitaxial Ordering of a Perylenetetracarboxylic Diimide-Melamine Supramolecular Network Driven by the Au(111)-(22 \times √3) Reconstruction. *Appl. Phys. Lett.* **2008**, *92*, 023102.
206. Krasnikov, S. A.; Doyle, C. M.; Sergeeva, N. N.; Preobrajenski, A. B.; Vinogradov, N. A.; Sergeeva, Y. N.; Zakharov, A. A.; Senge, M. O.; Cafolla, A. A., Formation of Extended Covalently Bonded Ni Porphyrin Networks on the Au(111) Surface. *Nano Res.* **2011**, *4*, 376-384.
207. Wagner, M.; Hansen, J.; deSouza-Machado, R.; Liang, S.; Tobin, J.; Mason, M.; Brandt, S.; Tan, Y.; Yang, A. B.; Brown, F., Surface Morphology and Growth of Agbr on Ag(111). *Phys. Rev. B* **1991**, *43*, 6405-6410.
208. Poirier, G. E.; Pylant, E. D., The Self-Assembly Mechanism of Alkanethiols on Au (111). *Science* **1996**, *272*, 1145-1148.
209. Jewell, A. D.; Tierney, H. L.; Sykes, E. C. H., Gently Lifting Gold's Herringbone Reconstruction: Trimethylphosphine on Au(111). *Phys. Rev. B* **2010**, *82*, 205401(6).
210. Iski, E. V.; Jewell, A. D.; Tierney, H. L.; Kyriakou, G.; Sykes, E. C. H., Controllable Restructuring of a Metal Substrate: Tuning the Surface Morphology of Gold. *Surf. Sci.* **2012**, *606*, 536-541.

211. Min, B.; Deng, X.; Pinnaduwa, D.; Schalek, R.; Friend, C., Oxygen-Induced Restructuring with Release of Gold Atoms from Au(111). *Phys. rev. B* **2005**, *72*, 121410(4).
212. Poirier, G. E., Characterization of Organosulfur Molecular Monolayers on Au(111) Using Scanning Tunneling Microscopy. *Chem. Rev.* **1997**, *97*, 1117-1127.
213. Jewell, A. D.; Kyran, S. J.; Rabinovich, D.; Sykes, E. C., Effect of Head-Group Chemistry on Surface-Mediated Molecular Self-Assembly. *Chemistry* **2012**, *18*, 7169-78.
214. Bellisario, D. O.; Jewell, A. D.; Tierney, H. L.; Baber, A. E.; Sykes, E. C. H., Adsorption, Assembly, and Dynamics of Dibutyl Sulfide on Au{111}. *J. Phys. Chem. C* **2010**, *114*, 14583-14589.
215. Jewell, A. D.; Tierney, H. L.; Zenasni, O.; Lee, T. R.; Sykes, E. C. H., Asymmetric Thioethers as Building Blocks for Chiral Monolayers. *Top. Catal.* **2011**, *54*, 1357-1367.
216. Rossel, F.; Brodard, P.; Patthey, F.; Richardson, N. V.; Schneider, W.-D., Modified Herringbone Reconstruction on Au(111) Induced by Self-Assembled Azure Islands. *Surf. Sci.* **2008**, *602*, L115-L117.
217. Jewell, A. D.; Sykes, E. C. H.; Kyriakou, G., Molecular-Scale Surface Chemistry of a Common Metal Nanoparticle Capping Agent: Triphenylphosphine on Au(111). *Acs Nano* **2012**, *6*, 3545-3552.
218. Peköz, R.; Johnston, K.; Donadio, D., Adsorption of Dichlorobenzene on Au and Pt Stepped Surfaces Using Van Der Waals Density Functional Theory. *J. Phys. Chem. C* **2012**, *116*, 20409-20416.
219. Björk, J.; Hanke, F.; Stafström, S., Mechanisms of Halogen-Based Covalent Self-Assembly on Metal Surfaces. *J. Am. Chem. Soc.* **2013**, *135*, 5768-75.
220. Fujita, D.; Amemiya, K.; Yakabe, T.; Nejoh, H., Anisotropic Standing-Wave Formation on an Au (111)-(23×√3) Reconstructed Surface. *Phys. Rev. Lett.* **1997**, *78*, 3904-3907.
221. Goyhenex, C.; Bulou, H., Theoretical Insight in the Energetics of Co Adsorption on a Reconstructed Au(111) Substrate. *Phys. Rev. B* **2001**, *63*.
222. Chen, W.; Madhavan, V.; Jamneala, T.; Crommie, M. F., Scanning Tunneling Microscopy Observation of an Electronic Superlattice at the Surface of Clean Gold. *Phys. Rev. Lett.* **1998**, *80*, 1469-1472.
223. Bürgi, L.; Brune, H.; Kern, K., Imaging of Electron Potential Landscapes on Au(111). *Phys. Rev. Lett.* **2002**, *89*, 176801(4).
224. Kamna, M. M.; Stranick, S. J.; Weiss, P. S., Imaging Substrate-Mediated Interactions. *Science* **1996**, *274*, 118-119.
225. Sykes, E. C. H.; Han, P.; Kandel, S. A.; Kelly, K. F.; McCarthy, G. S.; Weiss, P. S., Substrate-Mediated Interactions and Intermolecular Forces between Molecules Adsorbed on Surfaces. *Acc. Chem. Res.* **2003**, *36*, 945-953.
226. Sykes, E. C. H.; Han, P.; Weiss, P. S., Molecule/Metal Surface Interactions Evidenced Quantum Mechanically Via Tip-Induced Cs₂ Interaction with Friedel Oscillations on Au{111}. *J. Phys. Chem. B* **2003**, *107*, 5016-5021.
227. Somorjai, G. A., The Flexible Surface: New Techniques for Molecular Level Studies of Time Dependent Changes in Metal Surface Structure and Adsorbate Structure During Catalytic Reactions. *J. Mol. Catal. A* **1996**, *107*, 39-53.
228. Stranick, S. J.; Kamna, M. M.; Weiss, P. S., Atomic-Scale Dynamics of a Two-Dimensional Gas-Solid Interface. *Science* **1996**, *266*, 99-102.
229. Silien, C.; Buck, M.; Goretzki, G.; Lahaye, D.; Champness, N. R.; Weidner, T.; Zharnikov, M., Self-Assembly of a Pyridine-Terminated Thiol Monolayer on Au(111). *Langmuir* **2009**, *25*, 959-967.
230. Yoon, J. K.; Son, W.-j.; Chung, K.-H.; Kim, H.; Han, S.; Kahng, S.-J., Visualizing Halogen Bonds in Planar Supramolecular Systems. *J. Phys. Chem. C* **2011**, *115*, 2297-2301.
231. Han, P.; Mantooth, B. A.; Sykes, E. C. H.; Donhauser, Z. J.; Weiss, P. S., Benzene on Au{111} at 4 K: Monolayer Growth and Tip-Induced Molecular Cascades. *J. Am. Chem. Soc.* **2004**, *126*, 10787-10793.
232. Mantooth, B. A.; Sykes, E. C. H.; Han, P.; Moore, A. M.; Donhauser, Z. J.; Crespi, V. H.; Weiss, P. S., Analyzing the Motion of Benzene on Au{111}: Single Molecule Statistics from Scanning Probe Images. *J. Phys. Chem. C* **2007**, *111*, 6167-6182.

233. Kirakosian, A.; Comstock, M.; Cho, J.; Crommie, M., Molecular Commensurability with a Surface Reconstruction: Stm Study of Azobenzene on Au(111). *Phys. Rev. B* **2005**, *71*, 113409.
234. Cheng, Z. H.; Gao, L.; Deng, Z. T.; Jiang, N.; Liu, Q.; Shi, D. X.; Du, S. X.; Guo, H. M.; Gao, H.-J., Adsorption Behavior of Iron Phthalocyanine on Au(111) Surface at Submonolayer Coverage. *J. Phys. Chem. C* **2007**, *111*, 9240-9244.
235. Cheng, Z. H.; Gao, L.; Deng, Z. T.; Liu, Q.; Jiang, N.; Lin, X.; He, X. B.; Du, S. X.; Gao, H.-J., Epitaxial Growth of Iron Phthalocyanine at the Initial Stage on Au(111) Surface. *J. Phys. Chem. C* **2007**, *111*, 2656-2660.
236. Jiang, N.; Wang, Y.; Liu, Q.; Zhang, Y.; Deng, Z.; Ernst, K. H.; Gao, H. J., Polymorphism and Chiral Expression in Two-Dimensional Subphthalocyanine Crystals on Au(111). *Physical chemistry chemical physics : PCCP* **2010**, *12*, 1318-22.
237. Theobald, J. A.; Oxtoby, N. S.; Phillips, M. A.; Champness, N. R.; Beton, P. H., Controlling Molecular Deposition and Layer Structure with Supramolecular Surface Assemblies. *Nature* **2003**, *424*, 1029-1031.
238. Marschall, M.; Reichert, J.; Diller, K.; Klyatskaya, S.; Ruben, M.; Nefedov, A.; Wöll, C.; Kantorovich, L. N.; Klappenberger, F.; Barth, J. V., Meta-Positioning of Carbonitrile Functional Groups Induces Interfacial Edge-on Phase of Oligophenyl Derivatives. *J. Phys. Chem. C* **2014**, *?*, 140123150838008.
239. Mu, Z.; Shu, L.; Fuchs, H.; Mayor, M.; Chi, L., Two-Dimensional Self-Assembly of Linear Molecular Rods at the Liquid/Solid Interface. *Langmuir* **2011**, *27*, 1359-1363.
240. Yin, S.; Wang, C.; Qiu, X.; Xu, B.; Bai, C., Theoretical Study of the Effects of Intermolecular Interactions in Self-Assembled Long-Chain Alkanes Adsorbed on Graphite Surface. *Surf. Interface Analys.* **2001**, *32*, 248-252.
241. Rondeau-Gagne, S.; Neabo, J. R.; Desroches, M.; Larouche, J.; Brisson, J.; Morin, J. F., Topochemical Polymerization of Phenylacetylene Macrocycles: A New Strategy for the Preparation of Organic Nanorods. *J. Am. Chem. Soc.* **2013**, *135*, 110-113.
242. Smoluchowski, R., Anisotropy of the Electronic Work Function of Metals. *Phys. Rev.* **1941**, *60*, 661-674.
243. Jensen, S. C.; Baber, A. E.; Tierney, H. L.; Sykes, E. C. H., Dimethyl Sulfide on Cu{111}: Molecular Self-Assembly and Submolecular Resolution Imaging. *Acs Nano* **2007**, *1*, 423-428.